Alma Mater Studiorum · Università di Bologna

SCUOLA DI SCIENZE

Corso di Laurea Magistrale in Astrofisica e Cosmologia

The first *Chandra* study of Abell 795: a FR0 radio galaxy at the center of a sloshing cluster

Tesi di Laurea Magistrale

Presentata da:
Francesco Ubertosi

Relatore:
Chiar.ma Prof.ssa
Myriam Gitti
Correlatori:
Prof. Fabrizio Brighenti
Dott.ssa Eleonora Torresi

Appello II
Anno Accademico 2019/2020

Abstract

The environment of galaxy clusters offers the possibility to study the interaction between the Intra Cluster Medium (ICM) and the galaxies embedded in this hot, X-ray emitting gas. In this framework, the Active Galactic Nuclei (AGN) in the cores of the brightest cluster galaxies (BCG) have been suggested to be responsible for quenching the cooling of the surrounding ICM, and also to be fuelled by the (greatly reduced) inflow of cold cluster gas. In some cases, the multiphase medium in the central region of clusters shows evidences of surface brightness discontinuities, which might be shock fronts - likely produced by the AGN activity - or cold fronts. A method to discriminate between the two categories consists in measuring thermodynamical properties (temperature, pressure) inside and outside these edges. Many cold fronts in cool core clusters have been related to *sloshing* motions of the cool gas, produced by a non-head-on encounter with another cluster. This type of interaction is likely to displace the X-ray emitting gas away from the central AGN: observationally, this results in the presence of offsets between these two components. As a consequence, the reservoir of cold gas to be accreted by the central supermassive black hole might be regulated by the sloshing time scale, hence affecting the emission properties of the AGN. The resulting picture consists in a tight interplay between the BCG central activity and the surrounding environment.

This work is dedicated to the galaxy cluster Abell 795 ($z \sim 0.137$), which - as we discovered - is characterized by the mechanisms cited above. We performed a study of this cluster with two main aims: (i) to accurately investigate the X-ray properties of the cluster A795, (ii) to link the cluster properties with those of the BCG, a compact FR0 radio galaxy, in order to understand if the environment might affect the emission preventing the formation of an extended radio morphology.

In order to fulfill these goals, we exploited an archival, but still unpublished, *Chandra* 30 ks observation and performed a detailed analysis of both the cluster and the central source. We measured the general properties of this cluster, which suggest that this system has a weakly cool core, and that dynamical disturbances are at play. In particular, the morphological inspection of this cluster has revealed a complex central environment: we discovered a sloshing spiral extending from the X-ray peak to ≈ 180 kpc north-west; along this feature we detected two prominent cold fronts at ~ 60 kpc and ~ 178 kpc from the center. We probed the effects of sloshing on the cluster cooling properties, and determined the timescale that regulates the gas oscillation. In addition to this, the search for radio data in literature has provided indications for the presence of diffuse radio emission coincident with the sloshing region: we described the main properties of this extended

source, and we provided a tentative classification as a radio *mini halo*.
The X-ray analysis of the central FR0 suggested that, at least in this case, the environment is not the main responsible for the lack of extended radio emission, i.e. the ambient medium is not so dense to eventually cause the premature disruption of the jets.
Moreover, the study of the ICM has led to the possible identification of two depressions in the ICM, which have been analyzed to determine whether a FR0 radio galaxy can *excavate* X-ray cavities, and if their power is enough to offset cooling in A795.
This thesis work is organized as follows:

- In the **First Chapter** we describe the main properties of galaxy clusters, focusing on the cooling flow problem and the recent findings about cold fronts. We also introduce the FR0s radio galaxies, and discuss the hypothesis for their radio compactness.

- In the **Second Chapter** we outline the main procedure for calibrating the *Chandra* dataset, along with the description of the morphological tools used to investigate the ICM.

- In the **Third Chapter** we report the results of our study of A795; after the morphological inspection of the ICM, we produce radial profiles of thermodynamic variables to investigate the cooling properties of this cluster, and we determine the properties of the two cold fronts.

- In the **Fourth Chapter** we analyze the properties of the BCG and of the surrounding environment, to assess whether the ambient medium is affecting the jet propagation, thus preventing the growth of the radio galaxy.

- In the **Fifth Chapter** we present the interpretation of our discoveries in A795, and perform a comparison with low frequency, archival radio data of this galaxy cluster.

- In the **Sixth Chapter** we briefly summarize the main results of this thesis work.

Sommario

L'ambiente degli ammassi di galassie offre l'opportunità di esaminare l'interazione tra l'*intra cluster medium* (ICM) visibile nella banda X, e le galassie che vi risiedono. In questo contesto, è stato determinato che i Nuclei Galattici Attivi (AGN) nelle regioni centrali delle *brightest cluster galaxies* (BCG) sono i principali responsabili del ridotto raffreddamento dell'ICM, e che il materiale da loro accresciuto proviene dalla frazione di gas circostante che si raffredda efficientemente. In alcuni casi, nelle regioni centrali degli ammassi il mezzo multifase mostra evidenti discontinuità in brillanza superficiale, che possono essere *shock fronts* - probabilmente dovuti all'attività dell'AGN - o *cold fronts*. Per distinguere tra le due possibilità è necessario misurare le proprietà termodinamiche dell'ICM (temperatura, densità, pressione) all'interno e all'esterno di queste discontinuità. Molti *cold fronts* negli ammassi *cool core* si originano a causa di moti di *sloshing* del gas freddo, dovuti a passaggi ravvicinati di altri oggetti massicci. Questo tipo di interazione è in grado di dislocare il gas freddo dall'AGN centrale: da un punto di vista osservativo, è possibile rilevare una separazione tra le due componenti. Di conseguenza, la disponibilità di gas freddo del buco nero supermassiccio al centro della BCG potrebbe essere influenzata dai tempi scala dello *sloshing*, influendo sulle proprietà dell'emissione degli AGN. Il quadro che si configura prevede quindi forti interazioni tra l'attività nucleare della BCG e l'ambiente circostante.

Questo lavoro di tesi è dedicato allo studio all'ammasso di galassie Abell 795 ($z \sim 0.137$), che abbiamo scoperto possedere le proprietà di cui sopra. L'analisi è stata svolta con l'obiettivo di: (i) studiare accuratamente le proprietà dell'emissione X di A795, (ii) mettere in relazione le proprietà dell'ICM con le caratteristiche della BCG, una radio galassia compatta di tipo FR0, per capire se l'ambiente può impedire la formazione di una morfologia radio estesa.

Al fine di portare a termine questi obiettivi, abbiamo esaminato un'osservazione di archivio non ancora pubblicata del telescopio *Chandra* (con esposizione di 30 ks), compiendo un'analisi dettagliata sia dell'ammasso che della sorgente centrale. Sono state misurate le proprietà complessive di A795: i risultati suggeriscono che questo sistema ha un *weakly cool core*, e che sono presenti perturbazioni dinamiche. In particolare, l'analisi morfologica ha rivelato un complesso ambiente centrale: abbiamo scoperto una spirale dovuta allo *sloshing* che si estende fino a ≈ 180 kpc in direzione nord-ovest dal centro dell'ammasso; lungo la spirale - inoltre - sono presenti due *cold fronts* a una distanza di ~ 60 kpc e ~ 178 kpc dal picco X. Abbiamo investigato l'effetto dello *sloshing* sul raffreddamento dell'ICM, ed è stata prodotta una stima del tempo scala che regola l'oscillazione del gas nella buca di potenziale dell'ammasso. Inoltre, la ricerca di dati radio d'archivio ci ha permesso di evidenziare la presenza di emissione radio diffusa, coincidente con la regione di *sloshing*:

sono state descritte le proprietà di questa sorgente estesa, che abbiamo tentato di classificare come "mini alone".
L'analisi dell'emissione X della FR0 centrale suggerisce che, almeno in questo caso, l'ambiente non è il principale responsabile della mancanza di emissione radio estesa, non possedendo una densità tale da giustificare una prematura distruzione dei getti.
Infine, lo studio dell'ICM ha portato alla scoperta di due possibili depressioni nell'emissione X, che sono state analizzate per capire se una FR0 può effettivamente scavare cavità, e se la loro potenza è sufficiente ad impedire un intenso raffreddamento del gas in A795.
Questo lavoro di tesi è strutturato come segue:

- Nel **Primo Capitolo** descriviamo le proprietà principali degli ammassi di galassie, concentrandoci sul *cooling flow problem* e sulle scoperte recenti a proposito dei *cold fronts*. Sono anche introdotte the radio galassie FR0, e discutiamo le principali ipotesi riguardanti la loro compattezza.

- Nel **Secondo Capitolo** riportiamo le procedure di calibrazione applicate al dataset *Chandra*, e descriviamo gli strumenti utilizzati per l'analisi morfologica dell'ICM.

- Nel **Terzo Capitolo** presentiamo i risultati dello studio di A795; dopo la descrizione della morfologia dell'ICM, vengono studiati i profili radiali delle variabili termodinamiche per investigare l'efficienza del raffreddamento del gas in questo ammasso. Inoltre, vengono determinate le proprietà dei due *cold fronts*.

- Nel **Quarto Capitolo** esploriamo le proprietà della BCG e dell'ambiente circostante, per capire se l'ICM influisce sulla propagazione del getto e sull'estensione della radio galassia.

- Nel **Quinto Capitolo** intepretiamo le nostre scoperte su A795, e le confrontiamo con dati d'archivio radio a bassa frequenza di questo ammasso di galassie.

- Nel **Sesto Capitolo** riassumiamo brevemente i risultati principali di questo lavoro di tesi.

Contents

Chapter 1

Introduction

In this chapter the main theoretical background informations regarding the subject of this work are presented, dedicating in the first section particular importance to the physical parameters, composition and global properties of galaxy clusters. Giving the predominant role of ICM in this work, thermal and non-thermal features of the multi-phase gas embedded in clusters are discussed. In the second section the *cooling flow problem* is described while the third section is dedicated to the main characteristics of cold fronts. The fourth section reviews recent findings on the population of compact radio galaxies named FR0s, and the last section introduces the target of this thesis.

1.1 Galaxy Clusters

A complete definition of a cluster of galaxies is difficult to enucleate, since these structures are made of different type of matter (baryonic and non-baryonic), in very different states (gas, galaxies and stars). In addition to that, even single components (like the hot gas filling the cluster space) show peculiar behaviours from one cluster to another. Nevertheless, clusters possess a unique feature: they are the largest gravitationally collapsed concentrations of matter in the Universe (e.g., Bahcall 1999). Indeed, they have sizes that range from a few to several Mpc, and typical masses of 10^{13-15} $M_{\odot}$. Clusters typically consist of $10-1000$ galaxies (bound together by the cluster self gravity), which represent 2-5% of the total mass (visible and dark matter) of the galaxy cluster, while the majority of the mass is due to dark matter, with a mass fraction of $\sim$0.8 (Bahcall, 1999). This component is responsible for the formation and growth of these structures: clusters form by subsequent mergers of smaller over-densities of matter; the deep potential wells of dark matter guide the process of merging and evolution of clusters of galaxies (White and Rees, 1978). The remaining component is the hot (with temperatures as high as 10^8 K) and tenuous (with typical electron densities $n_e \approx 10^{-3}\mathrm{cm}^{-3}$) gas which fills the cluster's

space: the intra cluster medium (ICM), with a mass fraction of ∼0.15-0.20 (e.g., Mohr et al. 1999). The gas physical properties, such as temperature, surface brightness, and density are useful tools to investigate many mechanisms related to the ICM.
Historically, clusters' extragalactic nature became clear after the work of Hubble in the first decades of the nineteenth century; afterwards, the investigation of clusters began to cover a wide range of aspects: distribution and properties of galaxies belonging to small or giant clusters, the origin and evolution of clusters and their dynamical status. In this picture the work of George Abell was remarkably important: he produced a catalogue containing 1682 clusters; he operatively defined as cluster any region containing at least 30 galaxies brighter than $m_3 + 2^m$ within $R \approxeq 1.5h^{-1}$ Mpc from the structure's center[1], and with a redshift $z < 0.2$ (Abell, 1958). The availability of samples of galaxy clusters allowed for population studies to be performed. In particular, in Abell's second catalogue clusters are parted in two populations: while some clusters display a regular and spheroidal form, others show evidence of dynamical activity, due to the presence of substructures and irregularities in the spatial distribution of galaxies (Abell et al., 1989). In the last decades, this distinction has become more specific: X-ray analysis of the emitting gas has allowed to distinguish between *cool core* and *non-cool core* clusters. While the first category is composed of relaxed clusters, the second one contains systems that display evidences of recent or on-going merging processes; we address this classification in Sect. 1.2. In the following subsections, the properties of galaxy clusters components are presented in the following order: dark matter, galaxies, and intra cluster medium.

1.1.1 Dark matter

Clusters of galaxies provide evidence for the existence of dark matter in several ways; the first proof came with the definition of the *missing mass problem* by Zwicky in 1937: he applied the virial theorem to clusters, in order to measure the mass of the Coma cluster from its velocity dispersion. The virial theorem for gravitationally bound and self-gravitating systems reads: $2T + W = 0$, where W is the gravitational potential energy and T is the kinetic energy, defined as:

$$W = -\frac{1}{2}\sum_{i \neq j} \frac{G m_{\rm i} m_{\rm j}}{r_{\rm ij}} \qquad T = \frac{1}{2}\sum_{i} m_{\rm i} v_{\rm i}^2 \tag{1.1}$$

where $m_{\rm i}$ and $m_{\rm j}$ are the masses of the i-th and j-th galaxies, $r_{\rm ij}$ is the distance between them and $v_{\rm i}$ is the speed of the i-th galaxy; the application of this theorem to clusters leads

[1] m_3 refers to the magnitude of the brightest cluster member; the h-notation is used to express the uncertainties associated to the correct value of the Hubble parameter $H_0 = 100\,h$ km s^{-1} Mpc^{-1} (e.g., Kashlinsky and Jones 1991).

Figure 1.1: Hubble Space Telescope mosaic image of the Coma cluster of galaxies (Madrid et al., 2018).

to a relation between the total mass of the cluster M and the radial velocity dispersion $\sigma_{\rm r}$:

$$M_{\rm tot} = \frac{3R\sigma_{\rm r}^2}{G} \tag{1.2}$$

where R is the cluster radius.

Using this relation Zwicky measured the mass of the Coma cluster, and found that the result would require a cluster mass-to-light ratio of 68 $M_\odot/L_\odot$ (Zwicky, 1937). This result suggested that there had to be a significant fraction of mass in clusters that was not emitting any light. Indeed, Zwicky concluded that the galaxy mass estimates had to be revised upwards, although only with *gravitational lensing* it could be possible to obtain more accurate mass determinations (Biviano, 2000). Although the technique of lensing at the time was far from being possible, the *missing mass problem* constituted one of the first indirect evidence for the need of an additional, non-emitting component, which was later referred to as *Dark Matter*.

At the present day it is widely recognised that most of the mass of clusters is accounted for by the dark matter component, distributed as halos around the whole cluster, and sub-halos embedding single galaxies. According to ΛCDM-cosmological model, the formation of clusters starts with perturbations in the primordial matter density field. These perturbations grow through dark matter dominated gravitational accretion and form gravitationally-bound structures (Voit, 2005). Since clusters of galaxies are thought to be the last structures that have been formed (e.g., Zhang 2016), they are used as sensitive

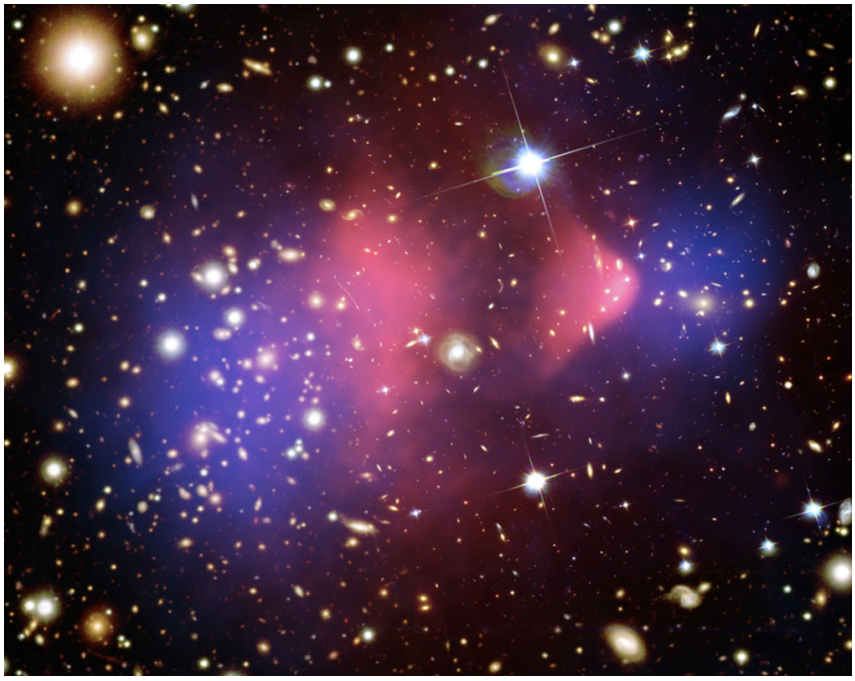

Figure 1.2: X-ray emission (pink) of ICM and mass concentration (blue) of the Bullet cluster, superimposed on the optical image Markevitch, 2005; Clowe et al., 2004.

probes for the cosmological models. Cluster abundance studies have produced strong constraints on the dark matter cosmological parameters (especially the dark + visible matter density parameter, Ω_m; Allen et al. 2011), and since the advent of lensing techniques the study of the nature of dark matter became possible. For example, by comparing lensing maps and X-ray images, a remarkable observational evidence that dark matter is made of non-interacting particles came from the study of the Bullet Cluster (Fig. 1.2): while the gas of the two merging sub-clusters shows clear signs of interaction, the lensing maps show that the potential wells (dominated by the mass of dark matter) of the two sub-clusters remain separate (Clowe et al., 2004).

1.1.2 Galaxies in clusters

Although galaxies inside clusters make up only $\approx 1\%$ of the system total mass, the overdensity of galaxies makes clusters quite easy to spot, especially in optical images. In particular, the Sloan Digital Sky Survey[2] has discovered more than 25,000 clusters with $z < 0.55$ and $M \geq 10^{14}$ $M_\odot$ (Rykoff et al., 2014). A general way to distinguish between large, rich clusters and smaller ones is by looking at their mass: while the term cluster refers to a virialized halo with mass greater than 10^{14} $M_\odot$, the term group is related to halos with masses around 10^{13} $M_\odot$; typically, rich clusters host 100-1000 galaxies while

[2]SDSS, a joint imaging and spectroscopic survey that works in the optical wavelength range and covers $\approx 15,000$ deg^2 of sky.

groups host 10-100 galaxies (Bower and Balogh, 2004).

Morphology: The study of galaxies inside clusters shows that there is a significant number of red ellipticals and S0 galaxies dominating these structures. These red sequence galaxies are no longer forming stars, and they lack large reservoirs of cold gas. Furthermore, while galaxies of this kind tend to be more concentrated in the central regions of clusters, the less numerous spiral galaxies are predominant in the outer region (e.g., Zhang 2016). This morphological segregation has first been noticed by Melnick and Sargent (1977), and has since been tried to explain by producing correlation between different morphological types and galaxies distribution parameters. The first idea considered the correlation between morphology and local projected galaxy density (Dressler, 1980); by studying 55 rich clusters Dressler found evidence of population gradients, indicating that the number of elliptical and S0 galaxies increases with increasing local galaxy density (see Fig. 1.3 panel *a*). Later works, such as Whitmore and Gilmore (1991), considered the cluster-centric normalized distance as the independent parameter and found that for small radii (approximately 0.5 Mpc) the elliptical fraction rises rapidly, while the spiral fraction is close to zero at the cluster center. In particular, they suggested that destructive mechanisms may be responsible for the relative fraction of the different types of galaxies.

In the last decades it has become clear that there exist mechanisms to quench star formation and transform galaxy morphologies: for example *ram pressure stripping* (Gunn and Gott III, 1972) consists in the removal of the interstellar medium (ISM) of galaxies while they move through the intergalactic medium. The ISM is subject to a pressure $P_{\rm ram}$ that depends on the galaxy speed $v_{\rm gal}$ and the ambient medium density $\rho_{\rm ICM}$ through:

$$P_{\rm ram} = \rho_{\rm ICM} v_{\rm gal}^2 \tag{1.3}$$

This pressure drags the ICM away from the galaxy, and it is particularly efficient if the galaxy speed is elevated - which is the case for the richest clusters, which display radial velocity dispersion of $400 - 1400$ km/s (Bahcall, 1999) - and if the galaxy moves in the central region of clusters, where number density of electrons reaches values of 10^{-3} cm^{-3}. Another mechanism could be *strangulation*, in which the supply of cold gas to the galaxy is halted: the warm gas phase residing in the galaxy halo is slowly stripped and removed; this might explain differences in terms of metallicity: while a rapid removal of gas - for example from ram pressure stripping - results in a passive galaxy with the same metallicity as its star forming progenitor, in the strangulation scenario the galaxy can continue to form stars from the already present interstellar medium, increasing its stellar metallicity in the process (Peng et al., 2015). Other effects include galaxy harassment (Moore et al.,

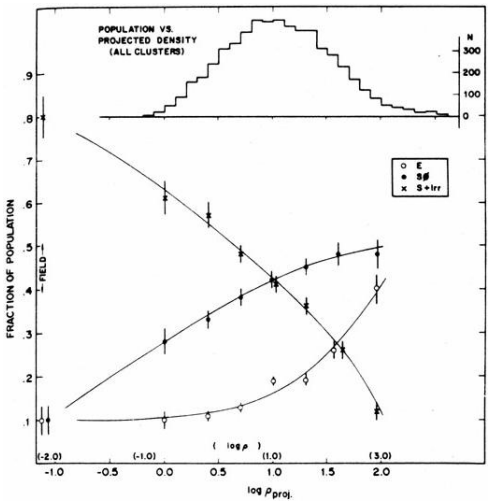

(a) *Morphology trends*

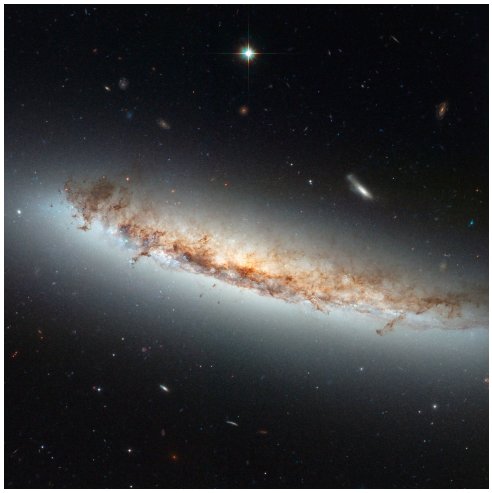

(b) *NGC4402*

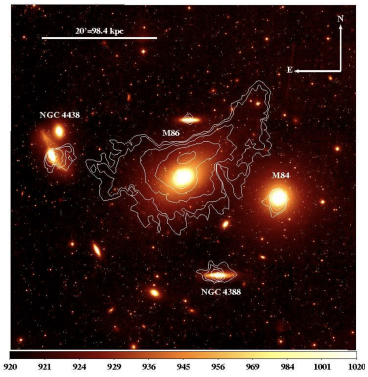

(c) *M86 - Virgo Cluster*

Figure 1.3: (a) The fraction of ellipticals, S0 and spiral galaxies as a function of the log of the local projected galaxy density (galaxies Mpc^{-2}); the histogram represents the number distribution of galaxies (Dressler, 1980). (b) HST optical (B, V filters) and infrared (I filter) image of galaxy NGC4402, credit: NASA & ESA. (c) r-band image of the region surrounding M86 (from the SDSS), with X-ray surface brightness contours overlaid in white (Ehlert et al., 2013).

1996), viscous-turbulent stripping (Nulsen, 1982), gas evaporation (Cowie and Songaila, 1977). In addition to indirect evidence for gas removal, these kind of processes have been observed in different spectral ranges: in Fig. 1.3 (panels *b* and *c*) two examples are displayed, showing how ram pressure stripping acts by removing gas from galaxies. While in NGC4402 optical image the disk of gas and dust appears curved as a result of the forces exerted by the external gas, the X-ray contours in Virgo Cluster reveal stripped gas tails extending to the north-west side of M86.

Galaxies distribution: It seems interesting to describe the distribution of galaxy in a rich cluster. The first analytical form proposed for the spatial distribution of galaxies in

clusters was Emden's bounded isothermal gas sphere model; this solution yields a profile slope that varies as (Bahcall, 1999):

$$\Sigma_g \sim \text{constant} \qquad \text{for} \quad r \leq R_c/3 \tag{1.4}$$

$$\Sigma_g \propto r^{-1.6} \qquad \text{for} \quad R_c \leq r \leq 10R_c \tag{1.5}$$

therefore

$$n_g \propto r^{-2.6} \quad \text{for} \quad R_c \leq r \leq 10R_c \tag{1.6}$$

where Σ_g and n_g are, respectively, the space and projected density profiles, and R_c is the cluster core radius.

The fact that Emden model fits quite well the data should not be taken as proof that clusters are isothermal spheres. In fact, different models have obtained equally good fit: the King profile (King, 1972) provides a successful description of cluster density profiles as well. In the central region, the King approximation for galaxy distribution writes:

$$\Sigma_g(r) = S_g^0(1 + r^2/R_c^2)^{-1} \tag{1.7}$$

$$n_g(r) = n_g^0(1 + r^2/R_c^2)^{-3/2} \tag{1.8}$$

with S_g^0 and n_g^0 are the central densities.

The King law was developed to describe the intensity profile of a spherically-symmetric stellar system, where the velocity dispersion of stars is isotropic and constant; although this and Emden's model provide good fits to the distribution of galaxies, it may be too simplistic to assume spherical symmetry and isothermality, as the former is not the case for many clusters which display clear signs of sub-clustering, while the assumption of the latter would imply that the mean velocity of galaxies inside a cluster as a function of radius is constant[3].

Nevertheless, it has been established that in the central regions of clusters, galaxies tend to be more concentrated: central number density of galaxies in rich compact clusters reaches values of $n_g^0 \sim 10^3 h^3$ galaxies per Mpc^{-3} (Bahcall, 1999). In particular in the last two paragraphs it has been pointed out that the central region of clusters are generally dominated by elliptical galaxies, and that in this dense ambient galaxies experience frequent interactions and mergers. This results are particularly inherent if the properties of the central brightest galaxy, or BCG, are discussed.

Properties of the BCG: Brightest cluster galaxies are the most massive galaxies (with M about 10^{13} $M_\odot$) and among the most luminous objects in the Universe at present

[3] Actually, radial dispersion velocity profile of numerous clusters show a clear decrease from the cluster's center to the outskirt (see for example Costa et al., 2018).

epoch (e.g., Cerulo et al. 2019). These giant elliptical galaxies are usually located near the geometric and kinematic center of their host clusters, and they do not appear to share the same luminosity profile of other cluster ellipticals: giant elliptical galaxies are usually well described by the *de Vaucouleurs law*:

$$\log I = \log I_e - 3.33\left[(r/r_e)^{1/4} - 1\right] \tag{1.9}$$

where r_e is the effective radius (the radius which contains half of the total light) and I_e is the surface brightness at r_e (de Vaucouleurs, 1948).
BGCs surface brightness profiles are well-described by a $r^{1/4}$ law in the central zone, but they show an excess of light in the outer parts (see Fig. 1.4): these features suggest that the evolution of the BCGs might be distinct from galaxy evolution in general (De Lucia and Blaizot, 2007).

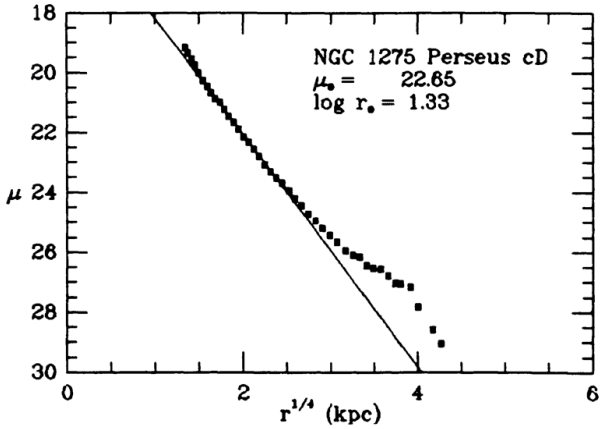

Figure 1.4: Surface brightness profile in units of mag arcsec^{-2} of NGC1275, the BCG of Perseus cluster; it is possible to see the deviation from the $r^{1/4}$ law in the outer radii (Schombert, 1986).

Theoretical models estimate that BCG grow in size through dry mergers (merger between galaxy with little gas fraction), with major mergers dominating in the early stages of formation and minor mergers becoming important at later stages; the formation of these galaxies is in good agreement with the hierarchical structure formation process predicted by dark matter cosmology models: as clusters combine to form more massive ones, galaxies inside clusters also merge to grow in mass and size (De Lucia and Blaizot, 2007). Therefore, the frequent galaxy interactions occurring in the central region of clusters are responsible for the formation and growth of these structures. BCGs are also related to many processes regarding the ICM in the central regions of clusters (see Subsect. 1.2.3), and the relations between the BCG centroid, the host cluster, and the properties of the emitting gas are fundamental topics discussed in recent papers (for example see Patel et al., 2006; Vantyghem et al., 2019; Russell et al., 2019).

1.1.3 The Intra Cluster Medium

While the total mass of clusters is dominated by dark matter, there is a significant baryonic contribution of $\sim 20\%$; the processes that involve baryons are indeed particularly significant for the dynamical and chemical evolution of galaxy clusters. The *intra cluster medium*, with $M_{gas} \sim 10^{13} - 10^{14} M_{\odot}$, comprises the majority of these baryons, and consists in a hot gas embedding galaxies which emits X-rays predominantly through thermal bremsstrahlung. In rich galaxy clusters, the hot gas reaches temperatures of 10^7-10^8 K; considering the relation $M_{tot} \propto T_{gas}^{3/2}$ (e.g., Kaiser 1986, the distinction between groups and clusters based on the mass can also be expressed in terms of ICM temperature: below 2×10^7 K it is usual to refer to groups, even though the transition is not sharp (Bykov et al., 2015).

Although the X-ray emission from the ICM is due to thermal processed, there is also a non thermal component whose presence is detectable in the radio frequency band and it appears to be related to diffuse radio sources. In fact, at the present day multi -wavelength studies of cluster of galaxies are essential to assess the properties and the dynamical state of the ICM. For the purpose and subject of this thesis it is then useful to discuss separately the properties of both - thermal and non-thermal - components.

Thermal component: The high temperature (0.5-15 keV[4]) of this component is set by the virialization process in the cluster's deep potential well: in the process of cluster formation a big fraction of the released gravitational energy is transformed into thermal energy that heats the ICM (Arnaud et al., 2010). This gas reaches electron number densities of $n_e \approx 10^{-2} - 10^{-3}$ cm^{-3} in the central regions that decrease to 10^{-4} cm^{-3} in the outer parts. The X-ray luminosity from this gas is due to thermal bremsstrahlung: for a gas emitting between E_1 and E_2 with uniform electron density n_e and a radius R_X it is possible to write:

$$L_X \propto n_e^2 R_X^3 T_X^{1/2} g(e^{-E_1/kT_X} - e^{-E_2/kT_X}) \tag{1.10}$$

where the Gaunt factor g (order of ≈ 1) is a slowly varying function of energy and temperature.

Typically, the X-ray luminosity of clusters in the 2-10 keV band is $\sim 10^{42.5} - 10^{45}$ erg s^{-1} (Bahcall, 1999). Apart from the continuum emission, in many clusters it is possible to detect emission lines from the ionized gas, composed by H, He and heavy elements (metals). In fact, in the soft X-ray band[5] there are several spectral lines which are suited for abundance measurements (Bykov et al., 2015): the detection of the 7 keV iron line

[4] 1 keV $\approx 1.16 \times 10^7$ K.

[5] between 0.1 and 10 keV

has allowed to assess an iron abundance in the intra cluster gas of [Fe/H] ~ 0.3 solar (Bahcall, 1999).

Since the ICM is highly ionized, Coulomb collisions are the dominant forms of interaction in the plasma; this yields a mean free path for particles in the ICM of:

$$\lambda_{\rm e} \sim \lambda_{\rm i} \sim 23\,{\rm kpc}\left(\frac{n_{\rm p}}{10^{-3}\,{\rm cm}^{-3}}\right)^{-1}\left(\frac{T}{10^{8}\,{\rm K}}\right)^{2} \tag{1.11}$$

where $n_{\rm p}$ is the particles number density and T is the gas temperature.

As the mean free path is typically smaller than the cluster size, the ICM can be treated as a fluid: in particular, a sound wave crosses the cluster over a time-scale $t_{\rm sc}$ given by:

$$t_{\rm sc} \sim 6.6 \times 10^{8}\,{\rm yr}\left(\frac{D}{\rm Mpc}\right)\left(\frac{T}{10^{8}\,{\rm K}}\right)^{2} \tag{1.12}$$

where D is the cluster size.

The sound crossing time-scale appears smaller than clusters typical age (a few Gyr), therefore the ICM may be described as in hydrostatic equilibrium (e.g., Molendi 2004). Among the first model of ICM it is possible to denote the hot ICM model proposed by Cavaliere and Fusco-Femiano (1976): they assumed that gas and galaxies are in equilibrium in the same potential $\phi(r)$; following this assumption the galaxy and gas distribution ($\rho_{\rm gal}$ and $n_{\rm gas}$) can be directly related through:

$$\frac{1}{n_{\rm gas}}\frac{d}{dr}\left(\frac{n_{\rm gas}kT}{\mu m_{\rm p}}\right) = -\frac{d\phi}{dr} = \frac{1}{\rho_{\rm gal}}\frac{d(\sigma_r^2\rho_{\rm gal})}{dr} \tag{1.13}$$

where μ is the mean molecular weight, $m_{\rm p}$ is the proton mass, T is the gas temperature, and $\sigma_{\rm r}$ is the galaxy velocity dispersion, assumed to be isotropic.

Assuming for simplicity that the gas has an isothermal equation of state, Eq. 1.13 reduces to:

$$\frac{n_{\rm gas}(r)}{n_{\rm gas}(0)} = \left[\frac{\rho_{\rm gal}(r)}{\rho_{\rm gal}(0)}\right]^{\beta} \quad \text{with} \quad \beta = \frac{\mu m_{\rm p}\sigma_r^2}{kT} \tag{1.14}$$

By using the empirical King model of Eq. 1.8 to describe the distribution of galaxies, the final result is:

$$n_{\rm gas}(r) = n_{\rm gas}(0)\left[1 + \left(\frac{r}{r_{\rm c}}\right)^{2}\right]^{-3\beta/2} \tag{1.15}$$

The solution obtained in Eq. 1.15 is referred to as *β-model*, and yields the advantage of having a small number of parameters and a simple form. Moreover, the surface brightness profile $S_{\rm x}(r)$ also seems to follow a β-model with slope of $-3\beta + 1/2$ (Bahcall and Lubin, 1993).

With the launch of modern, high resolution X-ray space telescopes, it became clear that

clusters do not follow completely the isothermal β-model: typically, temperature decreases towards the edges and, in some cases, towards the cluster center. In fact, from an X-ray perspective, clusters are found in two variants: those with a cool, dense (central density of $\sim 10^{-2}$ cm^{-3}) core and those lacking such features. Cool-core clusters are actually better described by a double β model, with two different slopes describing inner and outer part (Fig. 1.5 shows how the two β components provide a good fit to the surface brightness profile of the A1060 cluster).

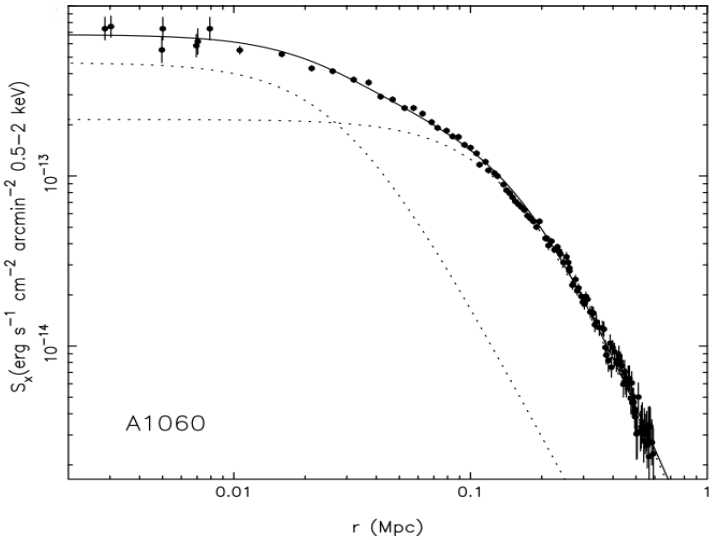

Figure 1.5: A1060 surface brightness profile, obtained with *ROSAT* and fitted with a double β-model; the dotted lines represent the two components (Xue and Wu, 2000).

It is possible to assume hydrostatic equilibrium as a first approximation when the whole cluster is considered and extremely high resolution studies are not required or possible (Arnaud et al., 2010): an important result that arises from this approximation is the possibility to compute the cluster mass (Bahcall, 1999). In the hydrostatic equilibrium model, the gas distribution follows:

$$\frac{dP_{\rm gas}}{dr} = -\frac{GM_{\rm tot}(\leq r)\rho_{\rm gas}}{r^2} \tag{1.16}$$

where $\rm P_{gas}$ and $\rho_{\rm gas}$ are the gas pressure and density, while $M_{\rm tot}(\leq r)$ is the total mass of the cluster enclosed within a radius r. By substituting in $P_{\rm gas}$ its definition ($P = \rho kT/\mu m_{\rm p}$) the cluster mass can be written as:

$$M_{\rm tot}(\leq r) = -\frac{kTr}{\mu m_{\rm p} G}\left(\frac{dln\rho_{\rm gas}(r)}{dlnr} + \frac{dlnT}{dlnr}\right) \tag{1.17}$$

where T is the gas temperature. By measuring radial temperature and density profiles, it is then possible to provide a measurement of a cluster mass.

Non-thermal component: When the ICM is investigated in the radio band, it is possible to find synchrotron emission related to diffuse sources. The different types of diffuse radio emission in clusters are:

- Halos: diffuse sources characterized by low surface brightness ($\sim \mu$Jy arcsec^{-2} at 20 cm (Feretti and Giovannini, 2008)) permeating the central regions of clusters. They typically reach sizes of about $\sim$ 1 Mpc, they display a regular morphology, and usually the radio surface brightness peak corresponds to the X-ray center. Their radio spectrum is usually steep ($\alpha \geq 1$), indicating that these are ageing radio sources. It is thought that radio halos emerge from violent cluster activity, since they are always found in merging clusters.

- Relics: diffuse extended sources, similar to halos in terms of low surface brightness, size and steep spectrum, but generally detected in the cluster peripheral regions. They are strongly polarized ($\sim 20\%$), and they are observable as elongated structures with the major axis almost perpendicular to the direction of the cluster center.

- Mini-Halos: although these structures could be seen as smaller versions of halos (since they have low surface brightness, regular morphology and sizes of a few hundreds of kpc), they do not seem to be related to violent merging processes. The study of mini-halos has been limited by their small number: the detection of these sources can be difficult, because it requires to be able to resolve the BCG radio emission and to separate it from the diffuse component. They are usually associated with cool core clusters, and it has been hypothesized that the re-acceleration of electrons responsible for the synchrotron emission is due to turbulence in the ICM (see e.g., Gitti et al. 2004; ZuHone et al. 2012a, 2015; Giacintucci et al. 2014).

The presence of this emission indicates that there are on-going non-thermal processes in the intra cluster medium, related to relativistic particles (electrons and protons) and magnetic fields in the cluster volume. The importance of this component is that it is extended to significant portions of the cluster, and it shows connections with other X-rays properties: this can be seen as an evidence that this diffuse radio emission carries information on the cluster history and evolution (Feretti and Giovannini, 2008).
The synchrotron radiation is produced by the spiralling motion of relativistic particles along magnetic field lines: A particle with energy $E = \gamma m_e c^2$ (γ is the Lorentz factor) in a magnetic field $\mathbf{B}$ is subject to a force given by $\mathbf{v}\times\mathbf{B}$ that compels it to follow a spiral path along the field lines, emitting radiation into a cone of half-angle $\approx \gamma^{-1}$. A standard assumption for astrophysical environments is that of a homogeneous population of electrons that can be described by a power law energy distribution between E and

E+dE:

$$N(E)dE = N_0 E^{-\delta} dE \tag{1.18}$$

Integrating over the contribution of each electron it is possible to obtain the total monochromatic emissivity $J(\nu)$, which is then written as:

$$J(\nu) \propto N_0 (B \sin\theta)^{1+\alpha} \nu^{-\alpha} \tag{1.19}$$

so that the total intensity spectrum follows a power-law with spectral index $\alpha = (\delta - 1)/2$. If a population of electrons is emitting synchrotron radiation, a particle's energy decreases with time following:

$$E = \frac{E_0}{1 + b(B \sin\theta)^2 E_0 t} \tag{1.20}$$

where E_0 is the initial energy, and $b = 2e^4/(3m_e^4 c^7) = 2.37 \times 10^{-3}$ c.g.s. units.
Therefore, the energy losses of each particle will result in a over-all modification of the synchrotron spectrum: after a certain time t^*, particles with initial energy E_1 will have lost more energy than those with initial energy $E_2 < E_1$; this produces a critical frequency $\nu*$ in the spectrum, such that for $\nu > \nu*$ the spectrum steepens. This means that spectra showing spectral breaks or steep spectral index are signs of an electron population that is *ageing*.
The total energy of a synchrotron source is due to the energy of electrons, protons, and the energy in magnetic fields: $E_{\rm tot} = E_{\rm el} + E_{\rm pr} + E_{\rm B}$. Assuming that the energy of protons is a fraction of the energy of electrons ($E_{\rm pr} = kE_{\rm el}$), it is possible to derive a condition of minimum energy: this occurs when the contributions of the magnetic field and the relativistic particles are approximately equal:

$$E_{\rm B} = \frac{3}{4}(1 + k) E_{\rm el} \tag{1.21}$$

This is why the minimum energy is referred to as equipartition value; the magnetic field that satisfies this condition depends on the minimum energy density $e_{\rm min} = E_{\rm min}/V\phi$ (where ϕ is the filling factor, usually assumed to be ~ 1) through:

$$B_{\rm eq} = \left(\frac{24\pi}{7} e_{\rm min}\right)^{1/2} \tag{1.22}$$

The power of this definition relies on the fact that $e_{\rm min}$ can be expressed in terms of observable parameters:

$$e_{\rm min} = 1.23 \times 10^{-12} (1 + k)^{4/7} (\nu_0)^{4\alpha/7} (1 + z)^{\frac{12+4\alpha}{7}} I_0^{4/7} d^{4/7} \tag{1.23}$$

where I_0 is the source brightness observed at frequency ν_0, d is the source depth along the line of sight, z is the source redshift and α is the spectral index of the radio emission. Although this definition provides a useful method to determine the magnetic field intensity, there are some uncertainties related to the ratio of the energy in relativistic protons to that in electrons, expressed by the factor k, and to the value of the volume filling factor ϕ (Feretti and Giovannini, 2008). Apart from synchrotron emission, the existence of intra-cluster magnetic fields is also probed by Faraday Rotation Measure of radio sources located behind and inside galaxy clusters (Clarke, 2004).
The radio emission of diffuse sources in galaxy clusters is due to magnetic fields with intensities in the range 0.1-10 μG and a population of relativistic electrons with Lorentz factor $\gamma \gg 1000$; the latter are probably (re-)accelerated to this energies by ICM shock waves and turbulence (for evidences in support of this explanation see e.g., Gitti et al. 2004; Brunetti and Jones 2014). As it is possible to see from Fig. 1.6, the diffuse emission is extended over the cluster scale.

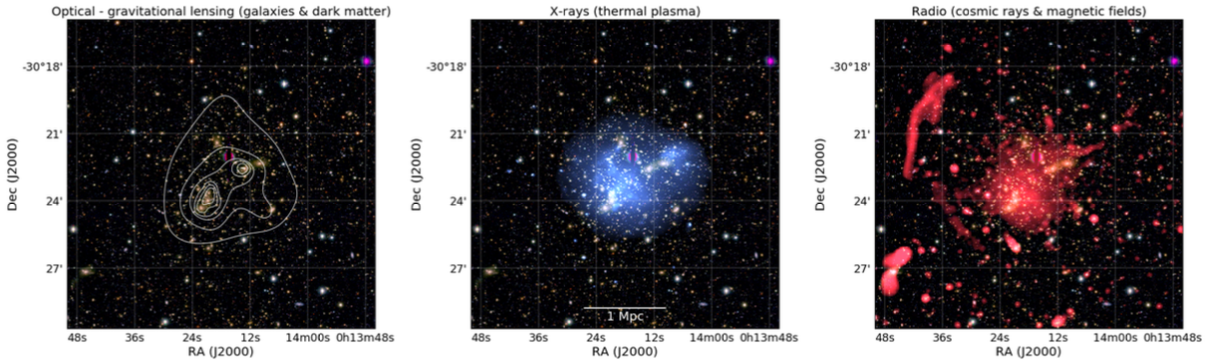

Figure 1.6: Galaxy cluster Abell 2744. *Left* panel: optical image obtained with *SUBARU* with white contours representing mass surface density derived from lensing; *central* panel: X-ray emission from thermal ICM (*CHANDRA*); right panel: 1.4 GHz *VLA* image tracing diffuse radio emission. Reproduced from Van Weeren et al. (2019).

Considering magnetic fields in clusters, their origin is still debated: they might result from the amplification of much weaker *seed* fields during merger and structure formation, although it is not clear how this *seed* fields have been generated (for a review about the origin of magnetic fields in clusters see e.g., Donnert et al. 2018).

1.1.4 Optical, radio and X-ray properties

This subsection provides an overview of the main information obtainable by studying the many emission mechanisms found in galaxy clusters, in particular through the consideration of how clusters appear when observed in specific spectral ranges. Considering the topic of this thesis, this subsection is particularly dedicated to processes which involve an

interaction between the X-ray emitting ICM and the galaxies hosted in galaxy clusters.

Optical and IR Optical radiation detected from galaxy clusters is mainly due to thermal emission mechanisms, in particular black body continuum and emission lines from the cluster galaxies. First of all, photometric studies of over-densities of galaxies allow for the detection of these structures: clusters and groups are usually identified by optical surveys as a concentration of red sequence galaxies (e.g., Rykoff et al. 2014); in addition to this, clusters photometric redshift can be inferred from optical colours . Cluster of galaxies are also discovered in infrared images, although this spectral range is more suitable for studying high redshift clusters (z > 1): at increasing distance z from the observer, galaxies spectra are shifted to longer wavelengths following:

$$\frac{\lambda_{\rm obs} - \lambda_{\rm i}}{\lambda_{\rm i}} = 1 + z \tag{1.24}$$

where $\lambda_{\rm obs}$ is the observed wavelength, and $\lambda_{\rm i}$ is the intrinsic, rest-frame wavelength of the incoming radiation; therefore, the optical emission from galaxies in high redshift clusters tends to be shifted in the infrared band.
Photometric studies of galaxies in clusters have allowed to discovery the morphological segregation that occurs in these objects (see Chap. 1.1.2), and they are in general used to determine whether the environment influences the evolution of galaxy populations (Braglia, 2008). Moreover, from optical imaging data it is possible to determine cluster masses: an estimator is the number count of cluster galaxies, but it is also possible to assess the cluster total mass by studying the gravitational lensing effects caused by the bending of light by the cluster mass distribution (for a review see e.g., Hoekstra et al. 2013).
Optical and infrared spectroscopy of clusters is also a powerful tool to determine structural, dynamical and energetic properties. From the study of spectral lines it is possible to determine the spectroscopic redshift of clusters (Fig. 1.7), and also the velocity dispersion of the cluster members. It the last years the study of emission lines related to the brightest cluster galaxies became an extremely important tool to explore the mechanisms occurring in the central regions of clusters (e.g., the Hα-emitting warm gas study of Hamer et al., 2016). The optical or infrared detection of cold gas near the BCG is fundamental to study the gas cycle and the possibility of enhanced star formation in the central galaxy.

Radio Studies at radio wavelengths allow the investigation of important components of galaxy clusters. As pointed out in Section 1.1.3, an important aspect of cluster radio emission is represented by the diffuse radio sources which prove that the ICM is mixed with non-thermal components, whose knowledge has increased over time due to sensitive

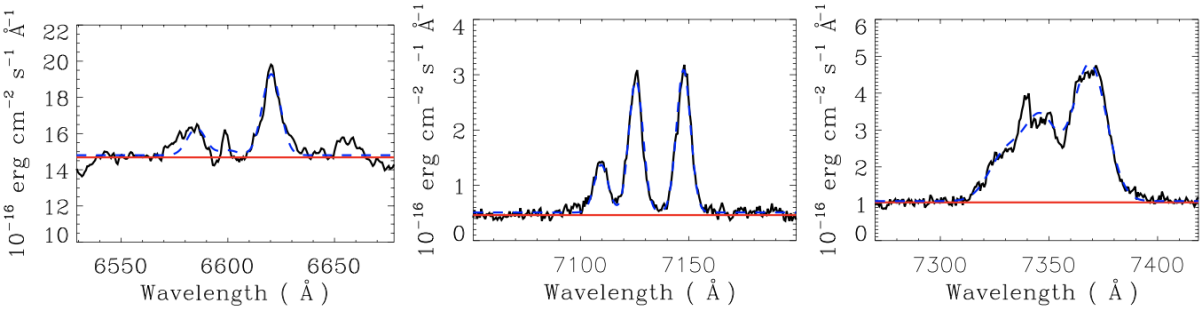

Figure 1.7: From *left* to *right*: optical spectra of NGC 5846, Abell 478, Abell 1348 clusters. These spectra show the Hα and [NII] lines, used to determine the redshift of these sources; the blue dashed line represents the best fit spectral model (Hamer et al., 2016).

radio images and theoretical studies. The discovery of diffuse cluster radio emission has been fundamental in terms of explaining important physical processes in clusters of galaxies: diffuse synchrotron sources are thought to be powered by the turbulence and shock structures of large-scale environments, therefore studies in the radio domain are essential proxy of shocks and turbulence even in cases where other wavebands could not be helpful (for reviews on diffuse radio emission see Feretti et al. 2012; Brunetti and Jones 2014).

The radio emission in clusters can also originate from individual galaxies in the form of a radio loud *Active Galactic Nucleus* (AGN), and it differs from the one observed in galaxies outside of clusters because it is often extended beyond optical boundaries (from a few kpc to about $\sim$ 1 Mpc) in a high density environment; this causes strong interactions between the radio emitting regions and the ICM, which are observed in *tailed radio galaxies* (Rudnick and OwEN, 1976) , low-power radio sources with a bent large scale radio emission, forming features similar to tails. These sources are divided in two categories: narrow-angle tailed sources (NAT) - which have a small angle between the tails -, and wide-angle tailed sources (WAT), which have a larger angle between the tails. The standard interpretation of the tailed radio morphology is that the jets are curved by ram pressure from the high-velocity host galaxy moving through the dense ICM (Feretti and Giovannini, 2008). The bending can be described by:

$$R \sim h \left(\frac{\rho_{\rm j}}{\rho_{\rm e}} \right) \left(\frac{v_{\rm j}}{v_{\rm g}} \right)^2 \tag{1.25}$$

where R is the radius of curvature, ρ is the density, v is the speed (j refers to jet, e to the external medium and g to the galaxy), and h is the scale height over which the ram pressure is transmitted to the jets. This equation allows to put important constraints on the jet and ICM dynamics. Spectral studies along the tails provide estimates of the

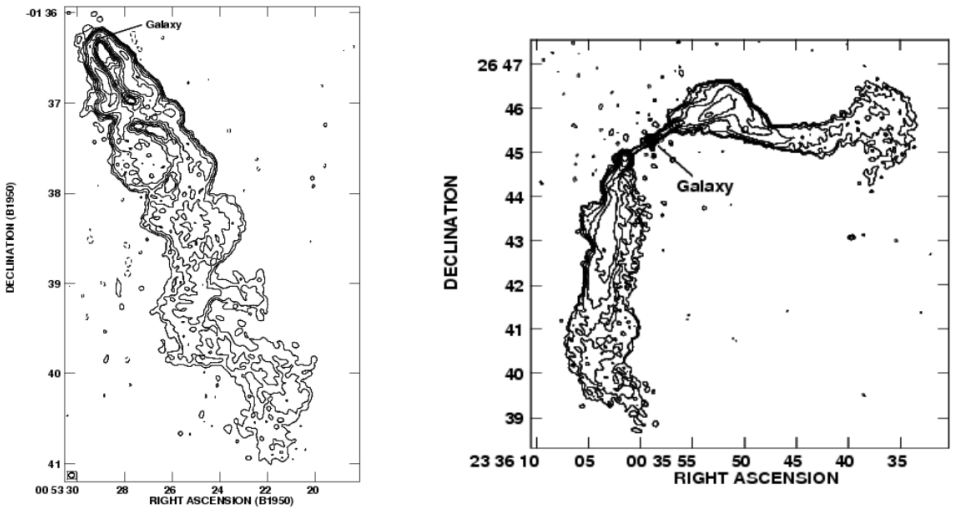

Figure 1.8: *Left*: NAT 0053-016 galaxy in the cluster A119; *right*: WAT 3C465 in the cluster A2634. Reproduced from Feretti and Giovannini, 2008.

age of the radio plasma: since spectral steepening are indicative of an ageing electron population, by measuring the frequency $\nu_{\rm b}$ at which the spectrum steepens it is possible to derive the age of the lobes:

$$t = 1060 \frac{B^{0.5}}{(B^2 + B_{\rm IC}^2)} [(1+z)\nu_{\rm b}]^{-0.5} \quad \text{Myr} \tag{1.26}$$

where B and B_{IC} are, respectively, the magnetic fields of the radio plasma and of the CMB, and z is the redshift.

By combining the extent of the tails with the radiative age t, it is possible to infer the galaxy speed within the cluster (e.g., Sebastian et al. 2017); furthermore, due to their presence in dense environments, WATs and NATs can be used to discover high-z galaxy clusters: while in X-ray and optical bands high-z studies imply consistent observational efforts, radio observation make these sources fairly accessible with high resolution (arc-second scale) set-up.

Radio observations have become extremely important to determine the properties of another sign of interaction between galaxy activity and ICM: deep X-ray observations toward cool core systems discovered X-ray cavities filled with synchrotron plasma visible at GHz frequency; for example clusters like Perseus and Hydra A display big cavity systems which indicate that the radio galaxy is significantly impacting the ICM, inflating bubbles in the thermal gas and driving weak shocks and sound waves through the intra cluster medium (McNamara and Nulsen, 2007). The study of the radio properties of these structures provides reliable informations on the cycles of activity of the central radio galaxy, and the total energy injected into the cluster ICM throughout the cluster lifetime (for an extended

explanation of this phenomenon, see Sect. 1.2).

X-ray Since the launch of the *Uhuru* X-ray satellite in 1970, many properties of sources associated with galaxy clusters were discovered: clusters of galaxies are the most common bright extragalactic X-ray sources, with luminosities up to $\approx 10^{43} - 10^{45}$ erg/s; their emission is extended over the cluster scale ($\approx$ few Mpc) and it does not show signs of time variability (unlike the spectra of compact sources associated with nuclei of galaxies), so that the emission is not the result of many compact sources, but truly diffuse (Sarazin, 1986). It is now established that this emission results from the hot, tenuous plasma which fills the cluster space. Three fundamental emission processes contribute to the radiation: free-free or bremsstrahlung radiation caused by the deflection of an electron due to the fly-by of an ion, recombination radiation, and de-excitation radiation of an electron changing the quantum level in an ion. All these radiative processes depend on the collision (i.e. close encounter) of an electron and a ion. Due to the very low density of ICM ($10^{-3} - 10^{-4}$ cm^{-3}) all the ions excited by collisions have sufficient time for radiative de-excitation before de-exciting collisions occur. Since the collision rates are function of temperature, that the shape of the resulting spectrum is a function of temperature and chemical composition (Böhringer and Werner, 2010); Fig. 1.9 shows an example of a galaxy cluster X-ray spectrum, with the emission lines of O, Ne, Mg, Si, S, Ar, Ca, Fe and Ni.

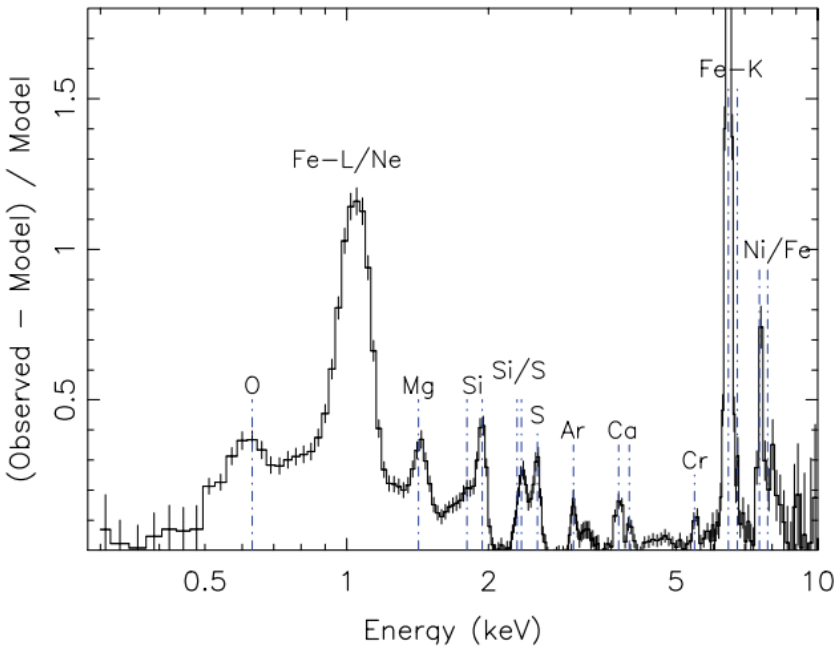

Figure 1.9: The X-ray spectrum of the cluster 2A 0335+096, observed with *XMM-Newton* EPIC (Böhringer and Werner, 2010).

Clusters of galaxies are extremely useful to study the nucleosynthesis and chemical enrichment of the Universe; the cluster potential well keeps all the metals produced by the stellar populations of the member galaxies within the cluster, and a dominant fraction of these metals is part of the hot ICM. Therefore, X-ray spectroscopy provides an accurate measure of metal abundances, which can put important constraints on the star formation history of clusters and the chemical evolution of the Universe.
Abundance profiles can be precise indicators of the dynamical state of the ICM: based on the Fe abundance profile (Fig. 1.10), De Grandi et al. (2004) concluded that the central abundance peak is due to the metals released by the stellar population of the BCG galaxy. However, the observed metal mass profiles are much less peaked than the optical light, which implies that the metals get mixed and transported out most probably by the AGN/ICM interaction: the bubbles of radio emitting relativistic plasma, produced by the jets of the AGN, uplift the metal rich gas from the central parts of the galaxy (Rebusco et al., 2005).

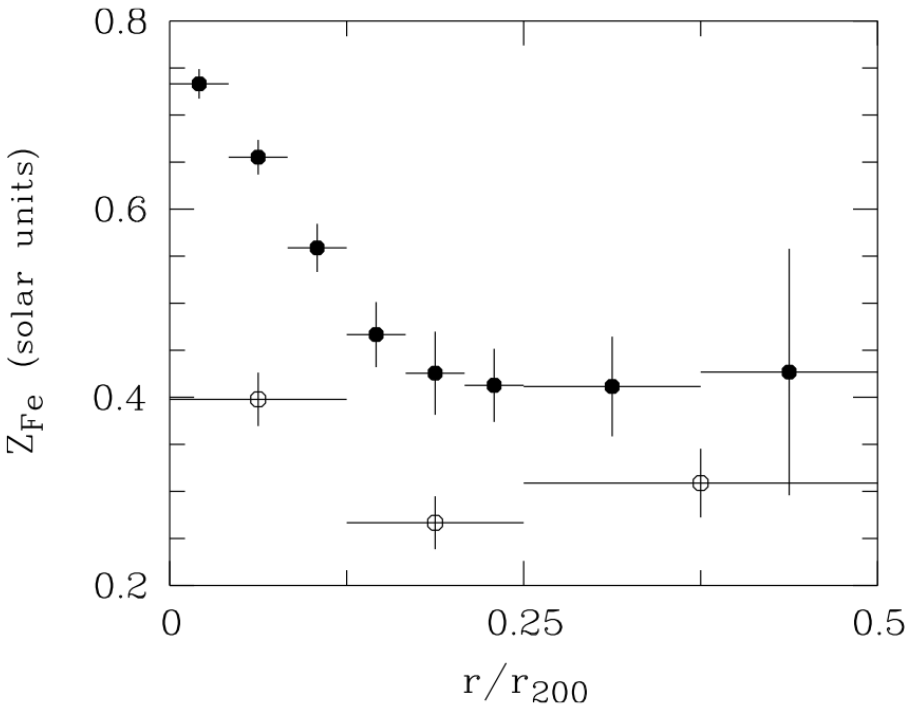

Figure 1.10: Average metallicity radial profile for cool core (filled circles) and non-cool core (open circles) clusters in the sample of De Grandi et al. (2004).

Global temperature estimates are also useful tools to build scale relations that can describe the population of clusters in the Universe. In the process of formation, galaxy clusters reach an equilibrium configuration described by the Virial Theorem. Considering a scenario in which only gravity is important, the object resulting from this event can be described through self-similar models: Numerical simulations such as the one performed

by Navarro et al. (1995) have shown that self similarity holds for the gas component of galaxy clusters if the effects of gravity and compressional heating are included, while dissipative, non-gravitational phenomena are excluded. As a consequence, in the hierarchical scenario predicted from ΛCDM the small structures which formed earlier are expected to be scaled down versions of the big ones. In this picture there are some useful relations between the X-ray properties of the gas that can be derived, once hydrostatic equilibrium is assumed (Giodini et al., 2013):

$$M_{\rm tot} \propto T_{\rm gas}^{3/2} \qquad\qquad L_{\rm X} \propto T_{\rm gas}^{2} \tag{1.27}$$

where $M_{\rm tot}$ is the cluster mass, $T_{\rm gas}$ is the ICM temperature and $L_{\rm X}$ is the X-ray luminosity emerging from the intra cluster medium because of bremsstrahlung radiation. These two equations hold for clusters where dissipative processes can be ignored; therefore, a departure from this prediction can be used to quantify the importance of non-gravitational processes.

Another useful quantity to characterize the ICM is the entropy S, which can be written as:

$$S = \frac{kT_{\rm gas}}{n_{\rm e}^{2/3}} \tag{1.28}$$

where $n_{\rm e}$ is the electron number density. It is then possible to define the following third scaling law: $S \propto T_{\rm gas} \propto M_{\rm tot}^{2/3}$ for purely gravitational heating. These relations are expected not to be applicable in the very central core of clusters (due to AGN activity) and in disturbed systems undergoing mergers. Indeed, recent surveys have found that scaling relations seem to hold quite well for massive cool core clusters (excluding the core), while low mass systems seem to depart from the self similarity hypothesis (Vikhlinin et al., 2009; Maughan et al., 2012).

1.2 Cooling flows

A fundamental topic regarding galaxy clusters and the intra cluster medium is the *cooling flow problem*, which has arisen since the gas has been observed to be cooling at rates smaller than predicted. In this section the standard cooling flow model is presented, and then the main issues of this model are listed. Following that, it is reported how different mechanisms have been proposed to explain the observational evidences for the need of a feedback process, leading to the *self-regulated feedback loop* that has been established as the favoured scenario to explain the cooling flow problem.

1.2.1 Standard cooling flows

Considering the emission from the hot ICM in clusters, it is possible to determine how this loss of energy for the gas impacts the global properties. First of all, the *cooling time* over which the ICM radiates away a significant fraction of its energy can be computed as the time taken for the gas to radiate its enthalpy per unit volume $H_{\rm v}$:

$$t_{\rm cool} \approx \frac{H_{\rm v}}{n_{\rm e} n_{\rm H} \Lambda(T)} = \frac{\gamma}{\gamma - 1} \frac{kT}{\mu X n_{\rm e} \Lambda(T)} \tag{1.29}$$

where $n_{\rm e}$ is the electron number density, $n_{\rm H}$ is the hydrogen number density, $\gamma = 5/3$ is the adiabatic index, $\mu \cong 0.6$ is the molecular weight, $X \approx 0.7$ is the hydrogen mass fraction and $\Lambda(T)$ is the cooling function (e.g., Gitti et al. 2012).
This relation can be approximated as $t_{\rm cool} \propto T^{\alpha}/n_{\rm e}$ (where -1/2 < α < 1/2 and $n_{\rm e}$ is the electron density), so that it is possible to point out that since the intra cluster gas is densest in the core of a cluster (Eq. 1.15), the cooling time $t_{\rm cool}$ is expected to be shortest in that region (Fabian, 1994). A cooling flow arises inside the *cooling radius* $r_{\rm cool}$, which is the radius at which $t_{\rm cool}$ is less than the time for which the system has been relaxed, usually assumed to be the look-back time at $z = 1$ (that is approximately 7.7 Gyr) (e.g., Gitti et al. 2012).
The standard model of cooling flow (Fabian, 1994) describes this process as pressure driven: the gas pressure at $r_{\rm cool}$ is due to the weight of the gas outside this radius, for which cooling is not efficient. Within $r_{\rm cool}$ the X-ray emitting gas is reducing its temperature, and in order to maintain the pressure at $r_{\rm cool}$, the gas density must rise, thus establishing an inflow of the gas to the central regions. This description holds, in particular, for an idealized, spherically symmetric, homogeneous cooling flow, in which the gas has a unique temperature and density at each radius. Although this is unlikely to be the case for every cluster in which the cooling is occurring, it is possible to see this model as a good description of the *mean* flow. Observed cooling times are significantly

longer than free-fall times, so the gas remains nearly hydrostatic as it cools; only in the very central regions the cooling is expected to be so fast that gas becomes thermally unstable and cools rapidly to lower temperatures. The mechanism described by Fabian is, to summarize, a steady, long-lived, pressure-driven inward flow of gas at a rate of up to 1000 $M_{\odot}yr^{-1}$.

It is possible to identify a few observational evidences for the cooling of the ICM: a sharply peaked X-ray surface brightness distribution is indicative of a cooling flow, because it denotes that the gas density is rising towards the center of the cluster. The fraction of clusters presenting this feature is considerable, so that it is usual to denote this category as *cool core clusters*: this type of clusters are about 90% of X-ray selected clusters with total mass $M_{\rm tot} \geq 10^{14}$ $M_{\odot}$, and about 50% of X-ray selected clusters with total mass $M_{\rm tot} \leq 10^{14}$ $M_{\odot}$ (Chen et al., 2007). The cooling region of cool core clusters usually occupies the inner $\sim$ 100 kpc, or $\sim$10% of the virial radius, therefore sharing approximately the same region as the BCG (McDonald et al., 2018).

An important aspect that regards the definition of cool cores is how they are actually distinguished from non-cool core clusters: since this division is not always sharp, it is essential to define some parameters that may unambiguously distinguish non-cool core clusters from cool core clusters. In order to accomplish this task it is possible to follow the work of Sanderson et al. (2009), who investigated the thermodynamic of the intra cluster medium across a statistical sample of 20 galaxy clusters analyzed with the *Chandra* X-ray satellite. For this sample they produced the plots presented in Fig. 1.11, which show that

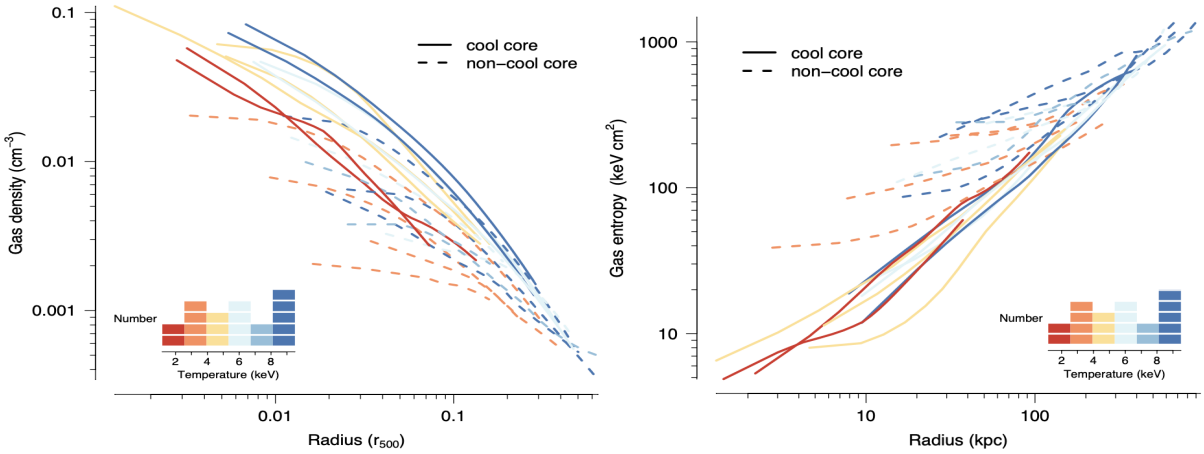

(a) *Density profile* **(b)** *Entropy profile*

Figure 1.11: *Left*: Gas density profile for each cluster, coloured according to the mean gas temperature; *right*: gas entropy profiles as a function of radius (Sanderson et al., 2009).

cool core clusters possess denser and more cuspy cores. The gas entropy is an extremely

important parameter, since it provides a measure of the thermodynamic state of the ICM; Sanderson et al. also produced the radial entropy profiles displayed in the right panel of Fig. 1.11: it is quite evident that non-cool core clusters have significantly higher entropy in the core and the divergence between the two types occurs within ~ 40 kpc.
In the standard model it is possible to quantify how strongly the cooling is actually occurring by determining the amount of matter which crosses $r_{\rm cool}$ and flows towards the center, that is the mass inflow rate $\dot{M}$ (Fabian, 1994). This quantity can be inferred through the measurement of the X-ray luminosity associated with the cooling region $L_{\rm cool}$, by assuming that it is the sum of the total thermal energy of the gas plus the work pdV done on the gas as it crosses $r_{\rm cool}$, radiated in dt:

$$L_{\rm cool} = \frac{dE}{dt} = \frac{(dE_{\rm th} + pdV)}{dt} \tag{1.30}$$

Since $pdV = (\rho kT/\mu m_{\rm p})dV = (dMkT)/(\mu m_{\rm p})$ the final definition of $L_{\rm cool}$ is:

$$L_{\rm cool} = \frac{5}{2}\frac{kT}{\mu m_{\rm p}}\dot{M} \tag{1.31}$$

where T is the gas temperature at $r_{\rm cool}$.
Usually $L_{\rm cool}$ ranges between $10^{42} - 10^{45}$ erg s^{-1}, accounting for the 10% of the total cluster luminosity. Values of $\dot{M} = 50 - 100$ M$_\odot$yr^{-1} deduced from Eq. 1.31 are typical for clusters cooling flows, and some systems show $\dot{M} > 500$ M$_\odot$yr^{-1} (such as A478, A2029 and Hydra A (Fabian, 1994)). Nevertheless, Fabian (1994) noted that surface brightness profiles were less peaked than they would have been is all the gas was flowing to the center.
Another evidence that the gas cools to low temperatures would be given by the spectral analysis of the central gas: the detection of low temperature components in the spectrum and the existence of strong emission lines (e.g. FeXVII) would mean that the gas is actually losing a big fraction of its thermal energy. As reported by Fabian (1994), observations performed with the Solid State Spectrometer (SSS) on the Einstein Observatory showed that there are low temperature components in the Perseus and Virgo clusters, and in particular in the case of the Perseus cluster the gas loses at least 90% of its thermal energy. For strong cooling flow clusters (such as A478) the presence of a soft X-ray excess was expected, but the SSS data showed that there was no excessive emission below 2 keV, and this was interpreted as the effect of an absorption mechanism intrinsic to the flow. Following the work of Fabian (1994), a good agreement with the data is obtained if an absorbed cooling spectrum plus an isothermal spectrum (to account for the outer gas projected along the line of sight) are implemented. The cooling flow spectrum is obtained by summing isothermal plasma model, inversely weighted by the cooling function at that

temperature $\Lambda(T)$:

$$L_{\rm cool}(\nu) = \frac{5}{2}\frac{\dot{M}}{\mu m_{\rm p}}\int_0^{T_{\rm max}}\frac{\epsilon_\nu(T)dT}{\Lambda(T)} \tag{1.32}$$

where $\epsilon_\nu(T)$ is the spectral emissivity of the gas.
In addition to that, it is possible to predict the total power radiated in an emission line by gas cooling isobarically in a steady flow given the cooling rate $\dot{M}$ and the contribution of a line to the cooling function $\Lambda_{\rm line}(T)$:

$$P_{\rm line} = \dot{M}\frac{\gamma}{\gamma-1}\frac{k}{\mu m_{\rm p}}\int_0^{T_{\rm i}}\frac{\Lambda_{\rm line}(T)}{\Lambda(T)}dT \tag{1.33}$$

where $T_{\rm i}$ is the temperature at which the gas starts cooling (McNamara and Nulsen, 2007).
X-ray observations made before the advent of higher resolution telescopes were fairly consistent with the cooling flow picture: in many clusters the ICM in the cluster core had been found to have short cooling times, high density and low temperature, which are evidences that the gas is actually cooling (e.g., Mushotzky and Szymkowiak 1988; Edge et al. 1992; Fabian et al. 1994). Furthermore, signatures of cooling had been found at other wavelength: filaments of Hα emission from ionized gas (Heckman, 1981), and bubbles of cold atomic and molecular gas (Edge, 2001). Nevertheless, several issues remained unresolved: the X-ray surface brightness profiles were not as peaked as expected from a homogeneous flow; the shape of soft X-ray spectra were inconsistent with a simple cooling flow, which had been tried to explain assuming the presence of an absorbing component (Allen and Fabian, 1997); moreover, there were some inconsistencies regarding the fate of the cooled gas: at the rate of 100s $M_\odot yr^{-1}$, the central galaxy should be very bright and blue if the cooled gas formed stars. In many cases they do have excess blue light indicative of an on-going star formation, but at rates which are a factor of 10 to 100 times lower than the X-ray deduced mass cooling rate (Fabian, 2002). These inconsistencies were confirmed by subsequent observation performed with new X-ray space telescopes, and as a consequence this subject has begun to be referred to as *cooling flow problem*.

1.2.2 Cooling flow problem

The cooling flow model has been challenged by the current generation of X-ray satellites, particularly by the high spatial resolution imaging of *Chandra* and the high spectral resolution of the *XMM-Newton* Reflection Grating Spectrometer (RGS). Spectral data have proved the absence or weakness of the soft X-ray line Fe XVII and of general evidence of gas cooling below 1-2 keV, indicating that the amount of gas cooling radiatively below about one-third of its original temperature is about ten times less than expected.

Historically, the cooling flow problem has been tried to be solved following two paths:

Suppresed emission: A proposed solution involved mechanisms capable of suppressing the normal signatures of radiative cooling below 1-2 keV: as mentioned above, the deficit of emission below 1 keV has been ascribed to absorption internal to the cooling flow; according to Fabian (2002), the X-ray emission lines from cold (below 3 keV) gas could be rendered undetectable if the absorption only operated on the colder gas - and not across the whole flow. Another possibility invokes a mixing process of hotter gas with cold gas that would produce cold blobs cooling rapidly: these bubbles of gas would likely be thermally unstable, with the denser cooler gas falling, shredding and mixing in the surrounding less dense parts; the thermal energy would then be radiated mostly in the UV rather than in the soft X-rays. Moreover, as reported by Mathews and Brighenti (2003), the presence of dust could both enhance the cooling process (by reducing the cooling time, so that cooling acts very rapidly) and reduce the X-ray emission from the cooling gas by a factor of at least 10. Despite this, they pointed out that although the presence of dust may have been confirmed by observations in the far infrared band (Temi et al., 2004), it seems unlikely that the dust-enhanced cooling can alone explain the weakness of X-ray cooling lines in clusters. A third idea considered metallicity variations across the cooling flow: at any fixed single temperature, a two-component plasma consisting of metal-rich and metal-poor phases is spectroscopically indistinguishable from a homogeneous plasma of mean metallicity $\bar{Z} = f_{\rm hi} Z_{\rm hi} + (1 - f_{\rm hi}) Z_{\rm lo}$, where the metal-rich phase has a metallicity $Z_{\rm hi}$ and accounts for a mass fraction $f_{\rm hi}$, and the metal-poor phase has a metallicity $Z_{\rm lo}$. The two spectra are not dissimilar because the strength of the continuum radiation is independent of Z, while that of the emission lines is directly proportional to Z: the reduction in the mass fraction of the enriched phase is therefore offset by the increased line strength (Fabian et al., 2001); the net effect of this two-component cooling flow is that the cooling lines from the whole flow are much weaker than they would be where the gas is fully mixed. However, in a subsequent study by Morris and Fabian (2003), it has been shown that while small scale metallicity variations might be present in the central regions of ICM, and they might contribute to a reduction of low temperature emission, this process in isolation cannot produce a reduction in equivalent width of the emission lines equal to that seen in data.

Heating sources: The other approach adopted to solve the cooling flow problem was the quest for energy-injection mechanisms which would compensate the cooling of the ICM. In the first models of cooling flow, the only source of heating taken into account was the gravitational heating occurring as the gas flows towards the center; other forms of heating such as supernovae, the effect of any central radio source or thermal conduction

were generally not included due to a lack of quantitative information on these processes (Fabian, 2002). Some heating sources are actually always expected in the central regions of clusters, but the problem with heating the gas consists in the fact that the gas appears to cool by a about a factor of three and then stop cooling: a mechanism capable of that is not obvious, since the gas does not appear to be accumulating at the lower temperature. According to Peterson and Fabian (2006), the profile of $t_{\rm cool}$ is similar in many clusters, with a common central minimum value for t_{cool} of about 200 Myr: this may suggest that heating is continuous (at least on time scales of 10^8 Myr) and spatially distributed.

Among the first possibilities, the effect of heating by supernova (SN) explosions associated with star formation in the cooling gas has been considered: for example, in the study of the cluster A1068 (McNamara et al., 2004) a comparison between the cooling luminosity of the gas and the heating power provided by SN explosions was attempted. They found that the SN luminosity is approximately $\sim 18\%$ of the cooling luminosity: therefore, according to McNamara et al., supernova explosions can reduce the level of cooling, but they would be unable to stop it entirely. A similar result can be found in Domainko et al. (2004), who investigated the feedback from intra-cluster SN on the ICM in cooling flow clusters: they argued that since intra-cluster SN can act as a distributed heating source[6] once the cooling flow has started, they might represent an interesting complement to heating models. In fact, they suggested that the significance of this additional heating depends on the particular cluster and it might cause a delay on the formation of cooling flows, but another heating mechanism is nevertheless required.

A second proposed heating mechanism was electron thermal conduction from the outer regions of clusters: the cluster gas beyond $r_{\rm cool}$ may provide a supply of thermal energy, since conduction could transfer heat into the cooler central regions. However, the rate of conduction is highly uncertain: as pointed out in Voigt et al. (2002), in the A2199 and A1835 clusters heat conduction might be sufficient to balance cooling only in the outer regions of the core (and only if there are no magnetic fields), while towards the innermost regions conduction is unable to influence cooling; as a result, in these cases heating by conduction merely reduces, but cannot prevent cooling.

Another hypothesis regards processes associated with relativistic AGNs outflows: at the beginning of the 90s it was known that BCGs in cool core clusters typically show signs of strong radio activity, but the importance of the active galactic nuclei responsible for the radio emission was underestimated due to their poor optical luminosity (Tabor and Binney, 1993); the situation changed since X-ray images of the Perseus and Cygnus A clusters taken with the *ROSAT* observatory showed signs of interaction between the radio

[6]Intra-cluster stars appear to belong to an old stellar population, so that only SN Type Ia should explode.

AGN and the hot atmosphere surroung them (Fabian, 2002): images of the two clusters revealed deficits in the X-ray emission, spatially coincident with regions of enhanced synchrotron emission. With the improvement in angular resolution ($\sim 1''$) provided by the *Chandra* X-ray observatory, it became clear that the cases of Perseus and Cygnus A are not isolated: in fact, the central regions of many cool core clusters are not relaxed, and their ICM is highly dynamic and not uniformly distributed, as there are signs of cavities on scales often approximately coincident with lobes of extended radio emission; in addition to that, new observations reveal highly disturbed structures in the cores of many clusters, such as shocks, ripples and sharp discontinuities (e.g., Gitti et al. 2012). The perturbation of the ICM appears to be caused by the effect of powerful radio jets from an AGN, which inflate bubbles of radio emitting plasma and create depressions in the hot, thermal gas surrounding them. Measurements of these cavities' properties, along with studies of the energetic of the radio jets have led to the understanding that cooling of gas in clusters is probably counteracted by the activity of the AGN. Nowadays it is believed that a mechanical feedback may be responsible for preventing runaway cooling of the ICM (McNamara and Nulsen, 2007, 2012), as bipolar outflows emanating from the BCG core inflate large bubbles while driving weak shocks, heat the ICM and induce a circulation of gas on scales of several 100s kpc.

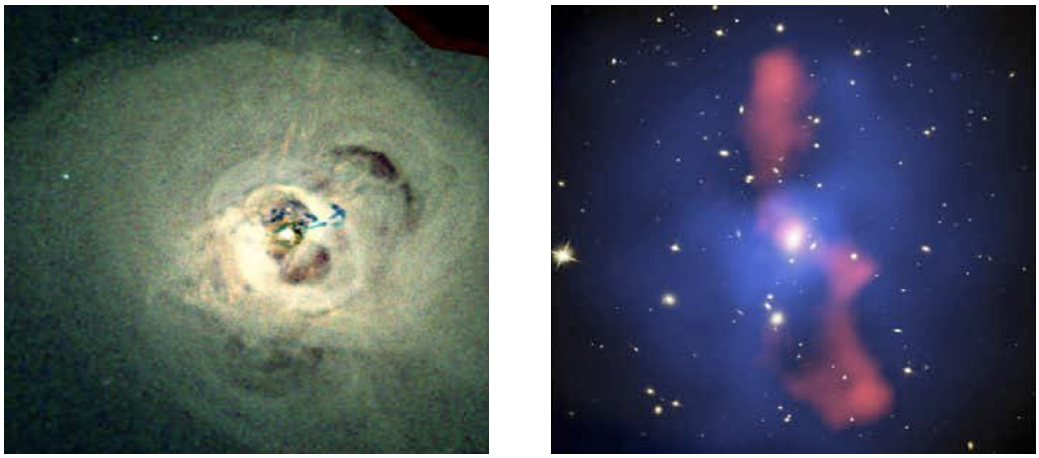

(a) *Perseus* **(b)** *MS 0735.6+7421*

Figure 1.12: *Chandra* images of two galaxy clusters displaying cavity systems and AGN-ICM interaction. Panel (*a*): *Chandra* observation ($\sim$ 105 kpc across) of the Perseus cluster (Fabian et al., 2006); Panel (*b*): multi-wavelength observations (630 kpc across) of the cluster MS 0735.6+7421; *Chandra* X-ray (blue), Hubble optical (yellow/white), and VLA radio (red); reproduced from McNamara et al. (2005).

1.2.3 AGN feedback: cavities and shocks

In the following paragraphs the main features of cavity and shocks found in the central regions of galaxy clusters are enlightened, providing an overview of the AGN heating process and the reasons for the need of a *self regulated feedback loop*.

Cavity properties: Cavity systems are usually found in pairs, and they consist in approximately elliptical X-ray surface brightness depressions, 20% to 40% below the level of the surrounding gas. During its initial stage, the tip of a radio jet advances supersonically into the surrounding medium until the radio lobes reach pressure balance with the surrounding hot ICM; while in the initial stage the cavity created by the tip of the jet might be long and narrow (thus making it difficult to detect), when the pressure within a radio lobe becomes comparable to the ram pressure of the jet it is possible that the cavity acquires a roughly spherical form. When the influence of the jet terminates, the cavity starts to rise outward under control of a buoyant force $F_{\rm g} = Vg(\rho_{\rm a} - \rho_{\rm b})$, where V is its volume, g is the local gravitational acceleration, $\rho_{\rm a}$ and $\rho_{\rm b}$ are, respectively, the ambient gas and the cavity densities. Its terminal speed, determined by balancing the buoyant force against the drag force, is then $v_{\rm t} \approx (4v_{\rm k}/3)\sqrt{2r/R}$ for a spherical cavity of radius r at a distance R from the cluster center. The Kepler speed $v_{\rm k} = \sqrt{gR}$ is approximately equal to the local sound speed, so that the terminal speed is subsonic (McNamara and Nulsen (2007) and references therein). It is possible to list three ways to infer a cavity age (Bîrzan et al., 2004):

- If a cavity rises through the ICM with a speed equal to the local sound speed $c_{\rm s} = \sqrt{\gamma kT/\mu m_{\rm p}}$ then the age of a cavity at distance R from the cluster center is the sound crossing time $t_{\rm s} = R/c_{\rm s}$.
- If a cavity is buoyantly rising at its terminal velocity $v_{\rm t}$, then the cavity age is the buoyancy-time $t_{\rm b} \sim 3R/(4v_{\rm k}\sqrt{2r/R})$.
- If the time required for the gas to refill the displaced volume of the cavity is considered, then the cavity age can be computed as $t_{\rm r} \sim 2\sqrt{r/g}$.

Typically the age estimates agree to within a factor of 2-3, and values for the cavity age are usually of a few 10^7 yr (Gitti et al., 2012); for example, in Vantyghem et al. (2014), the age of the four cavities pertaining to the galaxy cluster are estimated following the above three methods, and the various estimates agree within a factor of ~ 3.
Cavity diameters range from less than 1 kpc to approximately 200 kpc, with typical values around 20-30 kpc; a recent finding of a giant cavity can be found in Giacintucci et al. (2020), who discovered a huge cavity in the Ophiuchus cluster (with r $\sim$ 380 kpc). The

distribution of the ratio of projected nuclear distance (R) to radius (r) peaks at $R/r \approx 2$ and falls off rapidly beyond; this may indicate that cavities travel roughly their own diameters before they disintegrate or become too difficult to detect.
The knowledge of the statistical properties of cavities is limited by their detectability: as reported by McNamara and Nulsen (2007), cavities are easiest to detect when they are large and are located in the bright central regions of the clusters; in addition, while the presence of rims can enhance cavity contrast, processes of cavity disruption may reduce the probability of a detection. Rims are portions of shells surrounding many cavities, and they are typically cooler than the ambient gas, which suggests than they are composed of displaced gas dragged outward from the center by the rising cavities. The presence of these portions of rings make cavities more distinguishable from the ambient gas, so that their contrast is enhanced. An important issue regards cavity disruption, which is thought to be happening when Rayleigh-Taylor and shear instabilities are efficient: these effects can disrupt cavities, mixing their contents with the surrounding gas. However, it appears that cavities can also be fragmented without being destroyed: the numerous small cavities in M87 suggest that some processes (such as magnetic draping, see Lyutikov 2006) may contribute to stabilize these structures (McNamara and Nulsen, 2007). X-ray cavities are present in $> 70\%$ of cool core clusters, but due to the effects cited above their fraction could be underestimated (e.g., Gitti et al. 2012).

Cavity Heating: The total enthalpy of a cavity is given by the sum of the pV work done to displace the X-ray emitting gas while the radio bubble is inflated and the internal energy that provides the pressure supporting the cavities:

$$H = \frac{\gamma}{\gamma - 1} pV = \quad 2.5pV, \quad \text{for} \quad \gamma = 5/3 \tag{1.34}$$

$$4pV, \quad \text{for} \quad \gamma = 4/3 \tag{1.35}$$

where γ is the ratio of specific heats of the cavity plasma (McNamara and Nulsen, 2007, 2012); the choice for γ depends on whether the pressure support within cavities is supplied primarily by relativistic plasma ($\gamma = 4/3$) or non relativistic plasma ($\gamma = 5/3$).
It is typically assumed that the internal composition of the cavity is dominated by relativistic plasma, therefore $\gamma = 4/3$ and $H = 4pV$ (Bîrzan et al., 2004). Pressure p can be estimated through measurements of the temperature and density of the surrounding ICM, volume is computed from the cavity size under arbitrary assumptions on the cavity geometry. Studies of samples of X-ray cavities show that their enthalpies - measured with Eq. 1.35 - lie between $\sim 10^{55}$ erg and $\sim 10^{61}$ erg (see for example Diehl et al. 2008). When divided by the cavity age $t_{\rm cav}$(which can be computed following the three methods

discussed above), the observational measurements give an estimate of the cavity power $P_{\rm cav}$. However, this is only a lower limit of the true total mechanical power of the AGN, which is $P_{\rm jet} \gtrapprox P_{\rm cav}$; this is particularly important since the heating is thought to develop through the dissipation of the cavity enthalpy and through shocks driven by the AGN outburst (Gitti et al., 2012): the missing information regards weak shocks created by the motion of the jet through the ambient, which is expected to give a contribution to the total power. The problem with this component is that shocks are quite difficult to detect, and shock detections have been confirmed only for a sub-sample of clusters for which cavities are found; therefore, studies of AGN feedback in samples of clusters usually include only the cavity power (e.g., Bîrzan et al. 2004; Rafferty et al. 2006, 2008).

Once the cavity power is measured, it is possible to compare it with the gas luminosity inside the cooling radius $L_{\rm cool}$, which represents the luminosity that must be compensated for by heating to prevent cooling. The gas luminosity inside the cooling radius is estimated as the bolometric X-ray luminosity derived from a deprojection spectral analysis (see Sect. 1.2.3). *Chandra* observations revealed that the mechanical power of AGN (i.e. the cavity power P_{cav}) is comparable to or exceeds the X-ray luminosities of their cooling atmospheres (e.g., McNamara and Nulsen 2007, 2012), which means that jets are able to offset radiative cooling of the ICM. Fig. 1.13 (*left*) shows average cavity power plotted against the X-ray cooling luminosity for a sample of clusters: it is quite evident that the cavity power scales in proportion to the cooling X-ray luminosity, although with a big scatter (which is also due to the fact that cavity sizes and location are subject to uncertainties related to irregular shapes); typically, $\approx 4pV$ of power per cavity is observed, enough to offset cooling.

Therefore, it appears that the total mechanical power of the AGN can equal or exceed the cooling luminosity, and the ICM is being heated. However, it should be expected to see long cooling times in systems where heating dominates. In fact, expected heating rates should be sufficient to offset radiative cooling, otherwise cooled gas would be deposited at rates of many hundreds of solar masses per year in many clusters (in conflict with observations); on the other hand, if the balance is tipped in favour of heating, typical cooling times should exceed the Hubble time, which is in conflict with the observed high fraction of short cooling times. This suggests that a fine-tuned feedback process is strongly required to account for the high incidence of short cooling times and the reduced cooling rates (e.g., McNamara and Nulsen 2012). Considering this, it is now quite accepted the *self-regulated feedback loop*: the active galactic nucleus is fueled by a cooling flow that is itself regulated by feedback from the AGN; the radiative losses from the thermal ICM are balanced by mechanical heating from the central AGN over the system lifetime. Nevertheless, the details on how exactly the AGN feedback acts in heating the ICM and powering

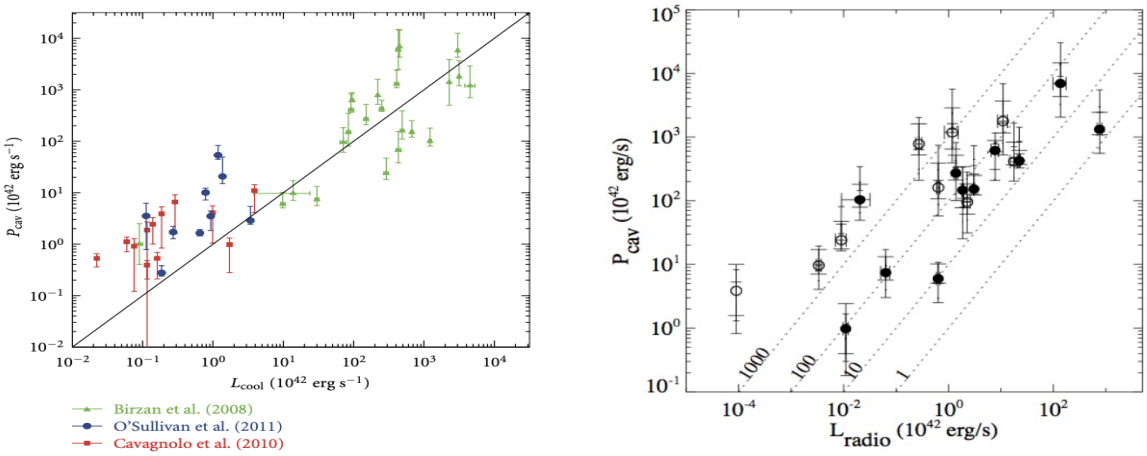

(a) P_{cav} *vs* L_{cool} **(b)** P_{cav} *vs* L_{radio}

Figure 1.13: *Left*: Cavity power of the central AGN vs the X-ray luminosity of the ICM inside the cooling region. Different symbols denote systems in different samples, while the diagonal line denotes $P_{\rm cav} = L_{\rm cool}$. Credit: Gitti et al. (2012); *right*: Cavity power of the central AGN vs integrated 10 MHz-10 GHz radio power $L_{\rm radio}$ for the cool core clusters in the sample of Bîrzan et al. (2008); dotted lines represent fixed ratios between cavity power and synchrotron luminosity.

the jets have not yet been assessed precisely, so that further investigations through multi wavelength studies are needed.

Radio luminosity as a proxy of cavity power A topic of interest regards the relation between the mechanical power and radio luminosity of the AGN. Calibrating such a type of relation would provide an estimate of the energy available from AGN directly from the radio data, thus avoiding the problem of cavity detectability in shallow X-ray images, which require long exposure times. Bîrzan et al. (2008) performed a study of a sample of galaxy clusters and derived the relation between the cavity power and the integrated 10 MHz-10 GHz radio luminosity. The result is appreciable in Fig. 1.13 (*right*), which shows that relatively modest radio sources may carry extraordinarily large mechanical powers: on average, the mean mechanical power is 100 times larger than the synchrotron power, and in some cases ~ 1000 times larger. By adding 18 galaxy groups to this sample, O'Sullivan et al. (2011) examined the relation between jet mechanical power and radio power finding the following best fitting power-law relationship:

$$\log P_{\rm cav} = (0.71 \pm 0.11) \log L_{\rm radio} + (2.54 \pm 0.21) \tag{1.36}$$

where $P_{\rm cav}$ and $L_{\rm radio}$ are in units of 10^{42} erg s^{-1}.
The use of integrated radio luminosity is considered by the authors as a superior cavity cavity power indicator compared to estimates at a single frequency, since it accounts for variations in spectral index between sources. As a confirmation of this hypothesis is it possible to report the study performed by Kokotanekov et al. (2017), who used new data from LOFAR's Multi-frequency Snapshot Sky Survey at the single frequency of 148 MHz, where it is expected to find emission from steep spectral index radio sources which could be signs of a former AGN activity. They found:

$$\log P_{\rm cav} = (0.51 \pm 0.14) \log L_{\rm radio} + (1.4 \pm 0.3) \tag{1.37}$$

and concluded that the large scatter obtained by using a single frequency luminosity is indeed a sign that the bolometric radio luminosity is a better predictor for the total jet power.

Weak shocks heating: In addition to the cavity heating, shocks driven by the AGN outburst contribute to the total energy released, resulting in an additional heating source for the ICM, especially close to the AGN. The shock strength is usually described by the Mach number of the shock $M \equiv v/c_{\rm s}$, where $c_{\rm s}$ is the sound velocity in the pre shock gas (*upstream* medium in Fig. 1.14) and v is the velocity of that gas with respect to the shock surface. Observationally it is possible to derive the density jump at the shock front from the surface brightness profile, and then from the Rankine-Hugoniot jump conditions the density jump (r) can be related to the Mach number:

$$M = \left[\frac{2r}{\gamma + 1 - r(\gamma - 1)}\right]^{1/2} \tag{1.38}$$

with γ indicating the adiabatic index.
Recently, elliptical surface brightness edges consistent with cocoon shock (driven by the cavities as they initially expanded), have begun to be detected (e.g., Gitti et al. 2012). Such shocks are quite difficult to detect since they are relatively weak (with Mach numbers $\sim 1 - 2$), so that they can be found only with deep *Chandra* exposures. The passage of a weak shock is expected to compress and heat the gas, but the effects of a single shock are thought to be largely negligible: when the shock has passed the gas returns to rest and its pressure settles to less than the pre-shock pressure because the gas has moved outward where gravity is weaker; therefore the reduction in pressure leaves the gas cooler than before the shock passed, as most of the residual energy gain from the shock remains as gravitational potential energy. Considering the Hydra A cluster, Nulsen et al. (2005) argued that the weak shock heating fails to compensate for radiative losses in cool cores.

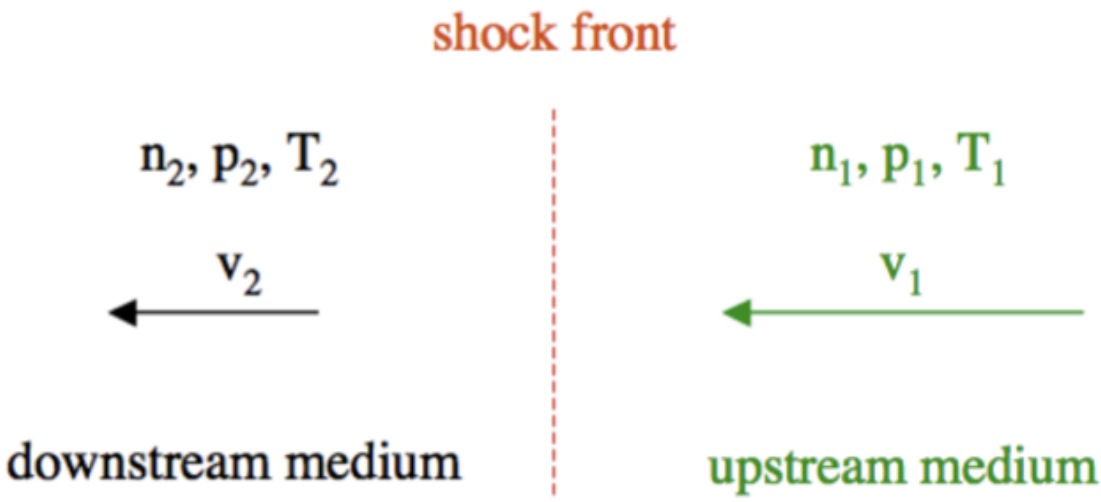

Figure 1.14: Schematic representation of a shock front, as seen in the shock rest frame; the downstream medium has already been shocked, while from the shock point of view the upstream medium is coming toward it with velocity v_1. Here n, p and T are, respectively, the gas electron density, pressure and temperature.

A different approach regards the study of weak shocks in M87 and NGC 5813: these two clusters have experienced multiple shocks, and the time interval between them is shorter than the cooling time, so that they might account for a fraction of the heat radiated in the inner regions of these systems. Since shock heating is more effective at small radii[7], it appears likely that at least for M87 and NGC 5813 multiple weak shock heating is responsible for preventing gas from cooling to low temperature in the inner regions, while other heating processes are required and more effective on larger scales (McNamara and Nulsen, 2012).

In addition to this, sound waves created by repeated outbursts (as those observed in the Perseus cluster, e.g., Sanders et al. (2016); see Fig. 1.15) could represent a significant heat source, as thermal conduction and viscosity cause the sound to dissipate and possibly generate significant heat. ICM simulation by Ruszkowski et al. (2004), has showed that it is possible that sound dissipation might be able to offset cooling in the long term. However, sound heating depends on transport coefficients which are highly uncertain for clusters, and sound waves detection is difficult (Graham et al., 2008).

[7]This happens because the shock strength decreases with radius and the energy injected is cubic in the shock strength (McNamara and Nulsen, 2012).

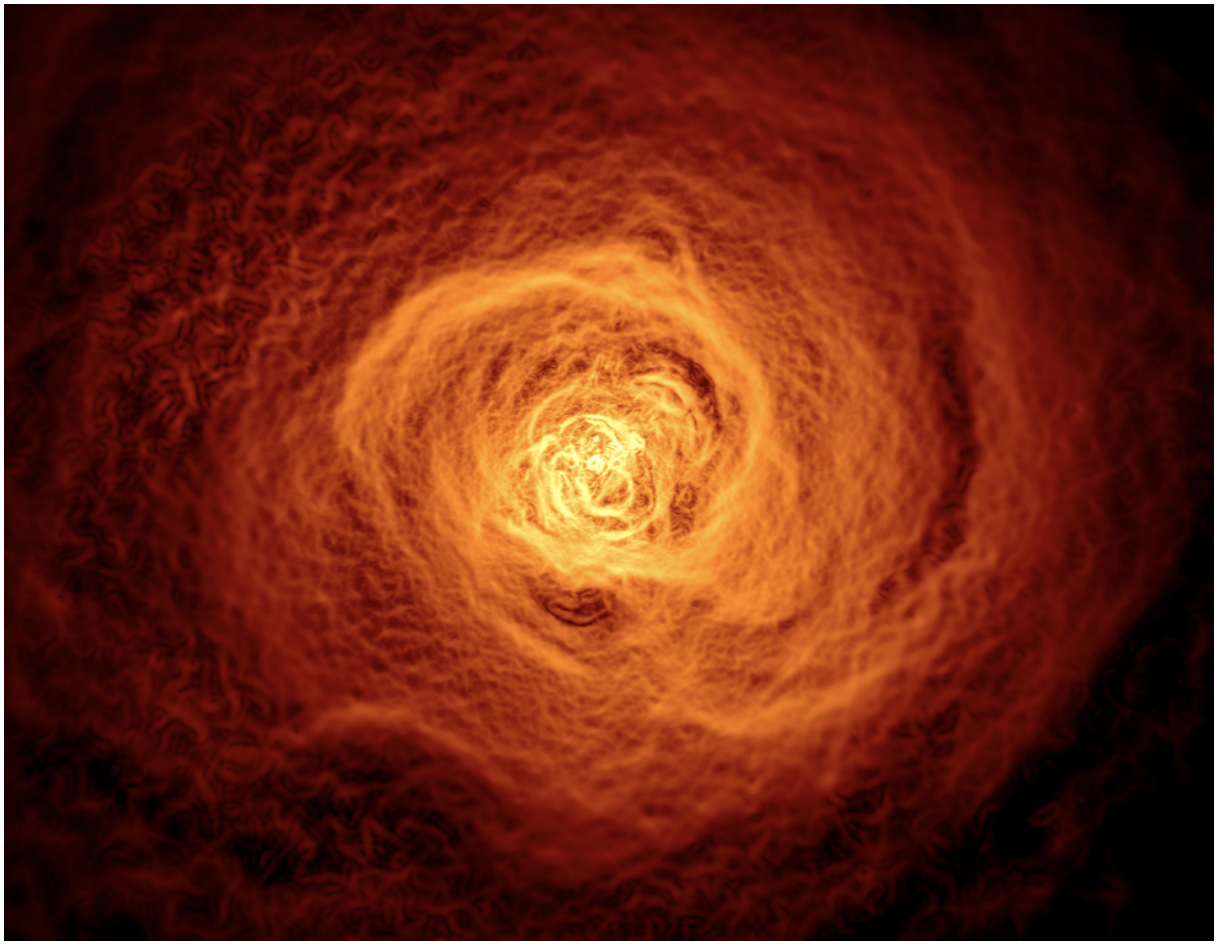

Figure 1.15: Chandra image of the central regions of the Perseus cluster, smoothed with an edge-detection algorithm to highlight surface brightness gradients (Sanders et al., 2016).

1.3 Cold fronts and sloshing

The high angular resolution of the *Chandra* X-ray telescopes corresponds, at $z \leq 0.05$, to a linear resolution of less than a kiloparsec, which is smaller than the typical mean free path of the intra cluster medium (Eq. 1.11). In particular, imaging of clusters at high resolution has enabled the discovery of sharp contact discontinuities between regions of gas with different entropies, which appear as jumps in surface brightness in the ICM. These structures have been named *cold fronts*, and they are detectable in merging clusters as well as around the central density peaks in cool core clusters.

The study of these edges allows to probe the intra cluster plasma properties over a wide range of scales, providing a remarkable tool to examine transport processes and magnetic fields. This section is dedicated to cold fronts, which are of high interest for what concerns this thesis; after a description of the main properties and subclasses of cold fronts, their importance for the study of the ICM is presented, highlighting both observational and

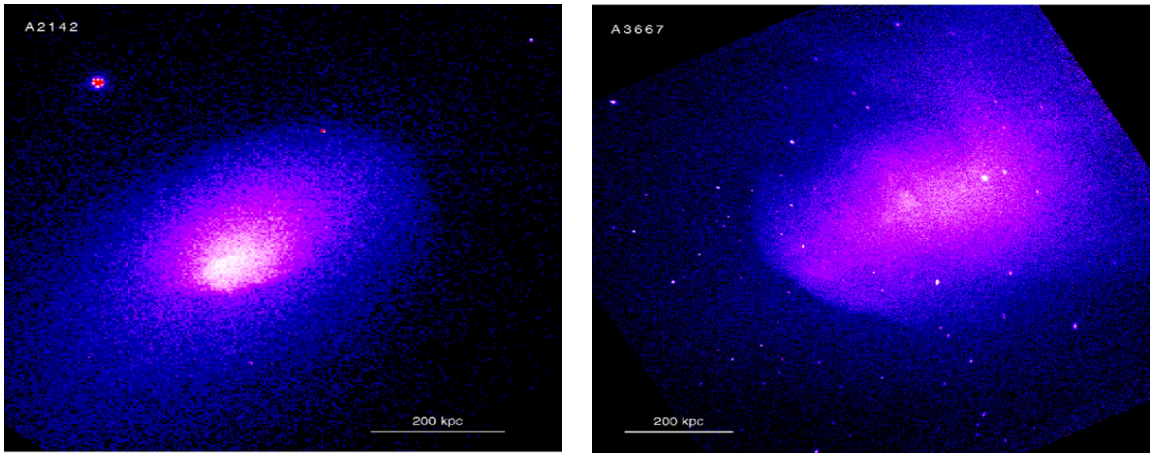

(a) *A2142* **(b)** *A3667*

Figure 1.16: *Chandra* X-ray images of clusters with the first discovered cold fronts, A2142 and A3667; reproduced from Markevitch and Vikhlinin (2007).

theoretical results.

1.3.1 Cold fronts: properties and classification

The first studies of cold fronts discovered that these features, whose appearance reminds of a shock discontinuity, were actually contact discontinuities: if these features were shocks, the gas on the denser, downstream side of the density jump would have to be hotter than that on the upstream side (see Fig. 1.14), but the temperature profiles for the A2142 cluster's edges obtained with *Chandra* (shown in Fig. 1.17 *right*) reveal an opposite situation, which rules out the shock interpretation (Markevitch et al., 2000). In particular, from the gas pressure profile it can be inferred that there is approximate pressure equilibrium between the two sides of the discontinuity; the relation between P_2/P_1 (downstream/upstream pressure ratio) and the Mach number M is:

$$\frac{P_2}{P_1} = \frac{2\gamma M^2 - (\gamma - 1)}{\gamma + 1} \tag{1.39}$$

with $\gamma = 5/3$ (e.g., Longair 2011).

Pressure equilibrium at the interface ($P_2 \approx P_1$) implies that $M^2 \approx 1$, and - in turn - $v_1 \lessapprox c_s$; therefore, cold fronts are contact discontinuities at the boundaries of gas clouds moving sub-sonically through a hotter and less dense surrounding gas (Markevitch and Vikhlinin, 2007).

The motion of gas within or between clusters and the presence of density gradients provide the conditions for the formation of cold fronts, which can be divided in two classes: *remnant core* cold fronts and *sloshing* cold fronts. Remnant core cold fronts form when a

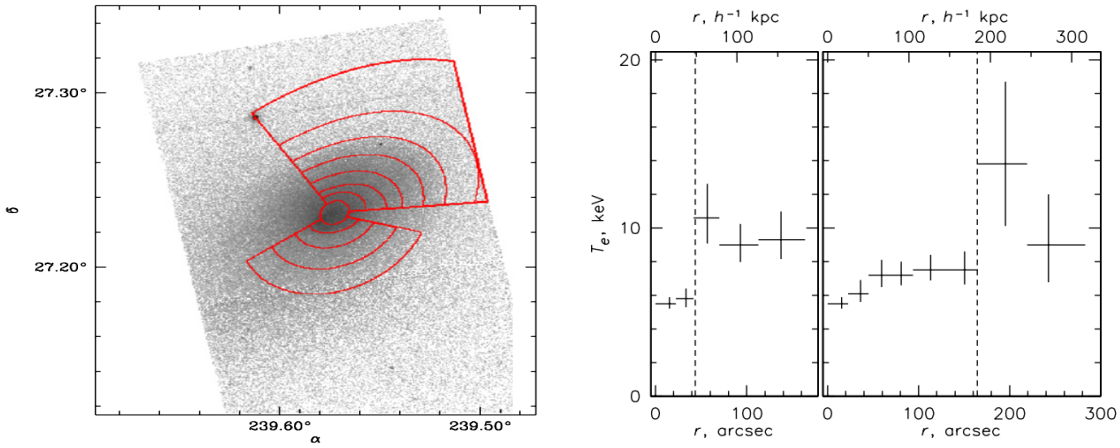

(a) *A2142* **(b)** *Temperature profiles across the edges*

Figure 1.17: Cold fronts in A2142 (Markevitch et al., 2000). (*a*): X-ray image with red overlays showing regions used for derivation of temperature profiles; (*b*): Temperature profiles for the southern edge (left plot) and the north-west edge (right plot).

galaxy, group or cluster moves through a hotter ambient plasma, and the resulting head wind strips off the outer layer of its atmosphere, while the sloshing cold fronts arise due to the action of a different mechanism: it is possible that some processes offset the bulk of the central ICM in a cluster from its hydrostatic equilibrium; the ICM then slowly oscillates around its hydrostatic equilibrium configuration (ZuHone and Roediger, 2016). The following paragraphs are intended to provide some informations on the characteristics of the two type of cold fronts.

Remnant core cold fronts: The growth of galaxy clusters through accretion of gas from cosmic filaments and merging with other structures is an on-going process, therefore it is expected to find merging clusters with cold front features. In fact, cold fronts have been observed in several galaxy clusters that are undergoing merging activity, and their study is essential to determine the dynamics of merger events. A recent example of remnant core cold front detection can be found in Botteon et al. (2018), who analyzed 15 merging and massive clusters observed with *Chandra* in order to detect X-ray edges: this resulted in the confirmed detection of 6 shocks and 8 cold fronts. It is possible to describe the mechanism responsible for the formation of such contact discontinuities, following the example of Markevitch and Vikhlinin (2007): when a gas density peak encounters a flow of ambient gas (a situation similar to the cold gas bubble moving through the ICM), a contact discontinuity quickly forms; since the two sides of the edge are supposed to be at pressure equilibrium, it seems reasonable that the outer, less dense layers of the moving cloud of gas are removed until the radius is reached where the pressure in the cold gas equals the pressure outside (see Fig. 1.18). The shear flow acting on the sides of the

front can be for simplicity reasons seen as symmetric, so that at the *stagnation point* (the forward tip of the front) there is no shear flow. The emergence of a discontinuity at the stagnation point is therefore due to the force exerted by ram pressure, pushes aside the gas layers not in pressure equilibrium with the flow. Therefore, the ratio of thermal pressure at the stagnation point (P_0) and the upstream pressure (P_1) is a function of the cloud speed:

$$\frac{P_0}{P_1} = \left(1 + \frac{\gamma - 1}{2} M^2\right)^{\frac{\gamma}{\gamma - 1}} \tag{1.40}$$

where M is the Mach number of the cloud relative to the upstream c_s.

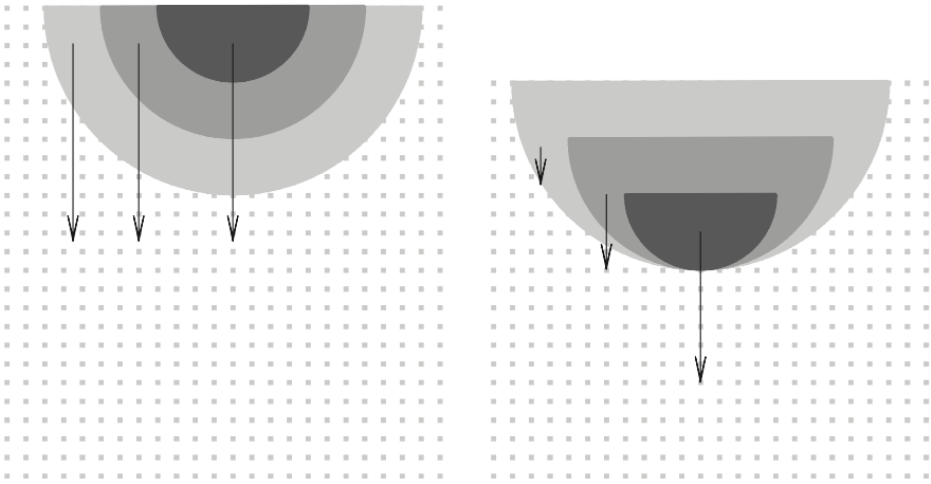

Figure 1.18: Sketch of the emergence of a density discontinuity from an initially continuous density distribution: the area-proportional drag force causes different deceleration of gases with different densities. Credit: Markevitch and Vikhlinin (2007).

Remnant core cold fronts have also been investigated through simulations, that in general show that when two sub-clusters collide, the outer regions of their ICM are shocked and stopped, while the gas cores seem to be dense enough to resist the shocks and the mixing induced by the merger (e.g. Asai et al. 2007).

Sloshing cold fronts: Apart from being present in merging clusters, cold fronts are also being found near the center of the cool core clusters, which typically show little or no signs of recent merging activity; these discontinuities often display arc structures usually curved around the central gas density peak (as an example A2029 cold front is shown in Fig. 1.19), and it is thought that the sloshing of the cold cluster gas is caused by some type of perturbation of the ICM: the passage of a small sub-cluster (through the main cluster or as an off-center passage that induces angular momentum) or of a sufficiently strong shock may result in sloshing cold fronts wrapped around the cluster core in a one-armed spiral-like pattern. The arrangement of sloshing cold fronts in clear spiral or

opposed arcs (with respect to the cluster core) is determined by the composite action of angular momentum injection and viewing angle (ZuHone and Roediger, 2016); moreover, it is possible to affirm that sloshing is a lasting process, so that clusters can appear quite relaxed while displaying the sloshing features: it seems that sloshing cold fronts may exist in the cores of $\sim 2/3$ of relaxed galaxy clusters (Ghizzardi et al., 2010).

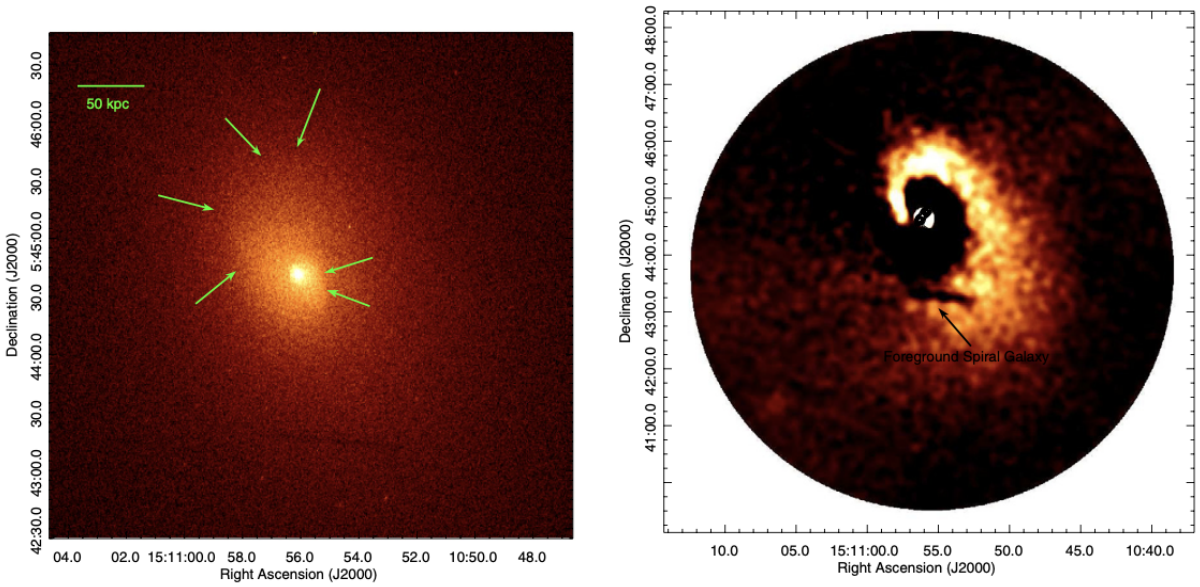

Figure 1.19: Sloshing in A2029. *Left*: *Chandra* X-ray image of the central part of the cluster, with green arrows indicating the spiral form; *right:* surface brightness residual image, highlighting the spiral surface brightness enhancement due to sloshing motions (Paterno-Mahler et al., 2013).

Since motions of gas in the cluster represent a deviation from the hydrostatic equilibrium assumption, it is possible to investigate how this can affect the derivation of the total mass based on this assumption (Eq. 1.17). This has been made, for example, by Markevitch et al. (2001) for the study of the cluster Abell 1795: using the gas profiles from the sector containing a cold front, the total mass within the edge radius was underestimated by a factor of 2, thus confirming that the presence of the sloshing front influences the total mass determination. However, it is possible to denote that usually the central cooling region contains only a few percent of the cluster total mass, so this error is relevant only for studies focusing on specific central features of the gravitational potential profile (Markevitch and Vikhlinin, 2007). In addition to this, since heavy elements in clusters are concentrated towards the center, the motion of a sloshing cold front should produce abundance discontinuities across the front (this was observed for example in A907 by Ueda et al. 2019).

Moreover, sloshing cold fronts have been analyzed to determine whether they could be related to the cooling flow problem. The currently favoured view is that AGN provide the

main source of heating through the interaction of the jets with the ICM, but other heating sources might contribute to the whole picture. One of the possible mechanism involves sloshing: in the first place, as the gas oscillates, the mechanical energy of the moving front might be converted into heat. Secondly, sloshing brings hot gas from outside the cool core into the cluster center, where it might come in contact with the cool gas; if the two phases mixed, then a heat transfer would cause a net heating of the central cluster regions (Markevitch and Vikhlinin, 2007). This idea has been investigated by ZuHone et al. (2012b) through MHD simulations of sloshing of the ICM in cool core clusters: they found that the combination of sloshing and an anisotropic thermal conduction can result in a heat flux to the core; this process alone cannot prevent a cooling catastrophe in the very central regions of the cool core ($r \sim 5$ kpc), where AGN feedback is needed, but it reduces the mass of gas that experiences substantial cooling outside that small radius. Observationally, a similar conclusion has been obtained by Ueda et al. (2019) for the A907 cluster sloshing front: while gas sloshing may play a significant role in heating the ICM, the remaining required power to prevent cooling is large enough to suppose that an additional heating source, such as the AGN feedback, is needed.

Sloshing cold fronts have also been related to processes observed at other wavelengths: first of all, radio mini-halos in sloshing-core clusters are generally found to be co-spatial with the sloshing region, suggesting a causal link between sloshing and mini-halos (see Fig. 1.20). It is possible that sloshing motions may amplify the magnetic fields and generate turbulence in the cool core, thus re-accelerating the relativistic electrons in mini-halos. This hypothesis has been tested by Giacintucci et al. (2019), who confirmed three new detection of mini halos, expanding the sample to 23 confirmed detection; indeed, they found that in $\approx 70\%$ of their cluster sample, the mini halo might be confined by the sloshing cold fronts in the core gas.

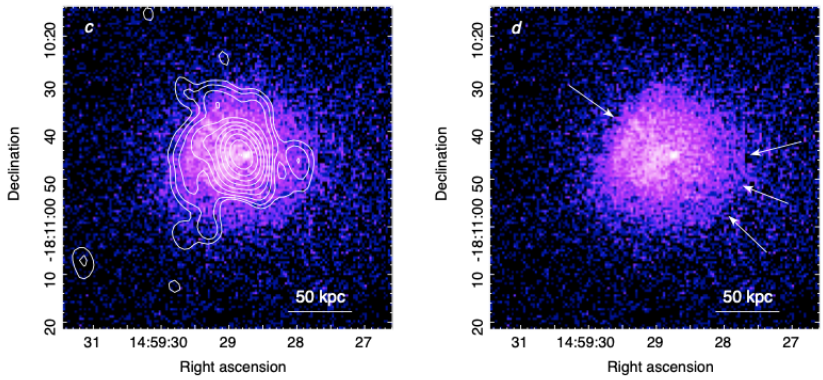

Figure 1.20: 0.5 - 4 keV *Chandra* image of the galaxy clusters AS780, with radio contours at 610 MHz showing the mini halo emission (*left*), and arrows indicating the position of two possible cold fronts (*right*) (Giacintucci et al., 2019).

Furthermore, studies of molecular gas with ALMA found that many sources display a molecular emission peak offset from the BCG: Russell et al. (2019) suggested that in systems where the distance between the AGN and molecular peak is $1-2$ kpc the offset is due to the entrainment of the molecular gas around uprising X-ray cavities. On the other hand, the RXJ0821 galaxy cluster features an offset of ~ 3 kpc which is thought to have another origin: Vantyghem et al. (2019) proposed that the molecular gas displacement in this system is caused by sloshing motions in the intra cluster medium, and that this mechanism could also be applicable to other systems, arguing that indications of sloshing may come from the offset between the X-ray peak and the BCG nucleus. In fact, the presence of offsets has been verified for many clusters (see for example Rossetti et al. 2016), and the link between sloshing, offset and AGN feedback has recently begun to be investigated (e.g. Pasini et al. 2019). Further inspection of this topic, along with new detections of offset and sloshing cold front, may contribute to delineate a more detailed picture.

1.3.2 Cold fronts and ICM transport properties

Cold fronts are extremely useful to investigate the ICM transport properties: the observed temperature jumps at cold fronts require that thermal conduction across the fronts is strongly suppressed; moreover, the width of cold fronts seems smaller than the Coulomb mean free path for the plasma particles (Eq. 1.11), thus showing that there might be mechanisms acting in the proximity of these edges that cause the suppression of transport properties (Markevitch and Vikhlinin, 2007). The investigation of this mechanisms requires to resolve extremely sharp features in X-ray images, and to improve the numerical description of the ICM, including effects of magnetic fields, viscosity and thermal conduction.

Kelvin-Helmholtz instability: Considering the physics behind the formation of cold fronts, it is possible to address the consequence of the velocity shear present across the sharp interface: in the absence of viscosity, at the interfaces the shear flow should develop Kelvin-Helmholtz instabilities (KHI) on a time scale of a few Myr for cold fronts in the ICM (ZuHone and Roediger, 2016). However, many cold fronts appear relatively undisturbed: as ZuHone and Roediger (2016). report, this might indicate that KHI are being suppressed, either by the action of a strong magnetic field aligned with the shear flow interface, or by a sufficient ICM viscosity. For instance, as a cold front moves through the magnetized medium, the field is aligned with the cold front surface as the flow stretches and wraps the field lines around the interface (see Fig. 1.21), resulting in the field amplification (Lyutikov, 2006; ZuHone and Roediger, 2016).

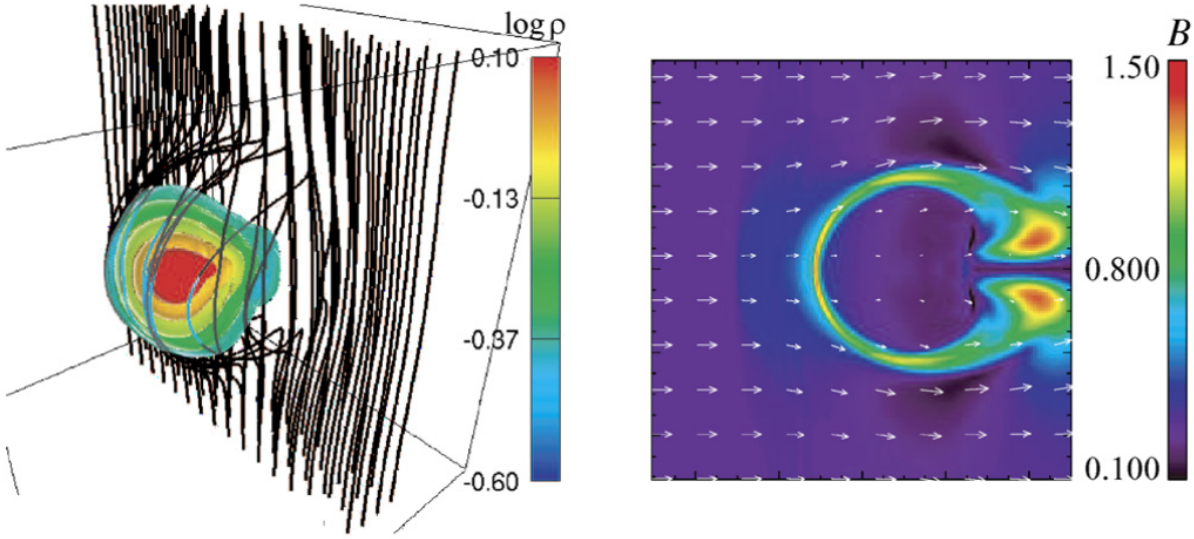

Figure 1.21: Simulation of the magnetic field draping around a cold front moving through a uniformly magnetized ICM. *Left:* The subcluster gas density (color) and the magnetic field lines; *right:* horizontal cross-section through the sub-cluster: compression of the field (colour) creates a layer around the front, in which the field is amplified. Reproduced from Asai et al. (2005).

This mechanism has been numerically tested both for remnant-core and sloshing cold fronts, showing that in the former the movement of the cold, dense gas through the ICM builds up a layer of amplified magnetic field on the *outside* of the interface, while in the latter the amplification occurs on the *inside* of the interface. In general, simulations show that for stronger initial field, the magnetic draping around the front becomes stronger, and more capable of suppressing KHI (ZuHone and Roediger, 2016). Following the argument of Markevitch and Vikhlinin (2007), the KHI instability is suppressed when:

$$\frac{B_1^2}{8\pi} + \frac{B_2^2}{8\pi} > \frac{1}{2}\frac{\gamma M^2}{1 + T_2/T_1} P_{\rm f} \tag{1.41}$$

where the notation "1" and "2" refers to the upstream and downstream side of the cold front, B is the magnetic field, T is the temperature and $P_{\rm f}$ is the pressure at the front interface.

For the sloshing cold front seen with *Chandra* in Abell 2204, Chen et al. (2017) proposed that magnetic fields with strength 24μG and 32μG along the west and east cold fronts, respectively, might be able to account for the KHI suppression: these magnetic field strengths are higher than typical cluster values ($B \approx 1 - 10\mu$G, e.g., Govoni and Feretti 2004), therefore indicating that amplification mechanisms are expected to be present.

Viscosity could suppress the growth of KHI under a specific length scale by smoothing the velocity gradient at the interface layer by momentum diffusion. Numerically, it appears

that a sufficient ICM viscosity is capable of suppressing KHI both in remnant core and sloshing fronts; moreover, this could prevent the mixing of cold gas with the ambient ICM (ZuHone and Roediger (2016) and references therein). On the contrary, the presence of KHI at sloshing fronts leads to characteristic signatures such as ragged appearance of the surface brightness edge: the Perseus observations (Ichinohe et al., 2019) reveal surface brightness fluctuations below the cold front, which may indicate the presence of KHI and an extremely low ICM viscosity in this cluster. Therefore, observing the presence or absence of KHI features around cold fronts can provide useful information on the plasma magnetic field and viscosity, whose potential combined effect has yet to be fully investigated through numerical simulations (ZuHone and Roediger, 2016).

Thermal Conduction: If the width of a cold front is smaller than electron and ions mean free paths (Eq. 1.11), diffusion of particles and heat should be very efficient across the interface; in addition, temperature and density jumps at the edge should be quickly smoothed by thermal conduction. Nevertheless, sharp cold front interfaces are present in many clusters, indicating that heat flux and particle diffusion are suppressed. This is the case for A3667 merging cluster, whose front has a width of ~ 4 kpc: if Coulomb diffusion is not suppressed, the front width should be several times $\lambda_{\rm diff} \approx 10-13$ kpc; the fact that the cold front is sharper than that implies that there is a mechanism for such suppression (Vikhlinin et al., 2001).

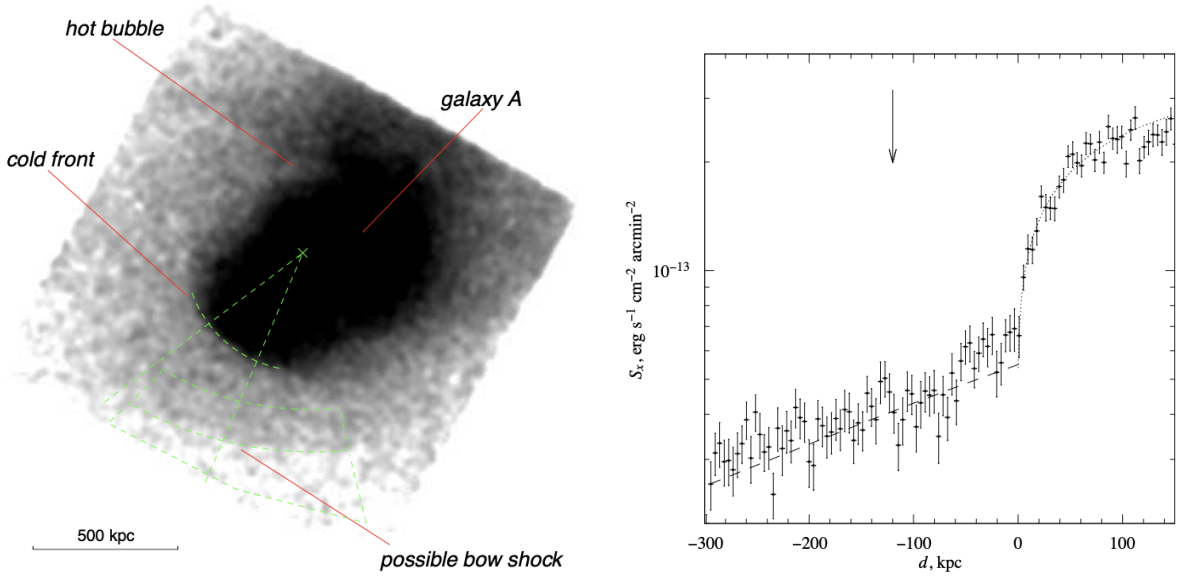

Figure 1.22: Panel *a*: smoothed 0.5-4 keV *Chandra* image of A3667; panel **b**: X-ray surface brightness profile across the cold front of A3667, showing a sharp jump at the edge position (Vikhlinin et al., 2001).

Similarly, the width of the sharp temperature discontinuities in the A2142 cluster cold

fronts led Ettori and Fabian (2000) to note that the heat flux across the interface must be suppressed by a factor of $\sim 250 - 2500$. It has been numerically investigated whether magnetic field draping could reduce the particles' mean free paths, hence reducing the efficiency of conduction. For remnant-core cold fronts Asai et al. (2007) found that a magnetic field layer is able to suppress conduction across the cold front; for sloshing cold fronts, ZuHone et al. (2012b) showed that the presence of magnetic field layers could not prevent thermal conductivity to smear out the front surfaces. More detailed simulations and future observations of these discontinuities are needed to obtain more information on these topics.

1.4 Active Galactic Nuclei

Nowadays it is known that *Super Massive Black Holes* (SMBH) are virtually present in every massive galaxy; the mass of these objects - in the range $10^6 - 10^9 M_\odot$ - correlates tightly with the velocity dispersions $\sigma_\star$ of their host bulges (Tremaine et al., 2002), through the relation:

$$\log(M_{\rm bh}[M_\odot]) = (8.13 \pm 0.06) + (4.02 \pm 0.32) \log\left(\frac{\sigma_\star}{200 kms^{-1}}\right) \tag{1.42}$$

This connection indicates that galaxies evolution is strongly related to the SMBH properties. Black holes are usually described in terms of their mass M, charge Q (assumed to be 0), and spin J: the latter can assume values in the range 0 (Schwarzschild BH) -1 (Kerr BH).
Approximately 99% of these object are silent, only the remaining $\approx 1\%$ show signs of activity; the latter category is referred to as *Active Galactic Nuclei* (AGNs). As it has been pointed out in Subsect. 1.2.3, the kinetic feedback from an AGN hosted in the BCG is fundamental to explain why the cooling rates are lower than expected. As there is a great variety of AGNs, it is important to deeply investigate the different kinds of accretion which, in turn, result in various feedback outcome. It is possible to classify AGNs as *radio-quiet* or *radio-loud* according to the ratio between the nuclear radio flux at 5 GHz ($F_{5\,\rm GHz}$) and the nuclear optical flux in the B band ($F_{\rm B}$):

$$R = \frac{F_{5\,\rm GHz}}{F_{\rm B}} \tag{1.43}$$

If $R > 10$ the AGN is classified as *radio loud* (RL) (Kellermann et al., 1989). The definition of radio-loud can also be based on the ratio between the radio luminosity $L_{5\,\rm GHz}$ and the X-ray luminosity $L_{2-10\,\rm keV}$:

$$\log R_X = \log\left(\frac{\nu L_\nu[5\,\rm GHz]}{L_{2-10\,\rm keV}}\right) \geq -4.5 \tag{1.44}$$

Considering the aim of this thesis, here we narrow our interest to *radio loud* AGNs, and in particular to the main differences between Fanaroff-Riley Type I, II and (newly discovered) Type 0 radio galaxies.

1.4.1 FRI and FRII sources

Radio loud AGNs (or *jetted* AGNs, see Padovani et al. 2017) display jets composed of relativistic plasma, and account for $\sim 10\%$ of the AGN population. According to the

jet inclination w.r.t. the observer line of sight, they are sub-classified as *blazars* and *radio galaxies* (Urry and Padovani, 1995). Blazars's output (the jet) points towards the observer, therefore the emission is amplified and the radio spectra are generally flat; on the other hand, Radio Galaxies have misaligned jets, so their emission is less affected by Doppler boosting effects (Urry and Padovani, 1995). Radio galaxies have been historically classified by Fanaroff and Riley (1974) on the basis of their radio morphology into Fanaroff-Riley Type I RGs (FRI) and Fanaroff-Riley Type II RGs (FRII): the former are *edge-darkened*, presenting bright jets and faint lobes, while the latter (*edge-brightened*) show bright lobes and collimated jets terminating in "hot spots". The distinction between these two types of radio galaxies translates into a distinction in radio power: the break luminosity $L(178\,\mathrm{MHz}) = 10^{26}\,\mathrm{W\,Hz^{-1}}$ is a useful diagnostic parameter to identify a FRI (lower luminosity) or a FRII (higher luminosity) (Tadhunter, 2016).

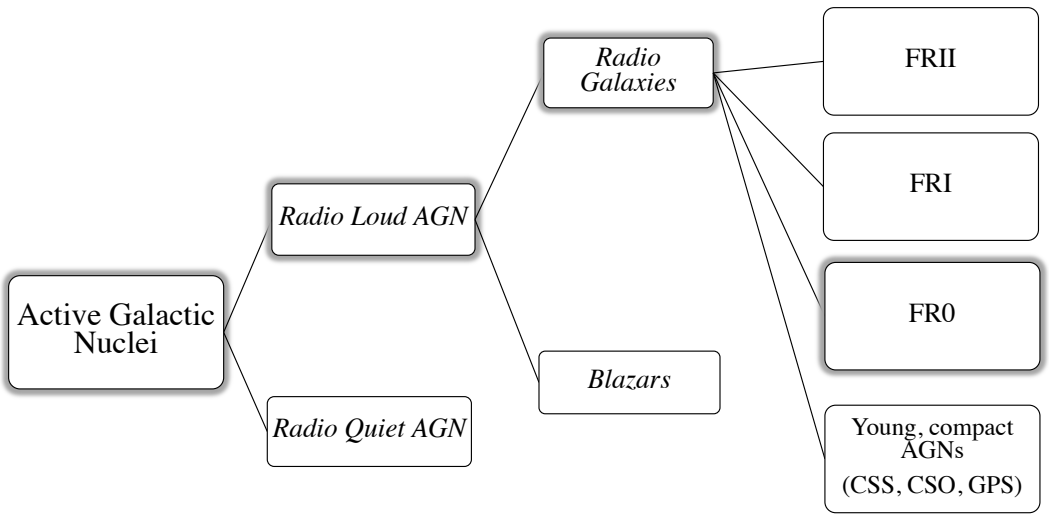

Figure 1.23: Schematic representation of the RL-AGNs classification.

The origin of the FRI/FRII dichotomy has not been fully understood yet: several hypothesis have been issued, from external agents - such as the interaction between the jets and the environment (e.g., Bicknell 1994), the host galaxy properties or merging events - to intrinsic factors, namely the different accretion mechanism in FRI and FRII (Ghisellini and Celotti, 2001).
To fully understand the following distinction between the main subclasses of *radio loud* AGNs, it seems important to list the components which contribute to the emission of these sources:

- *Core*: a very compact region ($\leq$ 1 pc) where the jet is launched; this region is

usually not resolved even with at the highest resolution of the VLBI[8], that is $\lessapprox 1$ milliarcsec.

- *Jets*: the main output of RL AGNs are the beams of relativistic plasma ejected by the central engine, which carry particles and energy from the inner regions (sub-parsec scale) to the outer ones (up to hundreds of kiloparsecs). Jets are usually bipolar, and their emission is mostly due to synchrotron in the radio band. As jets of powerful AGNs have been detected also in the X-ray band, it is possible that for some of these sources the synchrotron emission extends to the high energies; however, it has also been proposed that Inverse Compton scattering (either by the Cosmic Microwave Background or by the synchrotron emitting electrons) might be responsible for the X-ray radiation.

- *Lobes*: as jet excavate their way first through the ISM, then through ICM, the interaction between the relativistic plasma and the ambient medium can lead to the jet's structure destruction. This leads to the formation of extended bubbles of plasma emitting in the radio band which can reach sizes of several kiloparsecs. Considering galaxy clusters, the same radio lobes powered by the central AGN are the X-ray cavities which have been found to provide the most likely quenching mechanism for cooling flows.

- *Hot spots*: bright compact sources typically found in the lobes of FRII; they arise from the impact between the jets and the interstellar medium (ISM), which produces shock waves that re-accelerate the electrons responsible for the synchrotron radio emission.

A schematic representation of these components in FRI and FRII radio galaxies can be found in Fig. 1.24

Accretion: The rate of accretion of matter around a BH can be estimated by dividing the luminosity released by the accreting black hole ($L_{\rm acc}$) and the luminosity at which the gravitational force felt by the infalling material is balanced by the pressure of the out-coming radiation (*Eddington Luminosity* $L_{\rm Edd}$):

$$L_{\rm acc} = \eta \dot{M} c^2 \tag{1.45}$$

$$L_{\rm Edd} = \frac{4\pi G m_{\rm p} c}{\sigma_{\rm T}} M \sim 1.3 \times 10^{38} M/M_{\odot}\,{\rm erg/s} \tag{1.46}$$

[8]Very Long Baseline Interferometry, see e.g., Middelberg and Bach (2008).

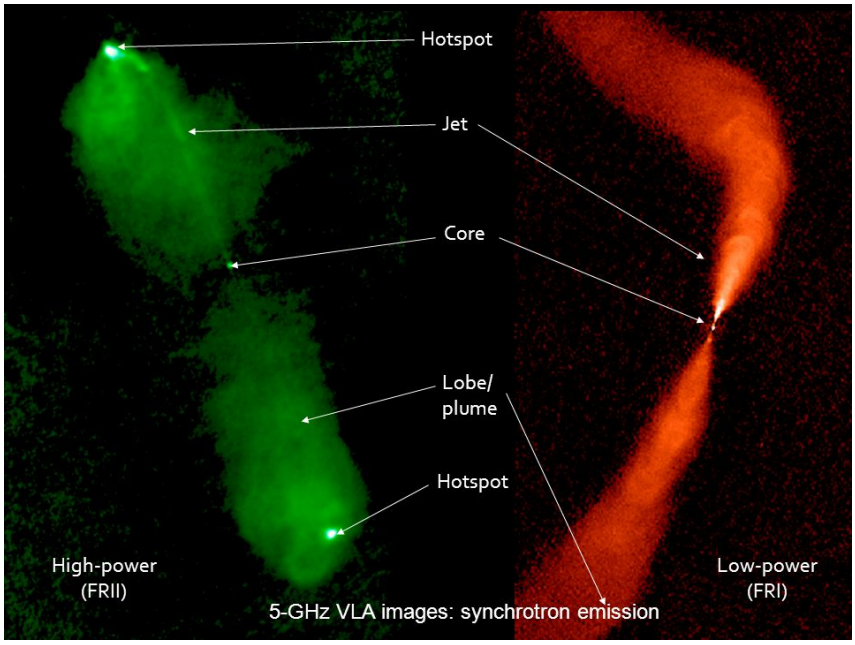

Figure 1.24: Main components of radio loud AGN in FRI and FRII radio galaxies (Evans et al., 2016).

where η is the efficiency at which the accreted mass is converted into energy, $\dot{M}$ is the rate at which mass is accreted, c is the speed of light, G is the gravitational constant, $m_{\rm p}$ is the proton mass, $\sigma_{\rm T}$ is the Thomson cross section and M is the black hole mass[9].
By measuring the luminosity of emission lines of elements excited by the central engine it is possible to obtain an estimate of $L_{\rm acc}$[10], while from the black hole mass it is possible to obtain $L_{\rm Edd}$: the ratio between the two provides an estimate of the accretion rate of the AGN:

- For $L_{\rm acc}/L_{\rm Edd} \approx 10^{-1} - 10^{-2}$ the accretion mechanism efficiently converts gravitational energy into radiation (*quasar mode*): the AGN is thought to be sustained by a geometrically thin, optically thick disk (see right panels of Fig. 1.25; Shakura and Sunyaev 1973), in which each element of the disk radiates as a black body.

- For $L_{\rm acc}/L_{\rm Edd} \leq 10^{-3}$ the disk is unable to radiate the viscosity-generated energy, leading to a geometrically thick and optically thin structure known as Advection-Dominated Accretion Flow (ADAF, Narayan and Yi (1994)), with electron temperature $T_{\rm e} \sim 10^{9-11}$ K and ion temperature $T_{\rm i} \sim 10^{12}$ K (see left panels of Fig. 1.25). In this case, the jet represents the bulk of the AGN energetic output (*jet-mode*).

A successive classification of radio galaxies was proposed by Laing et al. (1994) based on the optical emission lines. This classification is grounded on the fact that different

[9]For a review of accretion processes, see Czerny and You (2016).
[10]See for example Heckman et al. (2004) for the relation $L_{\rm bol} = L_{\rm acc} = 3500 L_{\rm [OIII]}$.

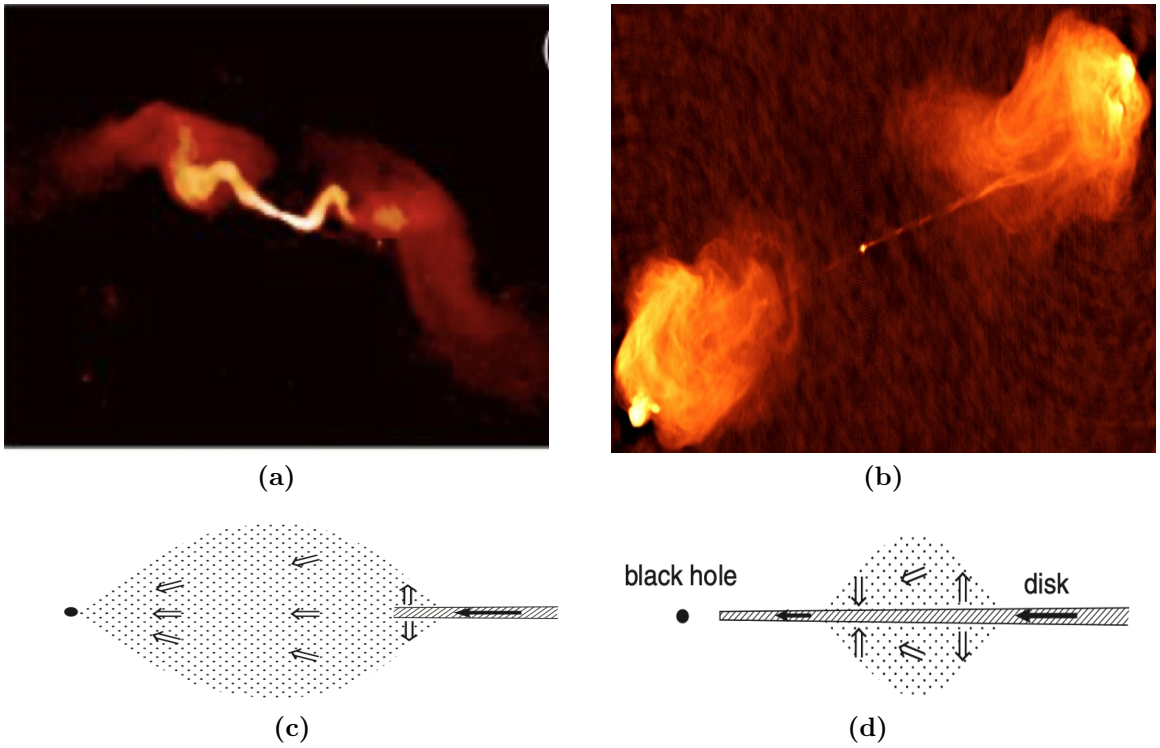

Figure 1.25: Panel **a**: the FRI radio galaxy 3C31 ar 1.4 GHz (Banfield et al., 2015); Panel **b**: the FRII radio galaxy Cygnus A (Credit: NRAO/AU); Panel **c**: scheme of an ADAF disk; Panel **d**: scheme of a Shakura-Sunyaev disk (Meyer et al., 2007).

excitation modes of the gas reflect different accretion regimes in the central engine of the AGN. For this reason, radio galaxies were divided into high-excitation (HERG) and low-excitation (LERG) radio galaxies. A more recent definition was proposed by Buttiglione et al. (2010), based on the excitation index parameter (EI):

$$EI = \log\left(\frac{[OIII]}{H\beta}\right) - \frac{1}{3}\left[\left(\frac{[NII]}{H\alpha}\right) + \log\left(\frac{[SII]}{H\alpha}\right) + \log\left(\frac{[OI]}{H\alpha}\right)\right] \tag{1.47}$$

Sources with $EI < 0.95$ are classified as Low Excitation Radio Galaxies (LERG), while sources with $EI > 0.95$ are classified as High Excitation Radio Galaxies (HERG). The vast majority of HERGs resides in FRII radio galaxies, while LERGs display both behaviours.

The environment of radio galaxies Nearby redshift ($z < 0.5$) FRIs are typically located in dense environments (galaxy groups and clusters), while FRIIs generally reside in isolated field galaxy (Hill and Lilly, 1991). Radio loud AGNs are typically hosted in elliptical galaxies, but the hosts of FRIIs tend to be bluer than those of FRIs, and usually show signatures of recent mergers - irregular morphology and/or relatively high star formation rates (see e.g., Baldi and Capetti 2008). These findings can be related

to the accretion mode: for example, Hardcastle et al. (2007) proposed a scenario for the different radiative efficiency of FRI/LERGs and FRII/HERGs which takes into account the difference source for the gas to be accreted. They proposed that a steady inflow of hot gas from the ambient medium of LERGs (i.e. the ICM of the host galaxy cluster or group) in the form of Bondi accretion might power an inefficient engine, and lead to the formation of an ADAF disk. On the contrary, cold gas (maybe provided by a wet merger) might both explain the enhanced star formation rate of the host of HERGs, and produce a radiatively efficient AGN with a Shakura-Sunyaev-like accretion disk.
More recently, Macconi et al. (2020) found a correlation between the Eddington scaled X-ray luminosity (considered as a proxy of the accretion) and the cluster richness of the ambient medium of different classes of radio galaxies (i.e. FRI-LERG, FRII-HERG and FRII-LERG). They found that the more efficient is the accretion, the less dense is the environment, suggesting that the latter would have a strong impact on the accretion regime.

1.4.2 Properties of FR0s: recent results

The advent of wide-field surveys in the optical and radio bands (SDSS, FIRST[11], NVSS[12]) allowed to investigate the population of radio galaxies in the mJy regime (e.g., Best and Heckman 2012): these observing programs have detected $\sim$ 18,000 radio galaxies with radio fluxes at 1.4 GHz higher than 5 mJy. Surprisingly, the bulk of this population in the Local Universe ($z < 0.05$) is dominated by low-luminosity compact objects characterized by a paucity of extended radio emission (unresolved at the 5" FIRST resolution); for this reason they were named Fanaroff-Riley Type 0 radio galaxies (FR0s, Baldi et al. 2015).
In order to univocally identify sources belonging to this class, Baldi et al. (2015) defined as FR0 any radio galaxy associated with a red massive early type galaxy, with a high mass BH ($\geq 10^8 M_\odot$), spectroscopically classified as low excitation radio galaxy, and with a radio size of $\leq 1 - 3$ kpc. The compactness of these objects is then the essential ingredient to distinguish FR0s from typical extended FRI radio sources.

Radio properties: As reported above, while FRIs usually show extended components in radio maps, FR0s are unresolved at the 5" resolution of the FIRST radio survey. A useful parameter to inspect whether the lobes or the core dominate the total flux is the *core dominance*, defined as the ratio between the emission from the radio core and the emission from the whole radio galaxy. Due to their compactness, FR0s display a core dominance higher by a factor of $\sim$ 30 than that of FRIs. Moreover, FR0s have [OIII]λ5007

[11]Faint Images of the Radio Sky at Twenty centimetres survey (Becker et al., 1995).
[12]National Radio Astronomy Observatory Very Large Array (VLA) Sky Survey (Condon et al., 1998).

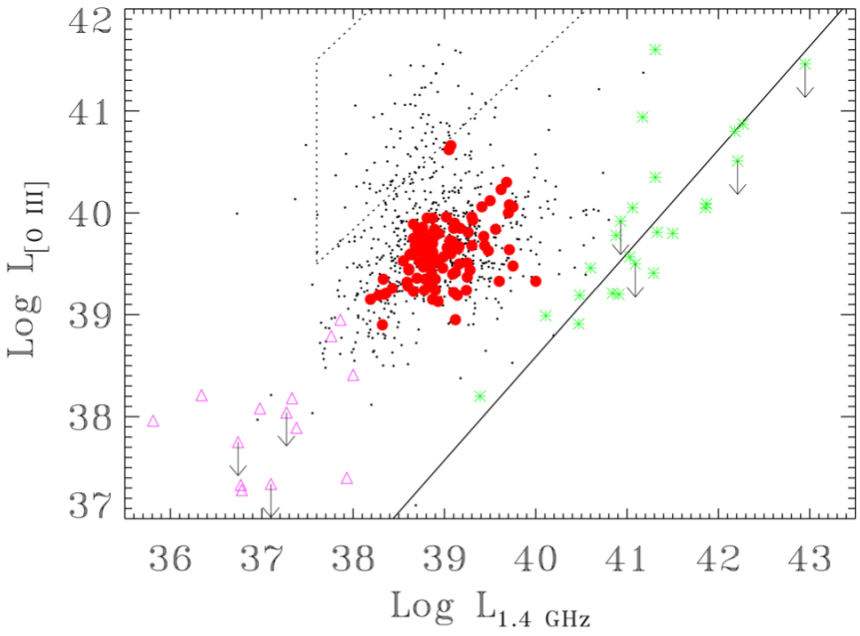

Figure 1.26: [OIII] Line luminosity versus 1.4 GHz radio luminosity, in erg s^{-1} (taken from Baldi et al. (2019b)); black points represent the low luminosity radio galaxies analyzed by Baldi and Capetti (2010), the solid line is the correlation for 3CR - FRIs sample (green stars), the dotted box indicates the region where usually radio-quiet galaxies are found; the red points are the FR0s selected by Baldi et al. (2018), while pink triangles are low power radio galaxies named Core Galaxies (see Balmaverde et al. (2006))

luminosity similar to that of FRIs, but lower total radio luminosity (see Fig. 1.26).The population of FR0s was selected from relatively shallow angular resolution surveys (5" for FIRST and 45" for NVSS), therefore single objects have been targeted with the VLA to improve the knowledge on the true extent of these AGNs: with a resolution of $\approx 0.2''$ at GHz frequencies, the VLA observations have revealed that FR0s remain compact below $\sim$ 1 kpc (Baldi et al. (2019a); see Fig. 1.27 for an example of FR0s' compactness). At

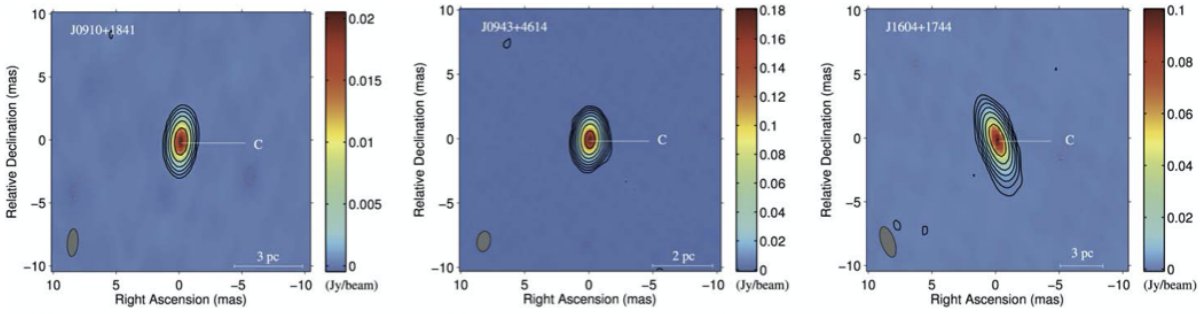

Figure 1.27: Parsec-scale structure of three FR0s targeted by the Very Long Baseline Interferometer (VLBI) at 8.4 GHz (Cheng and An, 2018).

lower frequencies, the search for extended emission has been performed by Capetti et al.

(2019), who resorted to a sample of 104 FR0s with redshift $z \leq 0.05$[13]: by inspecting the archive of the 150 MHz Giant Metrewave Radio Telescope (GMRT) survey named TGSS[14], they found that the FR0s detected in the TGSS images show unresolved radio component, confirming the lack of large scale emission[15]. Capetti et al. (2020a) observed the same sample with LOFAR[16] and reached analogous conclusions.
In addition to their morphology, MHz to GHz data have also been essential to characterize the radio spectra of FR0s, which appear rather flat, with a gentle spectral curvature towards GHz frequencies: this appears consistent with a core emission (Baldi et al., 2019b).

X-ray properties: with the aim of characterizing at high energy the central engine of FR0s radio galaxies, Torresi et al. (2018) conduced a systematic study in the 2-10 keV band of 19 FR0 galaxies with the following criteria:

- redshift z ≤ 0.15
- flux > 30 mJy and radio size of $\lessapprox 10$ kpc in FIRST data.
- Low excitation galaxy optical classification.
- With available data in the archives of the *XMM-Newton*, *Chandra*, *Swift* X-ray space telescopes.

The X-ray spectra of these sources have been found to be well fitted by a power-law component absorbed by galactic column density; there is no evidence for intrinsic absorption, possibly suggesting a depletion of cold matter in the circum-nuclear environment similarly to FRIs. The photon index is generally steep, with a medium value of $< \Gamma >= 1.9 \pm 0.3$. The luminosity of these sources has been calculated in the 2-10 keV band, leading to values in the range $L_X = 10^{40} - 10^{43}$ erg s^{-1}: by comparing the radio luminosity and the X-ray luminosity of the core, a correlation (see Fig. 1.28) between the two has been found to hold both for FR0s and for FRIs (as previously found for FRIs by Balmaverde et al. 2006), which suggests a non-thermal origin (i.e. the jet) for the X-ray emission:

$$\log(L_{2-10\,\mathrm{keV}}) = (7.8 \pm 0.6) + (0.8 \pm 0.1)\log(L_{5\,\mathrm{GHz}}) \tag{1.48}$$

The similarities with FRIs extend also to the accretion rate of these sources: estimates for the ratio $L_{\mathrm{acc}}/L_{\mathrm{Edd}}$ are in the range $10^{-3} - 10^{-5}$, leading the authors to suggest a radiatively inefficient (ADAF) accretion flow at work in the central engine.

[13] the catalogue, named FR0*CAT*, has been presented by Baldi et al. (2018).
[14] Tata Institute of Fundamental Research GMRT Sky Survey (Intema et al., 2017).
[15] They found one exception, but the extended radio emission might not be associated with the AGN.
[16] LOw Frequency ARray (Van Haarlem et al., 2013).

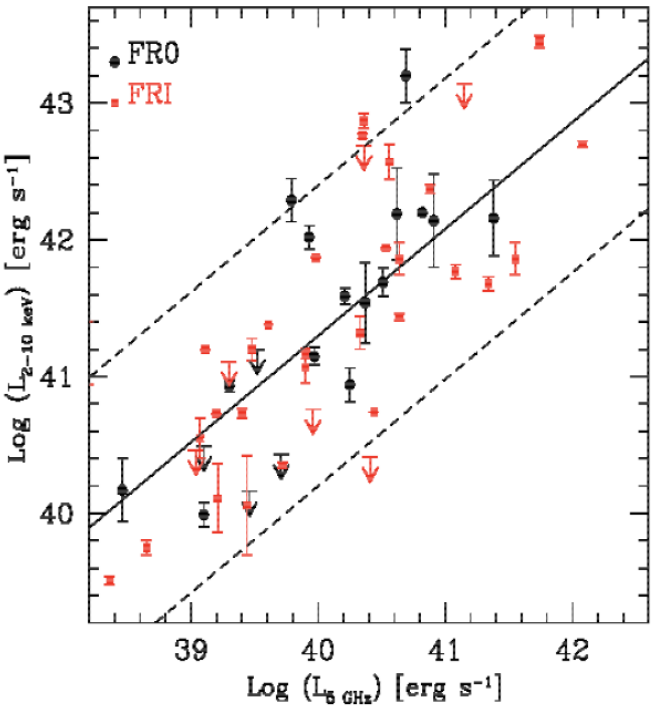

Figure 1.28: Plot of the X-ray luminosity versus radio core luminosity for FRIs (red points) and FR0s (black points), with the solid black line being the linear regression for the whole sample of radio galaxies (Eq. 1.48), and the dashed lines its uncertainties (Torresi et al., 2018).

The similarity in the X-ray properties between FR0s and FRIs suggests that the lack of the extended emission cannot be ascribed to a different accretion process occurring in the central engine.

Torresi et al. (2018) concluded that it is unlikely that beaming effects come into play, as the ratio between the [OIII] and the 2-10 keV luminosity, considered as a useful tool to distinguish between misaligned and aligned jets, is higher in FR0s and FRIs than in blazars, which are expected to show a more Doppler boosted X-ray emission. The entire class of FR0 cannot be explained as young radio sources. Indeed, Baldi et al. (2018) showed that the space density of FR0s at $z < 0.05$ is larger by a factor of ~ 5 than FRIs, definitely excluding the possibility that FR0s will all evolve into extended radio sources. As noticed by Capetti et al. (2019), it is possible that a fraction of the discovered FR0s are compact because they are young, but the overall properties of the population tend to exclude a significant contribution. As a consequence, compact FR0s seem to form a unique category of objects, for which the reason(s) behind the lack of large scale radio emission has to be fully explored.

Proposed scenarios for the compactness of FR0s:

- *Environment*: It has been proposed by Baldi et al. (2015) that the external medium of FR0s could possess peculiar features (density, clumpiness) capable of decelerate and eventually disrupt the relativistic jets: the entrainment of the galaxy medium would affect the jet stability, hence preventing its propagation beyond $1-3$ kpc from the center. However, the optical host magnitudes of FR0s (which give an indication of the ISM density) are similar to those of FRIs, suggesting that the galaxy-scale ISM environment might not be the answer. The host galaxy hot ($10^6 - 10^7$ keV) corona could also be responsible for the jet disruption: as reported by Capetti et al. (2020b), who explored the large-scale environment of FR0s in terms of number of neighbours, the ambient of FR0s is poorer than that of FRIs; they pointed out that the extent of jets indicates that they are propagating well inside the hot corona of their hosts, so the distribution of external galaxies is not likely to directly affect them. From an X-ray point of view, the analysis of the galactic environment would provide a complementary indication of the host conditions, for example the total gas mass, the density the hot phase of the ISM (the X-ray emitting corona), or the condition of the circum-galactic ambient. About 50% of the FR0s in the sample of Torresi et al. (2018) resides in a dense environment (either a galaxy cluster or a galaxy group), but due to the serendipity of their sources they could not provide a reliable estimate of the fraction of FR0s in dense environments. Nevertheless, it has been suggested that at least for a fraction of FR0s - who reside in cooling core clusters - the cool, dense central ICM could represent another source of frustration for the jets of these radio galaxies.

- *Intrinsic jet properties*: As reported by Baldi et al. (2019b), FR0s' jets are probably relativistic at parsec scale, but seem to be decelerating at larger scales; this results in a lower Lorentz factor $\Gamma_{\rm jet}$[17]: if the jet possesses an inner, weak, and short (< 1 kpc) relativistic spine, wrapped in a mildly relativistic ($v \sim 0.3c$) layer, a dense surrounding medium could be able to quickly decelerate it. The low values of $\Gamma_{\rm jet}$ in FR0s seem to be supported by the non-detection of one-sided kpc scale jets, which would indicate that relativistic boosting is present[18].

- *BH spin*: Baldi et al. (2015) suggested that the low $\Gamma_{\rm jet}$ might be associated with the parameters of the central SMBH: when the black hole's spin and mass assume extreme values, a radio loud AGN produces relativistic and stable jets, capable of excavating their way through the external medium and eventually inflate giant radio lobes. On the other hand, FR0s would be associated with less extreme values of the

[17]The Lorentz factor is a useful parameter to express relativistic speed: $\Gamma = \frac{1}{\sqrt{1-(v/c)^2}}$.

[18]On the contrary, many FRIs display strong jet asymmetries (Parma et al., 1987).

black hole parameters (relatively lower spin and mass), thus dominating the number density of radio galaxies in the local Universe. In this context, the higher number of galactic neighbours of FRIs found by Capetti et al. (2020b) would be consistent with a more intense galaxy evolution through mergers and black holes coalescence, which in turn might produce more massive, fast spinning black holes. The authors conclude that this picture has yet to be fully probed.

- *Recurrent activity*: a time dependent jet scenario, in which a sporadical nuclear activity would not be able to sustain the jet at large distances, could be explored (especially at low radio frequencies) by looking for evidences of a past activity. In this case, the presence of compact radio galaxies at the center of galaxy clusters has to be reconciled with the need of radio bubbles inflated by the central AGN to prevent runaway cooling: the detection of a past activity could both provide a heating source, and be consistent with an intermittent activity of the central radio source. This suggests that in the context of FR0s not only the jet launching mechanisms, but also the feedback-related phenomena should be investigated.

Up to now a final answer to the nature of FR0s has not yet been found; it is possible that many mechanisms are at play, with a possible strong connection between black hole properties and ambient density: slowly spinning SMBH could produce low $\Gamma_{\rm jet}$ jets, which in turn might be easily disrupted by the environment (Baldi et al., 2019b). In this thesis work, we aim to thoroughly characterize the conditions of the Intra cluster medium in the proximity of a FR0 at the center of a galaxy cluster, in order to provide further indications on the properties of these radio galaxies, and to understand if (at least for this source) the environment is of critical importance.

1.5 Our target: the galaxy cluster Abell 795

In the following chapter, we present the results of our X-ray study of the *Chandra* observation of the poorly studied galaxy cluster Abell 795 (A795). This system is located at a redshift of $z \sim 0.1374$ (Rines et al., 2013) and at RA, DEC = 09:24:05.3, +14:10:21.5. Previous X-ray observations of this cluster had been performed by the *Rosat All Sky Survey* (RASS, Ebeling et al., 1996), which measured a flux in the $[0.1 - 2.4]$ keV band of $f_X = 7.1 \times 10^{-12}$ erg cm^{-2} s^{-1}; however, no specific information on this galaxy cluster cooling properties and ICM conditions are available. Therefore, our work is the first X-ray dedicated study of A795, and considering the high resolution of the *Chandra* space telescope (~ 0.5"), with this analysis we will provide new, updated clues on this cluster's dynamical state and emission properties.

Figure 1.29: Composite-color (*g-r-i* filters) optical image of A795 (as surveyed by the SDSS), and centered on the brightest cluster galaxy J0924+14. The image f.o.v is $6.35' \times 9.7'$.

J092405.30+141021.5: the brightest cluster galaxy The optical appearance of this galaxy cluster (see Fig. 1.29) reveals an over-density of galaxies around the brightest cluster galaxy, J0924+14. This elliptical galaxy has been found to host a radio loud AGN, and has been classified by Torresi et al. (2018) as a Fanaroff-Riley Type 0 radio

galaxy: the main parameters used to categorize this active galactic nucleus (reported in Tab. 1.1) have been collected by Best and Heckman (2012), who suggested the LERG nature of this galaxy. In particular, by plotting the 4000Å-break parameter[19] against the luminosity of the [OIII] line (Fig. 1.30 panel *a*), our target BCG is found to lie in the non star-forming, low-excitation line AGN region. Moreover, the 1.4 GHz radio contours of the FIRST observation of this radio galaxy indicate a point-like, compact source (see Fig. 1.30 panel *b*), in line with the class-defining feature of FR0s of being compact, kpc-size radio sources.

	M_{star} [$M_\odot$]	4000Å-break	$L_{[OIII]}$ [erg s^{-1}]
J0924+14	4.2×10^{11}	1.76	$(5.37 \pm 0.05) \times 10^{40}$

Table 1.1: This table contains the stellar mass, the 4000Å-break and the [OIII]-line luminosity of J0924+14.

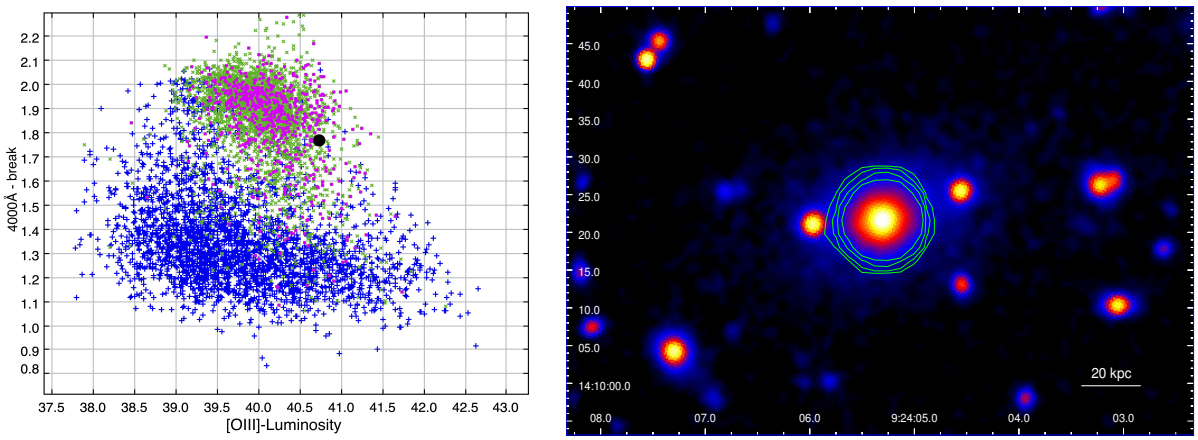

(a) **(b)**

Figure 1.30: Panel *a*: 4000Å-break vs [OIII]-line luminosity for the sample of galaxies presented in Best and Heckman (2012); blue points are the star-forming galaxies, green crosses are LERG galaxies, pink boxes are LERG compact galaxies, and the black circle marks the position of J0924+14. Credits: Dr. Paola Grandi. Panel *b*: SDSS *r*-band image of the innermost regions of A795, with 1.4 GHz FIRST radio contours (green); the first contour is at 5σ.

From an X-ray point of view, J0924+14 belongs to the sample of FR0s studied by Torresi et al. (2018); in particular, Torresi et al. (2018) measured a power law spectrum with

[19]The 4000Å-break is defined as the ratio between the average flux density in erg s^{-1} cm^{-2} Hz^{-1} between 4050 and 4250Åand that between 3750 and 3950Å, and is typically used to determine the star formation characteristics and the star population age of distant galaxies (see e.g. Bruzual et al., 1983; Poggianti and Barbaro, 1997).

$\Gamma = 1.8$ plus an `APEC` component with $kT = 1.3$ keV related to the thermal gas of cluster. They concluded that the X-ray incoming photons are produced in the jet, and that an inefficient, advection-dominated accretion flow powers the central engine. As reported in Subsect. 1.4.2, it is still unclear whether and how the environment of these radio galaxies affects their nuclear behaviour; this work is the first attempt to investigate the (uncertain) link between the X-ray properties of the ambient gas in which an FR0 has been found to reside, and the compactness of their radio emission.
The following cosmology is assumed for this thesis work: $H_0 = 70$ km/s/Mpc, $\Omega_{\rm m} = 0.3$, $\Omega_\Lambda = 0.7$. Considering the redshift of this cluster ($z = 0.1374$) the conversion between linear and angular scales is 2.43 kpc/". Every uncertainty in this work is reported at the 1σ confidence level.

Chapter 2

Chandra analysis: data reduction and morphological tools

The first section of this chapter is dedicated to the explanation of the main procedures which have been applied to the raw *Chandra* data, in order to obtain the final, *clean* dataset. The second section presents the main techniques (and software) implemented for the morphological analysis of our target galaxy cluster.

2.1 Reprocessing the observation

The data reduction has been performed using the tools of **CIAO: Chandra's data analysis system** (Fruscione et al., 2006), version 4.12. After a brief description of this observation, in the first section the main steps executed by the **chandra_repro** script are outlined. In the following section the correction for the astrometry and the removal of bad period of background is presented. In the last section, the search and choice for the correct **blank_sky** file, along with the reason why this file is necessary, are explained.

2.1.1 Instrument and dataset information

The observation of Abell 795, the reference cluster of galaxies for this work of thesis, has been performed by the *Chandra* X-ray observatory, a space telescope designed by NASA in order to observe at high resolution X-ray galactic and extra-galactic astrophysical sources. The instrument has been launched on July 23, 1999 and has since proved itself extremely useful to obtain new information on the detailed physics of clusters of galaxies. The *Chandra* telescope is composed of four nested mirrors, which can focus X-ray radiation onto the electronic detectors. The detector is a CCD imaging spectrometer (ACIS), which can be used in several configurations and allows to acquire simultaneously high resolution

Observation ID	11734
PI	Russell
Target Name	Abell 795
RA (J2000)	09 24 05.30
DEC (J2000)	+14 10 22.00
Instrument	ACIS-S
Data Mode	VFAINT
Date	2010-01-13
Exposure Time	29.74 ks

Table 2.1: This table contains the main informations about this observation; the data have been retrieved from *Chandra-data-archive* (https://cda.harvard.edu/chaser).

images and moderate resolution spectra. Six out of ten ACIS CCD are arranged in a 1×6 array (ACIS-S) which has been used to obtain detailed images of specific sources. If a large field of view is necessary, it is possible to use the ACIS-I configuration (four CCD arranged in a 2×2 array). The reference cluster has been observed in 2010 with the ACIS-S configuration. The starting set of data is summarized in Tab. 2.1, which contains the main information on this observation.

2.1.2 Creating event files

After retrieving the data, the first cleaning procedure requires running the **chandra_repro** script, which applies the most recent calibration: the script reprocesses a *Chandra* data set by reading files in the `primary` and `secondary` directories, and then performs the following actions:

- It creates a bad pixel file, by identifying pixels with a bad bias value or hot pixel, which have to be excluded from the analysis.
- It creates a `level=2` event file, which consists in a table of photons for which position, time of arrival and energy are stored. This photons have been filtered depending on `GRADE` or `STATUS` (which denote the probability that the photon is a real, good event).

By inspecting the header of the original event file it is possible to check that data have been acquired in the *very faint* (VFAINT) mode, which can be used to help distinguish between good X-ray events and bad events that are most likely associated with cosmic rays. Checking the mode of the observation is necessary, so that the correction provided by **chandra_repro** can work properly for this dataset. At the end of this reprocessing procedure, it is possible to visualize the event file and superimpose the field of view

regions: the result is appreciable in Fig. 2.1. From this action it is possible to deduce that the cluster lies in the S3 chip.

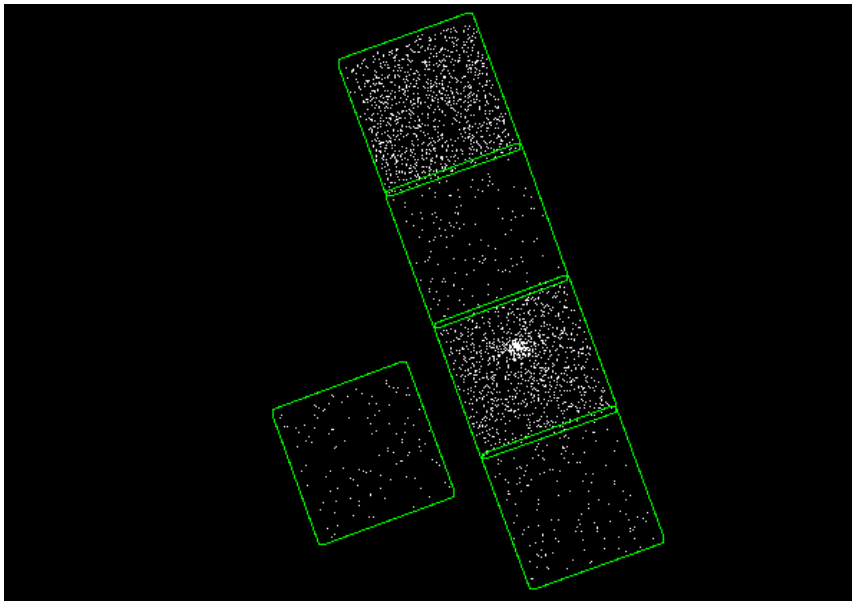

Figure 2.1: Image of the ACIS configuration for this observation; the four adjacent chips are ACIS S1-S4, while the left one is ACIS-I3. The scale is set to `log` to help visualization. The cluster A795 lies in the S3 chip.

2.1.3 Astrometry correction

The second reprocessing step consists in the correction of the astrometry: this is done when, for example, there is a specific desire to study precise offsets between the components of an astrophysical target. The *Chandra* 99% limit on positional accuracy is 1.4"; the astrometry correction aims to further improve this accuracy. Correcting the coordinates can be performed by following two different paths: it is possible to cross match sources with an external catalogue whose positions are believed to be more correct than the *Chandra* ones, but it is also possible to perform the cross matching with another *Chandra* observation, to obtain a relative correction. The latter method is usually carried out when long exposure, multiple images are available. In the case of A795 only our single, 29.7 ks exposure is available; therefore, the correction of absolute astrometry has been performed by referring to the `United States Naval Observatory` (USNO-A2.0) optical catalogue.
The coordinate correction is then performed by executing the following actions:

- In order to detect point sources in the main observation, a map of the PSF (Point Spread Function) across the CCD has to be created. The **mkpsfmap** tool takes an input image and calculates the PSF-size at each pixel in the image; the user can

control the *size* of the PSF with the choice of a particular ECF (*Encircled Counts Fraction*) value. This parameter ranges between 0 and 1; larger ECF values would produce broader PSFs.

- Once the PSF map is created, the **wavdetect** CIAO tool locates sources by correlating the image with wavelets[1] of different user selected scales, and then searches the results for significant correlations. By supplying a PSF map to the tool it is possible to better characterize the size of the output point sources.

- The following step consists in the cross matching between the external catalogue and the source list created by **wavdetect**: several transformation parameters are calculated and then used to shift the point sources to the reference position; the transformation which minimizes the difference is then returned as an output of the process.

- At last, the transformation is applied to the *Chandra* dataset by updating the aspect solution[2] and the event file.

We applied this procedure to ObsID 11734; it seems important to point out that the point sources found by **wavdetect** are, in general, excluded from the source image during the analysis, so that their emission does not contaminates the target (see Chap. 3). This requires a second run of wavdetect after the astrometry correction, in order to obtain a list of point sources with correct positions.

2.1.4 Removing background flares

In order to associate the correct blank-sky background dataset (Subsect. 2.1.5) to the reference observation, it is important to remove any background flare from the ACIS event file. To perform this action, first of all any bright source has to be removed from the dataset: this includes the point sources and the cluster. Subsequently, with the **dmextract** CIAO tool it is possible to extract a light curve from a selected region: the starting and ending time of the observation has to be provided, along with a bin size. Since the ACIS blank-sky background files were cleaned using a bin size of 259.28 seconds, it seems appropriate to use the same binning for the event data. The light curve is then cleaned with the **deflare** script, which gives as an output a file containing the *good time*

[1] Brief oscillation that begins at zero, increases and then returns to zero.

[2] In order to better sample the point spread function, X-ray telescopes can change the position of the optical-axis on the sky during an observation. Because of this dithering motion, photons coming from the same location will be registered on different parts of the detector during the observation. The aspect solution file contains the telescope optical axis direction and spacecraft roll angle as a function of time, which are used to reconstruct the *sky coordinate* celestial image.

EXPTIME1 (s)	EXPTIME2 (s)	Δt (s)
29744.315399	29744.315087	3.12×10^{-4}

Table 2.2: This table contains the exposure time for ObsID11734 before and after applying the correction for the astrometry, along with the difference Δt between the two times.

interval for the observation. In the case of A795, the light curved can be seen in Fig. 2.2. It is straightforward to denote that the bad time intervals (red color) represent a very small fraction of the total exposure time. Indeed, after this operation it is possible to check the difference between the old and the new exposure times: the values in Tab. 2.2 indicate that a negligible fraction of the observation has been lost after this procedure.

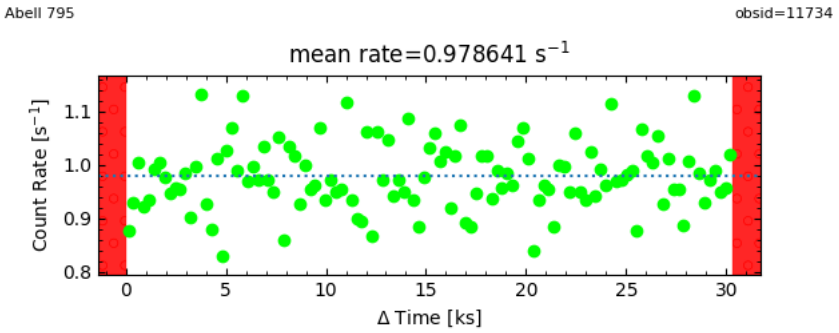

Figure 2.2: Background lightcurve; green points are considered as part of the good time interval, while the solid red line indicates the region excluded by **deflare**.

2.1.5 Blank-sky files: matching and normalization

In the case of extended sources, which might cover large fraction of the chip, determining the background locally might be arduous and not effective. For this reason, a set of experimental blank-sky datasets has been produced for *Chandra* ACIS. These files are useful when spectral analysis or surface brightness profile extractions are performed, since they can be used to create background spectra or background images. The ACIS blank-sky files are created from sets of observation of relatively empty fields, located at high galactic latitude and low, soft X-ray emission in the ROSAT All Sky Survey maps.
The **blanksky** CIAO tool selects among all available files the correct blank-sky file, then reprojects it to match the observation and then determines the proper scaling. If the `particle` method is selected, the scaling is computed with the high energy (9-12 keV) ratio of counts of the blank-sky and the observation.

Count rate normalization We performed an alternative method to scale the blank-sky event file. The blank-sky background event file given in output by **blanksky** might be characterized by some little differences in terms of *count rate* with respect to the observation local background. In order to evaluate this difference, it is possible to restrict the energy range of the blank-sky and of the observation to the 9-12 keV band, where only the background emission is expected to be present. By creating images in this energy range with **blanksky_image**, the number of counts of the blank-sky image and that of the observation event file should be equal, since the blank-sky file is scaled by the ratio of counts. This type of scaling is adequate when images have to be produced, but when a spectral analysis is performed, it is important that *count rates*, and not counts, are equal. The software `Xspec` normalizes the spectra by the ratio of exposure times: to obtain correct results, it is important to make sure that *count rates* of the blank-sky and the target event files are equal. In fact, the exposure time of blank-sky files is usually larger than that of typical observations: as a consequence, when dividing the count-normalized blank-sky and observation event file for their respective exposure time, two completely different count rates would be obtained (for the 9-12 keV band). This would make these files unuseful in terms of spectral analysis.
Therefore, in order to obtain count-rate-normalized blank-sky event files, the following steps may be executed:

- Restrict the blank-sky and observation event files to the 9-12 keV band and exclude the point sources and cluster emission.
- Use **dmextract** to obtain the count rate of the background ($\mathrm{CR_{back}}$) and that of the observation ($\mathrm{CR_{sour}}$).
- Rescale the blank-sky exposure time for the ratio of the background count rate and the source count rate, that is:

$$\text{new exposure time} = \text{old exposure time} \times \frac{\mathrm{CR_{back}}}{\mathrm{CR_{sour}}} \tag{2.1}$$

- Update the `EXPOSURE` and `BKGNORM` keyword in the header of the background event file with the new exposure time and the inverse of the count rates ratio, respectively.

This procedure, applied to the A795 dataset, has led to the creation of a background file which can be used both for spectral analysis and for images creation. It is important to denote that in order to obtain correct images from count-rate-normalized files, a further multiplication for the ratio of the exposure times (the automated procedure implemented

by `Xspec`) is necessary, since:

$$\frac{C_{sour}}{t_{sour}} = \frac{C_{back}}{t_{back}} \tag{2.2}$$

$$\text{then} \quad C_{back} = C_{sour} \tag{2.3}$$

$$\iff C_{back}^{new} = C_{back}^{old} \times \frac{t_{sour}}{t_{back}} \tag{2.4}$$

where C are the *counts*, and t is the *exposure time*.
Despite the fact that this procedure might seem redundant, it is a thorough method to obtain correct files both for spectral and imaging analysis. In particular, after the normalization procedure the background and observation count rate in the 9-12 keV band are:

$$CR_{back} = 1.0884446698 \quad \text{count/s} \tag{2.5}$$

$$CR_{sour} = 1.0884432842 \quad \text{count/s} \tag{2.6}$$

which are equal to the fifth decimal digit, so the normalization procedure can be considered as successful.

2.2 Morphological analysis tools

In this section, the main tools used for the morphological study of Abell 795 are presented. The data reprocessing has led to the creation of two event files, one for the target and one for the background. From these two event files it is possible to obtain images with a **dmcopy** command; this command allows for some filters to be applied: it is possible to select the energy range and to restrict the analysis to specific chips. The target and background images are in units of *counts/pixel*, which have to be transformed into surface brightness units to extract physical informations. This action requires the creation (with the **fluximage** tool[3]) of another file, the *exposure map*: this map accounts for the effective area and for the time spent to observe the field of view, and it is used to obtain the flux in every point of the image. The exposure map must have the same dimension of the target image, and has to be created for a specific energy range: the minimum, the maximum, and the effective energy have to be specified. There are several energy bands which can be used, for which an effective energy has been calculated and can be inspected in the `Chandra Source Catalog Energy Bands`; in general, the effective energy represents a center-band energy which corresponds to a high value for the effective area. Once an

[3]This tool creates exposure-corrected images and exposure maps for an observation.

appropriate energy band is selected, it is possible to run **fluximage**. The pixels of the ouput exposure map have units of cm^2 s.

2.2.1 Surface brightness radial profiles

A powerful tool to analyze images consists in the extraction of radial profiles of surface brightness: these can be used to inspect the presence of spatial trends of the emission, and to compute several morphological parameters which may serve as dynamical state indicators. The main `ciao-4.12` tool to extract surface brightness profiles is **dmextract**, which allows for the creation of `.fits` files to fit with `Sherpa`, a modelling and fitting application of `ciao`. In addition to this, during this work of thesis the capabilities of the external application `Proffit-1.5` (Eckert et al., 2011) have been explored: this software has been produced in order to provide a powerful and relatively simple tool for the analysis of galaxy cluster X-ray surface-brightness profiles. For the following steps, both the capabilities of `ciao-4.12` and Proffit have been tested.
In the first place, it is necessary to define regions for the extraction: a common method considers circular or elliptical multiple annuli centered in the proximity of the cluster center; in the second place, point sources which may lie inside the annuli have to be removed, so that their emission does not contaminate that of the cluster. The surface brightness will then be computed by taking the counts in each annulus and dividing by the area. The two software above both offer the possibility to calculate the surface brightness in physical units, once an exposure map has been provided. Moreover, by extracting from the same annuli the background counts, it is possible to extract background-subtracted surface brightness profiles.
In practice, in the i-th annulus, the surface brightness Σ_i - in counts $s^{-1}cm^{-2}$ $arcsec^{-2}$ - is computed as follows:

$$\Sigma_i = \frac{Img - Bkg}{Exp} \tag{2.7}$$

where Img and Bkg are, respectively, the image and background counts in the i-th annulus, while Exp is the exposure map in units of cm^2 s.
The extraction of different profiles in circular annuli (but also in sectors) has been performed with the same parameters with **dmextract** and `Proffit`, to prove that they yield the same result. The output is appreciable in Fig. 2.3, where the surface brightness is in units of counts s^{-1} $arcmin^{-2}$, since `Proffit` assumes $cm^2 = 1$[4] As it is possible to see from Fig. 2.3, the surface brightness profiles computed by the two software are consistent within errors, so that the choice to use one of the two over the other does not affect the

[4] `Proffit` has been optimized for *XMM-Newton*, whose exposure maps are in units of counts s^{-1}, while *Chandra*'s exposure maps have units of counts s^{-1} cm^{-2}.

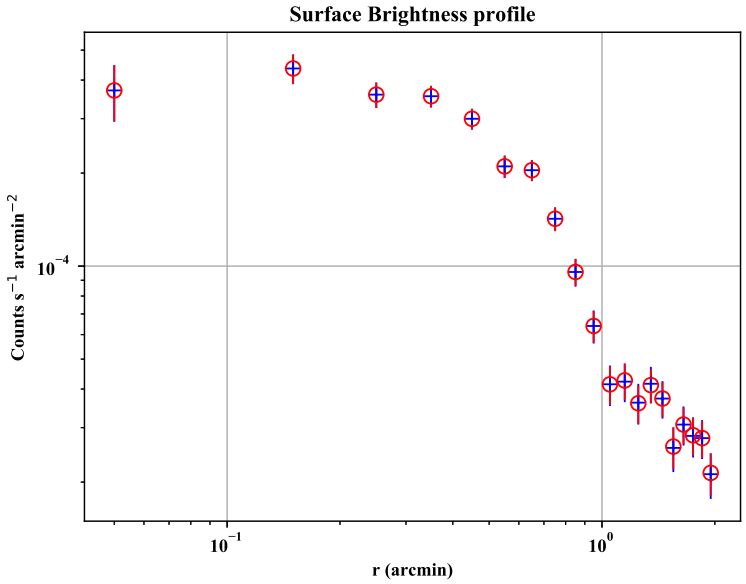

Figure 2.3: Example of surface brightness profile computed with **dmextract** (blue crosses) and `Proffit` (red circles).

results. Once a specific profile has been extracted, it is possible to fit it using the functions of `Sherpa` or `Proffit`. After choosing a fitting model, its parameters can be assigned an initial value and then thawed or frozen. If the `chi` statistics has been implemented, it is possible to evaluate the goodness of the fit by inspecting the reduced chi-square, which is given in output both by `Sherpa` and `Proffit`.
The difference in the exposure maps units between *Chandra* and *XMM-Newton* leads to inconsistencies when deprojecting with `Proffit` the surface brightness profile to obtain the density (see Sect. 3.2): in particular, `Proffit` returns a density profile in units of cm^{-5}. Therefore, to extract correct density profiles of *Chandra* data with `Proffit`, it is necessary to correct vignetting: normalizing the exposure map by the ratio between the exposure at the aimpoint and the exposure time returns a "time map"; the units of this image are then seconds, and by loading it on `Proffit` the resulting density profile is in the correct units of cm^{-3}.
With this software, it is possible to compute some morphological parameters which can be particularly useful to infer dynamical properties of galaxy clusters. In particular, once a radial profile has been extracted `Proffit` allows for the determination of:

- The *centroid shift* w (Mohr et al., 1993), which assesses the shift of the position of the X-ray centroid when changing the used aperture from a radius $R_{\rm max}$ (user

supplied) to the center of the cluster. This parameter is defined as follows:

$$w = \frac{1}{R_{\rm max}} \sqrt{\frac{\Sigma(\Delta_{\rm i} - \langle\Delta\rangle)^2}{N-1}} \tag{2.8}$$

where N is the number of considered apertures, and $\Delta_{\rm i}$ is the distance between the i-th centroid and the one obtained with aperture $R_{\rm max}$.

- the *surface brightness concentration* $c_{\rm SB}$ (Santos et al., 2008), which consists in the ratio between the total flux calculated within the central 40 kpc to the flux calculated within the central 400 kpc. Once a model has beed loaded, `Proffit` evaluates it to calculate the concentration following:

$$c_{\rm SB} = \frac{F(r \leq 40kpc)}{F(r \leq 400kpc)} \tag{2.9}$$

The user has to provide the cluster redshift to compute the relation between angular and physical scale[5].

2.2.2 Two-dimensional analysis

Apart from the extraction of one dimensional products, it is also possible to manipulate an image in order to enlight particular morphological trends. In this thesis, the following techniques have been implemented[6]:

- **Smoothing**: in order to enhance morphological patterns, it is possible to apply to the data a *filter fuction* that can attenuate the noise and other small scale features. This can be performed with **aconvolve**: with this tool the input image can be convolved with a 2D gaussian function, for which the sigma of each axis, along with the size of the function (in units of sigma) have to be supplied. The value of sigma determines the type of filter which is applied to the image: the convolution will preserve and enhance features larger than sigma, and suppress smaller features. Therefore, **aconvolve** performs a linear smoothing, which is satisfactory when the interesting details in the input are approximately the same size. However, in order to smooth at different scales (to enhance different size details), the **csmooth** tool might be more adequate: this algorithm smooths the input image until the signal-to-noise in each pizel is between the input limits. The background can be either computed from an annulus around each pixel, or supplied as an input.

[5] `Proffit` adopts $H_0 = 70$ km/s/Mpc, $\Omega_{\rm m} = 0.3$, $\Omega_\Lambda = 0.7$, which is the same cosmology as the one adopted for this work of thesis.

[6] the first two have been executed with `ciao-4.12` tools, the last one has been particularly fulfilled with the `Proffit` software (although the usage of `Sherpa` is possible).

- **Unsharp mask image**: this technique can be used to improve the contrast of an image, by smoothing an image with a gaussian of scale b, smoothing the same image with a gaussian of scale t (with $t \geq b$), and then subtract the two smoothed images, that is:

$$\hat{U} = I * b - I * t \tag{2.10}$$

  where $\hat{U}$ is the output *unsharp mask image*.
  The operation consists in a spatial band-pass filter that preserves spatial features larger than g but smaller than h. To make a contact with the previous technique, this operation can be performed by applying **aconvolve** twice to the input image, then the outputs can be subtracted. This strategy can be used to investigate the presence of discontinuities, depressions, or filaments in the X-ray image.

- **Residual image**: once a best fit model for the cluster emission has been established, it can be interesting to view the deviations of the data from it, in order to identify regions for which the assumption of the model are not acceptable. This can be executed with the **savedeviations** command, which computes the pixel-by-pixel residuals (in units of σ) between the data and the model. Since the model has been created for a 1D radial profile, the residuals indicate where there is a major deviation from the spherical symmetry assumption.
  It is also possible to produce the residual images using `Sherpa`, which fits the images using 2D-models; we verified that the two methods yield consistent results, therefore the `Proffit` residual images are presented in the following chapters.

Chapter 3

X-ray analysis: the ICM of A795

This chapter is dedicated to the study of A795's Intra Cluster Medium. In the first section, we present our results for the morphological analysis of this cluster, which revealed dynamical disturbances and substructures: we found two surface brightness discontinuities along a *sloshing* spiral. We further investigated the thermodynamical status of A795 by means of a radial spectral analysis, and we determined that the two discontinuities are cold fronts: these findings are unveiled in the second section.

3.1 Morphological Analysis

This section collects the results obtained by applying the methods described in section 2.2 to the *Chandra* observation of A795; the images of this clusters have been produced in the 0.5-2 keV band, where most of the emission concentrates. After the inspection of the overall appearance of this galaxy cluster, the properties of the two surface brightness discontinuities we found during the analysis are presented (see Fig. 3.1).

3.1.1 Investigating the presence of offsets

By inspecting the 0.5-2 keV image of A795 (shown in Fig. 3.2), it is possible to verify whether significant offsets between various components (central AGN, X-ray peak, X-ray centroid) are present. The coordinates of the central galaxy are available, and the search for point-like sources with **wavdetect** has provided a match for the central AGN. The X-ray peak corresponds to the brightest pixel in the image (AGN excluded). The choice for the brightest pixel depends on the smoothing applied: the small scale variations of the unsmoothed, full resolution image could prevent the identification of a single, brightest pixel. By smoothing the image with a Gaussian of 3 pixel FWHM we identified the pixel which contains the higher counts, and we chose it as the X-ray peak. Tab. 3.1

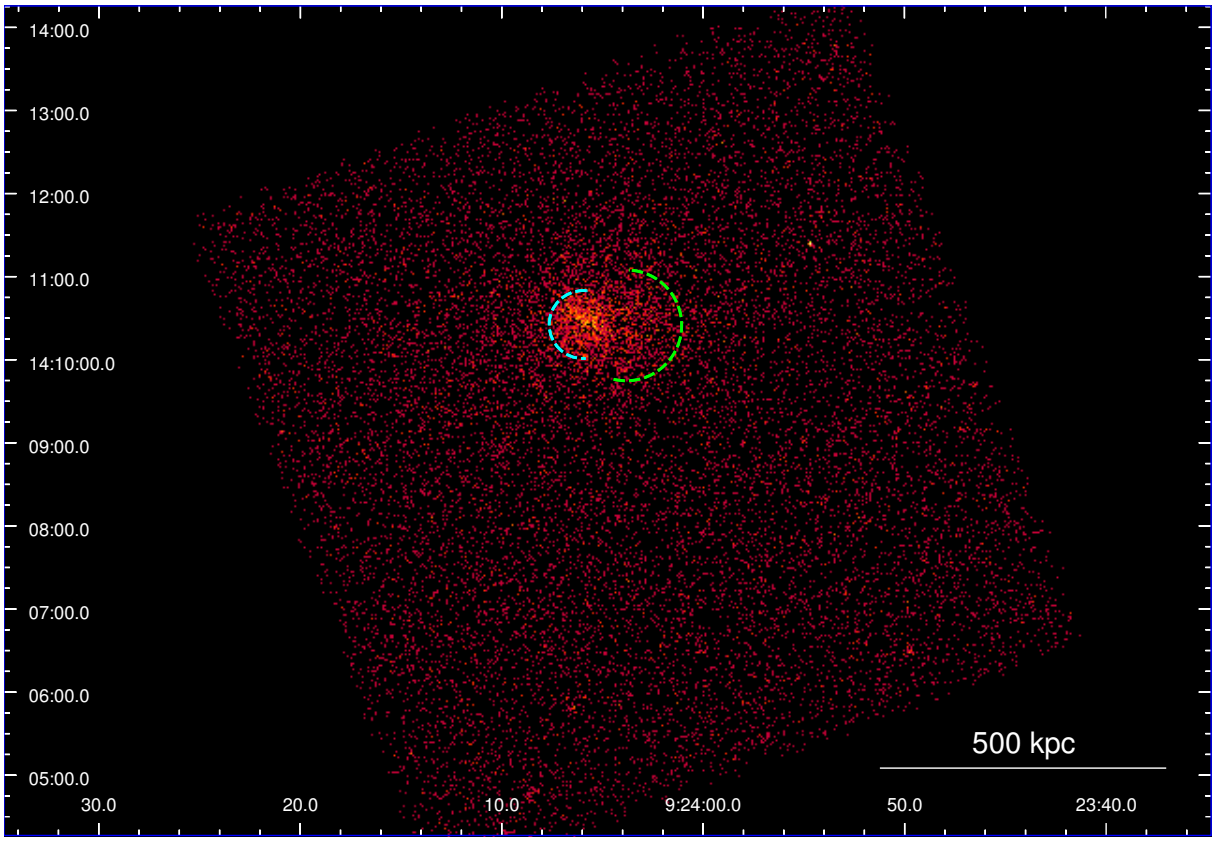

Figure 3.1: 0.5 -7 keV raw image of the chip 3, showing A795. The position of the two fronts is indicated with cyan and green arcs.

lists the results obtained: in particular, the AGN and the X-ray peak are located at an approximate distance of 7.3" (17, 7 kpc).

The presence of this spatial offset between the BCG and the X-ray peak could be indicative of dynamical disturbances. In fact, as it has been noted in the introducing chapter, in relaxed, undisturbed clusters the X-ray peak is spatially coincident with the brightest cluster galaxy. Other evidences for a unrelaxed system are presented in the following steps of the morphological analysis.

	RA(J2000)	DEC(J2000)
AGN	09 24 05.48	+14 10 23.54
X-peak	09 24 05.96	+14 10 25.50

Table 3.1: This table contains the coordinates of the central AGN and of the X-ray peak obtained from the 0.5-2 keV *Chandra* image.

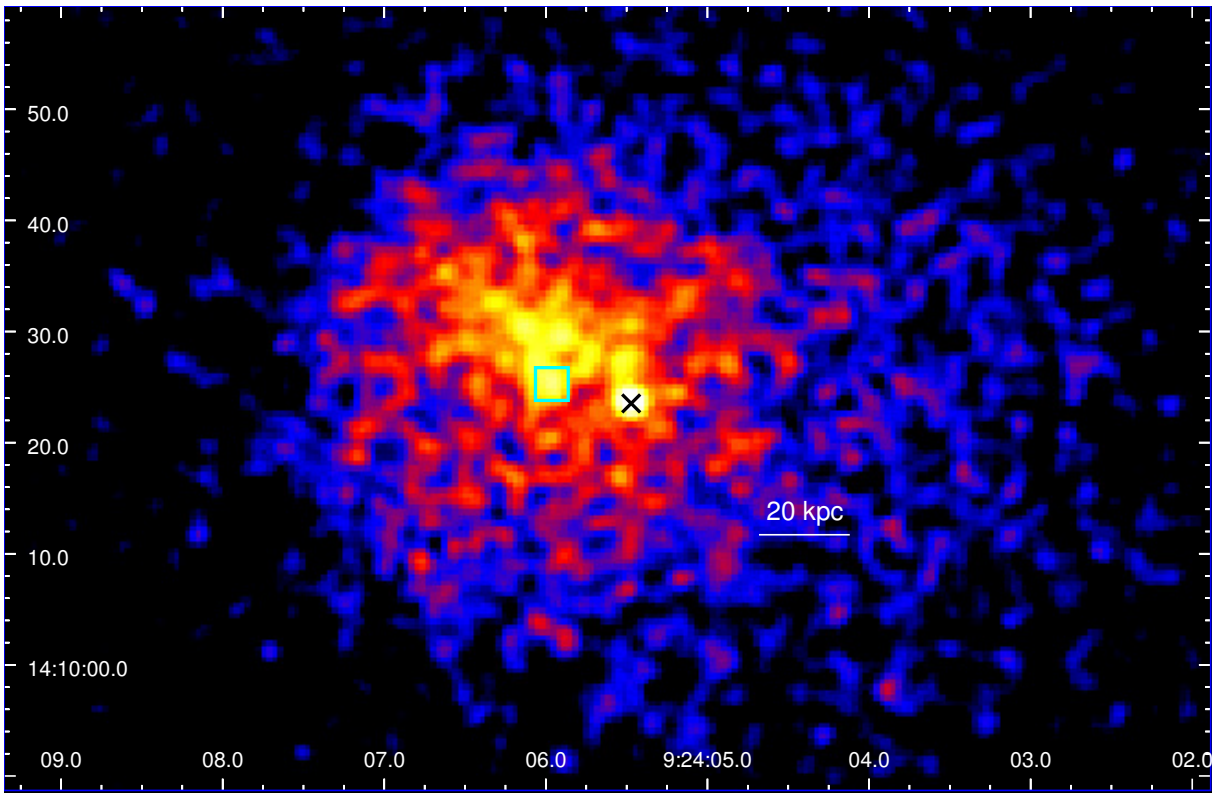

Figure 3.2: 0.5 -2 keV image of the central regions of A795. The image is Gaussian-smoothed with a kernel radius of 3 pixel. The black cross marks the position of the BCG, while the cyan box corresponds to the X-ray peak.

3.1.2 Surface Brightness profile

Considering the spatial offset discussed in the previous subsection, it has been chosen to center the surface brightness profiles on the X-ray peak, in order to be consistent with the ICM morphology properties. The 360° azimuthally averaged surface brightness profile has been extracted with `Proffit`, by providing the 0.5-2 keV source image, the 0.5-2 keV blanksky image, and the exposure map. It has been chosen to use circular annuli as extraction regions, centered on the X-ray peak, and to exclude the central AGN to avoid contamination from its emission (the study of the central radio galaxy is presented in Chap. 4). The annuli are uniformly spaced, with a 2" width each, and the last annulus is at 166.8" ($\approx$ 405.2 kpc)[1] from the surface brightness peak. The extraction has been performed with the method described in Sect. 2.2; the extraction regions and the resulting profile are appreciable in Fig. 3.3.

To fit the surface brightness profile, we considered the β-model, which `Proffit` defines:

$$S(r) = norm\left(1 + (r/r_c)^2\right)^{(-3\beta+0.5)} \tag{3.1}$$

[1]This is the largest distance that can be reached from the X-ray peak to the chip edge.

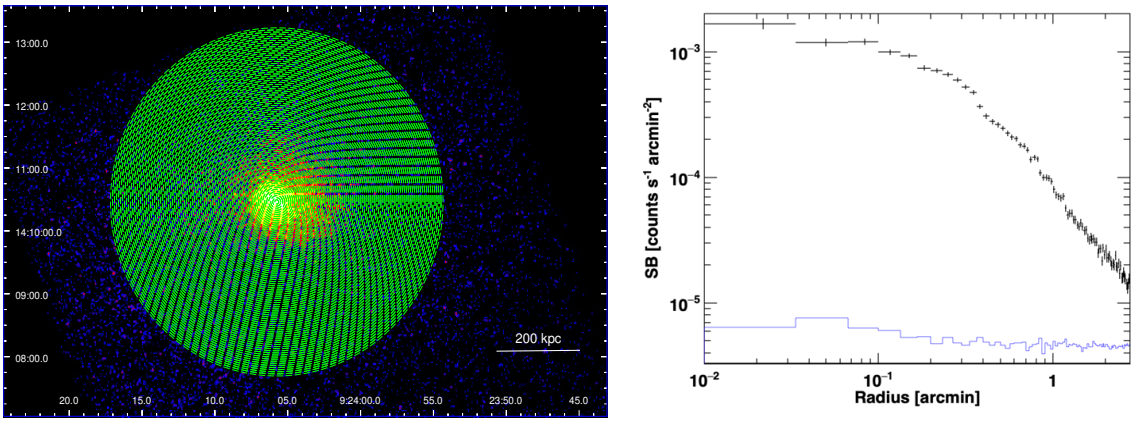

(a) *Extraction regions* **(b)** *SB profile*

Figure 3.3: Panel *a*: A795 0.5-2 keV exposure corrected image, smoothed with a Gaussian of 3 pixel FWHM; green circular annuli are the extraction regions for the surface brightness profiles. Panel *b*: A795 0.5-2 keV exposure corrected, background subtracted surface brightness profile (black points); the blue profile represents the background, extracted from the `blank-sky` 0.5-2 keV image.

where the free parameters are then normalization ($norm$), the parameter β, and the core radius r_c.

We fitted the extracted profile first with a single β-model, then with a double β-model. The best fit parameters are reported in the first two rows of Tab. 3.2. We note that the single β-model provides a smaller χ^2/D.o.f, indicating that the addition of a second β-model is not required. However, we note that the single beta model applied to the whole profile does not provide a remarkably good fit: by inspecting the residuals (Fig. 3.4, panel *b*) it is possible to observe an ondulating pattern, which suggests that there might be surface brightness discontinuities that are azymuthally averaged and contribute to the statistically significant departure of the reduced χ^2 from 1.00. The prevalence of a single β-model is a further evidence for the fact that this system might not be a strong cool-core, relaxed cluster: the same process which is also responsible for the observed offset between the BCG and the X-ray peak might have stretched and mixed the cooling region, thus reducing the central density peak. This hypothesis can be investigated with the spectral analysis of this cluster, which is presented in the following section.

To verify whether a slight, central enhancement in surface brightness is present (although not strong enough to allow for a double β-model successful fit), we excluded from the single β-model fit the inner 26.4" ($\sim$ 64.1 kpc) region: the choice of this radius derives from excluding the inner points progressively, and then selecting as our best guess the smaller χ^2/D.o.f β-model fit. The best fit parameters are presented in the last row of Tab. 3.2, and the fitted profile is shown in Fig. 3.4 (panel *a*).

	β_1	norm$_1^a$	$r_{c,1}^b$	$r_{c,2}^b$	ratio^c	χ^2/D.o.f
Single	$0.47^{+0.01}_{-0.01}$	$1.28^{+0.76}_{-0.71}$	$0.23^{+0.01}_{-0.01}$			124.8/80 (1.56)
Double	$0.47^{+0.01}_{-0.01}$	$1.19^{+1.58}_{-1.59}$	$0.23^{+0.01}_{-0.01}$	$0.24^{+0.16}_{-0.15}$	$0.07^{+0.05}_{-0.07}$	124.8/78 (1.60)
Single ($\geq 26.4''$)	$0.48^{+0.01}_{-0.01}$	$0.98^{+0.15}_{-0.16}$	$0.28^{+0.03}_{-0.03}$			94.6/67 (1.41)

Table 3.2: This table contains the best fit parameters for the three fits to the surface brightness profile in Fig. 3.3 (panel *b*).
[a] In units of 10^{-3} (counts s^{-1} arcmin^{-2}).
[b] In arcmin.
[c] Ratio between the normalization of the second β-model and the normalization of the first β-model.

Since the reduced χ^2 of this fit (1.41) is smaller than that of the β-model fit to the global profile, we infer that a small surface brightness enhancement is present within 26.4": we compare this estimate with the measured *cooling radius* in Subsect. 3.2.3.

Dynamical state indicators: In order to better characterize the dynamical state of Abell 795, we computed the *centroid shift* (w) and the *concentration* (c) parameters using the method described in Sect. 2.2. Since the concentration parameter is defined by referring to $S(< 400kpc)$, we provided for the computation of w a value of 400 kpc for $R_{\rm max}$, so that the dynamical indicators are applied to the same scale. The resulting values are $\mathbf{w = 0.03}$ and $\mathbf{c = 0.15}$.
Santos et al. (2008) defined three categories of cool cores: non-cool core ($c < 0.075$), moderate ($0.075 < c < 0.155$) and pronounced ($c > 0.155$) cool core. By considering the work of Mohr et al. (1993), large values of w (> 0.03) indicate that the centroid depends on the aperture, meaning that the cluster is morphologically irregular. The values for A795 seem to be consistent with the moderate/weak cool core interpretation presented in the above paragraph: the concentration parameter lies in the moderate cool-core category defined by Santos et al. (2008), and the centroid shift parameter corresponds to the threshold between relaxed and non-relaxed systems.

3.1.3 2D analysis of A795

In order to enhance morphological patterns, and to provide clues on this cluster's structure, we performed a two-dimensional analysis of A795, by producing residual and unsharp mask images. We used the **savedeviations** task of `Proffit` to obtain a map of pixel-by-pixel residuals between the data and the best fit model. The result is shown in Fig. 3.5 (panel *a*). It is quite evident the large scale spiral feature that deviates from the model assumptions. The same feature has also been found by producing unsharp mask images

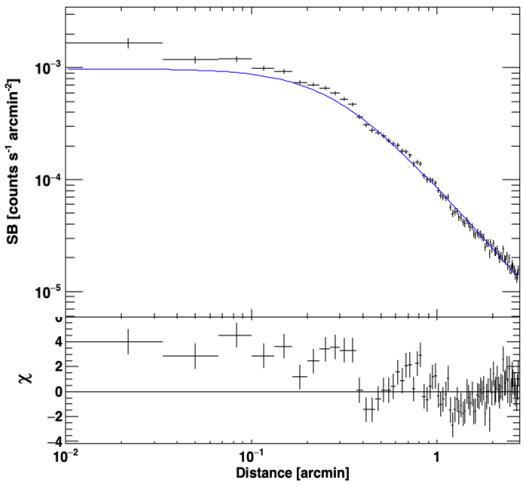

(a) *0.4'-2.78' β-model fit*

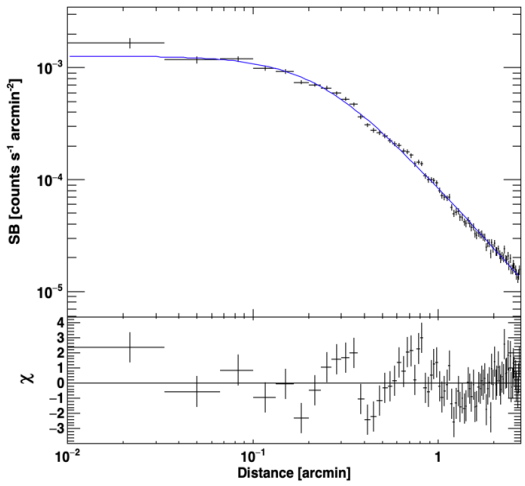

(b) *0'-2.78' β-model fit*

Figure 3.4: Panel *a*: A795 0.5-2 keV surface brightness profile (black points), fitted with a β-model (blue line) with the exclusion of the central 26.4". Panel *b*: A795 0.5-2 keV surface brightness profile(black points), fitted with a β-model (blue line). The lower panel of both plots shows the residuals from the best-fit model.

of this cluster: in particular, the subtraction of an image smoothed with a Gaussian of 5 pixel FWHM from the same image smoothed with a Gaussian of 20 pixel FWHM, has led to the creation of Fig. 3.5 (panel *b*), in which the spiral feature is again present. We hypothesized that this large-scale geometry might be the outcome of a *sloshing* mechanism, comparable to that observed in other clusters which display spiral morphology (see Sect. 1.3); this could explain the offset between the X-ray peak and the BCG: the displacement of the ICM from its original configuration could have stretched the central density peak, and explain the single β-model prevalence for the surface brightness profile.

The unsharp mask image is a flexible technique, since it can be used to investigate the presence of different scale morphological features by changing the smoothing scales. By producing another unsharp mask image by subtracting two images of the cluster (smoothed with a Gaussian of 2 and 10 pixel axes, respectively), we found two depressions close to the BCG (see Fig. 3.6, panel *a*). We named the two depression D1 and D2. The same depressions have also been detected in the residual image and in the original image. In order to measure their size, we decided to rely on the unsharp mask image, since it represents the image for which these two depressions are most evident. The properties of D1 and D2 are presented in Tab. 3.3.

We note that the other depressions visible in Fig. 3.6 do not represent a significant deviation w.r.t. the best β model fit, so we did not include them in our analysis. On the contrary, D1 and D2 show a deficit of $\approx 34\%$ and $\approx 21\%$ respectively, and they are at a

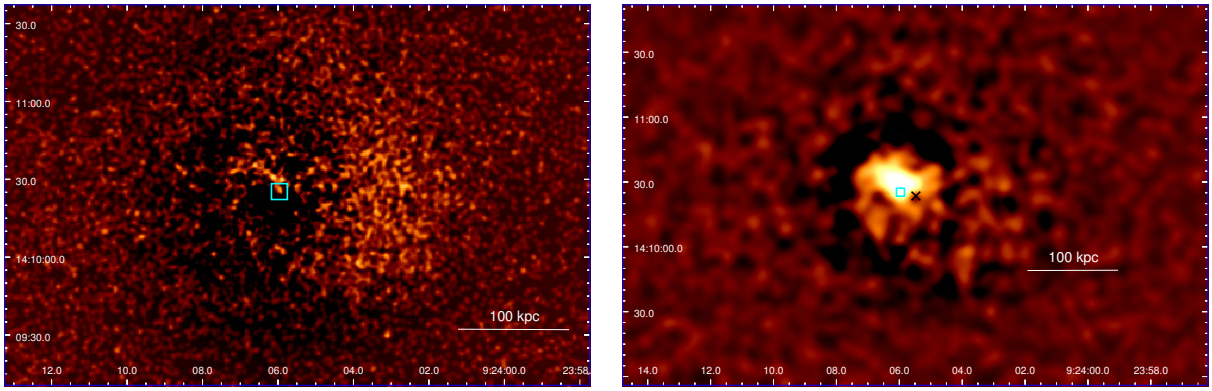

(a) *Residual image* **(b)** *Unsharp mask image*

Figure 3.5: Panel *a*: A795 0.5-2 keV residual image, Gaussian-smoothed with a kernel radius of 3 arcsec. Panel *b*: A795 0.5-2 keV unsharp mask image, obtained by subtracting two images smoothed with a Gaussian of 5 and 20 pixel axes, respectively. The black cross denotes the position of the BCG, while the cyan box indicates the X-ray peak.

roughly symmetric position with respect to the X-ray peak and the AGN, which is typical of X-ray cavities (see Subsect. 1.2.3). We also measured the cavity significance following the method of Hlavacek-Larrondo et al. (2015): we created an annulus that encompassed the cavities, and we divided it in 7 azimuthal sectors (see Fig. 3.6, panel *b*); we measured the surface brightness of each sector, and then estimated the cavities significance by comparing the surface brightness of the sector containing each cavity with the average of the adjacent sectors. We report the results in Tab. 3.3: according to Hlavacek-Larrondo et al. (2015), a significance between 1-3σ indicates that deeper observations are necessary to obtain a clear cavity detection, and that depressions with these significance values should be referred to as *putative* cavities.

	R_{max} (kpc)	R_{min} (kpc)	D (kpc)	Deficit (%)	Significance (σ)
D1	6.43	6.16	40.64	34.3	2
D2	9.85	4.64	27.68	21.3	1

Table 3.3: This table contains the main properties of the putative cavities D1 and D2; R_{max} and R_{min} are the semi-axes of the depressions, while D is the distance from the BCG. The deficit (%) is referred to the best fit beta model.

Given this finding and the proximity of this two depressions to the brightest cluster galaxy, we investigated if D1 and D2 could be X-ray cavities originating from the AGN activity. The results of this study are presented in the last chapter.

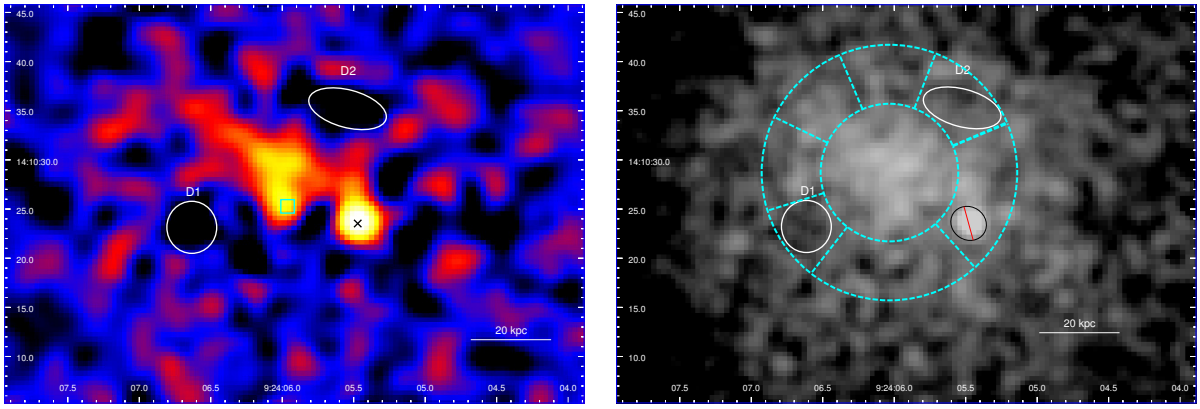

Figure 3.6: Panel *a*: A795 0.5-2 keV unsharp mask image, obtained by subtracting two images smoothed with a Gaussian of 2 and 10 pixel axes, respectively; the positions of the AGN (black cross), of the X-ray peak (cyan box), and of the two depressions are marked. Panel *b*: A795 0.5-2 keV image, with the cyan sectors used to compute the cavity significance, and the black ellipse indicating the AGN exclusion from the surface brightness estimate. Each image is Gaussian-smoothed with a kernel radius of 3 pixel.

3.1.4 Surface brightness discontinuities

The most evident features, which are directly recognizable in the original image (Fig. 3.1), are the two surface brightness discontinuities located on opposite sides to the center of the cluster. The two surface brightness discontinuities are spatially coincident with the large-scale spiral highlighted with the β-modelling and unsharp mask imaging techniques. The two discontinuities have been named E (east) and W (west).

We extracted surface brightness profiles along these two edges to obtain useful information on the jump significance and the discontinuities geometry. The profiles were extracted and fitted by using `Proffit`, which has been designed especially to deal with surface brightness jumps. We extracted the surface brightness profiles from circular sectors of variable opening angles, until we determined the full extension of the surface brightness jumps: the final, widest-opening angle extraction regions are presented in Fig. 3.7: to better visualize the jumps, we plotted only a fraction on the circular sectors: the actual bin size used for the analysis is 2".

We have fitted the profiles using the **bknpow** model provided by `Proffit`: this consists in a broken power law with a density jump, numerically projected along the line of sight, written as:

$$S(r) = norm \int F(\omega)^2 dl, \quad \text{with} \quad \omega^2 = r^2 + l^2, \tag{3.2}$$

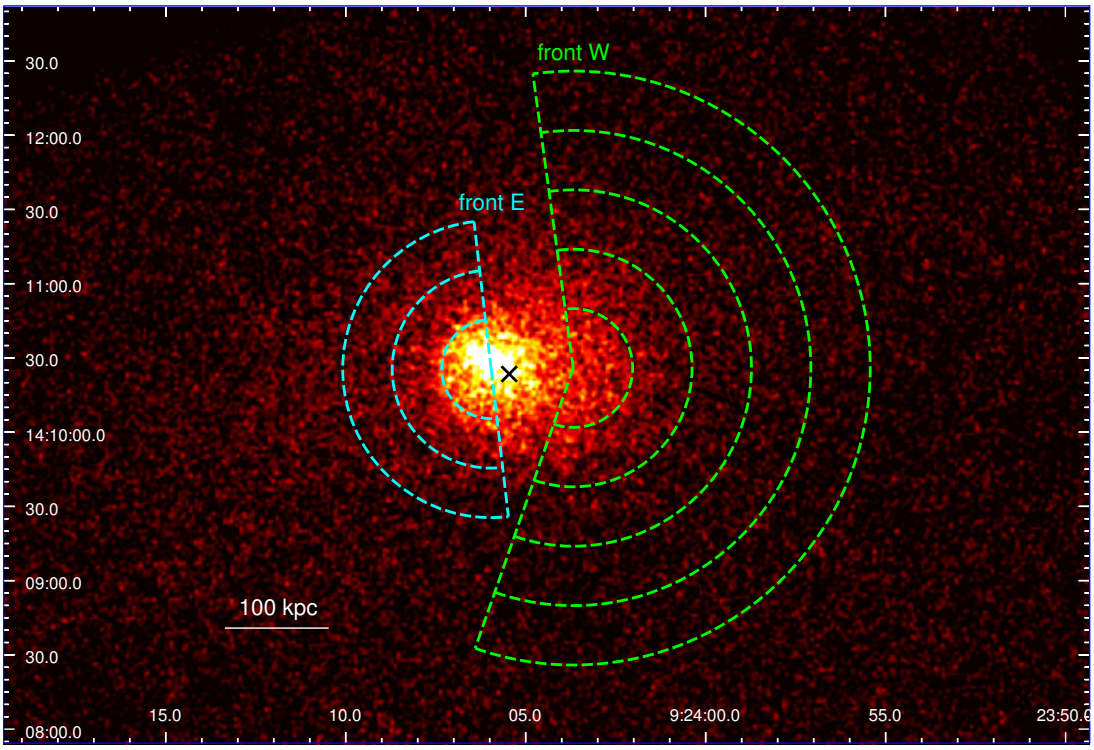

Figure 3.7: A795 0.5-2 keV image, Gaussian-smoothed with a kernel radius of 3 pixel. The green (west front) and cyan (east front) sectors trace the extraction regions; the black cross marks the position of the BCG.

where the integration is performed over the line of sight (dl), and $F(\omega)$ is the 3-dimensional density profile (in arbitrary units):

$$F(\omega) = \omega^{-\alpha_1} \quad \text{if} \quad \omega < \text{cutrad} \tag{3.3}$$

$$F(\omega) = \frac{1}{\text{jump}}\omega^{-\alpha_2} \quad \text{otherwise} \tag{3.4}$$

The free parameters of this model are the slopes before and after the jump, α_1 and α_2, the position of the jump (*cutrad*), and the jump in density (*jump*). The results of the fitting procedure are listed in Tab. 3.4, and we plotted the extracted profiles in Fig. 3.8. The extension of the two jumps is consistent with the spiral feature described in the previous paragraph, since the east front almost ends where the W front starts (see Fig. 3.9, panel *b*). In particular:

- Front E is located $\sim$ 67 kpc from the surface brightness peak, and consists in a density jump of $1.69^{+0.07}_{-0.07}$ (left arc in Fig. 3.9); the very high significance of the jump ($\approx 10\sigma$) is consistent with a sharp discontinuity.

- Front W is located at $\sim$ 170 kpc from the surface brightness peak, and consists in a density jump of $1.93^{+0.31}_{-0.26}$ (right arc in Fig. 3.9). This front has a lower significance

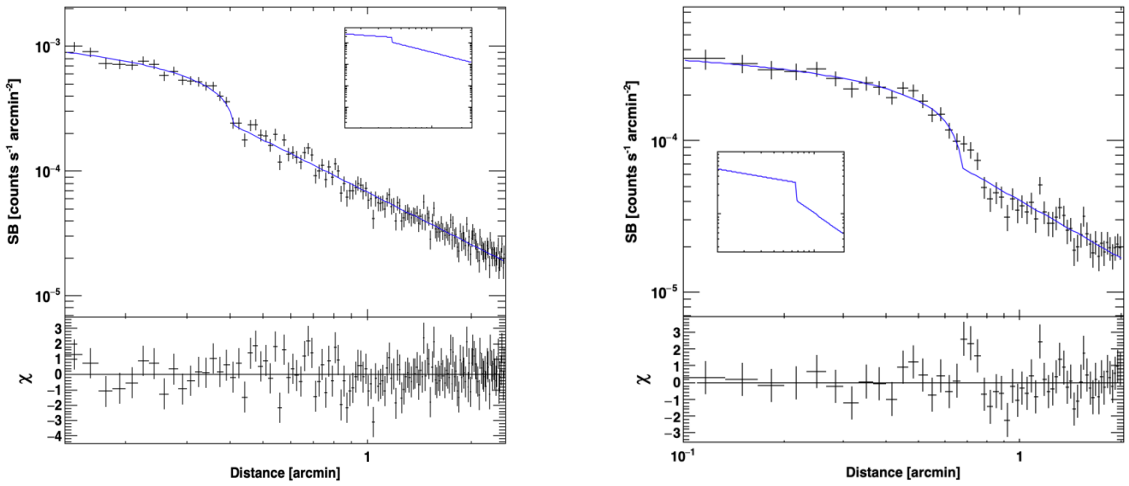

(a) *E edge* **(b)** *W edge*

Figure 3.8: Panel *a*: 0.5-2 keV surface brightness profile along the east discontinuity (black points), fit with a **bknpow** model (blue line). Panel *b*: 0.5-2 keV surface brightness profile along the W discontinuity (black points), fit with a **bknpow** model (blue line). In each plot, the best fit broken powerlaw model is also plotted in a small box.

Edge	α_1	α_2	cutrad[a]	norm[b]	jump[c]	jump$^d_{n_e}$	χ^2/D.o.f.
E	$0.35^{+0.10}_{-0.10}$	$1.20^{+0.01}_{-0.01}$	$0.409\ ^{+0.002}_{-0.001}$	$1.33^{+0.09}_{-0.09}$	1.57±0.27	$1.69^{+0.07}_{-0.07}$	139.1/137
W	$0.28^{+0.09}_{-0.09}$	$1.13^{+0.04}_{-0.05}$	$0.667\ ^{+0.015}_{-0.015}$	$0.28^{+0.03}_{-0.03}$	1.50±0.38	$1.93^{+0.31}_{-0.26}$	53.3/52

Table 3.4: Best fit parameters of the **bknpow** model used to describe the two surface brightness discontinuities.
[a] The position of the jump referred to the center of the sectors (arcmin).
[b] Normalization in units of 10^{-3} cts s^{-1} arcmin^{-2}.
[c] Surface brightness jump.
[d] Electron density jump (measured in Sect. 3.2).

($\approx 3\sigma$): the residuals of the profile in Fig. 3.8 (panel *b*) indeed show that the discontinuity is not as sharp as the east one.

The sloshing spiral might indicate that these features are actually cold fronts rather than shocks: we produced temperature, density and pressure profiles along these edges to discriminate between the two possibilities (Subsect. 3.2.5).

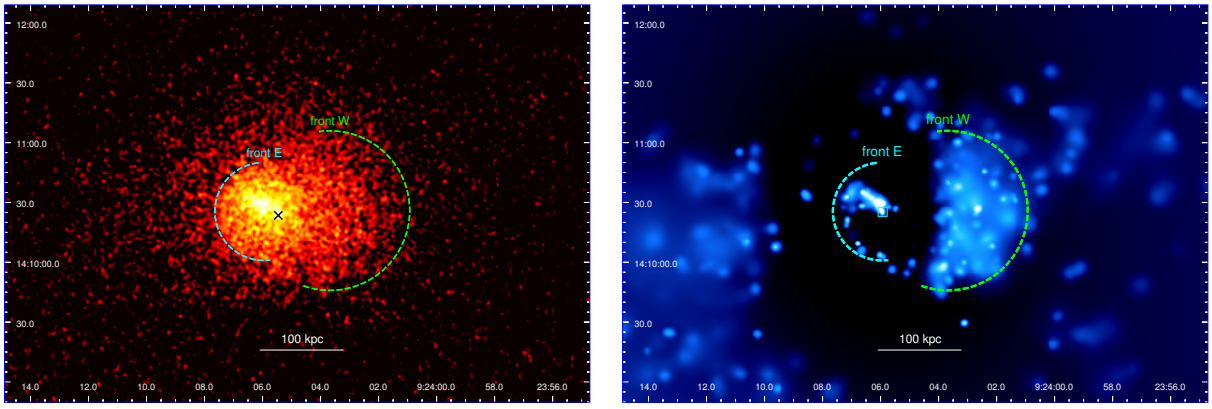

(a) *0.5 - 2 keV image* **(b)** *Residual image*

Figure 3.9: Panel *a*: A795 0.5 - 2 keV image, Gaussian-smoothed with a kernel radius of 3 arcsec; panel *b*: Residual image presented in Fig. 3.5 (panel *a*) smoothed with **csmooth** for a minimum S/N of 3. In both panels, the black cross marks the position of the BCG; the cyan and green arcs indicate the extension of the two fronts, and their position coincides with the best fit jump radius.

3.2 Spectral Analysis

In order to produce a detailed characterization of the thermodynamical properties of the galaxy cluster Abell 795, we performed a spectral analysis of the ICM; in particular, it is fundamental to investigate the gas temperature, pressure and density, to determine the classification of this object as a cool core system and the nature of the fronts. A common and effective method to perform the analysis consists in extracting the projected values of thermodynamical variables to obtain a first hint of the cluster's state, and then to perform a *deprojected* analysis which provides the final results - although with larger uncertainties. We extracted the spectra in the energy range 0.5 - 7 keV, where *Chandra* has the largest effective area. Beyond these values, instrumental errors and sky emission are likely to degrade data.

This section is organized as follows: in the first part, the overall spectral properties of the cluster are presented; in the second part, the temperature, density and pressure of the ICM extracted from circular concentric annuli are unveiled and commented, and estimates of the cooling radius and luminosity are calculated. The last part is dedicated to the thorough analysis of the two surface brightness discontinuities presented in Subsect. 3.1.4.

The spectra have been extracted resorting to the `specextract` tool of **ciao-4.12**, and fitted using **Xspec - v.6.26.1**; the **blanksky** event file (presented in Subsect. 2.1.5) has been used to extract the spectrum of the background.

3.2.1 A795: overall spectral properties

The global spectral properties of Abell 795 were deduced by extracting and fitting a spectrum from a region which included as much area of the chip 3 as possible. We chose a region of radius 167" (∼405 kpc) centered on the X-ray peak, which is visible in Fig. 3.10; we excluded an ellipse of major-semi axis 1.9" (∼ 4.6 kpc) and minor-semi axis of 1.7" (∼ 4.1 kpc) enclosing the central AGN, so that its emission would not contaminate that of the ICM. The extracted spectrum was binned so that every bin contained 25 counts,

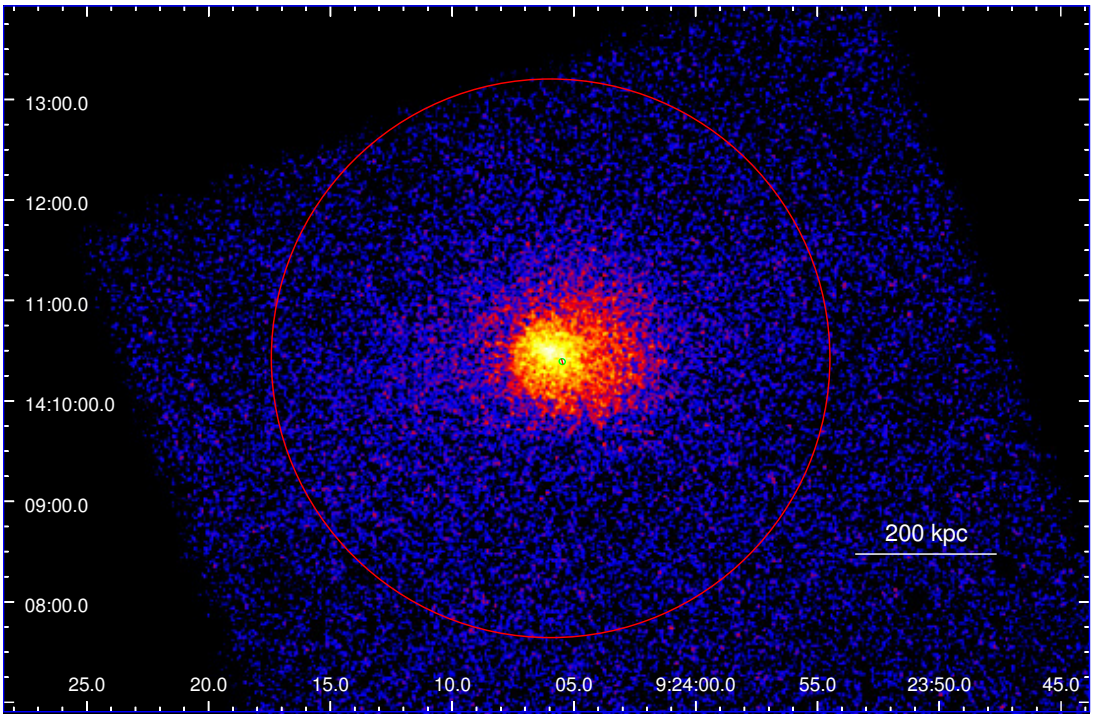

Figure 3.10: The region of radius 167" (∼ 405 kpc) used to obtain the general spectral properties of the cluster. The central ellipse used to exclude the AGN has a major semi-axis of 1.9" and a minor semi-axis of 1.7".

enough to use the Chi-statistics. We fit the spectrum with a model **tbabs∗apec**; the first term accounts for galactic absorption, which was fixed at the value $n_{\rm H} \approx 2.89 \times 10^{20}$ cm^{-2} [2] (Bekhti et al., 2016). The second term accounts for the emission of a collisional ionized gas, with parameters kT (temperature), Z (metal abundance in units of $Z_\odot$[3]), redshift z and *norm* (normalization of the spectrum). Tab. 3.5 lists the best fit parameters obtained by fitting the spectrum with this model.

The abundance of 0.38±0.05 $Z_\odot$ and the temperature of 4.63±0.12 keV (5.37±0.14×10^7 K) are consistent with values typically found in galaxy clusters (e.g., Böhringer and Werner

[2]obtained from https://heasarc.gsfc.nasa.gov/cgi-bin/Tools/w3nh/w3nh.pl by providing the coordinates of Abell 795.

[3]For this and every other **apec** model employed in this work, we used the table of abundances of Asplund et al. (2009).

Counts[a]	kT [keV]	Z [$Z_\odot$]	norm [10^{-3}]	χ^2/D.o.f.	$f^b_{2-10\,keV}$	$L^c_{2-10\,keV}$
29287 (86.1 %)	$4.63^{+0.12}_{-0.12}$	$0.38^{+0.05}_{-0.05}$	$7.25^{+0.09}_{-0.09}$	375/325	4.31	2.27

Table 3.5: This table contains the results of the fit to the overall spectrum (within 167" from the X-ray peak) of A795.
[a] Net photon counts (fraction w.r.t. the total counts from the same region).
[b] Flux in units of 10^{-12} erg cm^{-2} s^{-1}.
[c] Luminosity in units of 10^{44}erg s^{-1}.

(2010)). The temperature is not consistent with the value reported in Ebeling et al. (1996): the *Rosat 0.1-2.4 All Sky Survey* includes observation of this cluster, the study of which has led to measure a medium temperature for the ICM of 6.3 keV. However, the extraction region used to obtain this value had a radius of $\sim$ 816 kpc, approximately double in size with respect to ours. Therefore, it is likely that the difference with our result is due to the larger *Rosat* extraction region, which has included the outer (and possibly hotter) ICM, leading to a higher average temperature.

3.2.2 Radial profiles of thermodynamic variables

To investigate the state and composition of the ICM at different distances from the center, we extracted a spectrum from six circular, concentric regions centered on the X-ray peak[4]. In order to choose the number and extent of the annuli, the following criteria have been employed:

- In order to reach a compromise between the number of counts and the number of radial bins, we produced six regions which contained at least 4000 net counts in the 0.5-7 keV band.
- Considering the two surface brightness discontinuities discussed in Sect. 3.1.3, we chose the annuli so that no annulus crossed a front: in fact, if an annulus contained the emission coming from the two sides of the edge, determining the temperature of the ICM would have likely been problematic.

The six regions used for the radial spectral analysis are showed in Fig. 3.11; the spectra extraction was performed by binning counts so that each bin contained 25 counts.

Projected Analysis Each spectrum was fit with a **tbabs∗apec** model, with n_H fixed at the value of 2.89×10^{20} cm^{-2}, and redshift fixed at 0.1374. The result of the fit

[4] we excluded from the central annulus the counts coming from the AGN, using the same region as the one used in Sect. 3.1.3.

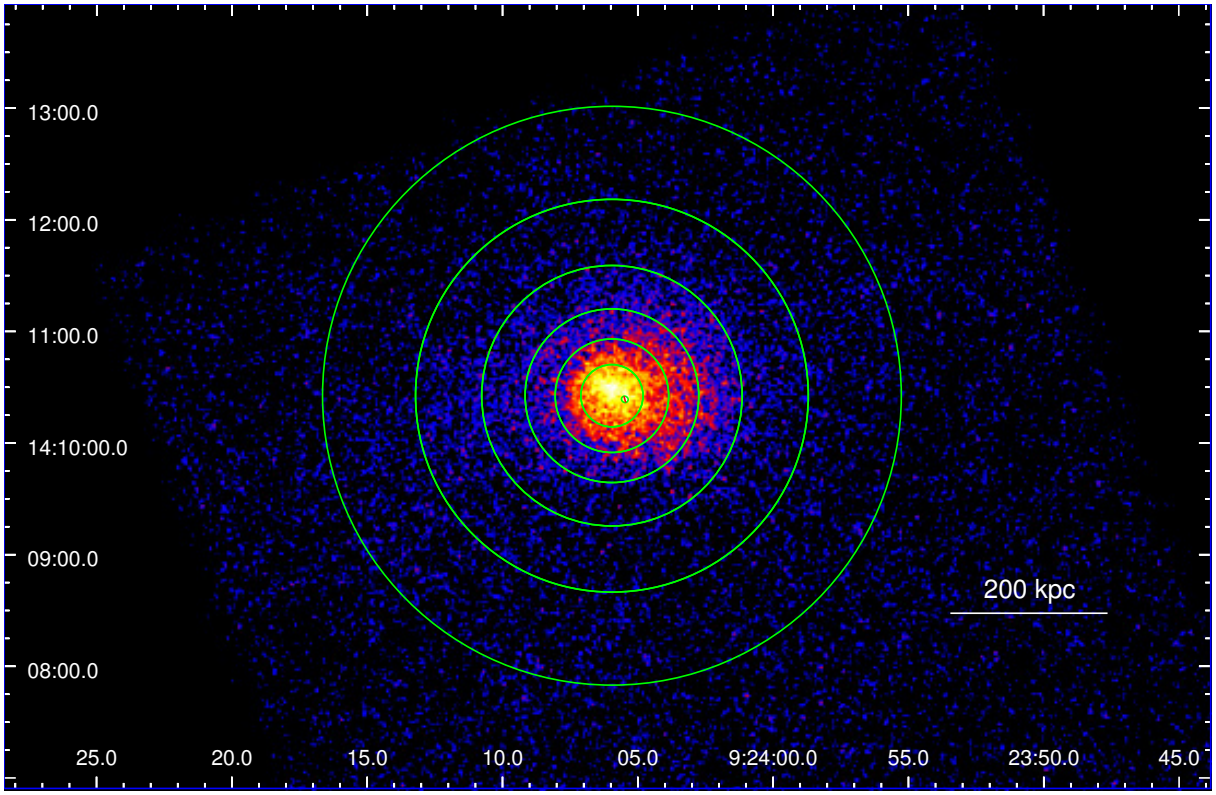

Figure 3.11: The annuli used to obtain radial profiles of thermodynamical properties of the cluster. The central ellipse used to exclude the AGN has a major semi-axis of 1.9" and a minor semi-axis of 1.7".

are listed in Tab. 3.6[5] The projected analysis does not allow for the computation of electron density to be performed, and the temperature of each annulus suffers from the contribution of the outer annuli. Nevertheless, the results listed in Tab. 3.6 provide a hint of the thermodynamical and chemical properties of this cluster: we plotted the temperature and the abundances against the distance from the center (see Fig. 3.12). The temperature seems to decline going from outer to inner regions, suggesting a higher cooling efficiency in the central kiloparsecs.

Considering the abundance profile, we note that to obtain detailed information about radial chemical enrichment in galaxy clusters, longer exposure times are generally required; however, it is possible to highlight the fact that the metallicity seems to decline going far from the center: according to the analysis of other cluster's abundance radial profiles (see Mernier et al., 2017) this result might indicate that central regions have experienced heavier enrichment due to the BCG.

We tried to thaw the column density parameter n_{H}, to check whether further absorption was needed to explain the observed spectrum. For each annulus, letting the column density

[5]The norm value is not presented in the table, as only with the *deprojected* analysis it is possible to link it to the electron density.

R_i - R_o [a]	Counts [b]	kT [keV]	Z [$Z_\odot$]	χ^2/D.o.f.
0 - 40.6 (0 - 16.7)	4298 (98.8 %)	$3.73^{+0.17}_{-0.17}$	$0.75^{+0.14}_{-0.13}$	122.9/114 (1.08)
40.6 - 74.1 (16.7 - 30.5)	4542 (97.6 %)	$4.31^{+0.28}_{-0.18}$	$0.66^{+0.14}_{-0.14}$	105.2/127 (0.83)
74.1 - 113.3 (30.5 - 46.6)	4497 (95.6 %)	$5.11^{+0.12}_{-0.12}$	$0.14^{+0.12}_{-0.11}$	135.5/131 (1.03)
113.3 - 170.0 (46.6 - 70.0)	4811 (91.2 %)	$4.89^{+0.27}_{-0.27}$	$0.56^{+0.15}_{-0.14}$	136.9/139 (0.98)
170.0 - 256.4 (70.0 - 105.5)	4780 (82.1 %)	$5.32^{+0.39}_{-0.32}$	$0.23^{+0.15}_{-0.14}$	156.1/156 (1.00)
256.4 - 377.8 (105.5 - 155.5)	5337 (70.9 %)	$5.07^{+0.36}_{-0.36}$	< 0.24	178.2/189 (0.94)

Table 3.6: This table contains the results of the fit to the spectra obtained from six circular annuli centered on the X-ray peak of A795.
[a] Inner and outer radius of the annulus in kpc (arcseconds).
[b] Net photon counts (fraction w.r.t. the total counts from the same region).

free to vary did not provided noticeable results: either the column density reached a value consistent within errors with the fixed value, or the χ^2/D.o.f. did not indicate a significant improvement. Given this finding, we maintained the galactic hydrogen column density fixed at its reference value for the rest of the analysis.
We also considered the possibility of the addition of a second thermal component, by fitting each annulus with a **tbabs∗(apec+apec)** model: we fixed the abundance parameters of the second **apec** component to the value of the first one, as the relatively low statistics in each annulus does not allow to constrain both temperature and abundances of two **apec** models. Again, we did not find a significant improvement in any annulus, as either the normalization of the second thermal component was much lower than that of the first one, or the χ^2/D.o.f. improvement was not statistically significant. For completeness, the best fit parameters for the double temperature model are presented in the Appendix.

Deprojected Analysis Due to the fact that the projected analysis provides quantities (temperature, abundances, densities, pressure) integrated along the line of sight, obtaining correct values requires to deproject the spectra. The same spectra used for the projected analysis have been loaded together on `Xspec` and fitted with a **projct∗tbabs∗apec**. As for the projected analysis, we freezed the column density and redshift to their reference values. The **projct** mixing model performs a 3-D to 2-D projection of ellipsoidal shells onto elliptical annuli, by inspecting the user-provided XFLT001, XFLT002, XFLT003 keywords in the header of the extracted spectrum; these correspond, respectively, to the major axis, minor axis, and orientation of the outer boundary of each annulus. The best fit results are listed in Tab. 3.7; fluxes and luminosities for every annulus in different bands are presented in the Appendix.
The deprojection model is complex, and leads to larger uncertainties: this is quite evident

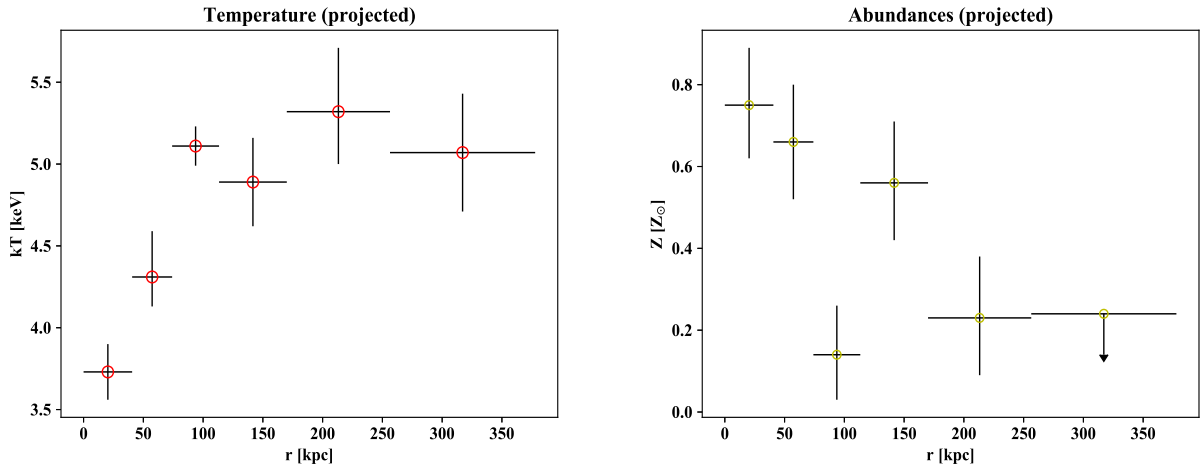

(a) (b)

Figure 3.12: Panel *a*: Projected temperature profile for A795. Panel *b*: Projected abundance profile for A795. Both profiles are centered on the X-ray peak; errorbars on the x-axis represent the bin width.

for the abundances, which are badly constrained and, in two annuli, we only obtained upper limits. For this reasons, we have not proceeded to further inquiry the chemical status of this cluster.

The first important result arising from the deprojection is the temperature profile of this cluster, presented in Fig. 3.13 (panel *a*). As it is possible to see, the temperature is lower in the inner regions, and rises going far from the center; this supports our consideration that in the projected analysis, the outer, hotter shells were contaminating the temperature of the inner shells.

The deprojected analysis is also fundamental in terms of deriving the electron density of the plasma. The *norm* parameter of the **apec** model is defined as:

$$norm = \frac{10^{-14}}{4\pi[D_{\rm A}(1+z)]^2} \int n_{\rm e} n_{\rm p} dV \tag{3.5}$$

where $D_{\rm A}$ is the angular distance from the source, z is the redshift, $n_{\rm e}$ and $n_{\rm p}$ are the electron and proton densities, and V is the volume of the emitting region. It is possible to revert this formula to get the electron density:

$$n_{\rm e} = \sqrt{10^{14} \left(\frac{4\pi \times norm \times [D_{\rm A}(1+z)]^2}{0.82V} \right)} \tag{3.6}$$

kT keV	Z $[Z_\odot]$	norm $[10^{-4}]$	n_e $[10^{-3}cm^{-3}]$	P_{ICM} $[10^{-10}erg\ cm^{-3}]$	K_{ICM} [keV cm^2]
$3.36^{+0.31}_{-0.24}$	$0.75^{+0.27}_{-0.23}$	$5.57^{+0.40}_{-0.40}$	$17.89^{+0.06}_{-0.06}$	$1.77^{+0.23}_{-0.19}$	49.12 $\pm$5.78
$3.82^{+0.32}_{-0.33}$	$1.07^{+0.32}_{-0.27}$	$7.29^{+0.53}_{-0.53}$	$9.09^{+0.33}_{-0.33}$	$1.02^{+0.12}_{-0.12}$	87.75 $\pm$9.47
$5.61^{+0.84}_{-0.70}$	< 0.5	$10.36^{+0.39}_{-0.35}$	$6.16^{+0.12}_{-0.10}$	$1.02^{+0.17}_{-0.14}$	166.98 $\pm$26.98
$4.58^{+0.48}_{-0.39}$	$0.64^{+0.24}_{-0.22}$	$11.53^{+0.63}_{-0.62}$	$3.58^{+0.09}_{-0.09}$	$0.48^{+0.06}_{-0.05}$	195.48 $\pm$24.14
$5.75^{+1.07}_{-0.88}$	$0.41^{+0.42}_{-0.36}$	$9.21^{+0.70}_{-0.70}$	$1.72^{+0.07}_{-0.07}$	$0.29^{+0.07}_{-0.06}$	399.94 $\pm$84.55
$5.07^{+0.36}_{-0.35}$	< 0.23	$24.11^{+0.78}_{-0.79}$	$1.58^{+0.03}_{-0.03}$	$0.24^{+0.02}_{-0.02}$	373.22 $\pm$30.70

Table 3.7: This table contains the results of the fit to the deprojected spectra obtained from six circular annuli centered on the X-ray peak of A795, and the resulting electron density, pressure, and entropy. The χ^2/D.o.f. is 832.7/856.

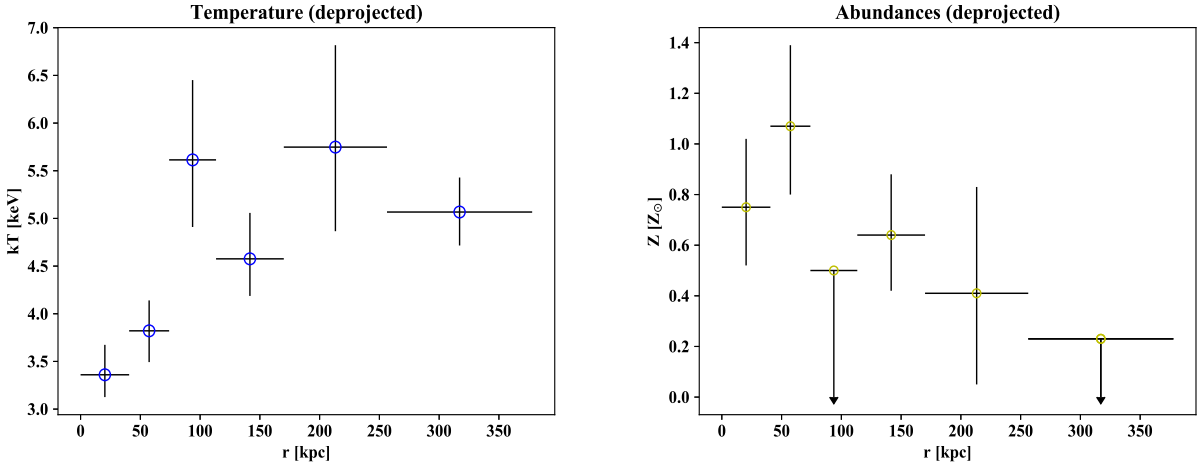

(a) **(b)**

Figure 3.13: Panel *a*: Deprojected temperature profile for A795. Panel *b*: Deprojected abundance profile for A795. Both profiles are centered on the X-ray peak; errorbars on the x-axis represent the bin width.

We computed the volume of each spherical shell starting from the radius values, and then obtained the electron density by using the *norm* parameter of the **apec** of each annulus: results are presented in Tab. 3.7, where we also report pressure ($P = 1.83 n_e kT$) and entropy ($K = kT/n_e^{2/3}$) of the ICM.

For completeness, we also computed the ICM density by deprojecting with `Proffit`[6] the surface brightness profile. This requires to provide a conversion factor defined as the ratio between the count rate and the *norm* parameter of the **apec** which describes the plasma. As the normalization parameter differs from one annulus to another, we have chosen to use the normalization of the overall spectrum of this cluster, described in Sect. 3.2.1.

[6]The routines are **deproject** and **density**.

Fig. 3.14 (panel *a*) shows the density profiles obtained with this method: uncertainties have been calculated with a Monte Carlo method, by generating and deprojecting random realizations of the surface-brightness profiles; the mean and dispersion of the output values are then computed to estimate the deprojected profile and its uncertainty. As it is possible to see, the density profiles from `Proffit` and from the spectral analysis are consistent with each other within errors, but the first one has a higher spatial resolution.

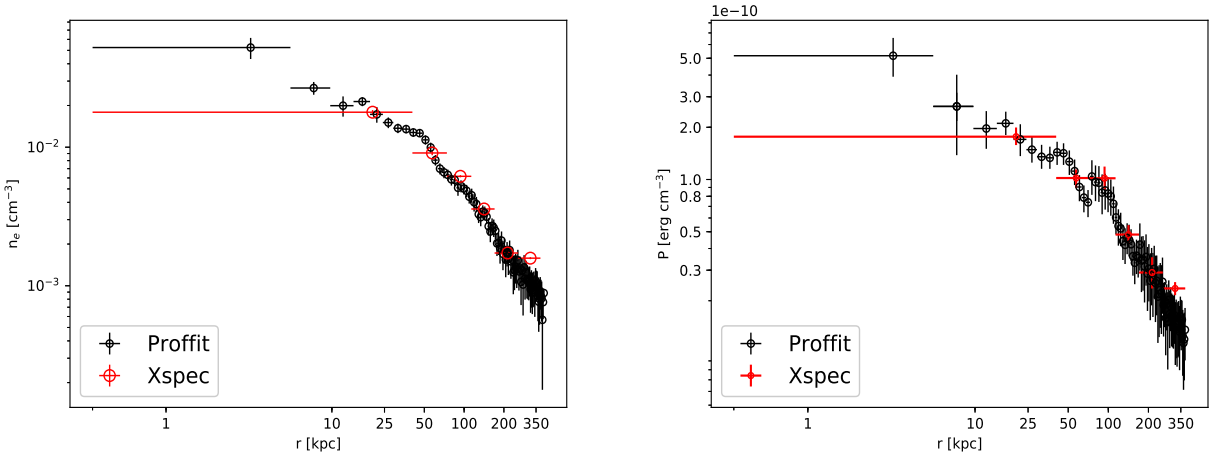

(a) **(b)**

Figure 3.14: Panel *a*: Electron number density profile for A795: black points have been obtained by deprojecting the surface brightness profile with `Proffit`, while the six red points have been obtained with Eq. 3.6 after the deprojected spectral analysis. Panel *b*: Pressure profile for A795 (colos are the same as in panel *a*).

We computed the pressure of the ICM $P_{\rm ICM} = 1.83 n_{\rm e} kT$, by combining the temperature profile from the spectral analysis with both the `Proffit` and `Xspec` density profiles. The two profiles are consistent within errors (see Fig. 3.14, panel *b*); column 5 of Tab. 3.7 lists the pressure measurements obtained from the temperature and density of the six annuli. We note that the shape of the pressure profile is caused by the combination of the undulating patterns of the density profile (Fig. 3.14, panel *a*) and of the temperature profile (Fig. 3.13, panel *a*), both caused by azimuthally averaging the two discontinuities; in particular, the third radial bin of the deprojected spectral analysis has a higher temperature than the adjacent bins, while the density shows a decreasing profile: this produces the peaked structure around ≈ 100 kpc in the pressure profile.

3.2.3 Cooling properties of A795

One of the aim of this thesis is to provide informations on the cooling properties of A795: we proceeded to compute the cooling time profile, using Eq. 1.29. We interpolated the cooling function from tables of Sutherland and Dopita (1993) for the deprojected metallicities Z and temperatures kT of the six annuli; we decided to use the `Proffit` density profile $n_e(r)$ because it allows for higher spatial resolution to be reached with respect to the six spectral points[7].

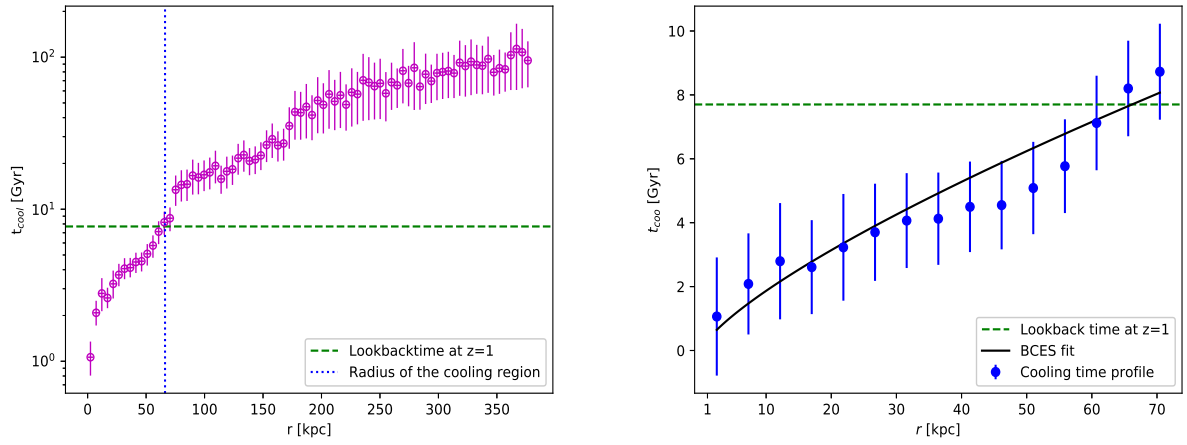

(a) **(b)**

Figure 3.15: Panel *a*: Cooling time profile of A795. Panel *b*: Results of the linear regression to the inner 70 kpc of the cooling time profile (while the fit was performed in the log − log space, here linear values are plotted to facilitate comparison with panel *a*).

The cooling time profile is presented in Fig. 3.15 (panel *a*): as expected, the cooling time is lower in the inner regions, and in the innermost point (2" from the X-ray peak) the cooling time is ≈ 1 Gyr. As pointed out in Sect. 1.2, the gas cools efficiently inside a radius r_{cool}, which is the distance from the center at which the cooling time is approximately 7.7 Gyr. As a first, by-eye estimate of this cooling radius, it is possible to identify the distance from the center at which the cooling time crosses the 7.7 Gyr horizontal line: this indicates a cooling region radius of ≈ 65.6 kpc. To obtain a reliable estimate of the cooling radius, we fitted the cooling time profile with a power-law relation in the form $\log(t_{cool[Gyr]}) = (A \pm \sigma_A)\log(r_{cool}[kpc]) + (B \pm \sigma_B)$, using the *Bivariate Correlated Errors and intrinsic Scatter* (BCES) library of `Python3.5.4`[8]. As reported by Bravi (2015), the

[7]The choice of using the `Proffit` density is due to its smaller radial bins, which enables to have a more refined local measurement of thermodynamical properties of the ICM; as a sanity check, we also computed the cooling time using the `Xspec` density and found consistent values.

[8]This method, developed by Akritas and Bershady (1996), performs a linear regression which takes into account measurement errors for $\log(t_{cool})$ and for $\log(r_{cool})$.

relation $\log(t_{\rm cool})$ - $\log(r_{\rm cool})$ deviates from linearity going far from the center, so it is recommended to use a radial range which contains roughly the expected value of $r_{\rm cool}$: given our by-eye estimate, we decided to reduce the fitting to the inner 70 kpc. The fitted profile is plotted in Fig. 3.15 (panel *b*); the algorithms returns parameters $A \pm \sigma_{\rm A}$ and $B \pm \sigma_{\rm B}$, which lead to the following best fit relation:

$$\log(t_{\rm cool}) = [0.75 \pm 0.08] \log(r_{\rm cool}) + [-0.47 \pm 0.11] \tag{3.7}$$

By substituting the value $t_{\rm cool} = 7.7$ Gyr, and propagating errors on A and B, we obtain a cooling radius $r_{\rm cool} = 66.2 \pm 3.2$ kpc (27.3 ± 1.3 arcseconds), which is consistent with our by-eye guess.

We can also compare this result with the size of the region excluded from the surface brightness profile of Sect. 3.1, which provided the best single β-model fit, that is $r_\beta = 26.4 \pm 2.0'' = 64.2 \pm 4.9$ kpc. It is possible to point out that $r_{\rm cool}$ and r_β yield a similar cooling region size, thus corroborating our hypothesis that in the inner $\approx 60 - 70$ kpc the radiative losses of the ICM are important: an enhanced surface brightness and a smaller than 7.7 Gyr cooling time provide the necessary conditions to classify A795 as a (weekly) cool core cluster.

As reported by Hudson et al. (2010), a weakly cool core displays a central cooling time of $1 < t_{\rm cool}[{\rm Gyr}] < 7.7$, which is coherent with our cooling time profile analysis *and* with the diagnostic parameter employed in Sect. 3.1. Strong cool core clusters (SCC), on the other hand, present cooling time $t_{\rm cool}[{\rm Gyr}] < 1$, which might be the case only for our central radial bin: the X-ray peak cooling time is $1.06^{+0.28}_{-0.26}$ Gyr, and its surface brightness is not consistent with the global single β-model profile of Fig. 3.4 (panel *b*); it is possible that only the X-ray peak has the properties of a very small ($r_{\rm SCC} = 2'' = 4.86$ kpc), strong cooling region.

Properties of the cooling region: to better investigate how the cooling of the ICM is affecting the central region of A795, we performed a spectral analysis of the emission inside the cooling region. Apart from characterizing the thermodynamical properties of the ICM, we aimed to obtain a valid estimate of the *cooling luminosity* of this cluster, which is essential to investigate the mass deposition rate $\dot{M}$ of the cooling gas and the cooling flow-related issues. To fulfil this purpose, we followed three methods:

- First, we fitted the spectrum of the cooling region with a **tbabs∗(apec+mkcflow)** model[9]: this method (*method1*) aims at describing the actual cooling gas within the cooling region with the **mkcflow** component, and at accounting for the ambient

[9]The **mkcflow** component describes the emission from ionized gas cooling from a temperature $kT_{\rm high}$ to a temperature $kT_{\rm low}$.

cluster atmosphere with the **apec**. The parameters of the thermal component were left free to vary; the abundance and $kT_{\rm high}$ of the **mkcflow** were tied to the thermal model, while $kT_{\rm low}$ was fixed to the minimum allowed value (0.0808 keV). The normalization of the **mkcflow** corresponds to the *mass deposition rate* $\dot{M}[M_{\odot}/yr]$ described in Sect. 1.2: to obtain an observational estimate of the mass deposition rate we left this parameter free. We computed the bolometric luminosity in the 0.1-100 keV band of the **mkcflow** and the **apec** components; the results are presented in the first row of Tab. 3.8.

- The second method (*method2*) takes into account more accurately the emission from the gas projected on the cooling region: we generated two concentric annuli, the first being the cooling region and the second extending from the cooling region to the edge of the chip 3. We fitted the spectra with a **projct∗tbabs∗apec** model, for which the parameters were left free to vary (except the column density $n_{\rm H}$ and the redshift). The results of this fit are presented in the second row of Tab. 3.8. We measured the luminosity of the **apec** component in the 0.1 - 100 keV band, and deduced a bolometric luminosity $L_{\rm bol,2} = (1.07 \pm 0.06) \times 10^{44}$ erg s^{-1}.

- For the third method, we fitted the spectra of the two concentric annuli with a **projct∗tbabs∗(apec+mkcflow)** model to subtract from the cooling region the contribution of the outer gas, and to describe properly the amount of cooling gas through the **mkcflow** component. We let free the abundance, the temperature and the normalization of the **apec** component in each region. The abundance and $kT_{\rm high}$ of the **mkcflow** were tied to the outer thermal model, while $kT_{\rm low}$ was fixed to the minimum allowed value (0.0808 keV). The normalization of the **mkcflow** was allowed to vary inside $r_{\rm cool}$, while it was fixed to zero outside $r_{\rm cool}$, where no efficient cooling is expected. We computed the 0.1-100 keV luminosity of the **apec+mkcflow** component, that is $L_{\rm bol} = 1.08 \pm 0.04 \times 10^{44}$ erg s^{-1}. From the **mkcflow** normalization we obtain a mass deposition rate of $\dot{M}_{\rm obs} = 7.00^{+6.13}_{-6.02}\, M_{\odot}/yr$. The third row of Tab. 3.8 lists the best fit parameters and the resulting luminosity for *method3*.

- At last, we tried a numerical approach: the bolometric X-ray luminosity can be defined as (e.g. Eke et al., 1998):

$$L_{\rm X} = \int_V m_{\rm e} n_{\rm i} \Lambda(T) dV, \tag{3.8}$$

where $n_{\rm i}$ is the ions density, $\Lambda(T)$ is the cooling function and V is the volume over which the luminosity is calculated; considering spherical shells of width dr, it is possible to write $dV = 4\pi r^2 dr$. We hypothesized that by resolving this integral

inside the cooling region, a good "theoretical" measurement of the cooling luminosity would have been obtained. By making direct use of the `Proffit` density profile and the cooling function of Sutherland and Dopita (1993), we performed the integration over the same spherical shells used for the surface brightness profile (i.e. with dr = 2" = 4.86 kpc). The resulting bolometric luminosity is $L_{\rm bol,4} = (0.93 \pm 0.07) \times 10^{44}$ erg s^{-1}.

For the first three methods, the errors on $L_{\rm bol}$ derive from the uncertainty on the cooling radius: we changed the size of the cooling region according to its error and measured the variation of luminosity; for the fourth method, we changed the upper limit radius of the integral from $r_{\rm cool} - \sigma_{r_{\rm cool}}$ to $r_{\rm cool} + \sigma_{r_{\rm cool}}$, and obtained the confidence interval for $L_{\rm bol}$.

	R_i - R_o [kpc]	kT [keV]	Z [$Z_\odot$]	$\dot{M}_{\rm obs}$ [$M_\odot/yr$]	χ^2/D.o.f.	$L^a_{\rm bol}$	$\dot{M}_{\rm CF}$ [$M_\odot/yr$]
1[b]	0-66.2	$4.12^{+0.22}_{-0.19}$	$0.72^{+0.10}_{-0.09}$	$7.16^{+6.30}_{-6.26}$	178/157 (1.13)	$0.05^{+0.02}_{-0.02}$ $1.16^{+0.06}_{-0.06}$	$4.77^{+1.92}_{-1.91}$
2	0-66.2 66.2-407.2	$3.87^{+0.14}_{-0.14}$ $5.03^{+0.15}_{-0.15}$	$0.74^{+0.11}_{-0.10}$ $0.28^{+0.06}_{-0.06}$		485/465 (1.04)	$1.07\ ^{+0.06}_{-0.06}$	108.7±6.1
3[c]	0-66.2 66.2-407.2	$4.04^{+0.23}_{-0.21}$ $5.03^{+0.15}_{-0.15}$	$0.77^{+0.12}_{-0.11}$ $0.28^{+0.06}_{-0.06}$	$7.00^{+6.13}_{-6.02}$	484/464 (1.04)	$1.08^{+0.04}_{-0.04}$ $1.03^{+0.05}_{-0.05}$ $0.05^{+0.02}_{-0.02}$	108.8±5.8
4	0-66.2					$0.93^{+0.07}_{-0.07}$	91.8±10.6

Table 3.8: Results of the four methods applied to the cooling region of A795.
[a] Bolometric luminosity, in units of 10^{44}erg s^{-1}.
[b] The cell corresponding to $L^b_{\rm bol}$ reports the **mkcflow** luminosity (first row), and the **apec** luminosity (second row).
[c] The cell corresponding to $L^b_{\rm bol}$ reports the (**apec**+**mkcflow**) (first row), the **apec** luminosity (second row), and the **mkcflow** luminosity (third row).

We proceeded to evaluate the cooling rate expected by these luminosities: the cooling flow classical model predicts that the power emitted within the cooling region $L_{\rm cool}$ is related to the amount of matter which crosses $r_{\rm cool}$ through:

$$\dot{M}_{\rm CF} = \frac{2}{5}\frac{\mu m_{\rm p}}{kT} L_{\rm cool} \tag{3.9}$$

We resorted to the measured values of $L_{\rm bol}$ to compute the classical cooling rate $\dot{M}_{\rm CF}$; the last column of Tab. 3.8 summarises the results for each method applied to the cooling region. It is possible to highlight the following results:

- For *method1*, the values of $\dot{M}_{\rm obs}$ and $\dot{M}_{\rm CF}$ are consistent within errors; this sanity check confirms that the normalization of the **mkcflow** is computed from the bolometric luminosity of this component. In addition to this, the $\dot{M}_{\rm obs}$ of this method is in agreement with the $\dot{M}_{\rm obs}$ of *method3*, thus indicating that we can place an upper limit on the $\dot{M}$ allowed by the observations of $\dot{M}_{\rm obs} \leq 7.16\, M_{\odot}/yr$.

- The second, third and fourth methods yield consistent bolometric luminosities and predicted mass deposition rates; we note that *method2* and *method3* provide similar results for the **apec** component: in fact, by inspecting the χ^2/D.o.f. it appears that the addition of the **mkcflow** component to *method2* did not represent a statistically significant improvement. This conclusion can be reached also by considering the luminosities of the two components: the luminosity of the single **apec** component is $L_{\rm bol,apec} = 1.03 \pm 0.05 \times 10^{44}$ erg s^{-1}, while that of the **mkcflow** is $L_{\rm bol,mkcflow} = 4.63 \pm 0.21 \times 10^{42}$ erg s^{-1}. Therefore, inside the cooling region the **mkcflow** accounts for only $\approx 4.5\%$ of the observed luminosity.

- Considering this, our best estimate for the cooling luminosity is given either by the bolometric luminosity of *method2*, or by the bolometric luminosity of the "numerical" *method4*, which are consistent within each other. We decided to adopt $L_{\rm cool} = L_{\rm bol,2} = 1.07^{+0.06}_{-0.06} \times 10^{44}$ erg s^{-1}.

It is now interesting to compare the mass deposition rate predicted by *method2* with the normalization of the **mkcflow** component of *method1*: though errors are large, it is quite evident that the predicted cooling rate $\dot{M}_{\rm CF} = 108.7 \pm 6.1\, M_{\odot}/yr$ overestimates the upper limit on the observed cooling rate $\dot{M}_{\rm obs} \leq 7.16\, M_{\odot}/yr$ by a factor of ≈ 10. This finding is coherent with the cooling flow problem (Sect. 1.2), and indicates that some feedback mechanism must be present in A795 to explain this difference and to prevent large amounts of gas to cool and flow to the center. We report our main hypothesis in the last chapter.

3.2.4 Hydrostatic Mass profile

As this thesis is the first X-ray dedicated study of A795, it is useful to provide a first measurement of the total mass of this cluster by means of its hydrostatic mass (Eq. 1.17). We note that there are several issues for this purpose: first of all, our analysis is limited by the chip size, so we cannot directly measure the total mass farther than ≈ 400 kpc from the cluster center; our estimate will then hold only for the central region of this cluster. Second of all, the sloshing motion of the ICM represents a non-negligible deviation from the hydrostatic assumption. Considering this, we calculated $M_{\rm tot}(r)$ nevertheless, as it

may represent within $\approx 10-40\%$ a reliable estimate of the true total mass (e.g., Rasia et al. 2006; Lau et al. 2009).

As reported by e.g., Gitti et al. (2012), one of the positive outcomes of fitting the X-ray surface brightness with a β-model is that it allows to have an analytical formula for the density profile; this results in the possibility of re-writing Eq. 1.17 as:

$$M_{\rm tot}(<r) = \frac{rkT}{G\mu m_{\rm p}}\left[\frac{3\beta r^2}{r^2+r_{\rm c}^2} - \frac{d\log T}{d\log r}\right] \tag{3.10}$$

where β and $r_{\rm c}$ are the β-model parameters.

In order to obtain an estimate of the temperature gradient in A795, we followed the same method used for the cooling time profile: the temperature profile of the deprojected spectral analysis was fitted in the $log-log$ space with a power-law using BCES; the best fit linear regression yields:

$$\log(T) = [\alpha \pm \sigma_\alpha]\log(r) + [\delta \pm \sigma_\delta] = [0.20 \pm 0.04]\log(r) + [2.98 \pm 1.04] \tag{3.11}$$

By substituting $d\log T/d\log r = \alpha$ in Eq. 3.10, and using the values of β and $r_{\rm c}$ from the best β-model fit to the surface brightness profile of A795 (Tab. **??**), we produced the hydrostatic mass profile of Fig. 3.16.

Rasia et al. (2006) reported that the use of β-model for the hydrostatic mass estimates lead to systematic uncertainties of $\sim 20\%$ with respect to the true mass estimate; moreover, Lau et al. (2009) noted that residual gas motions in the central regions of galaxy clusters (such as sloshing) represent an additional bias in the cluster mass estimate of $\approx 6-9\%$. Therefore, beside propagating the errors on kT, β, $r_{\rm c}$ and α, we added a 30% error to account for the approximation of using hydrostatic equilibrium to describe a disturbed system.

The mass profile of this cluster, in particular, gives a total mass of $M_{\rm tot,\,HD}(<380{\rm kpc}) = (9.9\pm3.7)\times10^{13}\,M_\odot$; Rines et al. (2013), who computed the total halo mass of 58 galaxy clusters (including A795) with optical observation and the *caustic technique* (see e.g. Diaferio et al., 2005), found a total enclosed mass of $M_{\rm tot}(<1.1\,{\rm Mpc}) = (3.5\pm0.1)\times10^{14}\,M_\odot$. This value is higher than ours, but it should be noted that it refers to a much larger region, approximately three times our enclosing radius. Considering Eq. 3.10, and imposing that $r \gg r_c$, it is possible to obtain as a first order approximation that $M_{\rm r} \propto r$: by rescaling our total mass by the difference in the enclosing radius (a factor of ≈ 3), we obtain $M_{\rm tot,HD}(<1.1\,{\rm Mpc}) \approx 3.0\pm1.1\times10^{14}\,M_\odot$. This value is consistent to the one reported in Rines et al. (2013), and indicates that our estimate of the hydrostatic mass profile is likely reliable.

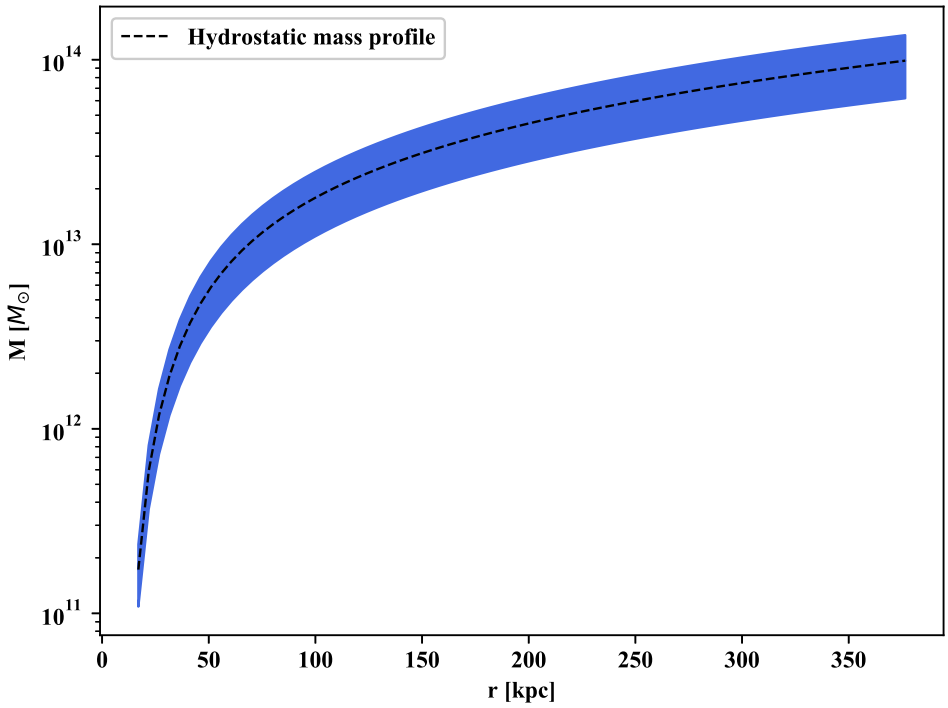

Figure 3.16: Hydrostatic mass profile $M_{\rm tot}(< r)$ of A795, derived with Eq. 3.10; the blue area represents the confidence region for the mass estimate.

3.2.5 Spectral analysis of the two edges: cold fronts or shocks?

The morphological tools of Subsect. 3.1.4 have highlighted the presence of two surface brightness discontinuities, the nature of which can be determined with a detailed spectral analysis: we aimed to obtain measurements of temperature, density and pressure on both sides of the fronts, to discriminate between the cold front and the shock front interpretation. For the former case, we should find lower temperature and higher density inside the interface, and pressure equilibrium at the edge; the latter case, instead, would be supported by higher temperature, density, and pressure inside the front. The sloshing of the ICM supports the cold front interpretation, since cold gas might have been displaced from the center, and contact discontinuities between different phases of the ICM might have been created.

We created four circular sectors for each front that followed the discontinuity[10]. Then we loaded the spectra on `Xspec` and implemented a **projct∗tbabs∗apec** model. The temperature, abundances and normalization parameter of the **apec** model were left free to vary, while the column density and redshift were fixed. To deproject the emission coming

[10]Using less than three sectors for the gas outside the front interface leads to large errorbars for the first sector after the discontinuity, thus preventing to confirm the temperature jump.

from sectors, the mixing model **projct** requires two additional keywords in the header of the spectra: these correspond to the starting and the ending angle of the sector. In the following paragraphs, the results of the spectral analysis of the east and the west jumps are presented.

East front The four extraction regions were chosen following the same criteria used for the radial study of the cluster: each region contains at least 1100 counts, and the sector following the discontinuity has been carefully chosen in order to avoid contamination from gas at different temperatures. In particular, we used the *cutrad* parameter obtained by fitting the surface brightness profile across the front to establish the position of the edge ($\sim$ 60 kpc from the X-ray peak); the final sectors are shown in Fig. 3.17, while Tab. 3.9 lists the properties of each sector and the resulting best fit parameters. We produced a

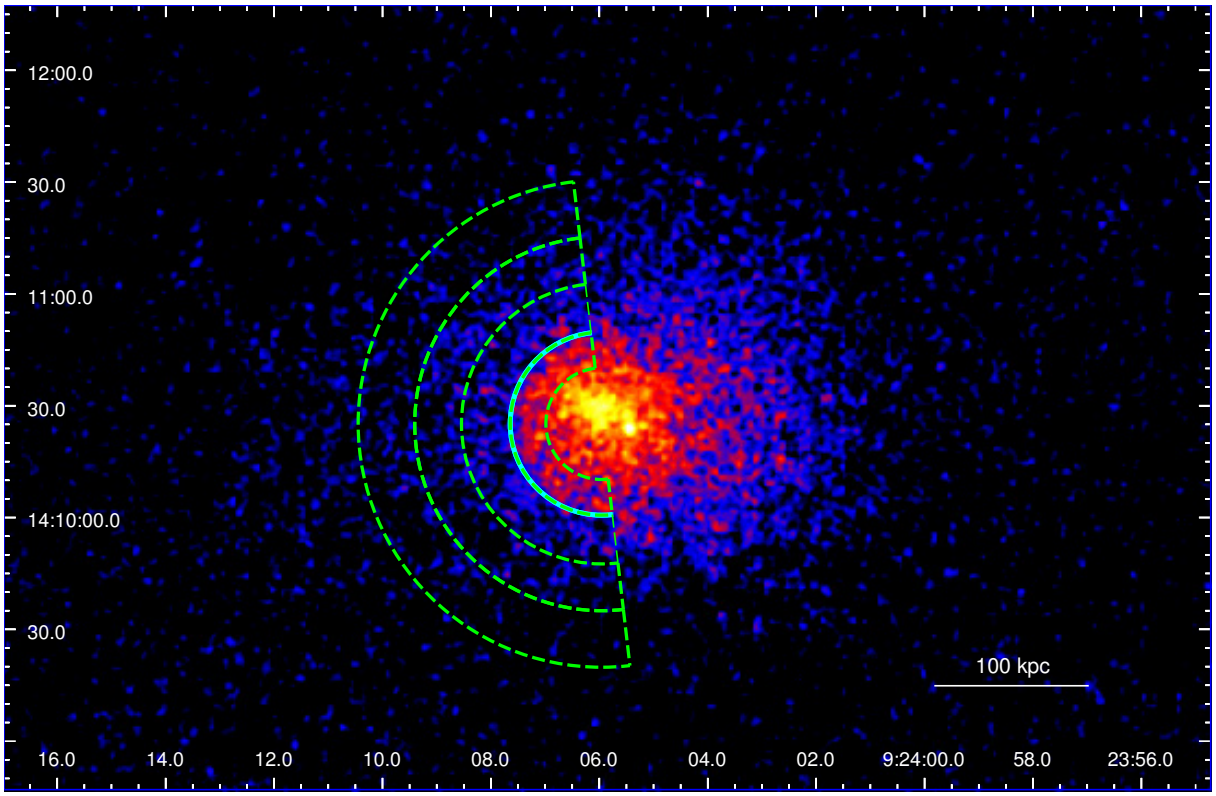

Figure 3.17: A795 0.5-7 keV image, Gaussian-smoothed with a kernel radius of 3 arcsec, with the four sectors used to study the thermodynamical properties of the east surface brightness jump. All sectors are centered in the X-ray peak, and the opening angle is 120°. The cyan arc follows the front.

temperature profile across the front by plotting temperatures against the distance from the center of the profile; in addition to this, we computed the electron number density from the *norm* parameter. The temperature profile in Fig. 3.19 (panel *a*) seems to confirm that this edge is indeed a cold front, since the inner side of the front is colder

R_i - R_o[a] kpc	Counts[b]	kT [keV]	Z [$Z_\odot$]	norm [10^{-4}]	n_e[c] [10^{-3}cm^{-3}]	P[d]
36.4 - 59.7	1660 (98.2 %)	$2.73^{+0.38}_{-0.28}$	$0.71^{+0.37}_{-0.29}$	$7.79^{+0.95}_{-0.89}$	$13.53^{+0.82}_{-0.77}$	$10.83^{+2.18}_{-1.72}$
59.7 - 91.4	1404 (95.3 %)	$5.03^{+1.79}_{-0.98}$	$1.16^{+0.92}_{-0.79}$	$4.83^{+0.77}_{-0.75}$	$5.81^{+0.46}_{-0.45}$	$8.59^{+2.33}_{-3.73}$
91.4 - 121.9	1147 (92.9 %)	$5.99^{+3.55}_{-2.04}$	< 1.5	$4.90^{+0.63}_{-0.92}$	$4.25^{+0.28}_{-0.40}$	$7.46^{+4.90}_{-3.24}$
121.9 - 158.7	1172 (88.8 %)	$5.20^{+0.97}_{-0.59}$	$0.59^{+0.41}_{-0.38}$	$10.85^{+0.86}_{-0.83}$	$4.38^{+0.17}_{-0.17}$	$6.67^{+1.50}_{-1.02}$

Table 3.9: This table lists the properties of the sectors used to analyze the east front (located at $\approx 24.7 = 60$ kpc from the X-ray peak), and the resulting best fit parameters. The χ^2/D.o.f. is 219.4/220
[a] Inner and outer radius of the sector; the center is the X-ray peak.
[b] Net photon counts (fraction w.r.t. the total counts from the same region).
[c] The electron number density has been obtained from the *norm* parameter using Eq. 3.6.
[d] ICM pressure across the front, in units of [10^{-11} erg cm^{-3}].

(and more dense) than the outer side; in particular, we measured a temperature ratio $T_{\rm out}/T_{\rm in} = 1.84 \pm 0.62$ and a density ratio of $n_{\rm in}/n_{\rm out} = 2.33 \pm 0.32$[11].
We computed the pressure of the ICM in each sector using the equation $P_{\rm ICM} = 1.83 n_e kT$: the profile of Fig. 3.19 (panel *e*) shows that there is pressure equilibrium at the interface, which is consistent with what has been observed for other sloshing cold fronts (e.g. Chen et al., 2017; Ichinohe et al., 2019).

West front The same procedure has been applied to the study of the west front; this discontinuity is located at a larger distance ($\approx 73.4'' = 178.2$ kpc) from the center of the cluster: sectors have been chosen in order to deal with enough counts (at least 1000) and to follow the discontinuity. As this front is more extended than the east one, and the surface brightness jump is less sharp (see Subsect. 3.1.4), large temperature error bars were expected: we changed the size and the center of sectors until a significant temperature jump was measured. Fig. 3.18 displays the sectors used for the spectral analysis, while the best fit results are listed in Tab. 3.10; the abundaces values are not reported, as we only measured upper limits.
The temperature, density, and pressure profile of Fig. 3.19 (right column) seem to confirm that this is indeed a second cold front, likely originated by the sloshing motion of the ICM. The temperature ratio is $T_{\rm out}/T_{\rm in} = 1.74 \pm 0.73$, with a little significance (as expected). Nevertheless, the density jump of $n_{\rm in}/n_{\rm out} = 1.91 \pm 0.16$ leads to pressure equilibrium at the interface, a further indication of the "cold front" nature of this (less pronounced) discontinuity.

[11] For temperature and density values see Tab. 3.9

The spectral analysis has then confirmed our hypothesis on the surface brightness discontinuities: the Intra Cluster Medium of A795 has been perturbed, and the gas sloshing has displaced the cool gas from the center, creating a spiral morphology with two temperature discontinuities. Given the large scale action of this mechanism, it is interesting to understand its implication on the feedback mechanisms: we examined the link between the cooling properties of this cluster and its peculiar appearance in the last chapter.

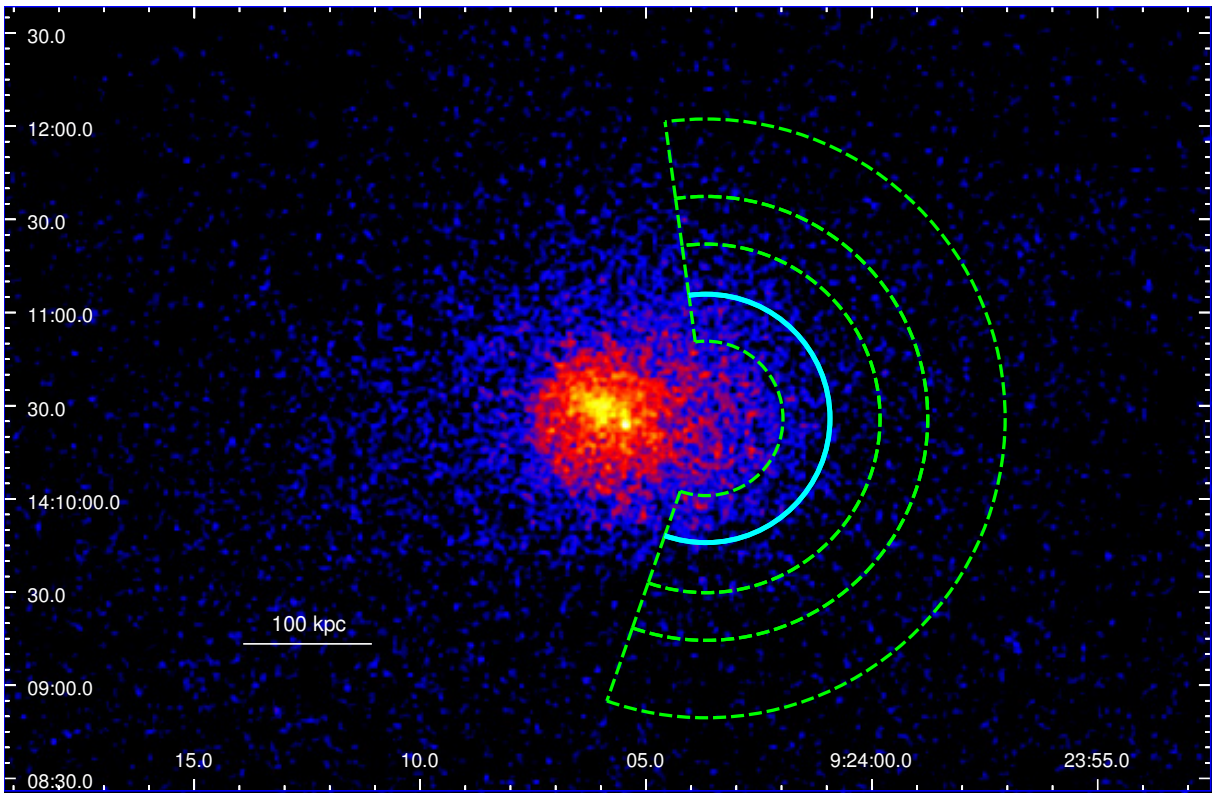

Figure 3.18: A795 0.5-7 keV image, Gaussian-smoothed with a kernel radius of 3 arcsec, with the four sectors used to study the thermodinamical properties of the west edge. All sectors are centered at (RA, DEC) = (09:24:03.68, +14:10:25.93), and the opening angle is 207°. The cyan arc follows the front.

R_i - R_o[a] kpc	Counts[b]	kT [keV]	norm [10^{-4}]	n_e[c] [10^{-3} cm^{-3}]	P[d] [10^{-11} erg cm^{-3}]
60.4 - 97.2	1593 (94.9 %)	$3.45^{+0.60}_{-0.40}$	$7.03^{+0.73}_{-0.66}$	$6.23^{+0.32}_{-0.29}$	$6.32^{+1.43}_{-1.04}$
97.2 - 136.3	1153 (88.3 %)	$6.01^{+2.65}_{-1.51}$	$4.46^{+0.33}_{-0.92}$	$3.26^{+0.12}_{-0.34}$	$5.75^{+2.75}_{-2.05}$
136.3 - 173.6	1041 (85.2 %)	$7.68^{+8.45}_{-2.47}$	$2.3^{+1.02}_{-0.54}$	$1.81^{+0.40}_{-0.21}$	$4.09^{+5.40}_{-1.79}$
173.6 - 234.1	1266 (77.2 %)	$5.22^{+1.07}_{-0.60}$	$11.52^{+0.40}_{-0.56}$	$2.42^{+0.04}_{-0.06}$	$3.70^{+0.82}_{-0.51}$

Table 3.10: This table lists the properties of the sectors used to analyze the west front (located at $\approx 73.4'' = 178.2$ kpc). The χ^2/D.o.f. is 185.4/187.
[a] Inner and outer radius of the sectors plotted in Fig. 3.18.
[b] Net photon counts (fraction w.r.t. the total counts from the same region).
[c] Electron number density.
[d] ICM pressure across the front.

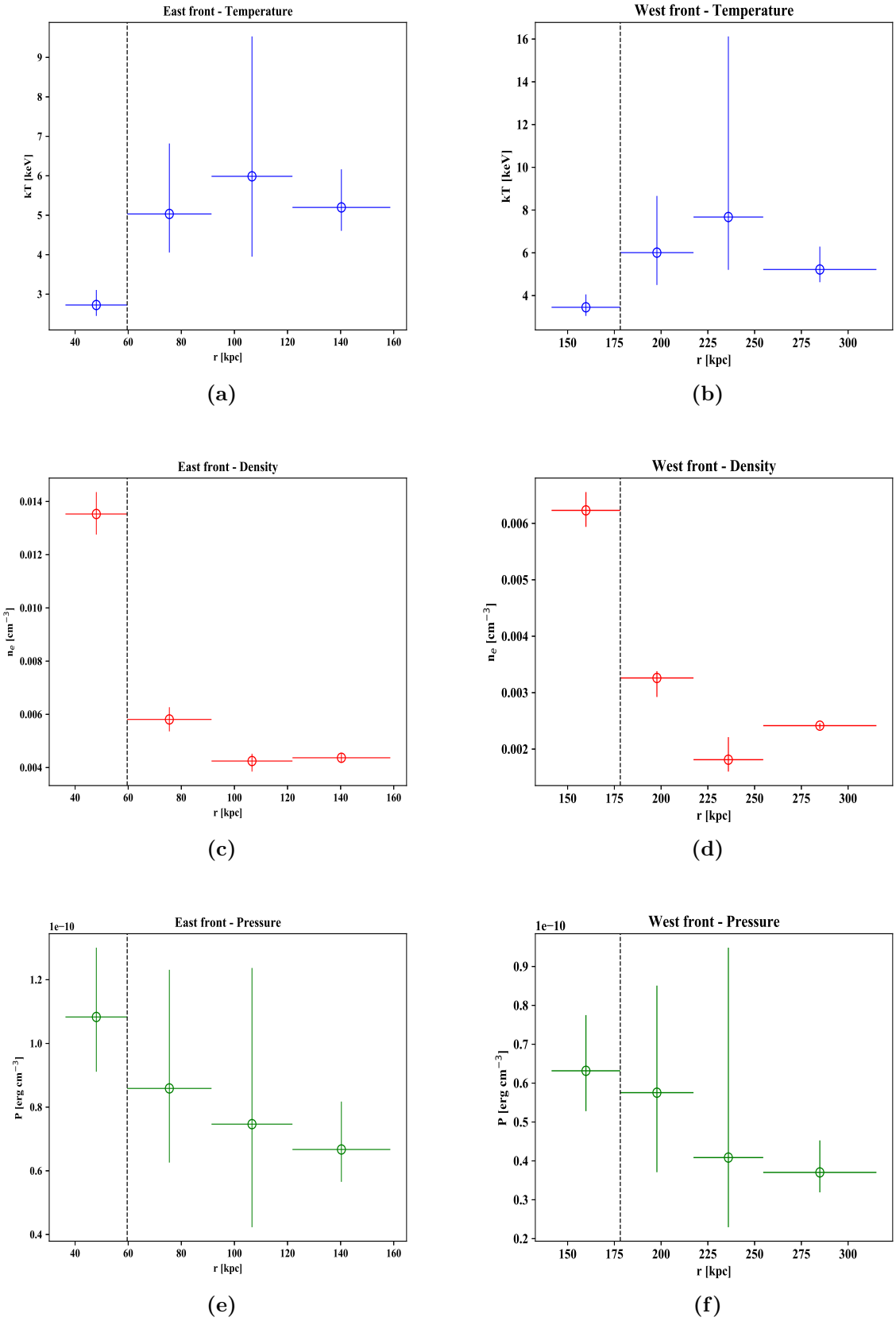

Figure 3.19: Temperature, density and pressure profiles across the east front (*left column*), and the west front (*right column*). Although sectors of Fig. 3.18 are not centered on the X-ray peak, here the x-axis of the plots indicates the distance of each sector from the X-ray peak.The black vertical line represents the position of the cold fronts.

Chapter 4

X-ray analysis: the central FR0

The *Chandra* observation of A795 offers the opportunity to investigate the link between the cluster environment and the properties of the radio-loud BCG. In particular, the FR0 J0924+14 displays a compact radio morphology: it is unresolved in the FIRST images, thus implying an upper limit on its size at 1.4 GHz of 5" ($\approx$ 12 kpc); Hogan et al. (2015) did not resolve the source with the VLA at 4.8 GHz (resolution of $\sim$ 3.4"), but they resolved it at 8.4 GHz, with a resolution of $0.2'' \approx 0.48$ kpc. This source has also been observed by MERLIN[1] at 5 GHz, which resolved a probably core-jet morphology with a largest linear size of 0.73 kpc (Kunert-Bajraszewska et al. 2010; see Fig. 4.1); in particular, there is a small elongation to the north-east direction, which could be interpreted as a jet.

The reasons behind the lack of extended radio emission of this population of AGN include: slowly spinning black holes which produce weak and slow jets, and/or frustration of the jet due to the external medium (e.g., Bodo et al. 2013); however, a final answer has not been found yet (see Sect. 1.4.2). Therefore, it is intriguing to probe the thermodynamical condition of the central regions of the ICM, and to design a scenario which might confirm or reject the hypothesis that the environment of FR0 radio galaxies affects the jet stability, leading to its inability to move through the external medium, and eventually to its premature disruption.

The first section of this chapter outlines the methods and main results of the fit to the X-ray spectrum of our target source. The second section is dedicated to the spectral study of the portions of Intra Cluster Medium that might be affecting the expansion of the jet; we will address the temperature and density of the environment, to look for critical differences with respect to the average properties of the ICM around FRI radio galaxies that might explain the different radio morphology. In the last section we discuss the results of

[1]Multi-Element Radio Linked Interferometer Network, a UK National Facility operated by the University of Manchester.

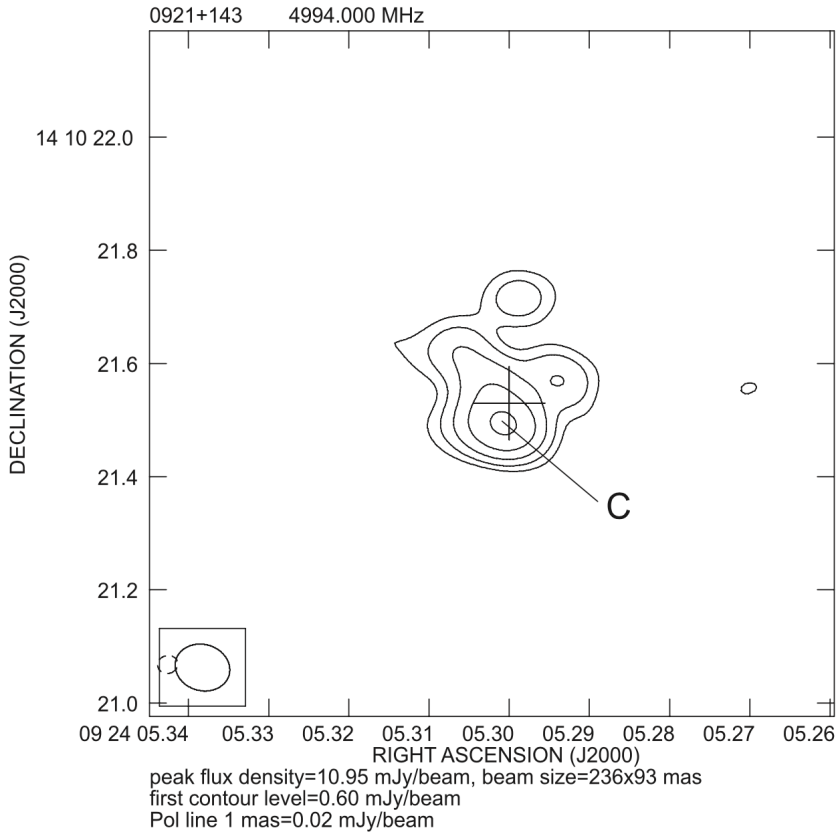

Figure 4.1: Merlin 5 GHz image of J0924+14; the first contour level corresponds to $\approx 3\sigma$. The cross indicates the center of the brightest cluster galaxy, while the C label indicates the supposed position of the nucleus.

our study, and discuss some hypothesis for the compactness of this radio-loud AGN.

4.1 Spectral properties of J0924+14

The *Chandra* data of J0924+14 have been already presented by Torresi et al. (2018) together with other 18 X-ray detected FR0s. In that work it was suggested that the X-ray emission of FR0s has a non-thermal origin, similarly to what is observed in FRIs. In order to be consistent with our analysis of the ICM of A795, and to dedicate more attention to this source, we performed a new analysis of the X-ray emission of the brightest cluster galaxy.

First of all, we had to decide the regions where to extract the spectrum of the source and of the background. We inspected the 0.5-7 keV image of the central source: as it is possible to see from Fig. 4.2 (panel *a*), the emission of J0924+14 has a roundish form, typical of point-like, unresolved sources; in fact, the X-ray peak of the ICM presents an offset from the BCG of $\sim$ 17 kpc, so we did not expect a significant contribution to the spectrum of this source from the cool phase of the Intra Cluster Medium. However, it

is likely that a fraction of the counts are due to the hot gas projected along the line-of-sight on the BCG: therefore, we decided to extract the background spectrum from an annulus surrounding the central source, so that both the projected, hot ICM and the cooler ambient gas contributions have been included. The choice for the point-source extraction region had to consider the extent of the emission attributable to the AGN, and the resulting fraction of counts in the 0.5 - 7 keV band due to *Chandra*'s encircled energy fraction.

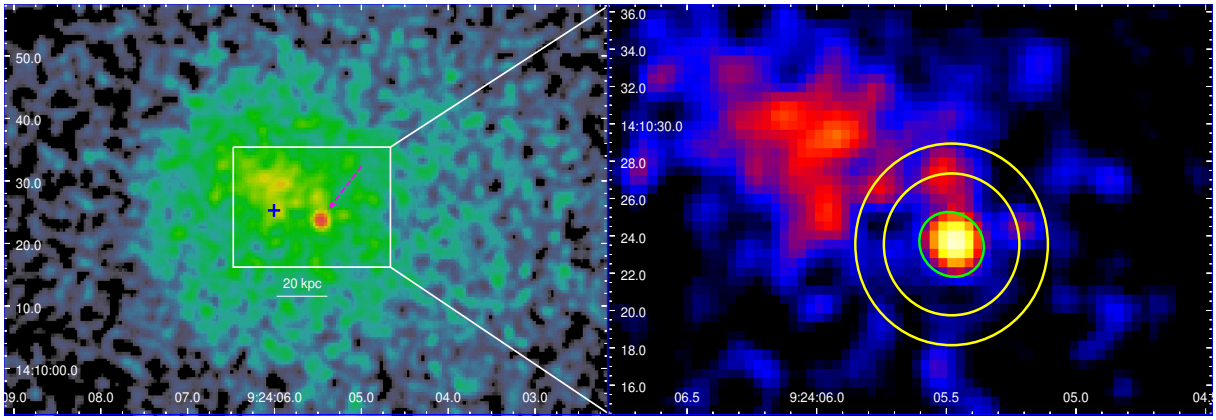

(a) **(b)**

Figure 4.2: Panel *a*: 0.5-7 keV image of A795, Gaussian-smoothed with a kernel radius of 3 pixels. The blue cross marks the position of the X-ray peak, while the pink arrow indicates the BCG. Panel *b*: same as in *a*, with the green ellipse representing the extraction region for the source spectrum and the yellow annulus that of the background spectrum.

In order to be consistent with the analysis of the ICM performed in Chap. 3, we extracted the spectrum of the central source from the same region excluded during the spectral analysis of the cluster (see Subsect. 3.2.2): since the final aim of this chapter is to understand the effect of the environment on the X-ray emission of the AGN, we decided to be coherent with our detailed analysis of the cluster gas[2]. The region is an ellipse centered onto the BCG of semi major-axis 1.86", semi minor-axis 1.68" and position angle 147.4°. The spectrum of the background has been extracted from a circular annulus surrounding the AGN that included a portion of the Intra Cluster Medium, extending from 3.8" to 5.4" from the center. The two extraction regions are showed in Fig. 4.2, panel *b*.

The source and background spectra have been extracted with **specextract**: since the source spectrum has 145 counts in the 0.5-7 keV band, we decided to group the data with five counts per bin and to use the Cash statistics (Cash, 1979). After loading the data on

[2]We point out that we tried different extraction regions for the AGN, with larger or smaller size, but the spectral analysis has yielded approximately equal results.

`Xspec`, we implemented a **tbabs∗po** model to fit the spectrum: while the first component is the galactic absorption, the second one is a power-law model, used to describe the emission from the AGN. The power-law model is defined as:

$$A(E) = KE^{-\Gamma} \tag{4.1}$$

where Γ is the photon index of the power-law, and K is the spectrum normalization at 1 keV, in units of photons keV^{-1} cm^{-2} s^{-1}. We fixed the galactic absorption to its reference value ($n_{\rm H} = 2.89 \times 10^{20}$ cm^{-2}), and left the photon index and the normalization free to vary. Tab. 4.1 lists the best fit parameters of this model, while Fig. 4.3 shows the spectrum and the model. In particular, we were able to constrain the power-law photon index to a value of $\Gamma = 2.45^{+0.33}_{-0.30}$ (1-sigma confidence error). We interpret this steep value as an evidence for the fact that the AGN is emitting most of its X-ray radiation in the soft band (0.5-2 keV).

Γ	normalization [photons keV^{-1} cm^{-2} s^{-1}]	C/D.o.f.
$2.45^{+0.33}_{-0.30}$	$5.59^{+0.83}_{-0.79} \times 10^{-6}$	$25.50/25^{a}$

Table 4.1: This table lists the best fit parameters for the **tbabs∗po** model.
[a] This value refers to the Cash statistic.

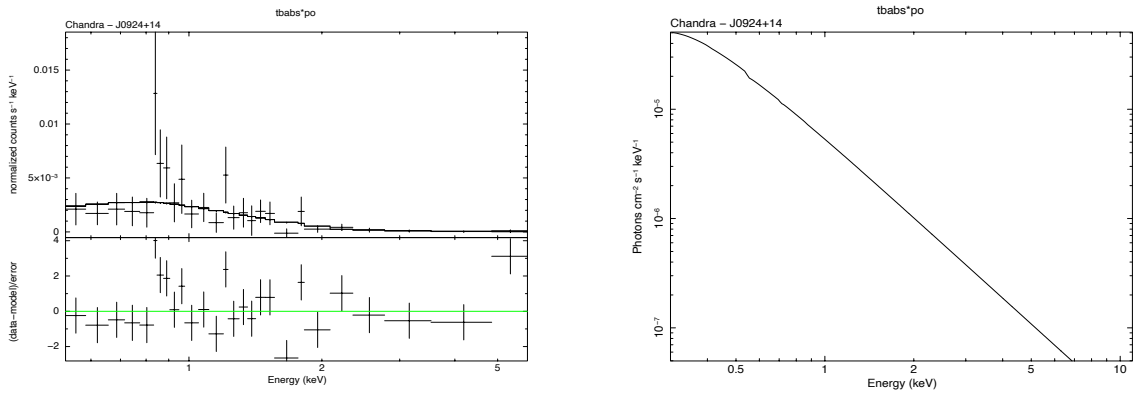

(a) **(b)**

Figure 4.3: Panel *a*: spectral data, together with the best-fit model (upper panel) and residuals (lower panel) for the **tbabs∗apec** model. Panel *b*: model used to fit the data of panel *a*.

Considering the spectrum of Fig. 4.3, there is a positive residual around ~ 5.4 keV: we inspected the background spectrum, and found that the background dominates the counts

above $\sim$ 4 keV, so the positive hard excess appears not to be related to intrinsic AGN emission. This can be also visualized by producing images in different bands: in the 0.5 - 2 keV image of Fig. 4.4 (panel *a*), the AGN is clearly visible, while in the 4.5-7 keV image in panel *b* the central emission fades into the background[3].

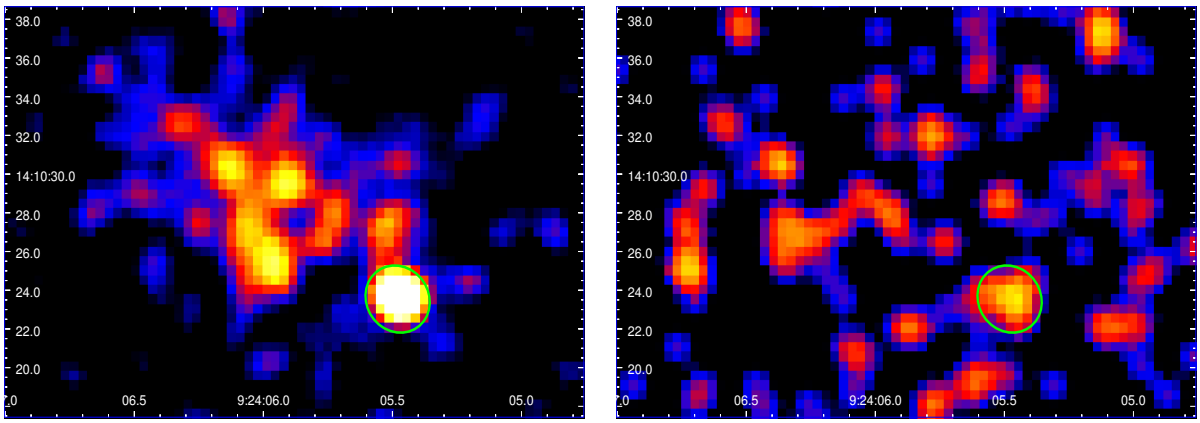

(a) **(b)**

Figure 4.4: Panel *a*: 0.5-2 keV image of the central regions of A795. Panel *b*: 4.5-7 keV image of the central regions of A795. Both images have been Gaussian-smoothed with a kernel radius of 3 pixels; the green ellipse marks the position of J0924+14 in each figure.

There are also positive residuals around $\sim$ 0.9 keV: we hypothesized that the addition of a thermal component, related to the cluster's gas, might better represent our data. We implemented a **tbabs∗(po+apec)** model to the source spectrum: given the low statistics, we fixed the metallicity to the value measured for the inner annulus of the deprojected spectral analysis of the ICM, that is $Z = 0.75\,Z_{\odot}$ (see Tab. 3.7), and left free to vary the normalization and temperature of the thermal component, and the normalization and photon index of the power-law. In Tab. 4.2 we compare the results of our fit to those of Torresi et al. (2018).

Our temperature and photon index estimates are consistent with the reference values, and the photon index value is still similar to that of the **tbabs∗po** model. The temperature of the thermal component is lower than that of the central ICM, that is $3.36^{+0.31}_{-0.24}$ keV: it is then possible that we are detecting the hot thermal corona of the elliptical brightest cluster galaxy. As reported by Sun et al. (2007), hot gas in ellipticals has temperatures of $\approx$ 1 keV, which is coherent with the value we measured. While this test has provided reasonable values both for the thermal and the power-law component, we decided to perform an F-test[4] to evaluate whether the additional component represents a significant

[3]We decided to produce the image in the 4.5-7 keV energy range to ensure the inclusion of only the hard emission.

[4]This method quantifies the improvement of a fit to data when one or more parameters are added to the starting model.

	kT [keV]	$norm^a_{\rm apec}$	Γ	$norm^a_{\rm PL}$	χ^2 (C)/D.o.f.
This work	$1.2^{+0.3}_{-0.2}$	$5.34^{+3.89}_{-3.08}$	$2.04^{+0.69}_{-0.94}$	$2.82^{+1.57}_{-1.83}$	$21.10/23^b$
Torresi et al. (2018)	$1.3^{+1.4}_{-0.6}$		1.8 ± 0.3		$3/9^c$

Table 4.2: This table lists the best fit parameters for the **tbabs∗(po+apec)** model.
[a] Normalizations of the **apec** and the power-law (PL), both in units of [10^{-6} photons keV^{-1} cm^{-2} s^{-1}].
[b] This value refers to the Cash statistic.
[c] This value refers to the Chi statistic.

improvement for our model. The F-test returned a value of 2.4: this implies that adding the **apec** model did not improve the fit enough to consider this thermal component as necessary to describe the spectrum. Therefore, it is not possible to confirm the detection of a hot corona - attributable to the brightest cluster galaxy. We then rejected this model due to the low significance of this fit, and concluded that although it is likely that the thermal emission from the cluster's gas (or the thermal hot corona of the elliptical host galaxy) affects the spectrum, our counts are not high enough to allow for an additional component to better describe our data. Deeper, future X-ray observation would probably allow to confirm or reject this hypothesis.
We also checked the possibility for intrinsic absorption to be present: by multiplying our starting model by a **ztbabs** component[5], we aimed to test whether the circum-nuclear ambient of the AGN was filled with cold, optically thick matter. We stress that we observed no negative residuals below $\approx$ 1 keV, and the photon index did not assume very low values, which would suggest the presence of an intrinsic absorber (Macconi, 2019). Indeed, this test returned only an upper limit for the intrinsic absorption of $n_{\rm H} < 0.5 \times 10^{22} cm^{-2}$: such a low value is similar to those found in FRIs-LERG (e.g. Balmaverde et al., 2006; Baldi and Capetti, 2008; Macconi, 2019), therefore we can confirm the conclusion reported by Torresi et al. (2018), that the circumnuclear environment of FR0s is not filled with cold, dense matter.
Given these sanity checks, we concluded that with our current statistics the best model to describe the X-ray emission of this FR0 is a simple absorbed power-law, characterized by a steep photon index and a prevalence of emission in the soft band. We computed the flux and luminosity of our target J0924+14 in different energy ranges: Tab. 4.3 reports our results.
In order to obtain new information on the accretion properties of this source, we computed its accretion rate in terms of the ratio $L_{\rm acc}/L_{\rm Edd}$: we used the [OIII]-line luminosity to derive the bolometric power of the AGN through the relation $L_{\rm acc} = L_{\rm bol} = 3500 L_{\rm [OIII]}$

[5]The free parameters are the intrinsic column density $n_{\rm H}$ [cm^{-2}] and the redshift z.

$F_{0.5-2\,keV}$	$L_{0.5-2\,keV}$	$F_{2-10\,keV}$	$L_{2-10\,keV}$	$F_{0.1-100\,keV}$	$L_{0.1-100\,keV}$
$1.34^{+0.24}_{-0.22}$	$6.73^{+1.19}_{-1.09}$	$0.79^{+0.28}_{-0.37}$	$4.01^{+1.40}_{-1.86}$	$2.75^{+0.40}_{-0.38}$	$13.82^{+2.03}_{-1.93}$

Table 4.3: Flux and luminosity in different bands for the power-law model used to describe the X-ray spectrum of J0924+14. Fluxes are in units of [10^{-14} erg cm^{-2} s^{-1}], while luminosities are in [10^{41} erg s^{-1}].

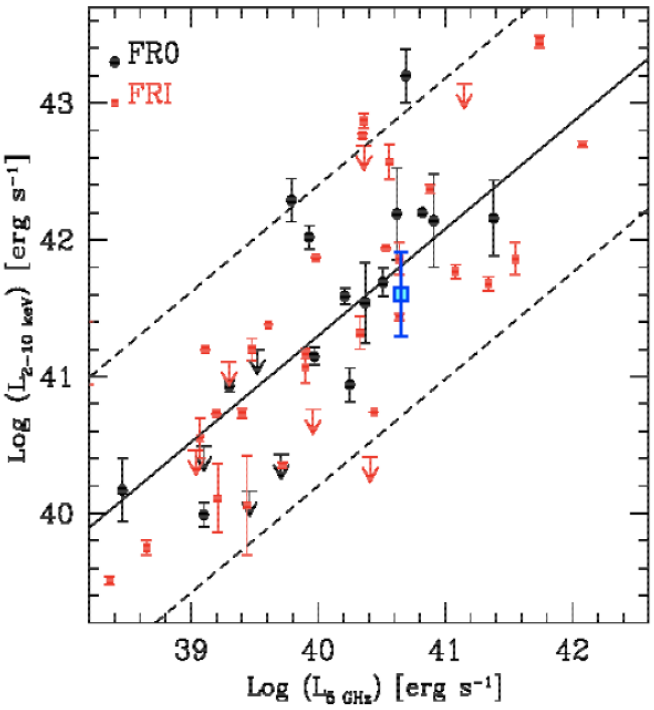

Figure 4.5: Plot of the X-ray luminosity versus radio core luminosity for FRIs (red points) and FR0s (black points), with the solid black line being the linear regression for the whole sample of radio galaxies (Eq. 1.48), and the dashed lines its uncertainties (Torresi et al., 2018). We over-plot our measurement for J0924+14 with a blue square.

(Heckman et al., 2004). To compute L_{Edd}, we determined the black hole mass from Eq. 1.42, using the stellar velocity dispersion reported in the SDSS Data Release 12 (Alam et al., 2015). Our results are presented in Tab. 4.4. The ratio of $L_{\rm acc}/L_{\rm Edd} = 3.8 \times 10^{-3}$ is low, and typical of FRIs - LERG sources in which the central engine is powered by an advection-dominated accretion flow (Torresi et al., 2018).

Moreover, by over-plotting on Fig. 1.28 our estimated value for the X-ray luminosity of this source $L_{2-10\,keV}$ (see Fig. 4.5), we find that it lies in the correlation strip shared by both FR0s and FRIs radio galaxies[6]. We conclude that our dedicated study to the

[6]The $S_{5\,\rm GHz}$ of J0924+14 has been retrieved by Kunert-Bajraszewska et al. (2010), who reports a value of $(9.00 \pm 0.01) \times 10^{-16}$ erg s^{-1} cm^{-2}, which corresponds to a luminosity $L_{5\,\rm GHz} = (4.52 \pm 0.05) \times 10^{40}$ erg s^{-1}.

$L^a_{[OIII]}$	L^b_{acc}	$\sigma_\star$ [km s^{-1}]	M_{BH} [$M_\odot$]	L^c_{Edd}	L_{acc}/L_{Edd}
$5.37^{+0.05}_{-0.05}$	$1.88^{+0.02}_{-0.02}$	261 ± 9	$3.9^{+1.7}_{-1.7} \times 10^8$	$4.9^{+2.1}_{-2.1}$	$3.8{\times}10^{-3}$

Table 4.4: This table reports the measurements used to determine the accretion rate L_{acc}/L_{Edd}.
[a] in units of 10^{40} erg s^{-1}.
[b] in units of 10^{44} erg s^{-1}.
[c] in units of 10^{46} erg s^{-1}.

emission of J0924+14 is consistent with the X-ray properties of the sample of Torresi et al. (2018), which indicate that the X-ray emission of FR0s originates from the jet, and that the nuclear properties of FR0s and FRIs are similar. Our target source then differs from typical FRIs only for the lack of extended emission. In the next section, we present the study of the Intra Cluster Medium of A795 in the proximity of J0924+14: by measuring the temperature and density of the ICM, we have searched for extreme environmental differences with respect to those of typical Fanaroff-Riley Type I AGNs at the center of galaxy clusters.

4.2 The ambient medium of J0924+14

In this section we explore the properties of the gas surrounding the FR0 J0924+14. An annulus of inner radius 2" and outer radius 12", centered on the BCG (see Fig. 4.6 panel *a*), has been used to extract the spectrum of the ambient gas. We associated a background using the **blanksky** event file and extracting the background spectrum from the same region. We loaded the data on `Xspec` and fitted the data in the 0.5 - 7 keV with a **tbabs∗apec** model; the temperature, metallicity and normalization of the **apec** component were left free to vary. The results of this fit are reported in the first row of Tab. 4.5: the temperature of kT $= 3.82 \pm 0.23$ keV is similar to that measured for the innermost annulus of the deprojected spectral analysis of Subsect. 3.2.2.
It seems important to consider the sloshing motion of the ICM which has been discussed in Chap. 3: by inspecting the form of the cool spiral of Fig. 3.5, we expect that the north-east side of the AGN, in the proximity of the X-ray peak, might have a lower temperature than the south-west side. As a consequence, we decided to split the annulus in two sectors, the first one including the X-ray peak, and the second one the remaining portion of the region. Fig. 4.6 (panel *b*) shows the two resulting sectors: we extracted the spectra of these regions, and implemented another **tbabs∗apec** to model the data. By looking at the best-fit results of Tab. 4.5 (second and third row), it is possible to

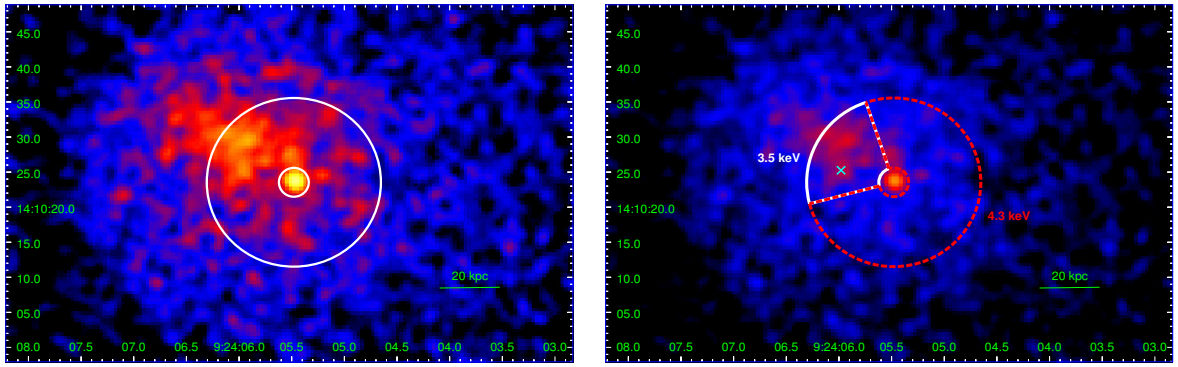

(a) **(b)**

Figure 4.6: Panel *a*: 0.5-7 keV image of the central regions of A795; the white annulus is the extraction region for the ambient gas spectrum. Panel *b*: 0.5-7 keV image of the central regions of A795; the cyan cross denotes the position of the X-ray peak; the white and red sectors are the extraction regions for the fit reported in Tab. 4.5: the best-fit temperature for each region is plotted. Both images have been Gaussian-smoothed with a kernel radius of 3 pixels

confirm our hypothesis that the ICM around the FR0 is multiphase, and subject to the temperature gradients induced by sloshing.

Region	Counts[a]	kT [keV]	Z [$Z_\odot$]	norm [10^{-4}]	χ^2/D.o.f.
Annulus	2475 (92.4 %)	$3.81^{+0.23}_{-0.23}$	$0.75^{+0.20}_{-0.18}$	$5.26^{+0.26}_{-0.26}$	77.13/70
North-east sector	871 (94.6 %)	$3.54^{+0.41}_{-0.33}$	$0.97^{+0.51}_{-0.38}$	$1.74^{+0.19}_{-0.19}$	30.04/26
South-west sector	1604 (91.3 %)	$4.30^{+0.30}_{-0.29}$	$0.86^{+0.30}_{-0.26}$	$3.34^{+0.21}_{-0.21}$	45.73/49

Table 4.5: This table contains the results of the fit to the ICM around J0924+14; the first row refers to the starting annulus of Fig. 4.6, panel *a*, while the second and third row report the values for the two sectors of Fig. 4.6, panel *b*.
[a] Net photon counts (fraction w.r.t. the total counts from the same region).

Next, we considered the density of the ambient medium: if the cluster's gas is preventing the propagation of radio jets, we should expect to find a high density environment, compared to that surrounding typical, extended FRIs in brightest cluster galaxies. By using Eq. 3.6, it is possible from the *norm* parameter of the **apec** component to obtain the electron density of the ICM n_e: for the whole annulus surrounding the AGN we find an electron density of $n_e = (2.87 \pm 0.09) \times 10^{-2}$ cm^{-3}. We stress that this result suffers from the contribution of the ICM projected along the line of sight: it is likely that our measure of the electron density is overestimated. This can be confirmed, for example, by comparing this value with the one - reported in Subsect. 3.2.2 - corresponding to the innermost annulus of the ICM radial spectral analysis, that overlaps with the extraction

region of Fig. 4.6: we found an electron density of $n_e = (1.79 \pm 0.06) \times 10^{-2}$ cm^{-3}, which is lower than that of the annulus surrounding the AGN. Nevertheless, these two estimates do not strongly disagree with each other, so it is possible to consider the density of the Intra Cluster Medium around J0924+14 as ranging between $1.7 - 2.9 \times 10^{-2}$ cm^{-3}.

4.3 Is the ICM preventing the jet expansion?

In this section we explore the possibility that the environment of J0924+14 is interfering with the jet propagation: as proposed by Baldi et al. (2015), a high density gas might be capable of decelerating and disrupting the radio jets. Here we discuss both the density of the surrounding medium, and the effects of sloshing-induced turbulence of the jet stability.

The density of the ICM In the previous section, we computed the density and temperature of the gas around the brightest cluster galaxy; the electron density of the central ICM ranges between $1.7 - 2.9 \times 10^{-2}$ cm^{-3}. It appears that the density we measured is in line with typical ICM density around FRIs at the center of galaxy clusters ($\approx 10^{-3} - 10^{-1}$ cm^{-3}, e.g., Haarsma et al., 2010; Mohr et al., 1999; McDonald et al., 2017): this suggests that if FR0s' compactness is due to the frustration and disruption of the jet on small scales ($\approx 1 - 15$ kpc), the local density of the hot Intra Cluster Medium is not responsible for it. In fact, our FR0's environment is typical of galaxy clusters, and shows no peculiarities or extreme values in terms of density which might be considered as the cause for the radio size of the brightest cluster galaxy. The local density of the ICM does not seem a crucial parameter that might explain the observed differences between the radio extension of FRIs and FR0s.

The effect of sloshing Another possibility might be that the sloshing, turbulent motion of the gas is capable of affecting the stability of radio jets. In section 4.2, we found that due to the sloshing motion of the cluster gas, there is a multiphase medium around J0924+14, with lower temperature (~ 3.5 keV) in the north-east direction, and higher temperature (~ 4.3 keV) in the south-west direction. This indicates that even the central regions are affected by the large scale oscillation described in Subsect. 3.2.2. Despite this finding, it should be noted that in clusters and groups displaying sloshing motions of the gas there are FRIs whose jets have not been disrupted. For example, the canonical FRI 3C449 is located at the center of a galaxy group displaying signs of sloshing (Lal et al., 2013): the authors argued that the gas motion is affecting the propagation of the jets only at the interface of the cold front they detected at ~ 30 kpc from the core. In particular, they suggested that when the jet crossed the density edge, it was partially

disrupted and inflated to form a radio lobe; however, in the proximity of the core, the jets do not appear to be affected by the sloshing motion (see Fig. 4.7). In addition to this, Kolokythas et al. (2020) recently showed that sloshing in NGC 1550 has bended the jets of the central AGN and affected the appearance of the radio lobes, but has not disrupted the jet at its base. Therefore, these observational evidences imply that unless there are intrinsic differences between the jets of FR0s and FRIs, sloshing alone is not capable of preventing the propagation of jets launched by radio galaxies.

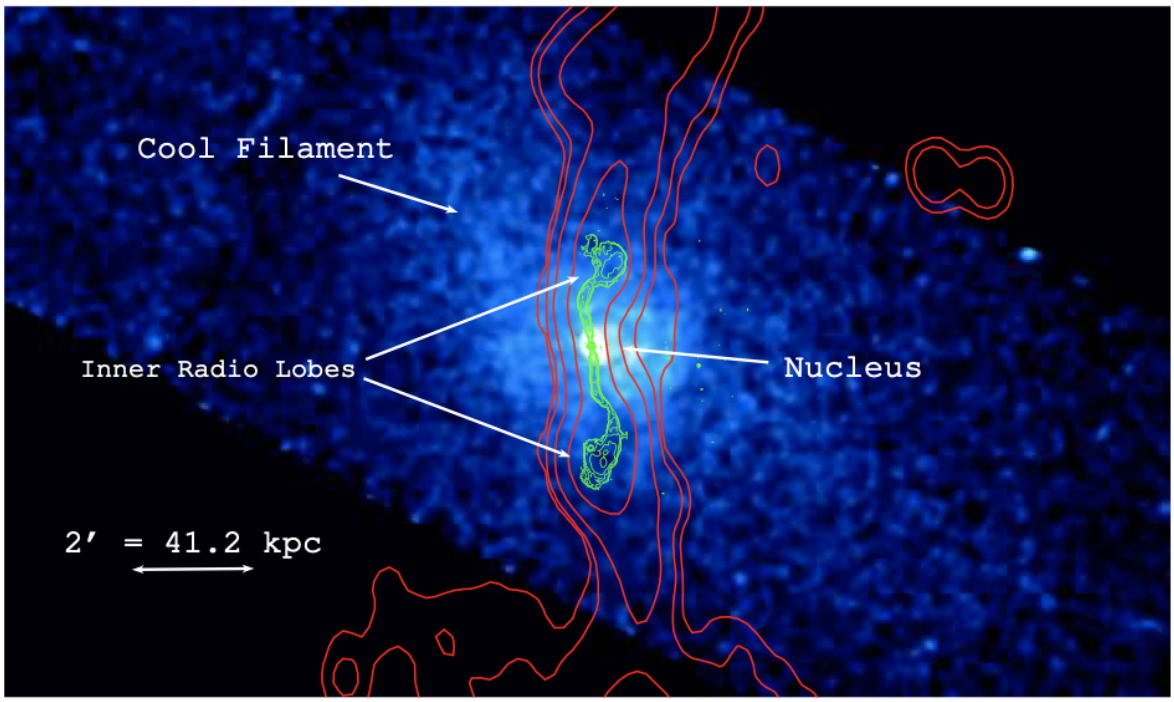

Figure 4.7: *Chandra* 0.5-2 keV image of 3C449, with 0.6 GHz (red) and 8.4 GHz (green) radio contours (Lal et al., 2013).

We point out that it has been proposed (Baldi et al. 2015; Garofalo and Singh 2019; Baldi et al. 2019b) that the jet's inability to propagate in the external medium might be explained in terms of the AGN parameters: a slowly spinning black hole surrounded by an advection dominated accretion flow would hardly produce strong, collimated, long-lasting jets. In this picture, we might speculate that for our specific case the sloshing gas might concur to the partial disruption of an already weak, low Lorentz factor jet. Therefore, the cluster ambient might facilitate the quenching of our radio galaxy, already characterized by an intrinsically weak jet; otherwise, every cluster displaying evidences of turbulent motion of the ICM should possess a radio compact brightest cluster galaxy - which is not true (for example, the sloshing galaxy cluster A2029 hosts an edge-darkened, extended FRI named PKS1508+059; Clarke et al. 2005; Paterno-Mahler et al. 2013). Apart from our hypotheses for the compactness of this specific source, it is important to remark the

fact that there are FR0s outside galaxy clusters and groups ($\sim 50\%$ of the sources in the sample of Torresi et al. 2018; e.g. Tol1326-379 Grandi et al. 2016), and not every galaxy cluster hosting a FR0 displays signs of sloshing (e.g. Abell 1831; Aktekin and Hudaverdi, 2014). Considering the putative intrinsic weakness of FR0's jet, it is likely that different mechanisms concur to the jet destruction: while for FR0s in the central regions of galaxy clusters the turbulence might reasonably impede the growth of the radio galaxy, in isolated FR0s there must be different mechanism, possibly related to the interstellar medium of the host.

Warm ionized gas around J0924+14 The Intra Cluster Medium is not the only turbulent gas phase that might be affecting the - possibly weak - jet of J0924+14: Hamer et al. (2016) studied the warm ionized gas dynamics in the cores of 73 galaxy clusters (including A795). Fig. 4.8 summarizes their results: the five panels show the continuum emission, the Hα flux map, the ratio of the [NII] to Hα, the line of sight velocity field and the FWHM[7]. They found that a cloud of Hα-emitting gas surrounds the brightest cluster galaxy; the cloud appears centered on the BCG, roughly spherical, with an extent of $\sim$ 11.1 kpc. On the contrary, in other clusters (e.g. NGC5044, A1991) the warm gas extends beyond the optical size of the galaxy and displays filaments and clumps: the authors concluded that the warm gas in A795 is in a "quiescent" state. However, by looking at the fourth panel it can be deduced that the gas in A795 has a velocity structure, and the fifth panel - which shows the FWHM of the Hα line - reveals that the line broadening of Hα around J0924+14 reaches $400 - 800$ km/s - the highest FWHM of their sample. This might suggest that we are seeing a system of Hα clouds along the line of sight, with high-velocity random motions.

As a note of caution, we point out that the Hα line broadening might be caused by non-gravitational kinematics, for example outflow motions: the warm gas velocity dispersion is a factor of $\gtrapprox 2$ greater than the stellar velocity dispersion ($\sigma_\star = 261 \pm 9$ km s^{-1}), suggesting that the hydrogen gas might not only be tracing the gravitational potential of the host galaxy, but could also be influenced by an additional non-virial component. The observation of Hamer et al. (2016) does not allow to further investigate this hypothesis: future observations of molecular gas (possibly with the high spatial resolution of ALMA[8]) could help us to trace the kinematics of the gas around J0924+14, and to understand whether warm gas is flowing out of the BCG.

It is also useful to consider the ratio of [NII]/Hα, which is sensitive to the excitation state of the gas: ratios above ~ 0.6 indicate that the AGN (and not star formation) provides

[7]The Full Width at Half Maximum of an emission line measures the velocity dispersion of the gas that emitted the line, therefore indicates the random motions of the gas particles.

[8]The Atacama Large Millimeter/Submillimeter Array, Wootten and Thompson (2009).

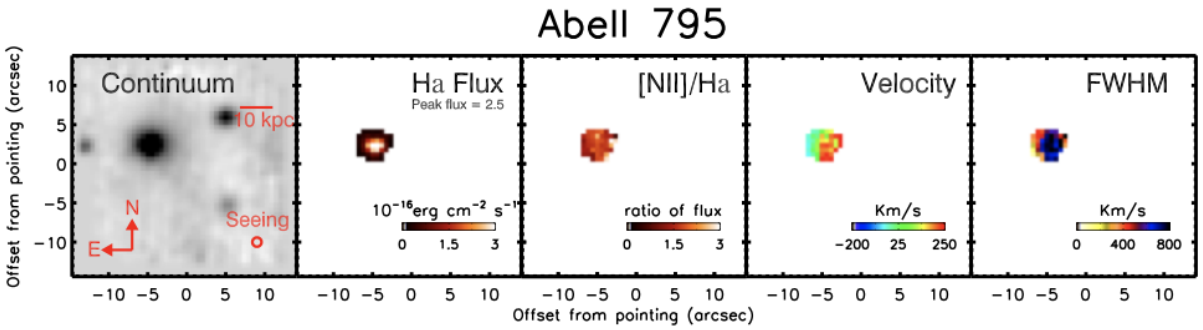

Figure 4.8: Maps of the spectral fit to the optical data of A795; from left to right the panels show the continuum emission, the Hα flux map, the ratio [NII]/Hα, the line of sight velocity profile of Hα and the FWHM of the emission line (Hamer et al., 2016).

significant contribution to the excitation. In fact, the third panel of Fig. 4.8 shows that $<$[NII]/Hα $>\approx$ 1.45, thus implying that a major source of excitation is provided by the central AGN. This supports the theory that the gas clouds are indeed quite close to the center of the BCG, as at large distances ($\gtrapprox$ 10 kpc, Hamer et al. 2016) the AGN ionizing radiation would not be able to sustain the excitation of the gas. Here we speculate that besides the sloshing motion of the ICM, the warm, turbulent, Hα-line emitting gas around J0924+14 might be slowing the jet expansion in the outer medium. To verify this hypothesis would require to model the clumpiness of these gas clouds, so that the jet frustration could also be compatible with the lack of X-ray absorbing cold gas suggested by the spectral modelling (Sect. 4.1). If future observations will detect molecular gas clouds - cospatial with the warm phase - it might become possible to put stronger constraints on the interaction of the jet and this gas, and to verify or reject the hypothesis that the cold gas is preventing the growth of the radio galaxy. Once again, however, it should be noted that Hα-emitting clouds (and even molecular gas) have also been detected around Fanaroff-Riley Type I radio galaxies at the center of galaxy clusters (e.g. Hydra-A; Hamer et al. 2016): this suggests that the jet has to be intrinsically weak to get easily disrupted by the warm and/or cold gas.

Conclusive remarks on the compactness of J0924+14 From our analysis we can conclude that the reason(s) behind FR0s' radio compactness has to be searched primarily in the intrinsic properties of the jet and/or BH spin. The environment can still play a role, although not the major one. In fact, our X-ray study of the environment of an FR0 has revealed a complex, multiphase and possibly turbulent ambient, but in line with typical properties of the ICM surrounding extended radio galaxies. This might highlight the critical role of the jet stability, and - in turn - of the black hole spin: unless the central engine of FR0s has peculiar parameters that lead to the formation of unstable jets, turbulence alone cannot explain the radio compactness.

We note that the sample of Hamer et al. (2016) comprises another cluster with a FR0 at its center, that is Abell 85 (Torresi et al., 2018). By chance, this cluster also displays signs of sloshing and interaction with at least two sub-clusters (Ichinohe et al., 2015). Our hypothesis on the environment of J0924+14 would greatly benefit from a direct, future comparison between Abell 795 and Abell 85, and could corroborate our hypothesis that the gas sloshing cannot be the only mechanism preventing the expansion of the radio galaxy. However, if the jet presents a low Lorentz factor and is launched by a slowly spinning black hole, then turbulence induced by the gas motion might quench the weak jet as soon as it enters the Intra Cluster Medium.

Chapter 5

Discussion

The morphological and spectral analysis presented in Chap. 3 has revealed that A795 has a weakly cool core: within $r_{\rm cool} = 66.2 \pm 3.2$ kpc the cooling time is lower than 7.7 Gyr, and in the innermost ≈ 5 kpc the gas cools even more efficiently, as the cooling time is ≈ 1 Gyr. Considering the classical cooling flow theory (sec. 1.2), a copious amount of cooled gas should cross $r_{\rm cool}$ and flow towards the inner regions: by using Eq. 1.31, from $L_{\rm X}$ inside $r_{\rm cool}$ we computed the expected cooling rate $\dot{M}_{\rm CF} = 109 \pm 6\, M_{\odot}/yr$. However, by fitting the spectrum of the ICM inside the cooling region with a multi-phase, cooling model, we obtained an upper limit on the observed cooling rate of $\dot{M}_{\rm obs} \leq 7\, M_{\odot}/yr$: we interpreted the difference between the expected and observed cooling rates (a factor of ≈ 10) as an indication that a heating mechanism has to be present, in order to reduce the cooling efficiency and prevent the strong inflow of gas.
As mentioned in Chap.1, a feedback from the AGNs hosted in the brightest cluster galaxies appears to be the most promising mechanism to heat the gas. The spatial anti-correlation between the lobes created by the central galaxy and the X-ray depression excavated by the radio plasma suggests a feedback loop scenario: the AGN is responsible for quenching the cooling of the surrounding ICM, and - in turn - it is fueled by the (greatly reduced) inflow of cold gas.
In this chapter, we dedicate our attention to the feedback mechanisms that might be inhibiting the cooling in A795: we assess the properties of the two putative cavities we identified in Sect. 3.1, to verify whether the expected cavity power could balance the cooling luminosity. We stress that the BCG of A795 hosts a Fanaroff-Riley Type 0 radio galaxy, whose X-ray emission has been studied in Sec. 4.1. This class of radio galaxies is peculiar since it is characterized by compact radio emission ($d \leq 10$ kpc), therefore it is not clear whether they are able of excavating X-ray cavities in the external medium. In the first section of this chapter we address the following questions:

- What are the properties of the two putative cavities in A795? Are they able to

balance cooling and heat the ICM of this system?

- Considering the small radio size of the FR0 hosted in the BCG, is it possible that in the past it was able to inflate radio lobes and excavate the two observed X-ray depressions?

Furthermore, our analysis (Chap. 3) showed that the ICM in A795 is sloshing: we discovered two surface brightness discontinuities on opposite sides of the cluster, which follow a spiral pattern that extends from the X-ray peak to ≈ 176 kpc north-west. By inspecting the density, temperature, and pressure profile across these edges we confirmed their *cold fronts* nature: the inner side of the front is colder than the outside, and the pressure is continuous. Therefore, we claim that some mechanism has perturbed the ICM, and induced an oscillating motion that has displaced cold gas from the center of the cluster.
The second section of this chapter is dedicated to our hypothesis on the dynamical history of A795: we compute the time-scales of the sloshing mechanism to obtain an estimate of the time that has passed since the perturbation was set. Besides this, we consider the effects of cold gas displacement and sloshing-induced turbulence on the cooling efficiency of the ICM, to probe whether this oscillation might represent an additional source of heating.
In the course of our study of A795, we have searched for other multi-wavelength data on this cluster. In particular, we inspected the data archive of the low-frequency radio surveys TGSS[1], GLEAM[2], and VLSS[3] to look for evidence a past radio activity of the radio galaxy and/or diffuse, extended radio emission over the cluster size. Interestingly, the TGSS images reveal extended radio emission - detected also by GLEAM and VLSS - which we interpret as a *mini-halo*, possibly related to the sloshing motion of the gas. The results of this study are presented in the last section of this chapter.

[1]TIFR GMRT sky survey at 150 MHz, with a resolution of 25" (Intema et al., 2017).
[2]GaLactic and Extragalactic All-sky Murchison Widefield Array survey across 72-231 MHz, with a resolution of 2 arcminutes (Hurley-Walker et al., 2017).
[3]VLA Low-frequency Sky Survey at 72 MHz, with a resolution of 80" (Cohen et al., 2007).

5.1 AGN feedback in Abell 795

Under the assumption that the two X-ray depressions presented in Sect. 3.1 are real cavities, we proceed by calculating the cavity enthalpy (Eq. 1.35), and the cavity power ($P_{\rm cav} = 4pV/t_{\rm age}$). Subsequently, we compare the result with the cooling luminosity $L_{\rm cool}$ (derived in Subsect. 3.2.3), to understand whether this putative cavity system could represent a source of heating for the ICM. We conclude this section by discussing whether the two depressions are real X-ray cavities, possibly inflated in the past by the jet of the central FR0 radio galaxy.

5.1.1 Properties of the two putative cavities

The morphological inspection of the central regions of A795 has revealed the presence of a pair of X-ray depressions (named D1 and D2 in Fig. 5.1), which show a deficit of $\sim 30\%$ and $\sim 20\%$ with respect to the best β-model fit to the cluster. They are located at approximately the same distance from the central AGN, and they have similar sizes; we interpret these two structures as putative X-ray cavities.

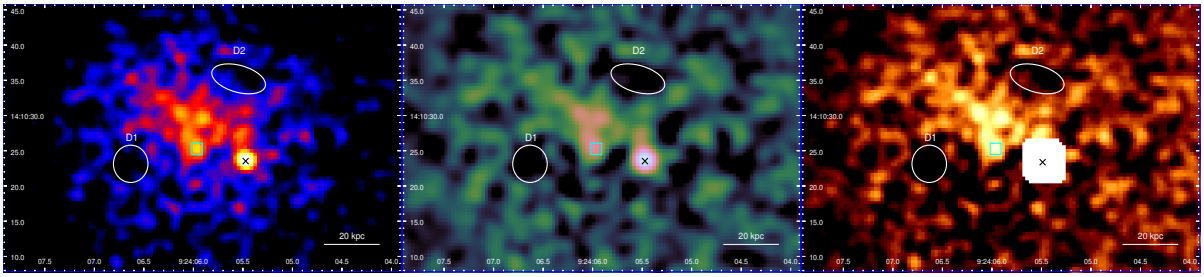

(a) **(b)** **(c)**

Figure 5.1: Panel *a*: 0.5-2 keV image of the central regions of A795, Gaussian-smoothed with a kernel radius of 3 pixels; panel *b*: A795 0.5-2 keV unsharp mask image, obtained by subtracting two images smoothed with a Gaussian of 2 and 10 pixel axes, respectively; panel *c*: A795 0.5-2 keV residual image, obtained by subtracting a β-model, and Gaussian-smoothed with a kernel radius of 3 pixels. In each panel, the white ellipses mark the position of the two putative cavities, the cyan box indicates the X-ray peak, and the black cross denotes the position of the AGN. The white pixels in the residual image are due to the exclusion of the AGN from the β-model fit.

We notice that the two cavities have different shapes: while D1 seems approximately spherical, D2 appears stretched and more elliptical; in fact, the shape of each cavity might suffer from how we selected the extent of the two cavities, and projection effects:

- First of all, we chose the size of the cavities by comparing the original image of A795, the unsharp mask image, and the best fit β-model residual image (see Fig.

5.1); although D1 and D2 are quite evident in each one of these picture[4], we found that the unsharp mask image better highlights their presence. However, their actual shape might slightly differ from one image to the other, leading to uncertainties in the true cavity shape.

- It is important to consider that projection effects might be present: if there is gas in front of (or behind) a cavity, or sloshing has displaced the ICM around the cavities, we might not be able to determine the actual shape of each depression.

Being aware of this, we assume that the 3D shape of each cavity is that of a prolate ellipsoid, and we compute the volume of each depression as $V = (4\pi/3)R^2_{\rm min}R_{\rm max}$; columns 2-6 of Tab. 5.1 list the cavities' sizes, distances from the AGN (D), distances from the X-ray peak (d), and volumes.

	R_{max} [kpc]	R_{min} [kpc]	D [kpc]	d [kpc]	V [kpc^3]	t_{age} [Myr]	pV [10^{58} erg]	P_{cav} [10^{43} erg s^{-1}]
D1	6.43	6.16	40.64	22.62	1022	42.4±2.0	2.0±0.5	1.5±0.4
D2	9.85	4.64	27.68	30.01	888	28.8±1.3	1.4±0.2	1.5±0.3

Table 5.1: This table contains the main properties of the putative cavities D1 and D2.

The cavity power We now describe the method used to calculate the cavity power $P_{\rm cav} = 4pV/t_{\rm age}$. To compute the pressure that the ICM exerts over the two cavities we consider the deprojected profile of Fig. 3.14: the higher spatial resolution of the `Proffit` profile allows for a local measurement of pressure around the two cavities. In particular, the pressure of the ICM around D1 and D2 is $P_{\rm ICM,\ D1} = (1.7 \pm 0.3) \times 10^{-10}$ erg cm^{-3} and $P_{\rm ICM,\ D2} = 1.4 \pm 0.2 \times 10^{-10}$ erg cm^{-3}, respectively.
To compute the age of the cavities, $t_{\rm age}$, we suppose that they are moving at the sound speed $c_{\rm s}$ of the ICM:

$$c_{\rm s} = \sqrt{\frac{\gamma kT}{\mu m_{\rm p}}} \tag{5.1}$$

$$t_{\rm age} = \frac{D}{c_{\rm s}}, \tag{5.2}$$

where D is the distance of the cavity from the BCG. Since both the two cavities are inside the innermost annulus used for the deprojected spectral analysis, we use the temperature measured within $r = 16.7$" (40.6 kpc) from the X-ray peak to compute $c_{\rm s}$, that is $kT =$

[4] As pointed out in Sec.3.1, other depressions are visible in the central regions; however, their deficit with respect to the best β model is of $5 - 11\%$, less than D1 and D2.

3.36 ± 0.28 keV. Therefore, the local sound speed is equal for the ICM around D1 and D2, and measures $c_s = 938 \pm 43$ km s^{-1}. We consider the distances from the AGN as the space travelled by each cavity since its formation; the resulting t_{age}, pV, and P_{cav} for each depression are reported in the last three columns of Tab. 5.1.

The balance between P_{cav} and L_{cool} As discussed in Subsect. 1.2.3, a strong evidence for the self-regulated feedback loop is that the estimated mechanical power of the AGN is high enough to balance the radiative losses of the cooling ICM: comparisons between the cavity power and the cooling luminosity of the ICM show that P_{cav} roughly scales in proportion to L_{cool} (e.g., McNamara and Nulsen 2007, 2012). It is then interesting to compare our estimate of the cavities power with the X-ray luminosity of the cooling region. We over-plot our estimate for our system of cavities on Fig. 1.13 (left panel): the power of D1 and D2 is summed to obtain the total $P_{cav} = 3.0 \pm 0.5 \times 10^{43}$ erg s^{-1}, and we use $L_{cool} = (1.07 \pm 0.06) \times 10^{44}$ erg s^{-1} (the method used to obtain this parameter is in Subsect. 3.2.3). As is it possible to see from Fig. 5.2, the putative system of cavities in

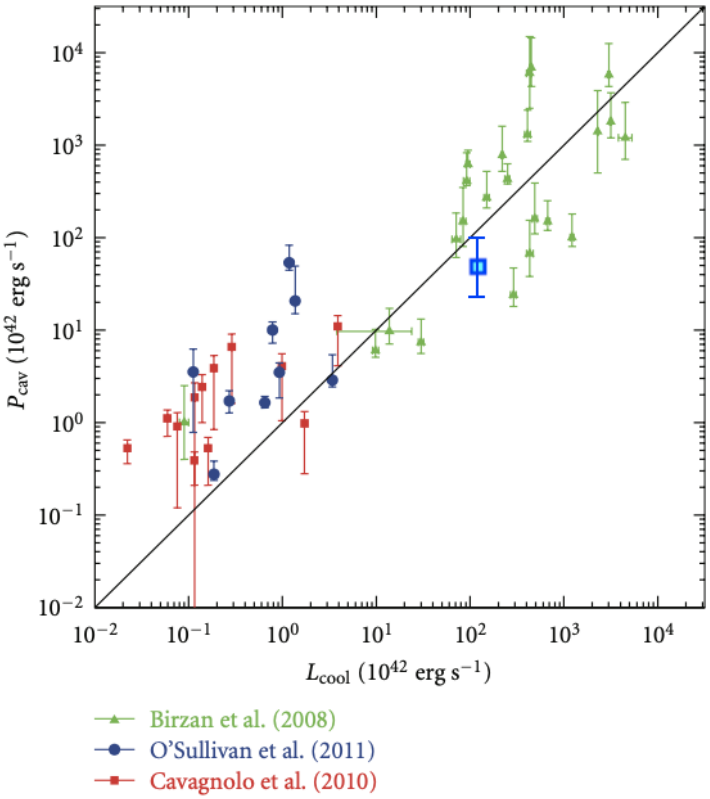

Figure 5.2: Cavity power of the central AGN vs the X-ray luminosity of the ICM inside the cooling region. Different symbols denote systems in different samples, while the diagonal line denotes $P_{cav} = L_{cool}$ (Gitti et al., 2012). The blue point represents the cavity system of A795.

A795 follows the distribution of the other galaxy clusters of the sample, indicating that if

the two depressions truly are cavities, their power is sufficient to offset radiative cooling, thus explaining the mismatch we found between the predicted and observed cooling rates.

5.1.2 Are the two X-ray depressions real cavities?

Considering the compactness of FR0s, it is unclear whether their jets are able to expand into the external medium and excavate cavities in the ICM. The two depressions in A795 are at a medium distance of $\approx$ 33 kpc (13.6") from the BCG: this separation is larger than the average size of FR0s at 1.4 GHz, that is $\sim 10 - 15$ kpc (Baldi et al., 2019b). Moreover, the FIRST observation did not detect 1.4 GHz radio emission corresponding to the two depressions. It is possible, however, that the structures are filled with an ageing electron population, emitting at lower frequencies. Therefore, we speculate that J0924+14 might have been able to produce these cavities in the past: considering the cavity age in Tab. 5.1, we can place a lower limit on the time that has passed since this event of $\Delta t \approx 3 - 4 \times 10^7$yr.

Detecting low frequency radio emission inside D1 and D2 would provide a strong evidence that they have been excavated by J0924+14 jets. Recently, Capetti et al. (2020a) have studied a sample of 66 FR0 at $z \leq 0.05$ observed by LOFAR[5] at 150 MHz; they found 12 extended sources, five of which have symmetric jets with total extent between 20 and 40 kpc, and three of which have a head-tail structure extending for $\sim$ 50 kpc (see Fig. 5.3). None of these sources was classified as extended in the FIRST images at 1.4 GHz. Therefore, it is not excluded that at lower frequencies FR0s can reach sizes comparable to the distance between J0924+14 and the two depressions we detected.

Unfortunately, high resolution, low frequency observation of A795 are not available. The GMRT observed this cluster at 150 MHz as part of the TGSS sky survey; in fact, we found evidences for a diffuse emission extending for $\sim$ 160 kpc around the cluster center, but the low resolution of this observation (the beam has a FWHM of 25" $\times$ 25"), compared to the angular size of our cavities ($\approx$ 5"), does not allow to investigate possible morphological connection with the two putative cavities. We discuss the properties and nature of this extended emission in the last section of this chapter.

In order to test the ability of J0924+14 to excavate the two observed depressions, we estimate the expected jet kinetic power ($P_{\rm jet,exp}$) from the radio luminosity of the galaxy's core, and compare it to the cavity power $P_{\rm cav}$. The true total mechanical power of the AGN would be $P_{\rm jet} \gtrapprox P_{\rm cav}$ (e.g. Gitti et al., 2012): as a consequence, the cavity power we measured for D1 and D2 has to be considered as a lower limit to the kinetic power required to excavate those depressions ($P_{\rm jet,X}$). If the expected jet kinetic power equals or exceed the X-ray measured cavity power, then our FR0 could have been able to inflate

[5]LOw Frequency ARray (Van Haarlem et al., 2013).

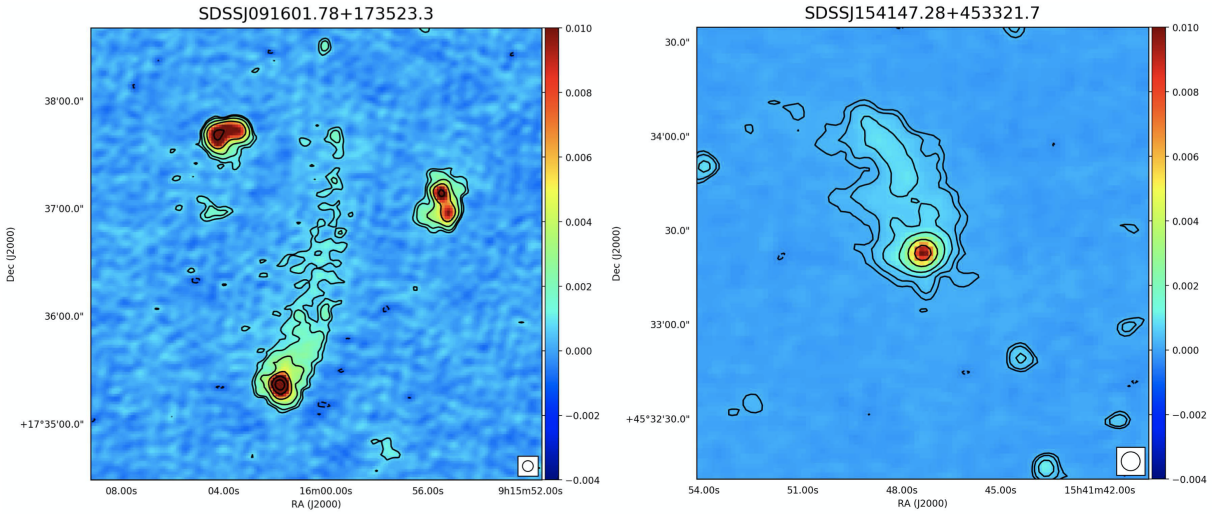

(a) **(b)**

Figure 5.3: LOFAR 150 MHz images of two extended FR0s at a resolution of 6"; the contours level are at -3,3,5,10,20,50,100 σ (the local r.m.s) (Capetti et al., 2020a).

radio bubbles and produce the observed depressions. Merloni and Heinz (2007) studied a sample of sub-Eddington[6] AGNs, and derived the following correlation between the observed radio core luminosity at 5 GHz and the jet kinetic power:

$$\log P_{\rm jet} = (0.54 \pm 0.09) \log L_{5\,\rm GHz} + 22.1^{+3.5}_{-3.5} \tag{5.3}$$

The observed radio core luminosity at 5 GHz of J0924+14 is $L_{5\,\rm GHz} = (4.52 \pm 0.05) \times 10^{40}$ erg s^{-1} (Kunert-Bajraszewska et al., 2010). By using the above relation we estimate a jet kinetic power of:

$$P_{\rm jet,exp} = (1.1 \pm 0.5) \times 10^{44}\,\rm erg/s \tag{5.4}$$

The use of this relation confirms that $P_{\rm jet,\,exp} \approx (1.1 \pm 0.5) \times 10^{44}$ erg s^{-1} $\gtrapprox P_{\rm cav} = (3.0 \pm 0.5) \times 10^{43}$ erg s^{-1}.

Merloni and Heinz (2007) noted that Eq.5.3 might be affected by boosting effects. Therefore, we also compute the intrinsic radio luminosity of the radio galaxy at 5 GHz, $L_{i,5\,\rm GHz}$, using the so-called *fundamental plane of black hole activity* (Merloni et al., 2003):

$$\log L_{i,5\,\rm GHz} = 0.60^{+0.11}_{-0.11} \log L_{\rm X} + 0.78^{+0.11}_{-0.09} \log M_{\rm BH} + 7.33^{+4.05}_{-4.07} \tag{5.5}$$

where $L_{\rm X}$ is the X-ray luminosity in the 2-10 keV band, and $M_{\rm BH}$ is the black hole mass. We use the 2-10 keV X-ray luminosity of Tab. 4.3 and the black hole mass of Tab. 4.4

[6]AGN with $L_{\rm acc}/L_{\rm Edd} \ll 1$, consistent with the measured values of Eddington-scaled accretion rate for FR0s (e.g. Torresi et al., 2018).

to compute the intrinsic radio luminosity, that is $L_{i,5\,\mathrm{GHz}} = (1.0 \pm 0.7) \times 10^{39}$ erg s^{-1}. Merloni and Heinz (2007) reported the following relation between $L_{i,5\,\mathrm{GHz}}$ and P_{jet}:

$$\log P_{\mathrm{jet}} = (0.81 \pm 0.11) \log L_{i,5\,\mathrm{GHz}} + 11.9^{+4.1}_{-4.4} \tag{5.6}$$

Using this alternative relation yields an expected jet kinetic power of $P_{\mathrm{jet,exp}} = (3.1 \pm 2.2) \times 10^{43}$ erg s^{-1}, which is lower than that of Eq. 5.4; however, it provides another evidence that $P_{\mathrm{jet,\,exp}} = (3.1 \pm 2.2) \times 10^{43}$ erg s^{-1} $\gtrapprox P_{\mathrm{cav}} = (3.0 \pm 0.5) \times 10^{43}$ erg s^{-1}. We conclude that the scenario where the AGN has a sufficient power to inflate the two observed depressions is energetically consistent.

We note that the two depressions are not symmetric with respect to the AGN: the radio lobes inflated by bipolar jets are expected to be approximately on opposite sides of the nucleus. We could speculate that the sloshing of the ICM has influenced the direction of motion of the two cavities, leading to the observed asymmetry. In fact, AGN-inflated radio bubbles are easily subject to gas motions and turbulence in the central regions of galaxy clusters (Morsony et al., 2010). The study of sloshing in A2495 by Pasini et al. (2019) seems relevant in this picture: they detected two generations of cavities, with the older pair displaying an asymmetry from the BCG similar to that of our cavities (Fig. 5.4).

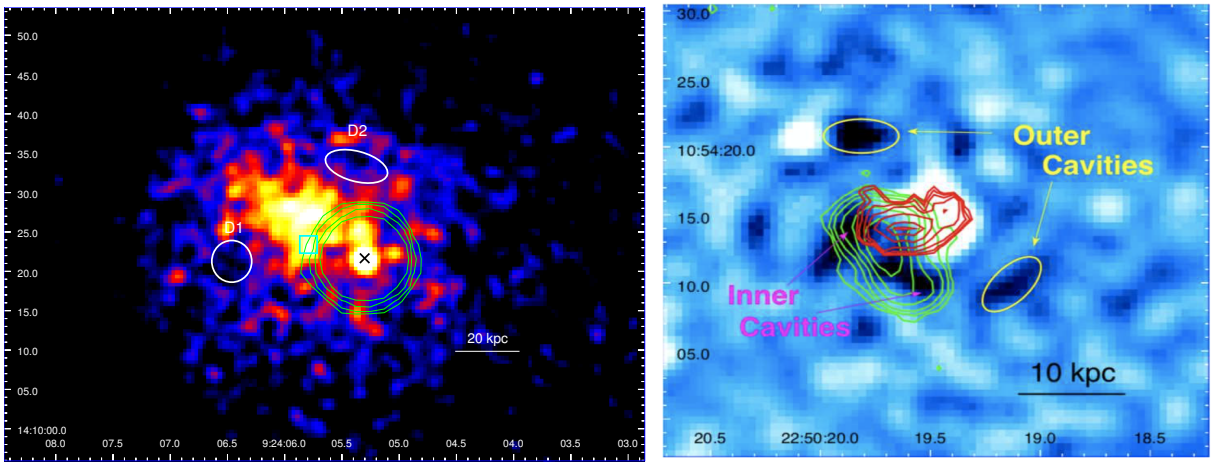

(a) **(b)**

Figure 5.4: Panel *a*: 0.5-2 keV image of the central regions of A795, Gaussian-smoothed with a kernel radius of 3 pixels; the white ellipses mark the position of the two putative cavities, the cyan box indicates the X-ray peak, and the black cross denotes the position of the AGN. The FIRST contours (green) are at 5, 10, 20, 40 × rms. Panel *b*: Residual image of A2495 showing the two cavity systems, with Hα contours (red) and 1.4 GHz radio contours (green) (Pasini et al., 2019).

By comparing the age difference between the two cavity systems and the sloshing timescale,

they argued that sloshing is regulating the activity of the central AGN. While we cannot explore this possibility, as we found only a pair of cavities, the scenario designed for A2495 might hold also for A795. In fact, the BCG in A2495 has a small radio size (≈ 14 kpc at 1.4 GHz), and they did not find evidences for radio emission coincident with the older cavities. Deeper X-ray observation combined with high-resolution, low frequency observation of A795 will be essential to probe the existence of multiple generations of cavities, possibly filled with an ageing electron population.

5.2 Sloshing in A795

The analysis of A795 has revealed a cold gas spiral wrapping around the cluster center; as reported in Sec. 1.3, the presence of sloshing cold fronts in cool core clusters has been interpreted as the consequence of a perturbation of the ICM, possibly by a minor merger or an off-center passage of a small galaxy cluster/group. The identification of the perturber usually requires tailored simulations (e.g. Roediger et al. 2011, 2012; Doubrawa et al. 2020), but with deep joint *Chandra-XMM-Newton* observations, some tentative direct identifications have been performed (e.g. Su et al. 2017). The depth of our *Chandra* observation of A795 does not allow to perform this kind of analysis; instead, we aim to estimate the *sloshing age* (i.e. the time that has passed since the perturbation has been set) from the thermodynamical analysis we performed on the ICM: the first part of this section reports our results. In the second part, we discuss the effects of the gas oscillation on the radiative cooling efficiency of the gas, and the possible heating provided by sloshing.

5.2.1 Sloshing timescale

In order to obtain a first, lower limit estimate on the sloshing timescale we compute the free fall time $t_{\rm fall}(r)$, defined as:

$$t_{\rm fall}(r) = \sqrt{\frac{2r^3}{GM(r)}} \tag{5.7}$$

where r is the distance from the cluster center, and $M(r)$ is the total mass profile.
This can be seen as the minimum time that is needed for the displaced gas at distance r from the X-ray peak to return to the center, if there was no outward pressure or other forces to counteract gravity. We produce the $t_{\rm fall}$ profile of Fig. 5.5, which indicates that the ICM at different radii would take $\sim$100 Myr to $\sim$250 Myr to collapse to the center. However, we expect the true time scale that regulates the sloshing motion to be higher

than the free fall time, as the entropy gradient is likely to induce an oscillation of the gas around its equilibrium position, and not a direct collapse to the center.

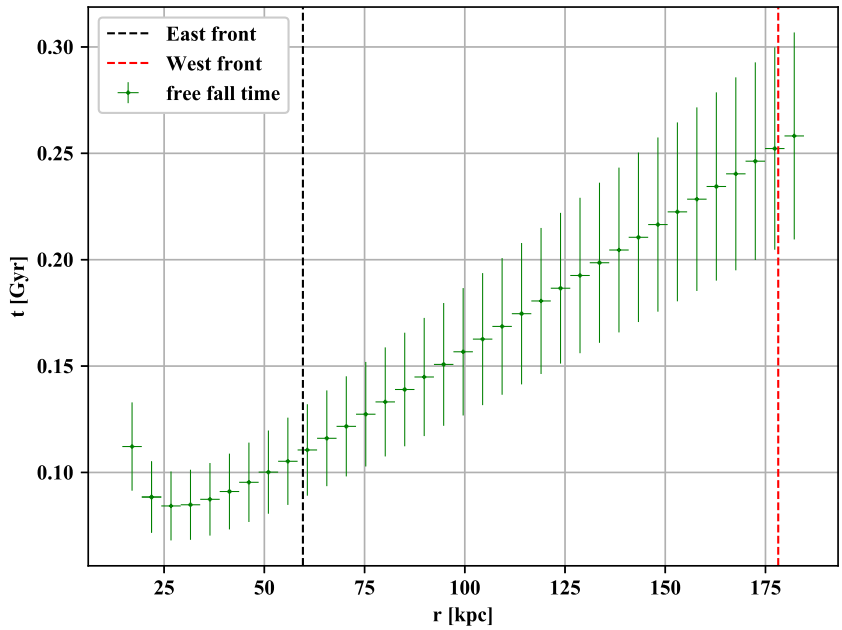

Figure 5.5: Free fall time profile of A795; the distance of each cold front from the cluster center is marked with a vertical dashed line.

Indeed, several studies of the sloshing age have considered that the motion of the gas around the cluster center can be approximated as an oscillating flow in a static, stable environment (e.g. Churazov et al. 2003; Su et al. 2017; Kolokythas et al. 2020); considering this, the approach to obtain t_{slosh} consists in calculating the Brunt-Väisälä frequency $\omega_{\rm BV}$ at each radius r (Balbus and Soker, 1990):

$$\omega_{\rm BV}(r) = \sqrt{\frac{3GM(r)}{5r^3}\frac{d\ln K}{d\ln r}} \tag{5.8}$$

where $K = kT/n_{\rm e}^{2/3}$ is the gas entropy, and $M(r)$ is the total mass within r; the sloshing timescale is then given by $t_{\rm slosh} = 2\pi/\omega_{\rm BV}$. Since the frequency is a function of the distance from the cluster center, the gas at different radii is expected to slosh on different timescales: according to Churazov et al. (2003), this produces several asymmetric structures at the same time on either side of the core (the observed cold fronts).
We use the hydrostatic mass profile computed in subsec. 3.2.4 for $M(r)$. For the entropy gradient $d\ln K/d\ln r$, we fit the entropy profile of the deprojected spectral analysis in the

log-log space using BCES; the best fit linear regression is:

$$\log(K) = [0.92 \pm 0.08] \log(r) + [-28.15 \pm 1.77] \tag{5.9}$$

We substitute the slope of the $\log K - \log r$ relation in Eq. 5.8; the resulting sloshing timescale profile $t_{\rm slosh}(r) = 2\pi/\omega_{\rm BV}(r)$ is presented in Fig. 5.6.

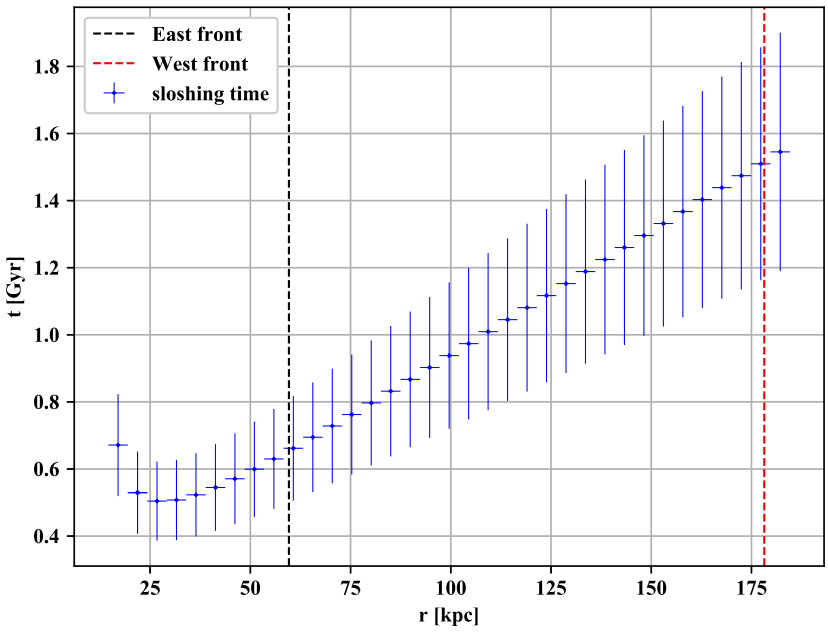

Figure 5.6: Sloshing timescale profile of A795; the distance of each cold front from the cluster center is marked with a vertical dashed line.

We note that $t_{\rm slosh}$ raises going far from the center; by considering the distance of the two cold fronts, we can infer the time that has passed since the creation of each discontinuity:

- the inner, east cold front is at a distance of 59.6 ± 0.3 kpc from the cluster center. This suggests a sloshing time of $t_{\rm slosh} \approx 0.66 \pm 0.16$ Gyr.
- the outer, west cold front is situated at 178.2 ± 2.2 kpc from the X-ray peak. The resulting age is $t_{\rm slosh} \approx 1.51 \pm 0.35$ Gyr.

As expected, the sloshing time scale computed with the Brunt-Väisälä frequency $\omega_{\rm BV}$ is higher than the free fall time, specifically by a factor of $\approx 5 - 6$ (we note that Su et al. 2017 found a similar difference between the two estimates in the Fornax cluster). We highlight that the sloshing time scale at the distance of the two cavities (≈ 0.5 Gyr) is larger than the age of the two depressions, thus suggesting that the observed shape of D1 and D2 has not been influenced by the gas motions.

To test whether our estimate is reasonable, we compare our results with the simulations of sloshing by Roediger et al. (2011): the ages of the simulated cold fronts at ~ 60 kpc and ~ 140 kpc are approximately 0.7 Gyr and 2 Gyr; these distances and timescales are comparable to those of our east and west cold fronts.
A further indication that our timescale estimate can be considered as a good approximation of the sloshing age is given by the mean $t_{\rm slosh}$ within the sloshing region[7], that is 0.96 ± 0.22 Gyr. This could be considered as the minimum time that has passed since the oscillation has been set (Churazov et al., 2003). Indeed, simulations of sloshing have found that cold fronts typically develop after ≈ 1 Gyr from the start of the perturbation (e.g. Roediger et al. 2011; ZuHone et al. 2012b; ZuHone and Roediger 2016), a value comparable with our mean $t_{\rm slosh}$.
We conclude that the event which has offset the ICM from its equilibrium configuration has occurred more than ≈ 1 Gyr ago, and that sloshing is responsible for the formation of the two cold fronts in A795.

5.2.2 Heating by sloshing

As reported in Sect. 1.3, it is possible that as the gas sloshes, the mechanical, turbulent energy of the moving fronts might be converted into heat. For Perseus, Churazov et al. (2003) estimated that the mechanical energy of cold fronts represents the 10-20% of the ICM thermal energy; in Abell 1795 the dissipation of the gravitational potential energy of the gas would account for about half of the gas thermal energy (Markevitch et al., 2001). This suggests that sloshing might be an additional mechanism - besides AGN heating - capable of offsetting radiative cooling.
Following the approach of Su et al. (2017) for the cold fronts in the Fornax cluster, here we aim to understand whether sloshing in A795 could represent a viable source of additional heating: only if the sloshing time scale is smaller than the typical cooling time of the ICM, the conversion of mechanical energy into heating is expected to be efficient. In Fig. 5.7 we plot the cooling and sloshing time profiles (panel *a*), and the ratio between the two as a function of radius (panel *b*).
Within the cooling radius, the sloshing time scale is $\approx 4 - 12$ times shorter than the cooling time, implying that if the turbulence induced by sloshing in A795 is actually being converted into thermal energy, the process is efficient.

[7]Here we define the sloshing region as the circle centered on the X-ray peak with radius equal to the distance of the outermost cold front, so 73.4" (178.2 kpc).

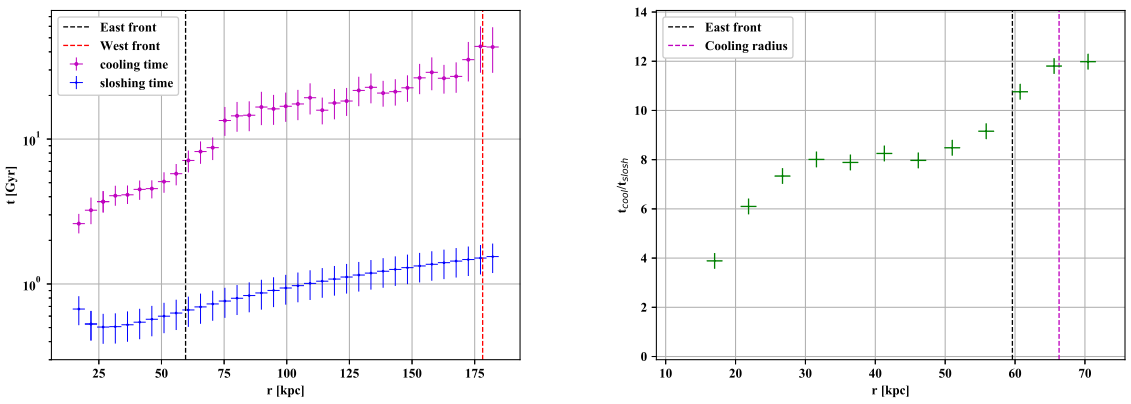

(a) **(b)**

Figure 5.7: Panel *a*: Sloshing time and cooling time profile in A795 within the radius of the outermost, west cold front. Panel *b*: Radial profile of the ratio $t_{\rm cool}/t_{\rm slosh}$.

5.3 Extended radio emission: a mini-halo detection?

In this section we present the results of our archival search for radio data of A795. We found observations of this cluster in the data archives of TGSS, GLEAM and VLSS: these low frequency sky surveys provide radio maps and flux measurements of their target, which we use to characterize the radio emission in this galaxy cluster.

5.3.1 Maps of diffuse radio emission

The TGSS data at 150 MHz, with a resolution of 25"×25" and a median noise of $\sigma \sim 3.5$ mJy/beam, represent the highest resolution, low frequency radio observation of A795: it has measured a total flux of $S_\nu[150\,\mathrm{MHz}] = 1186 \pm 118$ mJy, and the radio contours are shown in Fig. 5.8 (panel *a*). The emission is centered on the BCG, and has a largest linear size of 176.5" (428.8 kpc)[8]. The resolution of the TGSS does not allow for a detailed characterization of the shape of the diffuse emission, but the radio contours show that the extension is significant, with a roundish shape at the center and two smaller protrusions in the north and south-west directions. A similar situation emerges from the VLSS images (Fig. 5.8, panel *b*), which have a resolution of 80" and an average rms map sensitivity of $\sigma \sim 130$ mJy/beam at 74 MHz: the shape of the extended emission resembles that of the TGSS, but the lower spatial resolution results in a worst characterization of the sub-components; the total flux is $S_\nu[74\,\mathrm{MHz}] = 4180 \pm 470$ mJy.
In addition to the 74 MHz and 150 MHz observations, GLEAM survey reports total flux measurements of A795 across 76-227 MHz, which can help us to constrain the shape of the

[8]Measured from the 3σ contour.

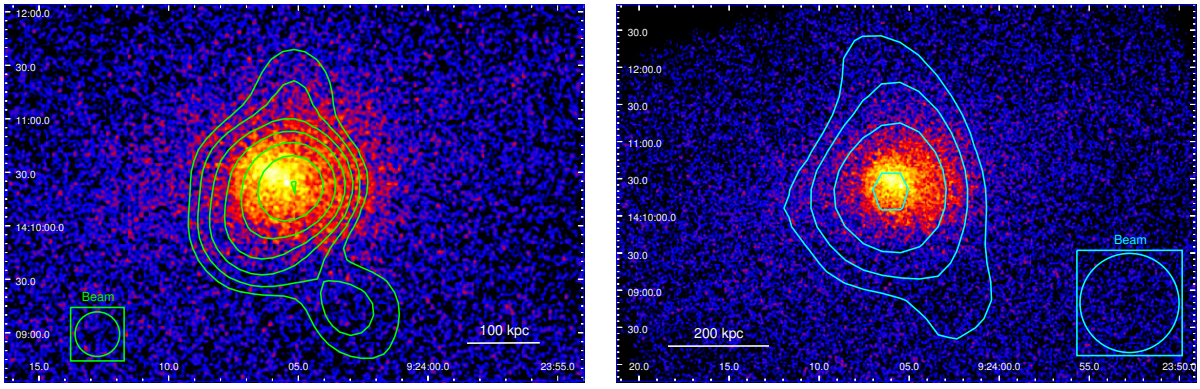

(a) (b)

Figure 5.8: 0.5-7 keV images of A795, Gaussian-smoothed with kernel radius 3 pixels. The green contours at 3, 6, 12, 24, 48, 96, 192 × rms are from the TGSS at 150 MHz (panel *a*), while the cyan contours at 3, 6, 12, 24 × rms are from the VLSS at 74 MHz (panel *b*).

low frequency spectrum. The spatial resolution of the radio maps is 160", which prevents us from obtaining further information on the extension and shape of the radio emission.

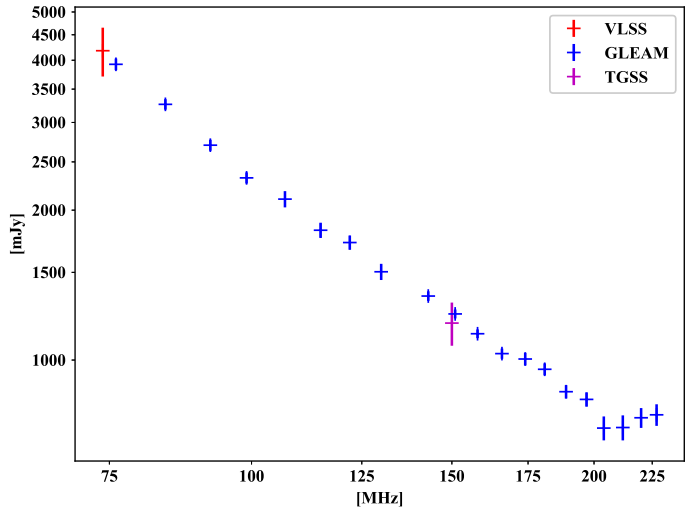

Figure 5.9: Low frequency spectrum of archival radio data for A795.

In Fig. 5.9 we plot the spectrum of A795, by combining the low frequency measurements of VLSS, GLEAM and TGSS; the data points frequencies and fluxes are available in the Appendix. As it is possible to see, from 74 MHz to 227 MHz the spectrum shows a single steep component. We claim that the extended radio emission in A795 is due to the possible presence of a mini-halo in the galaxy cluster core, possibly related to the two cold fronts. In the next paragraphs, we argue that the shape of the radio emission is

consistent with the properties of known mini halos, and we show that the low frequency fluxes exceed those expected from the AGN in the BCG, thus indicating that an extended emission is indeed present.

5.3.2 Morphological features

In order to measure the size of the extended radio emission we consider the TGSS images, which provide the best angular resolution among the low frequency observations of A795. Following the approach of Giacintucci et al. (2013), we measure the maximum and minimum radius of the 150 MHz emission from the 3σ contour, and we combine them to obtain an average radius of the diffuse emission with:

$$R = \sqrt{R_{\rm max} \times R_{\rm min}} \tag{5.10}$$

The resulting size of the mini halo is $R = \sqrt{88.3'' \times 50.4''} = 66.7''$ ($\sim$162 kpc). This value is consistent with typical mini-halo sizes of $\approx 50 - 200$ kpc (e.g. Cassano et al. 2008; Giacintucci et al. 2013; Gitti et al. 2018; Giacintucci et al. 2019), and the roundish shape resembles the typical shape of mini halos.

It has been proposed that the reacceleration for the electrons responsible for the radio emission is due to turbulent motion in the cool core of galaxy clusters (e.g. Gitti et al. 2002; ZuHone et al. 2012a, 2015; Bravi et al. 2016); in this picture, the sloshing motion of the ICM might be a reasonable source of reacceleration: in sloshing clusters with a mini halo, the synchrotron emission appears co-spatial with the sloshing region, and confined within the detected cold fronts (e.g. Hlavacek-Larrondo et al. 2013; Giacintucci et al. 2019). In Fig. 5.10 we over-plot the TGSS radio contours on the β-model residual image of A795: the radio emission is approximately co-spatial with the sloshing region; the contours nicely follow the shape of the west front, and on the east side the mini halo appears to be confined within the negative residual spiral. We then conclude that the shape of the extended emission in A795 is consistent with the typical morphology of radio mini halos in cool core clusters.

We also consider the possibility that the two protrusions on the north and south-east side might not belong to the mini halo: given their roundish shape and their position at approximately opposite sides of the cluster center, we wonder if they could be radio lobes produced by a past activity of the AGN in the BCG. In order to be detected only at 74 MHz and 150 MHz (the FIRST images at 1.4 GHz do not show evidence for emission corresponding to the two substructures), the radio plasma would have to be very old, possibly with an ultra-steep spectrum. The evolutionary properties of FR0s have not been fully explored yet, but it seems unlikely that they experienced a very old radio

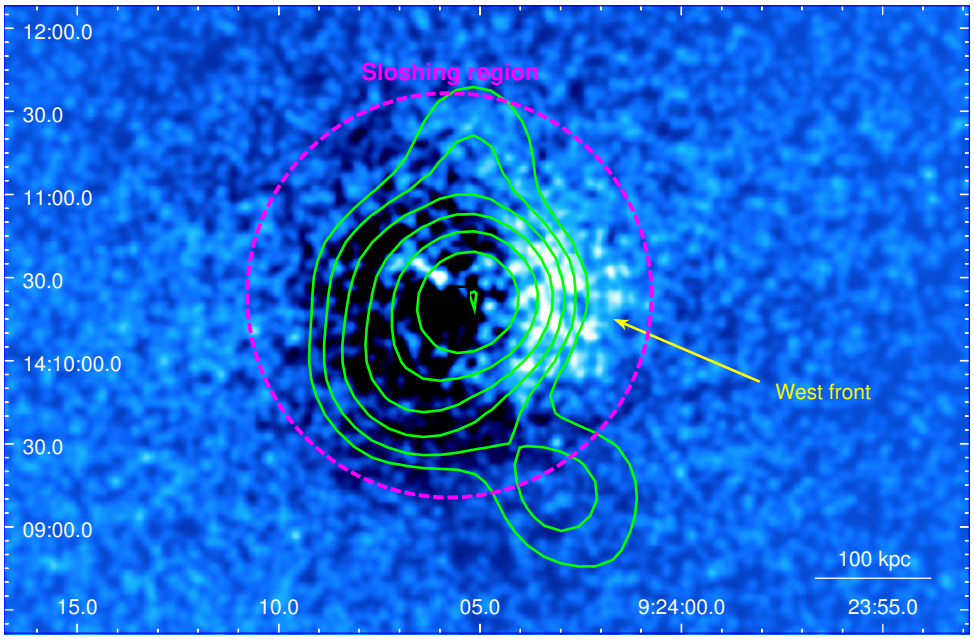

Figure 5.10: Residual image of A795, with TGSS radio contours (green) as in Fig. 5.8. The dashed magenta circle indicates the extension of the sloshing region, defined as the circle with radius equal to the distance of the outermost cold front from the cluster center.

activity that was able to produce extended emission on scales of a few $\sim$ 100 kpc (e.g., Capetti et al. 2019). Moreover, restarted sources typically display high Eddington-scaled accretion rates, i.e. > 0.01 (e.g. Wu 2009; Bruni et al. 2019), while for J0924+14 we found $L_{\rm acc}/L_{\rm Edd} = 3.8{\times}10^{-3}$. It is also possible that the radio emission arises from unresolved (or barely-resolved) background sources, such as radio galaxies. Unfortunately, the literature search for objects with coordinates comparable to that of the two lobes returned no evidences for the presence of radio galaxies.

Another indication that the two "bubbles" might belong to the mini halo, is that they coincide with regions of enhanced X-ray surface brightness (see Fig. 5.10). A past activity of the AGN would have left signs in the ICM, in particular we should expect to find X-ray cavities coincident with the two extensions. However, the residual image of A795 reveals that the bubbles (especially the northern one) do not coincide with any depression in surface brightness. In addition to this, the two cavities of Sect. 3.1 are located north-east of the radio galaxy, which is also the direction of the jet observed at 5 GHz (see Fig. 4.1); on the contrary, the position of the two extended bubbles does not match the jet direction of motion: while a change in the jet direction is not impossible, it adds a further complication to the interpretation of the two bubbles as radio lobes.

We conclude that the two extensions have unlikely originated from a past radio activity of the BCG, and they probably belong to the extended emission centered on the cluster, which we interpret as a candidate mini halo.

5.3.3 Low frequency spectral index

To conclude, we perform a measurement of the spectral index at low frequencies: this could be useful for future studies of the extended radio emission. We anticipate that due to the relatively large errors of surveys flux measurements, we expect the spectral index to be associated with larger uncertainties. Moreover, the *uv* plane coverage and the flux measurements extraction regions are different from one survey to the other.
A common difficulty regarding spectral studies of mini halos consists in accurately separating the diffuse emission from that of the AGN in the brightest cluster galaxy (e.g. Van Weeren et al. 2014). To accomplish this task, we proceed with the following steps:

- Considering a single power-law spectrum $S_\nu \propto \nu^{-\alpha}$, we calculate the spectral index of the emission of J0924+14 between 5 GHz (MERLIN, Kunert-Bajraszewska et al. 2010) and 8.4 GHz (VLA, Hogan et al. 2015): at these two frequencies the radio galaxy has been resolved, therefore we expect the resulting flux measurements not to be affected by the extended emission.

- We extrapolate the AGN emission to the lowest and highest frequency of the GLEAM, which measured 3925.4 ± 105.1 mJy at 76 MHz and 776.3 ± 38.7 mJy at 227 MHz: even though the extended emission is poorly resolved by the GLEAM survey, the flux measurements at different frequencies have been performed using the same extraction region; after the extrapolation, we derive the residual fluxes which would arise from the mini halo emission at 76 MHz and 227 MHz.

- We use the residual fluxes to compute the low frequency spectral index of the diffuse radio emission.

The application of this procedure has produced the results shown in Tab. 5.2. We measure mini halo fluxes of $S_{\rm MH}(227\,{\rm MHz}) = 455.2 \pm 124.4$ mJy and $S_{\rm MH}(76\,{\rm MHz}) = 3035.2 \pm 423.2$ mJy: the corresponding powers are $P_{\rm MH}(227\,{\rm MHz}) = 22.5 \pm 4.3 \times 10^{24}$ W/Hz and $P_{\rm MH}(76\,{\rm MHz}) = 152.7 \pm 15.7 \times 10^{24}$ W/Hz, respectively. These values agree with typical mini halos low frequency power measured by LOFAR (e.g., Savini et al., 2019) VLA (e.g., Richard-Laferrière et al., 2020) and GMRT (e.g., Murgia et al., 2010; Van Weeren et al., 2014).
The core spectral index is $\alpha_{\rm c} = \alpha_{5-8.4\,{\rm GHz}} = 0.93 \pm 0.09$, and the diffuse emission spectral index is $\alpha_{\rm MH} = \alpha_{76-227\,{\rm MHz}} = 1.73 \pm 0.86$. As expected, the associated uncertainty is quite large; nevertheless, our estimate for $\alpha_{\rm MH}$ is consistent with typical mini halos spectral indices (e.g. Giacintucci et al. 2013, 2019) - albeit a bit steeper.
We conclude that the extended radio emission in A795 is a candidate mini halo, probably connected to the sloshing motions of the ICM. Future LOFAR observations at low

$S_{c,\ 5GHz}$	$S_{c,\ 8.4GHz}$	α_c	S^a_{MH}	P^b_{MH}	S^b_{MH}	P^d_{MH}	α_{MH}
$18.0^{+0.2}_{-0.2}$	$11.1^{+0.1}_{-0.1}$	$0.93^{+0.09}_{-0.09}$	$455.2^{+124.4}_{-124.4}$	$22.5^{+4.3}_{-4.3}$	$3035.2^{+432.2}_{-432.2}$	$152.7^{+15.7}_{-15.7}$	$1.73^{+0.86}_{-0.86}$

Table 5.2: Parameters used to determine the spectral index of the diffuse emission between 76 MHz and 227 MHz, and resulting spectral indices for the core (α_c) and the diffuse emission (α_{MH}), respectively.
[a] Residual flux in mJy at 227 MHz obtained by subtracting from the total flux the estimated core contribution.
[b] Mini halo power at 227 MHz, in units of [10^{24} W/Hz].
[c] Residual flux in mJy at 76 MHz obtained by subtracting from the total flux the estimated core contribution.
[d] Mini halo power at 76 MHz, in units of [10^{24} W/Hz].

frequency, and with a high angular resolution would greatly help us to confirm or reject this hypothesis.

Chapter 6

Conclusions

In this thesis work we unveiled for the first time the X-ray properties of Abell 795, a weakly cool core galaxy cluster displaying signs of dynamical disturbances. We further explored the relation between the FR0 hosted in the BCG and the surrounding environment. Here we summarize our main results.

- We determined the global properties of the ICM in A795: within 405 kpc from the cluster center, we measured a metallicity of 0.38 ± 0.05 $Z_{\odot}$, a temperature $kT = 4.6 \pm 0.1$ keV, and a luminosity $L_{\mathrm{X,\ 2\text{-}10\ keV}} = 2.27 \times 10^{44}$ erg s^{-1}. The total hydrostatic mass enclosed within this radius is $M_{\mathrm{tot}} = (9.9 \pm 3.7) \times 10^{13}\, M_{\odot}$. From the spatially-resolved spectral analysis of the ICM we deduced that A795 is a weakly cool core cluster, with cooling time of $t_{\mathrm{cool}} < 7.7$ [Gyr] inside a cooling radius $r_{\mathrm{cool}} = 66 \pm 3$ kpc.

- We discovered a cool ICM spiral in A795, which indicates that the gas is sloshing: this mechanism is responsible for the formation of the two observed surface brightness discontinuities, and explains the offset between the X-ray peak and the brightest cluster galaxy. The spectral study of the two edges has confirmed their cold fronts nature: for the east front we measured a temperature ratio $T_{\mathrm{out}}/T_{\mathrm{in}} = 1.84 \pm 0.62$, a density ratio of $n_{\mathrm{in}}/n_{\mathrm{out}} = 2.33 \pm 0.32$ and a pressure ratio $P_{\mathrm{in}}/P_{\mathrm{out}} = 1.26 \pm 0.54$, while the west front has $T_{\mathrm{out}}/T_{\mathrm{in}} = 1.74 \pm 0.73$, $n_{\mathrm{in}}/n_{\mathrm{out}} = 1.91 \pm 0.16$, and $P_{\mathrm{in}}/P_{\mathrm{out}} = 1.09 \pm 0.71$.

- By computing the timescale over which the gas oscillates at each radius, we inferred that the perturbation of the ICM has been set $\gtrapprox 1$ Gyr ago. Moreover, since the ratio between the cooling time and the sloshing timescale is ≈ 10 inside r_{cool}, we speculated that if the mechanical energy of the cold fronts is converted into thermal energy (thus concurring to the heating of the ICM), this process is efficient.

- The 150 MHz archival data for this cluster revealed the presence of a diffuse, extended radio emission: the low frequency flux of this component exceeds the flux extrapolated from the high frequency (5-8 GHz) emission of the central AGN; considering this finding, and the roundish shape of the extended emission (with $R = 66.7'' \approx 162$ kpc), we classified it as a candidate mini halo. At 227 MHz, the mini halo flux is $S_{\rm MH,\ 227} = 455.2 \pm 124.4$ mJy, and the resulting power is $P_{\rm MH,\ 227} = 22.5 \pm 4.3 \times 10^{24}$ W/Hz. At 76 MHz the diffuse flux is $S_{\rm MH,\ 76} = 3035.2 \pm 423.2$ mJy, and the resulting power is $P_{\rm MH,\ 76} = 152.7 \pm 15.7 \times 10^{24}$ W/Hz. We estimated a low frequency spectral index of the candidate mini-halo of $\alpha_{\rm MH} = 1.73 \pm 0.86$ between 76 MHz and 227 MHz. It is possible that the electrons responsible for the radio emission have been re-accelerated by the turbulent motion of the ICM, since the diffuse source and the sloshing region are approximately co-spatial.

- The X-ray emission of J0924+14, the FR0 at the center of A795, is typical of radio loud AGN powered by radiatively inefficient, advection dominated accretion flows: we measured a steep photon index $\Gamma = 2.45^{+0.33}_{-0.30}$, and an Eddington-scaled accretion rate of $L_{\rm acc}/L_{\rm Edd} = 3.8 \times 10^{-3}$. In order to understand whether the environment is critical for explaining the radio compactness of this source, we compared the temperature, density, and dynamics of the surrounding ICM with those of ICM around typical FRIs in brightest cluster galaxies, and found similar values: we concluded that the environment alone cannot explain the observed radio size of this new class of sources, and that an intrinsic jet weakness is likely necessary.

- We identified two putative cavities at ≈ 33 kpc from the central AGN: by measuring their power ($P_{\rm cav} = (3.0 \pm 0.5) \times 10^{43}$ erg s^{-1}) and comparing it to the bolometric luminosity within the cooling region ($L_{\rm cool} = (1.07 \pm 0.06) \times 10^{44}$ erg s^{-1}), we found that these cavities might be able to offset and reduce the cooling efficiency in A795.

- Although it is not clear whether FR0s' jets are able to excavate cavities in the ICM, the jet kinetic power of the FR0 in A795, $P_{\rm jet} = (3.1 \pm 2.2) \times 10^{43}$ erg s^{-1}, equals $P_{\rm cav}$: considering this, we argued that the central AGN could have had the power to produce the two observed depressions.

This is the first X-ray dedicated study of A795 and of the link between this cluster and the central FR0 radio galaxy. Future multi-wavelength studies will surely provide additional clues on the properties of this cluster and on the interaction between the central AGN and the surrounding environment. In particular, deeper X-ray observations of this cluster and possibly tailored simulations will allow to better characterize the sloshing dynamics. Future LOFAR high resolution observations of A795 will be also essential to perform a

detailed study of the extended emission and to explore the low frequency emission of the central FR0.
We also note that the radio galaxy J0924+14 is not the unique FR0 in a cluster of galaxies. Therefore, a comparison of the central and environmental properties of other FR0s in clusters will be useful to confirm our results and to better characterize the behaviour of this new class of radio sources.

Appendix A

Radial spectral analysis: additional results

In the first table of this appendix, we report the results of the fit with a **tbabs∗(apec+apec)** model to the six annuli used for the projected radial analysis of thermodynamic variables presented in Sect. 3.2: we fixed the abundance parameters of the second apec to the value of the first one, and let the other parameters free to vary. The last two columns report the f-test value and probability for the addition of the second thermal component. In the second table, we list the fluxes and luminosities for every annulus of the deprojected spectral analysis of A795.

	kT_1 [keV]	kT_2 [keV]	Z [$Z_\odot$]	$norm_1$ [10^{-4}]	$norm_2$ [10^{-4}]	χ^2/D.o.f.	F-test	P^b
1	$0.43^{+0.14}_{-0.15}$	$3.85^{+0.18}_{-0.17}$	$0.86^{+0.17}_{-0.15}$	$0.13^{+0.11}_{-0.05}$	$9.18^{+0.20}_{-0.43}$	119.8/112 (1.07)	1.46	0.24
2	< 12.8	$2.97^{+0.54}_{-0.31}$	$0.57^{+0.17}_{-0.15}$	$3.88^{+1.16}_{-1.43}$	$7.73^{+0.98}_{-1.65}$	99.0/125 (0.79)	3.91	0.02
3	< 6.84	$4.33^{+1.05}_{-2.28}$	$0.14^{+0.12}_{-0.11}$	< 9.06	$7.08^{+4.36}_{-4.57}$	135.3/130 (1.04)	0.16	0.69
4	<8.61	$4.19^{+0.58}_{-1.05}$	<0.73	$3.56^{+7.16}_{-3.19}$	$7.63^{+3.22}_{-7.45}$	135.8/137 (0.99)	0.58	0.56
5	$5.37^{+0.41}_{-0.33}$	< 3.7	$0.24^{+0.15}_{-0.14}$	$11.85^{+0.04}_{-0.04}$	< 0.03	154.6/154 (1.01)	0.75	0.48
6	$5.37^{+0.55}_{-0.43}$	$0.86^{+0.35}_{-0.32}$	< 0.30	$13.45^{+0.05}_{-0.10}$	$0.02^{+0.15}_{-0.01}$	176.7/187 (0.95)	0.78	0.46

Table A.1: This table contains the results of the fit with a **tbabs∗(apec+apec)** to the spectra obtained from the six circular annuli (described in Sect. 3.2) centered on the X-ray peak of A795.
[a] Inner and outer radius of the annulus in kpc (arcseconds).
[b] F-test probability.

	F[a] 0.1 - 2.4 keV	L[b] 0.1 - 2.4 keV	F[a] 2 - 10 keV	L[b] 2 - 10 keV	F[a] 0.1 - 100 keV	L[b] 0.1 - 100 keV
1	7.78	3.64	5.28	2.85	12.66	6.38
2	8.12	3.78	6.38	3.38	14.33	7.22
3	8.00	3.72	6.91	3.61	15.03	7.57
4	8.57	3.99	7.24	3.80	15.78	7.95
5	8.64	4.01	7.64	3.98	16.47	8.30
6	9.89	4.60	8.15	4.28	18.06	9.09

Table A.2: Fluxes and luminosities in different bands of the six annuli used for the deprojected analysis of Sect. 3.2. The first two columns are in the range 0.1 - 2.4 keV (*ROSAT* band), the third and fourth columns are in the 2 - 10 keV band, and the last two columns are the bolometric values (0.1 - 100 keV).
[a] in units of 10^{-13} erg s^{-1} cm^{-2}.
[b] in units of 10^{43} erg s^{-1}.

Appendix B

Archival radio data for A795

Survey	ν [MHz]	$S^a_{\rm peak}$	$\sigma^b_{\rm peak}$	$S^c_{\rm tot}$	$\sigma^d_{\rm tot}$
VLSS	74	3098	109	4180	470
GLEAM	76	3930	105	3925	105
	84	3268	79	3262	79
	92	2707	69	2700	69
	99	2428	60	2322	60
	107	2111	79	2104	79
	115	1829	65	1823	64
	122	1728	57	1722	57
	130	1510	56	1504	56
	143	1352	30	1344	30
	151	1245	26	1238	26
	158	1137	23	1129	23
	166	1038	24	1030	24
	174	1013	30	1005	29
	181	966	27	958	26
	189	872	27	864	27
	197	842	28	834	28
	204	737	41	730	40
	212	739	43	732	42
	220	774	36	766	35
	227	785	39	776	39
TGSS	150	733	74	1186	118

Table B.1: Radio flux measurements of A795 from the surveys VLSS, GLEAM, TGSS.
[a] Peak flux density of the source, in mJy/beam.
[b] RMS uncertainty for the peak flux, in mJy/beam.
[c] Total flux of the radio source, in mJy.
[d] RMS uncertainty for the total flux, in mJy.

Bibliography

Abell, G. O. (1958). The distribution of rich clusters of galaxies. *The Astrophysical Journal Supplement Series*, 3:211.

Abell, G. O., Corwin Jr, H. G., and Olowin, R. P. (1989). A catalog of rich clusters of galaxies. *The Astrophysical Journal Supplement Series*, 70:1–138.

Akritas, M. G. and Bershady, M. A. (1996). Linear regression for astronomical data with measurement errors and intrinsic scatter. *arXiv preprint astro-ph/9605002*.

Aktekin, E. and Hudaverdi, M. (2014). The analysis of temperature and metallicity for A1831 observations of SUZAKU. *cosp*, 40:E1–4.

Alam, S., Albareti, F. D., Prieto, C. A., Anders, F., Anderson, S. F., Anderton, T., Andrews, B. H., Armengaud, E., Aubourg, É., Bailey, S., et al. (2015). The eleventh and twelfth data releases of the Sloan Digital Sky Survey: final data from SDSS-III. *The Astrophysical Journal Supplement Series*, 219(1):12.

Allen, S. and Fabian, A. (1997). The spatial distributions of cooling gas and intrinsic X-ray-absorbing material in cooling flows. *Monthly Notices of the Royal Astronomical Society*, 286(3):583–603.

Allen, S. W., Evrard, A. E., and Mantz, A. B. (2011). Cosmological parameters from observations of galaxy clusters. *Annual Review of Astronomy and Astrophysics*, 49:409–470.

Arnaud, M., Pratt, G., Piffaretti, R., Böhringer, H., Croston, J., and Pointecouteau, E. (2010). The universal galaxy cluster pressure profile from a representative sample of nearby systems (REXCESS) and the YSZ–M500 relation. *Astronomy & Astrophysics*, 517:A92.

Asai, N., Fukuda, N., and Matsumoto, R. (2005). Three-dimensional MHD simulations of X-ray emitting subcluster plasmas in cluster of galaxies. *Advances in Space Research*, 36(4):636–642.

Asai, N., Fukuda, N., and Matsumoto, R. (2007). Three-dimensional magnetohydrodynamic simulations of cold fronts in magnetically turbulent ICM. *The Astrophysical Journal*, 663(2):816.

Asplund, M., Grevesse, N., Sauval, A. J., and Scott, P. (2009). The chemical composition of the Sun. *Annual review of astronomy and astrophysics*, 47.

Bahcall, N. A. (1999). Clusters and superclusters of galaxies. *Formation of Structure in the Universe/Ed. by A. Dekel, JP Ostriker. Cambridge: Cambridge University Press*, page 135.

Bahcall, N. A. and Lubin, L. M. (1993). Resolving the beta-discrepancy for clusters of galaxies. *arXiv preprint astro-ph/9311061*.

Balbus, S. A. and Soker, N. (1990). Resonant excitation of internal gravity waves in cluster cooling flows. *The Astrophysical Journal*, 357:353–366.

Baldi, R., Capetti, A., and Massaro, F. (2018). FR0CAT: a FIRST catalog of FR0 radio galaxies. *Astronomy & Astrophysics*, 609:A1.

Baldi, R. D. and Capetti, A. (2008). Recent star formation in nearby 3CR radio-galaxies from UV HST observations. *Astronomy & Astrophysics*, 489(3):989–1002.

Baldi, R. D. and Capetti, A. (2010). Spectro-photometric properties of the bulk of the radio-loud AGN population. *Astronomy & Astrophysics*, 519:A48.

Baldi, R. D., Capetti, A., and Giovannini, G. (2015). Pilot study of the radio-emitting AGN population: the emerging new class of FR0 radio-galaxies. *Astronomy & Astrophysics*, 576:A38.

Baldi, R. D., Capetti, A., and Giovannini, G. (2019a). High-resolution VLA observations of FR0 radio galaxies: the properties and nature of compact radio sources. *Monthly Notices of the Royal Astronomical Society*, 482(2):2294–2304.

Baldi, R. D., Torresi, E., Migliori, G., and Balmaverde, B. (2019b). The High Energy View of FR0 Radio Galaxies. *Galaxies*, 7(3):76.

Balmaverde, B., Capetti, A., and Grandi, P. (2006). The Chandra view of the 3C/FR I sample of low luminosity radio-galaxies. *Astronomy & Astrophysics*, 451(1):35–44.

Banfield, J. K., Wong, O., Willett, K. W., Norris, R. P., Rudnick, L., Shabala, S. S., Simmons, B. D., Snyder, C., Garon, A., Seymour, N., et al. (2015). Radio Galaxy Zoo: host galaxies and radio morphologies derived from visual inspection. *Monthly Notices of the Royal Astronomical Society*, 453(3):2326–2340.

Becker, R. H., White, R. L., and Helfand, D. J. (1995). The FIRST survey: faint images of the radio sky at twenty centimeters. *The Astrophysical Journal*, 450:559.

Bekhti, N. B., Flöer, L., Keller, R., Kerp, J., Lenz, D., Winkel, B., Bailin, J., Calabretta, M., Dedes, L., Ford, H., et al. (2016). HI4PI: a full-sky H i survey based on EBHIS and GASS. *Astronomy & Astrophysics*, 594:A116.

Best, P. and Heckman, T. (2012). On the fundamental dichotomy in the local radio-AGN population: accretion, evolution and host galaxy properties. *Monthly Notices of the Royal Astronomical Society*, 421(2):1569–1582.

Bicknell, G. V. (1994). Decelerating relativistic jets, BL-LAC objects, and the Fanaroff-Riley classification.

Bîrzan, L., McNamara, B., Nulsen, P., Carilli, C., and Wise, M. (2008). Radiative efficiency and content of extragalactic radio sources: toward a universal scaling relation between jet power and radio power. *The Astrophysical Journal*, 686(2):859.

Bîrzan, L., Rafferty, D. A., McNamara, B., Wise, M., and Nulsen, P. E. (2004). A systematic study of radio-induced X-ray cavities in clusters, groups, and galaxies. *The Astrophysical Journal*, 607(2):800.

Biviano, A. (2000). From Messier to Abell: 200 years of science with galaxy clusters. *arXiv preprint astro-ph/0010409*.

Bodo, G., Mamatsashvili, G., Rossi, P., and Mignone, A. (2013). Linear stability analysis of magnetized relativistic jets: the non-rotating case. *Monthly Notices of the Royal Astronomical Society*, 434(4):3030–3046.

Böhringer, H. and Werner, N. (2010). X-ray spectroscopy of galaxy clusters: studying astrophysical processes in the largest celestial laboratories. *The Astronomy and Astrophysics Review*, 18(1-2):127–196.

Botteon, A., Gastaldello, F., and Brunetti, G. (2018). Shocks and cold fronts in merging and massive galaxy clusters: new detections with Chandra. *Monthly Notices of the Royal Astronomical Society*, 476(4):5591–5620.

Bower, R. G. and Balogh, M. L. (2004). The difference between clusters. *Clusters of Galaxies: Volume 3, Carnegie Observatories Astrophysics Series: Probes of Cosmological Structure and Galaxy*, 3:325.

Braglia, F. G. (2008). *Study of optical properties and galaxy populations of galaxy clusters*. PhD thesis, lmu.

Bravi, L. (2015). *Connection between X-ray and radio properties of cool-core galaxy clusters hosting radio mini-halos*. PhD thesis.

Bravi, L., Gitti, M., and Brunetti, G. (2016). On the connection between radio mini-halos and gas heating in cool core clusters. *arXiv preprint arXiv:1603.00368*.

Brunetti, G. and Jones, T. W. (2014). Cosmic rays in galaxy clusters and their nonthermal emission. *International Journal of Modern Physics D*, 23(04):1430007.

Bruni, G., Ursini, F., Panessa, F., Bassani, L., Bazzano, A., Bird, A., Chiaraluce, E., Dallacasa, D., Fiocchi, M., Giroletti, M., et al. (2019). Probing restarting activity in hard X-ray selected giant radio galaxies. *arXiv preprint arXiv:1902.01657*.

Bruzual, A. et al. (1983). Spectral evolution of galaxies. I-Early-type systems. *The Astrophysical Journal*, 273:105–127.

Buttiglione, S., Capetti, A., Celotti, A., Axon, D. J., Chiaberge, M., Macchetto, F. D., and Sparks, W. B. (2010). An optical spectroscopic survey of the 3CR sample of radio galaxies with z 0.3-II. Spectroscopic classes and accretion modes in radio-loud AGN. *Astronomy & Astrophysics*, 509:A6.

Bykov, A., Churazov, E., Ferrari, C., Forman, W., Kaastra, J., Klein, U., Markevitch, M., and de Plaa, J. (2015). Structures and components in galaxy clusters: observations and models. *Space Science Reviews*, 188(1-4):141–185.

Capetti, A., Baldi, R. D., Brienza, M., Morganti, R., and Giovannini, G. (2019). The low-frequency properties of FR 0 radio galaxies. *Astronomy & Astrophysics*, 631:A176.

Capetti, A., Brienza, M., Baldi, R., Giovannini, G., Morganti, R., Hardcastle, M., Rottgering, H., Brunetti, G., Best, P., and Miley, G. (2020a). The LOFAR view of FR 0 radio galaxies. *arXiv preprint arXiv:2008.08099*.

Capetti, A., Massaro, F., and Baldi, R. (2020b). Large-scale environment of FR 0 radio galaxies. *Astronomy & Astrophysics*, 633:A161.

Cash, W. (1979). Parameter estimation in astronomy through application of the likelihood ratio. *The Astrophysical Journal*, 228:939–947.

Cassano, R., Gitti, M., and Brunetti, G. (2008). A morphological comparison between giant radio halos and radio mini-halos in galaxy clusters. *Astronomy & Astrophysics*, 486(3):L31–L34.

Cavaliere, A. and Fusco-Femiano, R. (1976). X-rays from hot plasma in clusters of galaxies. *Astronomy and Astrophysics*, 49:137–144.

Cerulo, P., Orellana, G. A., and Covone, G. (2019). The evolution of brightest cluster galaxies in the nearby Universe–I. Colours and stellar masses from the Sloan Digital Sky Survey and Wide Infrared Survey Explorer. *Monthly Notices of the Royal Astronomical Society*, 487(3):3759–3775.

Chen, H., Jones, C., Andrade-Santos, F., ZuHone, J. A., and Li, Z. (2017). Gas sloshing in Abell 2204: constraining the properties of the magnetized intracluster medium. *The Astrophysical Journal*, 838(1):38.

Chen, Y., Reiprich, T., Böhringer, H., Ikebe, Y., and Zhang, Y.-Y. (2007). Statistics of X-ray observables for the cooling-core and non-cooling core galaxy clusters. *Astronomy & Astrophysics*, 466(3):805–812.

Cheng, X.-P. and An, T. (2018). Parsec-scale radio structure of 14 Fanaroff–Riley Type 0 Radio Galaxies. *The Astrophysical Journal*, 863(2):155.

Churazov, E., Forman, W., Jones, C., and Böhringer, H. (2003). XMM-Newton observations of the Perseus cluster. I. The temperature and surface brightness structure. *The Astrophysical Journal*, 590(1):225.

Clarke, T., Blanton, E., and Sarazin, C. (2005). The Radio/X-ray Connection in Abell 2029. *xrrc*, pages 7–08.

Clarke, T. E. (2004). Faraday rotation observations of magnetic fields in galaxy clusters. *arXiv preprint astro-ph/0412268*.

Clowe, D., Gonzalez, A., and Markevitch, M. (2004). Weak-lensing mass reconstruction of the interacting cluster 1E0657–558: Direct evidence for the existence of dark matter. *The Astrophysical Journal*, 604(2):596.

Cohen, A., Lane, W., Cotton, W., Kassim, N., Lazio, T., Perley, R., Condon, J., and Erickson, W. (2007). The VLA low-frequency sky survey. *The Astronomical Journal*, 134(3):1245.

Condon, J. J., Cotton, W., Greisen, E., Yin, Q., Perley, R. A., Taylor, G., and Broderick, J. (1998). The NRAO vla sky survey. *The Astronomical Journal*, 115(5):1693.

Costa, A., Ribeiro, A., and de Carvalho, R. (2018). The shape of velocity dispersion profiles and the dynamical state of galaxy clusters. *Monthly Notices of the Royal Astronomical Society: Letters*, 473(1):L31–L35.

Cowie, L. L. and Songaila, A. (1977). Thermal evaporation of gas within galaxies by a hot intergalactic medium. *nature*, 266(5602):501–503.

Czerny, B. and You, B. (2016). Accretion in active galactic nuclei and disk-jet coupling. *Astronomische Nachrichten*, 337(1-2):73–81.

De Grandi, S., Ettori, S., Longhetti, M., and Molendi, S. (2004). On the iron content in rich nearby clusters of galaxies. *Astronomy & Astrophysics*, 419(1):7–18.

De Lucia, G. and Blaizot, J. (2007). The hierarchical formation of the brightest cluster galaxies. *Monthly Notices of the Royal Astronomical Society*, 375(1):2–14.

de Vaucouleurs, G. (1948). Recherches sur les nebuleuses extragalactiques. In *Annales d'Astrophysique*, volume 11, page 247.

Diaferio, A., Geller, M. J., and Rines, K. J. (2005). Caustic and weak-lensing estimators of galaxy cluster masses. *The Astrophysical Journal Letters*, 628(2):L97.

Diehl, S., Li, H., Fryer, C. L., and Rafferty, D. (2008). Constraining the nature of X-ray cavities in clusters and galaxies. *The Astrophysical Journal*, 687(1):173.

Domainko, W., Gitti, M., Schindler, S., and Kapferer, W. (2004). Feedback from intra-cluster supernovae on the ICM in cooling flow galaxy clusters. *Astronomy & Astrophysics*, 425(2):L21–L24.

Donnert, J., Vazza, F., Brüggen, M., and ZuHone, J. (2018). Magnetic field amplification in galaxy clusters and its simulation. *Space Science Reviews*, 214(8):122.

Doubrawa, L., Machado, R., Laganá, T., Lima Neto, G., Monteiro-Oliveira, R., and Cypriano, E. (2020). Simulations of gas sloshing induced by a newly discovered gas poor substructure in galaxy cluster Abell 1644. *Monthly Notices of the Royal Astronomical Society*, 495(2):2022–2034.

Dressler, A. (1980). Galaxy morphology in rich clusters-implications for the formation and evolution of galaxies. *The Astrophysical Journal*, 236:351–365.

Ebeling, H., Voges, W., Böhringer, H., Edge, A., Huchra, J., and Briel, U. (1996). Properties of the X-ray-brightest Abell-type clusters of galaxies (XBACs) from ROSAT All-Sky Survey data—I. The sample. *Monthly Notices of the Royal Astronomical Society*, 281(3):799–829.

Eckert, D., Molendi, S., and Paltani, S. (2011). The cool-core bias in X-ray galaxy cluster samples-i. method and application to HIFLUGCS. *Astronomy & Astrophysics*, 526:A79.

Edge, A. (2001). The detection of molecular gas in the central galaxies of cooling flow clusters. *Monthly Notices of the Royal Astronomical Society*, 328(3):762–782.

Edge, A., Stewart, G., and Fabian, A. (1992). Properties of cooling flows in a flux-limited sample of clusters of galaxies. *Monthly Notices of the Royal Astronomical Society*, 258(1):177–188.

Ehlert, S., Werner, N., Simionescu, A., Allen, S., Kenney, J., Million, E., and Finoguenov, A. (2013). Ripping apart at the seams: the network of stripped gas surrounding M86. *Monthly Notices of the Royal Astronomical Society*, 430(3):2401–2410.

Eke, V. R., Navarro, J. F., and Frenk, C. S. (1998). The evolution of x-ray clusters in a low-density universe. *The Astrophysical Journal*, 503(2):569.

Ettori, S. and Fabian, A. (2000). Chandra constraints on the thermal conduction in the intracluster plasma of A2142. *Monthly Notices of the Royal Astronomical Society*, 317(3):L57–L59.

Evans, D., Lee, J., Hardcastle, M., Kraft, R., Turner, J., Worral, D., Birkinshaw, M., and Croston, J. (2016). Energy transport processes in radio-loud Active Galactic Nuclei.

Fabian, A. (2002). Cluster cores and cooling flows. *arXiv preprint astro-ph/0210150*.

Fabian, A., Arnaud, K., Bautz, M., and Tawara, Y. (1994). ASCA observations of cooling flows in clusters of galaxies. *The Astrophysical Journal*, 436:L63–L66.

Fabian, A., Mushotzky, R., Nulsen, P. E., and Peterson, J. (2001). On the soft X-ray spectrum of cooling flows. *Monthly Notices of the Royal Astronomical Society*, 321(1):L20–L24.

Fabian, A., Sanders, J. S., Taylor, G., Allen, S., Crawford, C., Johnstone, R., and Iwasawa, K. (2006). A very deep Chandra observation of the Perseus cluster: shocks, ripples and conduction. *Monthly Notices of the Royal Astronomical Society*, 366(2):417–428.

Fabian, A. C. (1994). Cooling flows in clusters of galaxies. *Annual Review of Astronomy and Astrophysics*, 32(1):277–318.

Fanaroff, B. L. and Riley, J. M. (1974). The morphology of extragalactic radio sources of high and low luminosity. *Monthly Notices of the Royal Astronomical Society*, 167(1):31P–36P.

Feretti, L. and Giovannini, G. (2008). Clusters of galaxies in the radio: relativistic plasma and ICM/radio galaxy interaction processes. In *A Pan-Chromatic View of Clusters of Galaxies and the Large-Scale Structure*, pages 143–176. Springer.

Feretti, L., Giovannini, G., Govoni, F., and Murgia, M. (2012). Clusters of galaxies: observational properties of the diffuse radio emission. *The Astronomy and Astrophysics Review*, 20(1):54.

Fruscione, A., McDowell, J. C., Allen, G. E., Brickhouse, N. S., Burke, D. J., Davis, J. E., Durham, N., Elvis, M., Galle, E. C., Harris, D. E., et al. (2006). CIAO: Chandra's data analysis system. In *Observatory Operations: Strategies, Processes, and Systems*, volume 6270, page 62701V. International Society for Optics and Photonics.

Garofalo, D. and Singh, C. B. (2019). FR0 radio galaxies and their place in the radio morphology classification. *The Astrophysical Journal*, 871(2):259.

Ghisellini, G. and Celotti, A. (2001). The dividing line between FR I and FR II radio-galaxies. *Astronomy & Astrophysics*, 379(1):L1–L4.

Ghizzardi, S., Rossetti, M., and Molendi, S. (2010). Cold fronts in galaxy clusters. *Astronomy & Astrophysics*, 516:A32.

Giacintucci, S., Markevitch, M., Brunetti, G., ZuHone, J. A., Venturi, T., Mazzotta, P., and Bourdin, H. (2014). Mapping the particle acceleration in the cool core of the galaxy cluster RX J1720. 1+ 2638. *The Astrophysical Journal*, 795(1):73.

Giacintucci, S., Markevitch, M., Cassano, R., Venturi, T., Clarke, T. E., Kale, R., and Cuciti, V. (2019). Expanding the sample of radio minihalos in galaxy clusters. *The Astrophysical Journal*, 880(2):70.

Giacintucci, S., Markevitch, M., Johnston-Hollitt, M., Wik, D., Wang, Q., and Clarke, T. (2020). Discovery of a giant radio fossil in the Ophiuchus galaxy cluster. *The Astrophysical Journal*, 891(1):1.

Giacintucci, S., Markevitch, M., Venturi, T., Clarke, T. E., Cassano, R., and Mazzotta, P. (2013). New detections of radio minihalos in cool cores of galaxy clusters. *The Astrophysical Journal*, 781(1):9.

Giodini, S., Lovisari, L., Pointecouteau, E., Ettori, S., Reiprich, T., and Hoekstra, H. (2013). Scaling relations for galaxy clusters: properties and evolution. *Space Science Reviews*, 177(1-4):247–282.

Gitti, M., Brighenti, F., and McNamara, B. R. (2012). Evidence for AGN feedback in galaxy clusters and groups. *Advances in Astronomy*, 2012.

Gitti, M., Brunetti, G., Cassano, R., and Ettori, S. (2018). Radio-continuum surveys with SKA and LOFAR: a first look at the perspectives for radio mini-halos. *Astronomy & Astrophysics*, 617:A11.

Gitti, M., Brunetti, G., Feretti, L., and Setti, G. (2004). Particle acceleration in cooling flow clusters of galaxies: the case of Abell 2626. *Astronomy & Astrophysics*, 417(1):1–11.

Gitti, M., Brunetti, G., and Setti, G. (2002). Modeling the interaction between ICM and relativistic plasma in cooling flows: The case of the Perseus cluster. *Astronomy & Astrophysics*, 386(2):456–463.

Govoni, F. and Feretti, L. (2004). Magnetic fields in clusters of galaxies. *International Journal of Modern Physics D*, 13(08):1549–1594.

Graham, J., Fabian, A., and Sanders, J. (2008). Detecting sound-wave-like surface brightness ripples in cluster cores. *Monthly Notices of the Royal Astronomical Society*, 391(4):1749–1757.

Grandi, P., Capetti, A., and Baldi, R. D. (2016). Discovery of a Fanaroff–Riley type 0 radio galaxy emitting at γ-ray energies. *Monthly Notices of the Royal Astronomical Society*, 457(1):2–8.

Gunn, J. E. and Gott III, J. R. (1972). On the infall of matter into clusters of galaxies and some effects on their evolution. *The Astrophysical Journal*, 176:1.

Haarsma, D. B., Leisman, L., Donahue, M., Bruch, S., Böhringer, H., Croston, J. H., Pratt, G. W., Voit, G. M., Arnaud, M., and Pierini, D. (2010). Brightest Cluster Galaxies and Core Gas Density in REXCESS Clusters. *The Astrophysical Journal*, 713(2):1037.

Hamer, S., Edge, A., Swinbank, A., Wilman, R., Combes, F., Salomé, P., Fabian, A., Crawford, C., Russell, H., Hlavacek-Larrondo, J., et al. (2016). Optical emission line nebulae in galaxy cluster cores 1: the morphological, kinematic and spectral properties of the sample. *Monthly Notices of the Royal Astronomical Society*, 460(2):1758–1789.

Hardcastle, M., Evans, D., and Croston, J. (2007). Hot and cold gas accretion and feedback in radio-loud active galaxies. *Monthly Notices of the Royal Astronomical Society*, 376(4):1849–1856.

Heckman, T. (1981). Optical emission-line gas associated with dominant cluster galaxies. *The Astrophysical Journal*, 250:L59–L63.

Heckman, T. M., Kauffmann, G., Brinchmann, J., Charlot, S., Tremonti, C., and White, S. D. (2004). Present-day growth of black holes and bulges: the Sloan Digital Sky Survey perspective. *The Astrophysical Journal*, 613(1):109.

Hill, G. J. and Lilly, S. J. (1991). A change in the cluster environments of radio galaxies with cosmic epoch. *The Astrophysical Journal*, 367:1–18.

Hlavacek-Larrondo, J., Allen, S., Taylor, G., Fabian, A., Canning, R., Werner, N., Sanders, J., Grimes, C., Ehlert, S., and von der Linden, A. (2013). Probing the Extreme Realm of Active Galactic Nucleus Feedback in the Massive Galaxy Cluster, RX J1532. 9+ 3021. *The Astrophysical Journal*, 777(2):163.

Hlavacek-Larrondo, J., McDonald, M., Benson, B., Forman, W., Allen, S., Bleem, L., Ashby, M., Bocquet, S., Brodwin, M., Dietrich, J., et al. (2015). X-ray cavities in a sample of 83 spt-selected clusters of galaxies: Tracing the evolution of agn feedback in clusters of galaxies out to z= 1.2. *The Astrophysical Journal*, 805(1):35.

Hoekstra, H., Bartelmann, M., Dahle, H., Israel, H., Limousin, M., and Meneghetti, M. (2013). Masses of galaxy clusters from gravitational lensing. *Space Science Reviews*, 177(1-4):75–118.

Hogan, M., Edge, A., Hlavacek-Larrondo, J., Grainge, K., Hamer, S., Mahony, E., Russell, H., Fabian, A., McNamara, B., and Wilman, R. (2015). A comprehensive study of the radio properties of brightest cluster galaxies. *Monthly Notices of the Royal Astronomical Society*, 453(2):1201–1222.

Hudson, D. S., Mittal, R., Reiprich, T. H., Nulsen, P. E., Andernach, H., and Sarazin, C. L. (2010). What is a cool-core cluster? a detailed analysis of the cores of the X-ray flux-limited HIFLUGCS cluster sample. *Astronomy & Astrophysics*, 513:A37.

Hurley-Walker, N., Callingham, J. R., Hancock, P. J., Franzen, T. M., Hindson, L., Kapińska, A., Morgan, J., Offringa, A. R., Wayth, R. B., Wu, C., et al. (2017). GaLactic and Extragalactic All-sky Murchison Widefield Array (GLEAM) survey–I. A low-frequency extragalactic catalogue. *Monthly Notices of the Royal Astronomical Society*, 464(1):1146–1167.

Ichinohe, Y., Simionescu, A., Werner, N., Fabian, A., and Takahashi, T. (2019). Substructures associated with the sloshing cold front in the Perseus cluster. *Monthly Notices of the Royal Astronomical Society*, 483(2):1744–1753.

Ichinohe, Y., Werner, N., Simionescu, A., Allen, S., Canning, R., Ehlert, S., Mernier, F., and Takahashi, T. (2015). The growth of the galaxy cluster Abell 85: mergers, shocks, stripping and seeding of clumping. *Monthly Notices of the Royal Astronomical Society*, 448(3):2971–2986.

Intema, H., Jagannathan, P., Mooley, K., and Frail, D. (2017). The GMRT 150 MHz all-sky radio survey-First alternative data release TGSS ADR1. *Astronomy & Astrophysics*, 598:A78.

Kaiser, N. (1986). Evolution and clustering of rich clusters. *Monthly Notices of the Royal Astronomical Society*, 222(2):323–345.

Kashlinsky, A. and Jones, B. J. (1991). Large-scale structure in the Universe. *Nature*, 349(6312):753–760.

Kellermann, K. I., Sramek, R., Schmidt, M., Shaffer, D. B., and Green, R. (1989). VLA Observations of Objects in the Palomar Bright Quasar Survey. *The Astrophysical Journal*, 98:1195.

King, I. R. (1972). Density data and emission measure for a model of the Coma cluster. *The Astrophysical Journal*, 174:L123.

Kokotanekov, G., Wise, M., Heald, G., McKean, J., Bîrzan, L., Rafferty, D., Godfrey, L., De Vries, M., Intema, H. T., Broderick, J., et al. (2017). LOFAR MSSS: The scaling relation between AGN cavity power and radio luminosity at low radio frequencies. *Astronomy & Astrophysics*, 605:A48.

Kolokythas, K., O'Sullivan, E., Giacintucci, S., Worrall, D. M., Birkinshaw, M., Raychaudhury, S., Horellou, C., Intema, H., and Loubser, I. (2020). Evidence of AGN feedback and sloshing in the X-ray luminous NGC 1550 galaxy group. *Monthly Notices of the Royal Astronomical Society*.

Kunert-Bajraszewska, M., Gawroński, M., Labiano, A., and Siemiginowska, A. (2010). A survey of low-luminosity compact sources and its implication for the evolution of radio-loud active galactic nuclei–i. radio data. *Monthly Notices of the Royal Astronomical Society*, 408(4):2261–2278.

Laing, R., Jenkins, C., Wall, J., and Unger, S. (1994). The First Stromlo Symposium: The Physics of Active Galaxies. *GV Bicknell, MA Dopita, & PJ Quinn (San Francisco, CA: ASP)*, 201.

Lal, D. V., Kraft, R. P., Randall, S. W., Forman, W. R., Nulsen, P. E., Roediger, E., ZuHone, J. A., Hardcastle, M. J., Jones, C., and Croston, J. H. (2013). Gas sloshing and radio galaxy dynamics in the core of the 3C 449 group. *The Astrophysical Journal*, 764(1):83.

Lau, E. T., Kravtsov, A. V., and Nagai, D. (2009). Residual gas motions in the intracluster medium and bias in hydrostatic measurements of mass profiles of clusters. *The Astrophysical Journal*, 705(2):1129.

Longair, M. S. (2011). *High energy astrophysics*. Cambridge university press.

Lyutikov, M. (2006). Magnetic draping of merging cores and radio bubbles in clusters of galaxies. *Monthly Notices of the Royal Astronomical Society*, 373(1):73–78.

Macconi, D. (2019). *Radio morphology-accretion mode link in FRII low-excitation radio galaxies*. PhD thesis.

Macconi, D., Torresi, E., Grandi, P., Boccardi, B., and Vignali, C. (2020). Radio morphology–accretion mode link in Fanaroff–Riley type II low-excitation radio galaxies. *Monthly Notices of the Royal Astronomical Society*, 493(3):4355–4366.

Madrid, J. P., O'Neill, C. R., Gagliano, A. T., and Marvil, J. R. (2018). A wide-field map of intracluster globular clusters in Coma. *The Astrophysical Journal*, 867(2):144.

Markevitch, M. (2005). Chandra observation of the most interesting cluster in the universe. *arXiv preprint astro-ph/0511345*.

Markevitch, M., Ponman, T., Nulsen, P., Bautz, M., Burke, D., David, L., Davis, D., Donnelly, R., Forman, W., Jones, C. c., et al. (2000). Chandra observation of Abell 2142: Survival of dense subcluster cores in a merger. *The Astrophysical Journal*, 541(2):542.

Markevitch, M. and Vikhlinin, A. (2007). Shocks and cold fronts in galaxy clusters. *Physics Reports*, 443(1):1–53.

Markevitch, M., Vikhlinin, A., and Mazzotta, P. (2001). Nonhydrostatic gas in the core of the relaxed galaxy cluster A1795. *The Astrophysical Journal Letters*, 562(2):L153.

Mathews, W. G. and Brighenti, F. (2003). Hot gas in and around elliptical galaxies. *Annual Review of Astronomy and Astrophysics*, 41(1):191–239.

Maughan, B., Giles, P., Randall, S., Jones, C., and Forman, W. (2012). Self-similar scaling and evolution in the galaxy cluster X-ray luminosity–temperature relation. *Monthly Notices of the Royal Astronomical Society*, 421(2):1583–1602.

McDonald, M., Allen, S., Bayliss, M., Benson, B., Bleem, L., Brodwin, M., Bulbul, E., Carlstrom, J., Forman, W., Hlavacek-Larrondo, J., et al. (2017). The remarkable similarity of massive galaxy clusters from z 0 to z 1.9. *The Astrophysical Journal*, 843(1):28.

McDonald, M., Gaspari, M., McNamara, B., and Tremblay, G. (2018). Revisiting the cooling flow problem in galaxies, groups, and clusters of galaxies. *The Astrophysical Journal*, 858(1):45.

McNamara, B. and Nulsen, P. (2007). Heating hot atmospheres with active galactic nuclei. *Annu. Rev. Astron. Astrophys.*, 45:117–175.

McNamara, B. and Nulsen, P. (2012). Mechanical feedback from active galactic nuclei in galaxies, groups and clusters. *New Journal of Physics*, 14(5):055023.

McNamara, B., Nulsen, P., Wise, M., Rafferty, D., Carilli, C., Sarazin, C., and Blanton, E. (2005). The heating of gas in a galaxy cluster by X-ray cavities and large-scale shock fronts. *nature*, 433(7021):45–47.

McNamara, B. R., Wise, M., and Murray, S. (2004). The insignificance of global reheating in the A1068 cluster: Multiwavelength analysis. *The Astrophysical Journal*, 601(1):173.

Melnick, J. and Sargent, W. (1977). The radial distribution of morphological types of galaxies in X-ray clusters. *The Astrophysical Journal*, 215:401–407.

Merloni, A. and Heinz, S. (2007). Measuring the kinetic power of active galactic nuclei in the radio mode. *Monthly Notices of the Royal Astronomical Society*, 381(2):589–601.

Merloni, A., Heinz, S., and Di Matteo, T. (2003). A fundamental plane of black hole activity. *Monthly Notices of the Royal Astronomical Society*, 345(4):1057–1076.

Mernier, F., de Plaa, J., Kaastra, J. S., Zhang, Y.-Y., Akamatsu, H., Gu, L., Kosec, P., Mao, J., Pinto, C., Reiprich, T. H., et al. (2017). Radial metal abundance profiles in the intra-cluster medium of cool-core galaxy clusters, groups, and ellipticals. *Astronomy & Astrophysics*, 603:A80.

Meyer, F., Liu, B., and Meyer-Hofmeister, E. (2007). Re-condensation from an ADAF into an inner disk: the intermediate state of black hole accretion? *Astronomy & Astrophysics*, 463(1):1–9.

Middelberg, E. and Bach, U. (2008). High resolution radio astronomy using very long baseline interferometry. *Reports on Progress in Physics*, 71(6):066901.

Mohr, J. J., Fabricant, D. G., and Geller, M. J. (1993). An X-ray method for detecting substructure in galaxy clusters-application to Perseus, A2256, Centaurus, Coma, and Sersic 40/6. *The Astrophysical Journal*, 413:492–505.

Mohr, J. J., Mathiesen, B., and Evrard, A. E. (1999). Properties of the intracluster medium in an ensemble of nearby galaxy clusters. *The Astrophysical Journal*, 517(2):627.

Molendi, S. (2004). The intra-cluster medium. In *AIP Conference Proceedings*, volume 703, pages 345–354. American Institute of Physics.

Moore, B., Katz, N., Lake, G., Dressler, A., and Oemler, A. (1996). Galaxy harassment and the evolution of clusters of galaxies. *nature*, 379(6566):613–616.

Morris, R. and Fabian, A. (2003). Some effects of small-scale metallicity variations in cooling flows. *Monthly Notices of the Royal Astronomical Society*, 338(4):824–836.

Morsony, B. J., Heinz, S., Brüggen, M., and Ruszkowski, M. (2010). Swimming against the current: simulations of central AGN evolution in dynamic galaxy clusters. *Monthly Notices of the Royal Astronomical Society*, 407(2):1277–1289.

Murgia, M., Eckert, D., Govoni, F., Ferrari, C., Pandey-Pommier, M., Nevalainen, J., and Paltani, S. (2010). Gmrt observations of the ophiuchus galaxy cluster. *Astronomy & Astrophysics*, 514:A76.

Mushotzky, R. and Szymkowiak, A. (1988). Einstein Observatory solid state detector observations of cooling flows in clusters of galaxies. In *Cooling flows in clusters and galaxies*, pages 53–62.

Narayan, R. and Yi, I. (1994). Advection-dominated accretion: A self-similar solution. *arXiv preprint astro-ph/9403052*.

Navarro, J. F., Frenk, C. S., and White, S. D. (1995). Simulations of X-ray clusters. *Monthly Notices of the Royal Astronomical Society*, 275(3):720–740.

Nulsen, P. (1982). Transport processes and the stripping of cluster galaxies. *Monthly Notices of the Royal Astronomical Society*, 198(4):1007–1016.

Nulsen, P. E., McNamara, B., Wise, M., and David, L. (2005). The cluster-scale AGN outburst in Hydra A. *The Astrophysical Journal*, 628(2):629.

O'Sullivan, E., Giacintucci, S., David, L. P., Gitti, M., Vrtilek, J. M., Raychaudhury, S., and Ponman, T. J. (2011). Heating the hot atmospheres of galaxy groups and clusters with cavities: the relationship between jet power and low-frequency radio emission. *The Astrophysical Journal*, 735(1):11.

Padovani, P., Alexander, D., Assef, R., De Marco, B., Giommi, P., Hickox, R., Richards, G., Smolčić, V., Hatziminaoglou, E., Mainieri, V., et al. (2017). Active galactic nuclei: what's in a name? *The Astronomy and Astrophysics Review*, 25(1):2.

Parma, P., Fanti, C., Fanti, R., Morganti, R., and De Ruiter, H. (1987). VLA observations of low-luminosity radio galaxies. VI-Discussion of radio jets. *Astronomy and Astrophysics*, 181:244–264.

Pasini, T., Gitti, M., Brighenti, F., Temi, P., Amblard, A., Hamer, S., Ettori, S., O'Sullivan, E., and Gastaldello, F. (2019). A BCG with offset cooling: is the AGN feedback cycle broken in A2495? *The Astrophysical Journal*, 885(2):111.

Patel, P., Maddox, S., Pearce, F. R., Aragón-Salamanca, A., and Conway, E. (2006). An imaging survey of a uniform sample of brightest cluster galaxies and intracluster light. *Monthly Notices of the Royal Astronomical Society*, 370(2):851–883.

Paterno-Mahler, R., Blanton, E. L., Randall, S. W., and Clarke, T. E. (2013). Deep Chandra observations of the extended gas sloshing spiral in A2029. *The Astrophysical Journal*, 773(2):114.

Peng, Y., Maiolino, R., and Cochrane, R. (2015). Strangulation as the primary mechanism for shutting down star formation in galaxies. *Nature*, 521(7551):192–195.

Peterson, J. R. and Fabian, A. C. (2006). X-ray spectroscopy of cooling clusters. *Physics reports*, 427(1):1–39.

Poggianti, B. and Barbaro, G. (1997). Indicators of star formation: 4000 Angstrom break and Balmer lines. *arXiv preprint astro-ph/9703067*.

Rafferty, D., McNamara, B., and Nulsen, P. (2008). The regulation of cooling and star formation in luminous galaxies by active galactic nucleus feedback and the cooling-time/entropy threshold for the onset of star formation. *The Astrophysical Journal*, 687(2):899.

Rafferty, D., McNamara, B., Nulsen, P., and Wise, M. (2006). The feedback-regulated growth of black holes and bulges through gas accretion and starbursts in cluster central dominant galaxies. *The Astrophysical Journal*, 652(1):216.

Rasia, E., Ettori, S., Moscardini, L., Mazzotta, P., Borgani, S., Dolag, K., Tormen, G., Cheng, L., and Diaferio, A. (2006). Systematics in the X-ray cluster mass estimators. *Monthly Notices of the Royal Astronomical Society*, 369(4):2013–2024.

Rebusco, P., Churazov, E., Böhringer, H., and Forman, W. (2005). Impact of stochastic gas motions on galaxy cluster abundance profiles. *Monthly Notices of the Royal Astronomical Society*, 359(3):1041–1048.

Richard-Laferrière, A., Hlavacek-Larrondo, J., Nemmen, R., Rhea, C., Taylor, G., Prasow-Émond, M., Gendron-Marsolais, M., Latulippe, M., Edge, A., Fabian, A., et al. (2020). On the relation between mini-halos and AGN feedback in clusters of galaxies. *arXiv preprint arXiv:2007.01306*.

Rines, K., Geller, M. J., Diaferio, A., and Kurtz, M. J. (2013). Measuring the ultimate halo mass of galaxy clusters: Redshifts and mass profiles from the hectospec cluster survey (HECS). *The Astrophysical Journal*, 767(1):15.

Roediger, E., Brüggen, M., Simionescu, A., Böhringer, H., Churazov, E., and Forman, W. R. (2011). Gas sloshing, cold front formation and metal redistribution: the Virgo cluster as a quantitative test case. *Monthly Notices of the Royal Astronomical Society*, 413(3):2057–2077.

Roediger, E., Lovisari, L., Dupke, R., Ghizzardi, S., Brüggen, M., Kraft, R., and Machacek, M. (2012). Gas sloshing, cold fronts, Kelvin–Helmholtz instabilities and the merger history of the cluster of galaxies Abell 496. *Monthly Notices of the Royal Astronomical Society*, 420(4):3632–3648.

Rossetti, M., Gastaldello, F., Ferioli, G., Bersanelli, M., De Grandi, S., Eckert, D., Ghizzardi, S., Maino, D., and Molendi, S. (2016). Measuring the dynamical state of Planck SZ-selected clusters: X-ray peak–BCG offset. *Monthly Notices of the Royal Astronomical Society*, 457(4):4515–4524.

Rudnick, L. and OwEN, F. N. (1976). Head-tail radio sources in clusters of galaxies. *The Astrophysical Journal*, 203:L107–L111.

Russell, H., McNamara, B., Fabian, A., Nulsen, P., Combes, F., Edge, A., Madar, M., Olivares, V., Salomé, P., and Vantyghem, A. (2019). Driving massive molecular gas flows in central cluster galaxies with agn feedback. *Monthly Notices of the Royal Astronomical Society*, 490(3):3025–3045.

Ruszkowski, M., Brüggen, M., and Begelman, M. C. (2004). Cluster heating by viscous dissipation of sound waves. *The Astrophysical Journal*, 611(1):158.

Rykoff, E., Rozo, E., Busha, M., Cunha, C., Finoguenov, A., Evrard, A., Hao, J., Koester, B., Leauthaud, A., Nord, B., et al. (2014). Redmapper. I. algorithm and SDSS dr8 catalog. *The Astrophysical Journal*, 785(2):104.

Sanders, J., Fabian, A., Russell, H., Walker, S., and Blundell, K. (2016). Detecting edges in the X-ray surface brightness of galaxy clusters. *Monthly Notices of the Royal Astronomical Society*, 460(2):1898–1911.

Sanderson, A. J., O'Sullivan, E., and Ponman, T. J. (2009). A statistically selected Chandra sample of 20 galaxy clusters–II. Gas properties and cool core/non-cool core bimodality. *Monthly Notices of the Royal Astronomical Society*, 395(2):764–776.

Santos, J. S., Rosati, P., Tozzi, P., Böhringer, H., Ettori, S., and Bignamini, A. (2008). Searching for cool core clusters at high redshift. *Astronomy & Astrophysics*, 483(1):35–47.

Sarazin, C. L. (1986). X-ray emission from clusters of galaxies. *Reviews of Modern Physics*, 58(1):1.

Savini, F., Bonafede, A., Brueggen, M., Rafferty, D., Shimwell, T., Botteon, A., Brunetti, G., Intema, H., Wilber, A., Cassano, R., et al. (2019). A LOFAR study of non-merging massive galaxy clusters. *Astronomy & Astrophysics*, 622:A24.

Schombert, J. M. (1986). The structure of brightest cluster members. i-surface photometry. *The Astrophysical Journal Supplement Series*, 60:603–693.

Sebastian, B., Lal, D. V., and Rao, A. P. (2017). Giant Metrewave Radio Telescope Observations of head–tail radio galaxies. *The Astronomical Journal*, 154(4):169.

Shakura, N. I. and Sunyaev, R. A. (1973). Black holes in binary systems. Observational appearance. *Astronomy and Astrophysics*, 24:337–355.

Su, Y., Nulsen, P. E., Kraft, R. P., Roediger, E., ZuHone, J. A., Jones, C., Forman, W. R., Sheardown, A., Irwin, J. A., and Randall, S. W. (2017). Gas sloshing regulates and records the evolution of the Fornax cluster. *The Astrophysical Journal*, 851(1):69.

Sun, M., Jones, C., Forman, W., Vikhlinin, A., Donahue, M., and Voit, M. (2007). X-ray thermal coronae of galaxies in hot clusters: ubiquity of embedded mini-cooling cores. *The Astrophysical Journal*, 657(1):197.

Sutherland, R. S. and Dopita, M. A. (1993). Cooling functions for low-density astrophysical plasmas. *The Astrophysical Journal Supplement Series*, 88:253–327.

Tabor, G. and Binney, J. (1993). Elliptical galaxy cooling flows without mass drop-out. *Monthly Notices of the Royal Astronomical Society*, 263(2):323–334.

Tadhunter, C. (2016). Radio AGN in the local universe: unification, triggering and evolution. *The Astronomy and Astrophysics Review*, 24(1):10.

Temi, P., Brighenti, F., Mathews, W. G., and Bregman, J. D. (2004). Cold dust in early-type galaxies. I. Observations. *The Astrophysical Journal Supplement Series*, 151(2):237.

Torresi, E., Grandi, P., Capetti, A., Baldi, R. D., and Giovannini, G. (2018). X-ray study of a sample of FR0 radio galaxies: unveiling the nature of the central engine. *Monthly Notices of the Royal Astronomical Society*, 476(4):5535–5547.

Tremaine, S., Gebhardt, K., Bender, R., Bower, G., Dressler, A., Faber, S. M., Filippenko, A. V., Green, R., Grillmair, C., Ho, L. C., et al. (2002). The slope of the black hole mass versus velocity dispersion correlation. *The Astrophysical Journal*, 574(2):740.

Ueda, S., Ichinohe, Y., Kitayama, T., and Umetsu, K. (2019). Line-of-sight gas sloshing in the cool core of Abell 907. *The Astrophysical Journal*, 871(2):207.

Urry, C. M. and Padovani, P. (1995). Unified schemes for radio-loud active galactic nuclei. *Publications of the Astronomical Society of the Pacific*, 107(715):803.

Van Haarlem, M. P., Wise, M. W., Gunst, A., Heald, G., McKean, J. P., Hessels, J. W., de Bruyn, A. G., Nijboer, R., Swinbank, J., Fallows, R., et al. (2013). LOFAR: The low-frequency array. *Astronomy & astrophysics*, 556:A2.

Van Weeren, R., de Gasperin, F., Akamatsu, H., Brüggen, M., Feretti, L., Kang, H., Stroe, A., and Zandanel, F. (2019). Diffuse radio emission from galaxy clusters. *Space Science Reviews*, 215(1):16.

Van Weeren, R., Intema, H., Lal, D., Andrade-Santos, F., Brüggen, M., De Gasperin, F., Forman, W., Hoeft, M., Jones, C., Nuza, S., et al. (2014). A distant radio mini-halo in the Phoenix galaxy cluster. *The Astrophysical Journal Letters*, 786(2):L17.

Vantyghem, A., McNamara, B., Russell, H., Edge, A., Nulsen, P., Combes, F., Fabian, A., McDonald, M., and Salomé, P. (2019). An enormous molecular gas flow in the RX J0821+ 0752 galaxy cluster. *The Astrophysical Journal*, 870(2):57.

Vantyghem, A., McNamara, B., Russell, H., Main, R., Nulsen, P., Wise, M., Hoekstra, H., and Gitti, M. (2014). Cycling of the powerful AGN in MS 0735.6+ 7421 and the duty cycle of radio AGN in clusters. *Monthly Notices of the Royal Astronomical Society*, 442(4):3192–3205.

Vikhlinin, A., Burenin, R., Ebeling, H., Forman, W., Hornstrup, A., Jones, C., Kravtsov, A., Murray, S., Nagai, D., Quintana, H., et al. (2009). Chandra cluster cosmology project. II. samples and X-ray data reduction. *The Astrophysical Journal*, 692(2):1033.

Vikhlinin, A., Markevitch, M., and Murray, S. (2001). A moving cold front in the intergalactic medium of A3667. *The Astrophysical Journal*, 551(1):160.

Voigt, L., Schmidt, R., Fabian, A., Allen, S., and Johnstone, R. (2002). Conduction and cooling flows. *Monthly Notices of the Royal Astronomical Society*, 335(1):L7–L11.

Voit, G. M. (2005). Tracing cosmic evolution with clusters of galaxies. *Reviews of Modern Physics*, 77(1):207.

White, S. D. and Rees, M. J. (1978). Core condensation in heavy halos: a two-stage theory for galaxy formation and clustering. *Monthly Notices of the Royal Astronomical Society*, 183(3):341–358.

Whitmore, B. C. and Gilmore, D. M. (1991). On the interpretation of the morphology-density relation for galaxies in clusters. *The Astrophysical Journal*, 367:64–68.

Wootten, A. and Thompson, A. R. (2009). The Atacama large millimeter/submillimeter array. *Proceedings of the IEEE*, 97(8):1463–1471.

Wu, Q. (2009). The black hole mass, Eddington ratio and M BH–σ [OIII] relation in young radio galaxies. *Monthly Notices of the Royal Astronomical Society*, 398(4):1905–1914.

Xue, Y.-J. and Wu, X.-P. (2000). The Lx-T, Lx-σ, and σ-T relations for groups and clusters of galaxies. *The Astrophysical Journal*, 538(1):65.

Zhang, Y. (2016). Looking wider and further: The evolution of galaxies inside galaxy clusters. Technical report.

ZuHone, J., Brunetti, G., Giacintucci, S., and Markevitch, M. (2015). Testing secondary models for the origin of radio mini-halos in galaxy clusters. *The Astrophysical Journal*, 801(2):146.

ZuHone, J., Markevitch, M., Brunetti, G., and Giacintucci, S. (2012a). Turbulence and radio mini-halos in the sloshing cores of galaxy clusters. *The Astrophysical Journal*, 762(2):78.

ZuHone, J., Markevitch, M., Ruszkowski, M., and Lee, D. (2012b). Cold fronts and gas sloshing in galaxy clusters with anisotropic thermal conduction. *The Astrophysical Journal*, 762(2):69.

ZuHone, J. A. and Roediger, E. (2016). Cold fronts: probes of plasma astrophysics in galaxy clusters. *Journal of Plasma Physics*, 82(3).

Zwicky, F. (1937). On the masses of nebulae and of clusters of nebulae. *The Astrophysical Journal*, 86:217.

Ringraziamenti

Non ho alcun dubbio quando affermo che l'impegno speso per portare a termine questo percorso è stato completamente ripagato dalla gioia di potermi dedicare all'astrofisica. Questa possibilità la devo ad alcune persone che vorrei ricordare qui, al termine di questo elaborato, ma che sono state presenti durante la scrittura di ogni pagina.
Inizio da chi ha seguito il mio lavoro in questi mesi: ringrazio la mia relatrice, professoressa Myriam Gitti, per l'attenzione dedicata a questo progetto, per la sua disponibilità e professionalità. Ringrazio il mio correlatore, professor Fabrizio Brighenti, per i validi e preziosi suggerimenti su alcuni aspetti complessi dell'analisi. Ci terrei anche a ringraziare entrambi per l'impegno che dedicate al corso *Ammassi di Galassie*, che è stato fonte di ispirazione e di grande interesse per me. Ringrazio la mia correlatrice, dottoressa Torresi, e la professoressa Grandi, per l'insostituibile contributo a questo lavoro.
Ringrazio i miei genitori per avermi sostenuto in questi anni e per avermi sempre incoraggiato a fare ciò che mi rende felice. Grazie a voi e a mia sorella Sara, per la curiosità che dimostrate ogni volta che parliamo di astrofisica. Ringrazio anche Giada, per la felicità che mi ha regalato essere compagni di questo viaggio, e Davide, per la spensieratezza di ogni momento condiviso.
In questi cinque anni, ogni giorno è stato reso più leggero da una persona che ha sempre saputo quale fosse la cosa giusta da fare, che ammiro per l'affetto che ha saputo riservarmi, e per la profonda intelligenza che dimostra in ogni gesto. Grazie Villiam.

Grazie a tutti.